

UNIVERSITÀ
DEGLI STUDI
DI PADOVA

Head office: Università degli Studi di Padova

Department of Chemical Sciences

Ph.D. COURSE IN SCIENCE AND ENGINEERING OF MATERIALS AND
NANOSTRUCTURES

XXXV CYCLE

**DESIGN, REALIZATION AND CHARACTERIZATION OF INNOVATIVE
ANODE MATERIALS FOR LOW AND INTERMEDIATE TEMPERATURE
DIRECT METHANE SOLID OXIDE FUEL CELLS**

Coordinator: Ch.mo Prof. Giovanni Mattei

Supervisor: Ch.mo Prof. Antonella Glisenti

Ph.D. Candidate: Enrico Squizzato

"We happy? Vincent!?! We happy?"

"Yeah, we are happy!"

(Pulp Fiction)

Summary

ABSTRACT	9
Chapter 1: Introduction	11
1.1 <i>Overview</i>	11
1.2 <i>A sustainable device: Fuel Cell</i>	14
1.2.1 Fuel cell introduction	14
1.2.2 Fuel cell typologies	15
1.2.3 Solid Oxide Fuel Cell (SOFC) theory	18
1.2.4 Reversible SOC (R-SOC)	23
1.2.5 Symmetrical SOFC (S-SOFC)	24
1.2.6 SOFC challenges	25
1.2.7 SOFC thermodynamic	26
1.2.8 From Hydrogen to Methane	28
1.2.9 Methane from Biogas: it's green!	29
1.2.10 Methane oxidation reaction	30
1.3 <i>Lowering of the operating temperatures</i>	34
1.4 <i>Peroovskites</i>	36
1.5 <i>Outline and aim of the thesis</i>	38
Chapter 2: Characterization techniques and cell fabrication	45
2.1 <i>X-Ray Diffraction (XRD)</i>	45
2.2 <i>H₂-Temperature Programmed Reduction (H₂-TPR)</i>	45
2.3 <i>Scanning Electronic Microscopy (SEM)</i>	45
2.4 <i>Specific surface area determination</i>	46
2.5 <i>X-Ray Photoelectron Spectroscopy (XPS)</i>	46
2.6 <i>Methane oxidation catalytic tests</i>	46
2.7 <i>Cells manufacturing</i>	47
2.8 <i>Electrochemical Impedance Spectroscopy (EIS) experimental setup</i>	48
2.9 <i>Electrochemical Impedance Spectroscopy (EIS) theory</i>	49
Chapter 3: La_{0.6}Sr_{0.4}MnO₃, from powder to IT-SOFCs anode fueled by CH₄	53
3.1 <i>Introduction</i>	53
3.2 <i>Material synthesis</i>	57
3.2.1 La _{0.6} Sr _{0.4} MnO ₃ nanofibers preparation	57

3.2.2 $\text{La}_{0.6}\text{Sr}_{0.4}\text{MnO}_3$ powders preparation	58
3.3 <i>Morphological Characterization</i>	59
3.4 <i>Compositional Characterization</i>	61
3.5 <i>Temperature Programmed Reduction (H_2-TPR) and N_2-adsorption-desorption</i>	63
3.6 <i>Methane oxidation catalytic activity test</i>	66
3.7 <i>Electrochemical Impedance Spectroscopy</i>	67
3.8 <i>Equivalent Circuit-Based Modeling</i>	67
3.9 <i>Electrochemical Impedance Spectroscopy in Air</i>	69
3.10 <i>Electrochemical Impedance Spectroscopy in Methane</i>	75
3.11 <i>Effect of the Electrode Thickness</i>	79
3.12 <i>Conclusions</i>	81
Chapter 4: Chemical and electrochemical characterization of $\text{La}_{0.8}\text{Sr}_{0.2}\text{MnO}_3$ and $\text{La}_{0.6}\text{Sr}_{0.4}\text{Cu}_{0.1}\text{Mn}_{0.9}\text{O}_3$	89
4.1 <i>Introduction</i>	89
4.2 <i>XRD</i>	93
4.3 <i>H_2-TPR</i>	97
4.4 <i>Methane oxidation catalytic tests</i>	100
4.5 <i>Morphological characterization</i>	104
4.6 <i>EDX-XPS</i>	108
4.7 <i>Symmetrical cell characterization</i>	110
4.7.1 <i>L8S2M EIS in air</i>	111
4.7.2 <i>LSCuM in air</i>	113
4.7.3 <i>L8S2M EIS in CH_4</i>	115
4.7.4 <i>LSCuM EIS in CH_4</i>	117
4.8 <i>Complete cell test</i>	119
4.8.1 <i>Complete cell L8S2M</i>	121
4.8.2 <i>Complete cell LSCuM</i>	123
4.9 <i>Conclusions</i>	127
Chapter 5: Cu@GDC 2% Pd as Anode Material for Direct Methane LT-SOFCs	133
5.1 <i>Introduction</i>	133
5.2 <i>Material synthesis</i>	138
5.2.1 <i>Cu@GDC nanopowders synthesis</i>	138
5.2.2 <i>LSCuM in air</i>	138
5.3 <i>Structural, Chemical and Morphological Characterization of the electrode</i>	140
5.4 <i>Symmetrical cells EIS characterizations</i>	143

5.5 Full cell electrochemical characterization	147
5.6 Measurements in NH ₃	149
5.7 Conclusions	152
Chapter 6: Raman <i>ex situ</i> and <i>in situ</i> spectroscopy characterization	157
6.1 Raman theory	157
6.2 Ex situ and in situ Raman spectroscopy experimental setup	161
6.3 Experimental test protocols	162
6.4 Ex situ measurements	163
6.5 In situ measurements	168
6.5.1 LSM powders	168
6.5.2 L8S2M and LSCuM	171
6.5.3 Cu@GDC 2% Pd wt. electrode	174
Chapter 7: Conclusions and outlook	179
Appendix: List of papers published during my Ph.D.	189
Squizzato, E., et al. (2021). <i>Energies</i> , 14(12), 3602.	190
Sanna, C., et al. (2022). <i>Electrochimica Acta</i> , 409, 139939.	191
Squizzato, E., et al. (2021). <i>Int. J. Hydrog. Energy</i> , 46(48), 24555-24566.	192
Cavazzani, J., et al. (2022). <i>Int. J. Hydrog. Energy</i> , 47(29), 13921-13932.	193
d'Andrea, G., et al. (2022). <i>E3S Web Conf.</i> (Vol. 334, p. 04009). EDP Sciences.	194
Cavazzani, J., et al. (2022). <i>E3S Web Conf.</i> (Vol. 334, p. 04008). EDP Sciences.	195
Acknowledgements	197

Abstract

The Solid Oxide Cells (SOFC) are high temperature electrochemical devices able to convert with high efficiency the chemical energy of a fuel into electric energy and reverse. Ni/YSZ is the state of art electrode material, while hydrogen is the mainly used fuel in the nowadays commercial devices. The usage of green hydrogen must be the main goal of our research in the energetic field. Anyway, it is unrealistic to think that in a very short time our cities can be ready to use hydrogen as main fuel. A possible compromise could be the usage of biogas, that can be produced in a green way from the biowaste of our agriculture activities. Since the main component of biogas is methane, in this work, the possibility to implement methane fueled Solid Oxide Fuel Cells in our cities is investigated.

The main problem to achieve this result is to identify a new anodic material that can replace the state of art Ni based cermet. Indeed, Ni strongly catalyze carbon coking and this lead in a short application time to the surface poisoning. In addition, is consolidated the knowledge about the mechanical breakage of Ni/YSZ when exposed to carbon containing molecules. Therefore, new Ni free anode materials will be discussed in this work.

The choice of the candidate material was made trying to transform a handicap to an opportunity. If we must avoid the state of art anode material, why not try to use a compound that is possible to use both as anode and both as cathode? In this way, the productive costs can be considerably lowered. Otherwise, why not try to lower the working temperatures of this technology with the consequent lowering of the operative costs?

Before the show up of the proposed materials and their results, a general introduction to the technology and its challenge is given.

Different composition and Cu doped formulation of $\text{La}_{1-x}\text{Sr}_x\text{MnO}_3$ (LSM), state of art cathode material, were synthetized and characterized. The effective realization of the desired compound is confirmed by X-Ray Diffractometry (XRD), while the morphology of the powders is observed by Scanning electronic Microscopy (SEM). The surface chemical composition is studied by X-Ray Photoelectron Spectroscopy (XPS), while the surface area of all the samples is calculated by BET analysis performed on N_2 Adsorption-desorption isotherm. One of the most important goals of this work is the confirmation of the LSM stability in reductive atmospheres (H_2 and CH_4), that was confirmed by XRD after

Temperature Programmed Reduction (H₂-TPR) and the catalytic tests. In fact, the catalytic properties of this material towards methane oxidation were studied through a Gas Chromatographer (GC) and, finally, the electrochemical activity through Electronic Impedance Spectroscopy (EIS). Must be mentioned the attempt to increase the performances by changing the morphology. For this reason, LSM nanofibers, synthesized by Prof. Costamagna's research group from University of Genova, were characterized and compared with LSM powders.

To lower the working temperature to about 500 °C, another solution was investigated. In this case avoiding noble metal does not give satisfactory results from an applicative point of view. What we can do is to limit the quantity of noble metals and trying to enhance their properties by downsizing the dimension of the metal catalysts to a nanoscale. The creation of nanoparticles can significantly improve the catalytic performances through the creation of new crystalline planes. A Cu/GDC cermet with Pd nanoparticle infiltration was investigated.

These two different solutions that can be effective for two different tasks, must have a common requirement: avoiding the carbon deposition on the electrode surface. For this reason, quantitative and qualitative analyses of the carbon deposition was studied by Raman Operando Spectroscopy performed at Danmarks Tekniske Universitet (DTU) under the supervision of Prof. Peter Holtappels.

Chapter 1: Introduction

1.1 Overview

“If we fail to match climate rhetoric with climate actions, we condemn ourselves to a hotter, more volatile earth, with worsening disasters and mass displacement.” These words from António Guterres, the actual UN Secretary-General at the World Economic Forum (17th January 2022), remind us that humanity cannot postpone any longer to face up to one of the most difficult challenges that the human history has ever dealt with. Population growth, on the 15th of November were reached 8 billion people in the world, has led to an increase in the consumption of electricity and natural resources. ^[1]

Nearly 13% of the world's humans are suffering from the need to find the necessary energy consumption (electricity), and Sub-Saharan Africa and South Asia account for 89% of the total electricity shortage. It has been estimated that 40% (more than three billion) of the world's humans must bear the health cost of air pollution due to dirty energy sources for cooking and heating that emit large quantities of greenhouse gas (GHG). The consumption of solid fuel for this purpose has been reported to be very high in sub-Saharan Africa (77%) and South Asia (61%).

Therefore, increasing energy demand has become the main reason to invests in safe, green, efficient and sustainable energy sources.^[2] Energy consumption and economic growth are linked, and, for this reason, it is not possible to think about solving environmental problems by reducing our energy demand. How it is possible to see in **Figure 1**, there is an evident overlapping between the countries with the highest GDP and the countries with the highest GHG emissions (e.g., USA and China). It is for this reason that it should be unfair and selfish if the most developed countries would ask the poorest countries to lower their energy consumption now that they are trying to rise in the world economy. Furthermore, most of the worst episodes of climate change (e.g., hurricanes, floods, drought, desertification, etc.) are set in the poorest corners of the world.

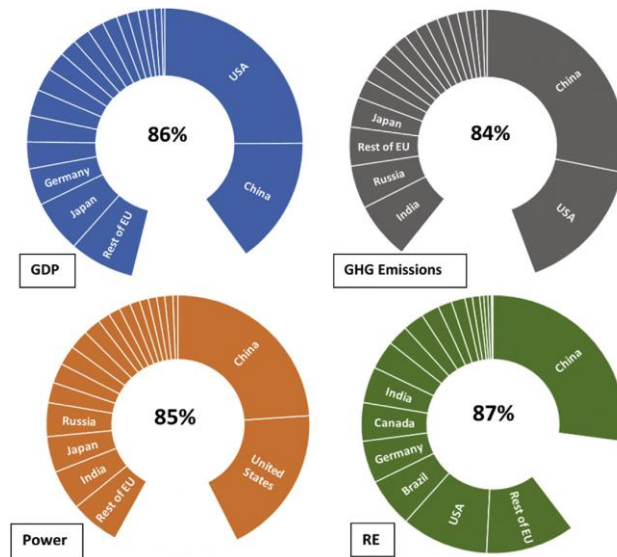


Figure 1: G20 share of global GDP, Greenhouse Gas (GHG) emissions, power consumption and share of renewable energy (RE) installed capacity. As it possible to observe, there is a correspondence between the countries with the biggest GDP and higher values of GHG emissions.

Nowadays, the percentage of energy produced by alternative and renewable sources of energy (hydro, water, solar, ...) is about 27% and it is still low if we want to achieve the goals on CO₂ emissions stated by the last international agreement. [3] This is in contrast with the last projection about investments on renewables. These studies attest those governments and institutions that most aggressively adopt the energy transition and facilitate faster flow of capital investments for renewable energy development will witness far more economic growth and benefit. [4]

Anyway, renewable energies present some problematics that must be solved to reach the transition to a 100% sustainable energy production system. The most significant problematic is the marked variation of energy production over time and in geographic diffusion. It is easy to realize that solar and wind exposition in a well determined location cannot be every time the same. But the interruption is not the only problem, being also problematic when the peak of energy production is reached. Often there are extreme but short-lived peaks that require a very large capacity of energy storage that usually is not convenient to have, due to the costs of these plants and the very rare effective use. So, the main problems can be summarized in storage rate and volume. Several can be the possible ways to store renewable energy, as an example concentrated solar thermal heat storage, Pumped Hydro Storage (PHS), but maybe the two most versatile and promising are batteries and chemical storage.

Batteries, in these last years, are at their peak of interest: the scientific community and the public opinion are enthusiastic about their possibilities. What it is not well known is that even batteries have very important challenge to face up. One of these are the costs. To store the large quantities of energy involved in the green energy production, very big implants must be realized. The biggest implant, to date, is set in Fairbanks (Alaska, USA) and it weighs 1300 t, but can store and deliver 46 MW for 5 min. This means, in other words, that a typical large power station for 24 h would require storage of 24,000 MWh, and at this rate it would cost \$38 billion. Around 30 times the cost of a single coal-fired station. ^[5] In addition, but this is more known from the public opinion, there are several problems about durability and recycling of the devices.

A solution and a better energy storing system can be given by the production of chemicals. Using chemicals for energy storage is an efficient mean, since it is possible to store in a smaller plant huge quantity of energy; also, energy transportation is easier and cheaper than traditional modes. This energy can be later used and converted into electrical energy through Fuel Cells. The most used chemical is hydrogen, due to its high energy density and relatively easy production through water electrolysis. ^[6] Hydrogen can be stored in the liquid form, but it requires a refrigeration system with a very low setpoint (20 K), due to the low boiling point. A second approach is the use of metal hydride, where the gas is stored through the reaction of the gas with the selected metal. The major drawback of this method is its low mass absorption capacity. The most used solution is to store the gas at 200-250 bar. But the ratio of stored hydrogen to weight is very small. In addition, it presents some drawbacks related to the high inflammability with broadly spaced ignition limits in air (lower explosion limit 4% by volume, upper explosion limit 75.6% by volume) and low ignition energy (0,017 mJ for a stoichiometric air mixture). ^{[7], [8]}

A possible alternative could be the usage of biofuel. A biofuel is an organic matter obtained from the residue of plants and animal dung, through a biological process rather than a geological one. Typical biofuels include ethanol, biodiesel, bio-alcohols, green diesel, syngas, and solid biomass. ^[9]

In this work it will be discussed how it is possible to go further to these problematics through the exploitation of green biofuels and how the material science can play a leading

role on the fight to climate change and the achievement of the goals mentioned by the UN president António Gutierrez.

1.2 A sustainable device: Fuel Cell

1.2.1 Fuel cell introduction

Fuel Cells (FC) are devices that allow converting chemical energy of the fuels into electric power with high efficiency and with low environmental impact. The electrochemical reactions occur between two different chemical species: a fuel (mainly hydrogen but for some FCs other molecules are possible) to oxidize and an oxidizer (commonly air) to reduce.

[10]

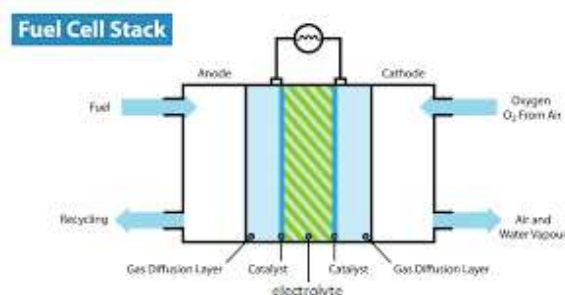


Figure 2: Scheme representing the main reactions and the structure of a generic fuel cell.

These devices offer several advantages, i.e., there are not combustion processes, so there are not pollutant by-products (oxidation product being water when using hydrogen as a fuel) and the fuel chemical energy is converted with higher efficiency into electric power. In addition, no mobile parts are present in the device, which is fundamental to have a more reliable, but also silent device. Being characterized by good efficiencies also in low power case, fuel cells are suitable for portable applications and automotive industry.

Obviously, there are also some disadvantages, which research in this field needs to overcome. One of them is the need to use highly pure hydrogen, that should be obtained through a green process with high efficiency. There are also some problems with hydrogen storage and transportation, with consequently high costs. A possible way to face up to these problems, is the use of high temperature fuel cells, in which hydrogen can be originate in situ by internal reforming and that can operate also with fuels different from very pure hydrogen.

1.2.2 Fuel cell typologies

The fuel cells are classified according to the choice of electrolyte, fuel and consequently from the working temperature. At low temperatures (50 – 250 °C) we have:

- Proton Exchange Membrane Fuel Cell (PEMFC);
- Alkaline Fuel Cell (AFC);
- Phosphoric Acid Fuel Cell (PAFC).

At higher temperatures (650 – 1000 °C) the main important typologies of fuel cell are:

- Molten Carbonate Fuel Cell (MCFC);
- Solid Oxide Fuel Cell (SOFC).

Fuel cells can also be distinguished on the base of the used fuel:

- Direct Methanol Fuel Cell (DMFC).

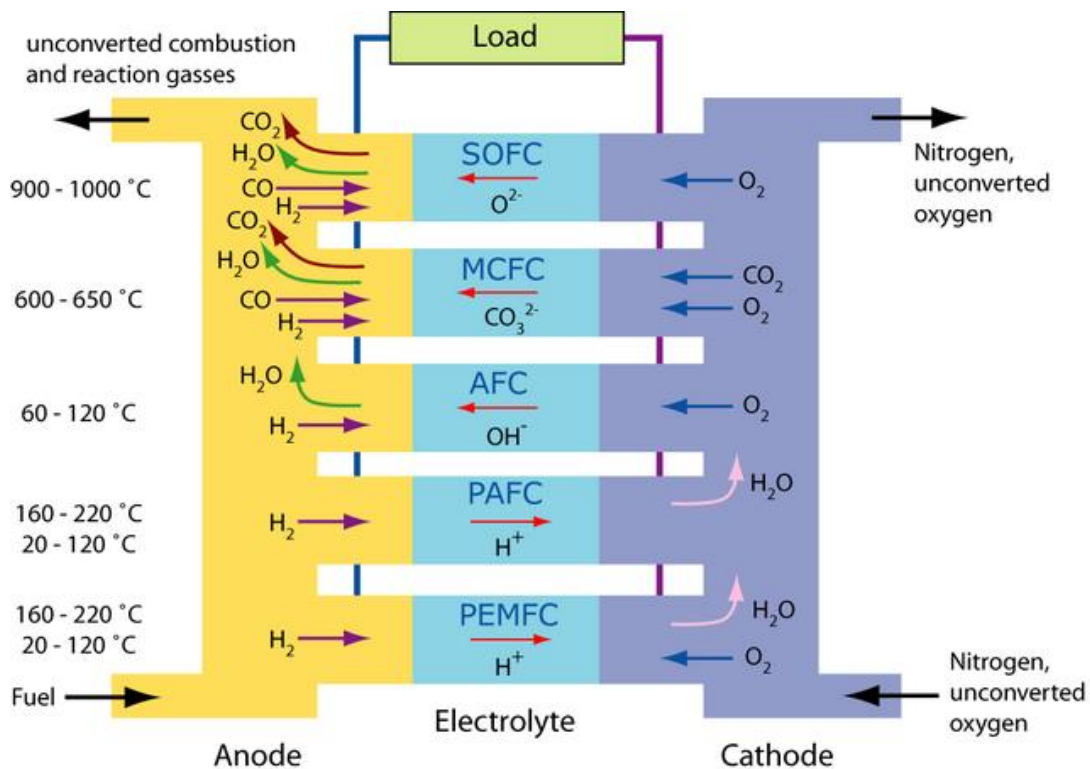
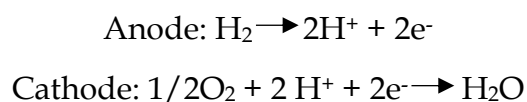


Figure 3: Different typologies of fuel cell with relative electrolyte, fuel and working temperature.

Proton Exchange Membrane Fuel Cell (PEMFC)

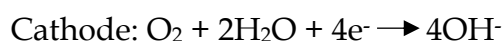
PEMs are characterized by a polymeric electrolyte (e.g., Nafion membranes) that allows the exchange of protons between two porous electrodes but denies the passage of electrons. The chemical involved reactions are:



This fuel cell typology can reach an efficiency of about 50% and presents high power density (1.35 kW/litre for automotive fuel cell). What makes very interesting this typology is the relative low operating temperature (60 – 80 °C that allows to reach very quickly the operating temperature, and this is fundamental for start-and-stop applications (automotive industry, portable applications). The problems are related to the slow kinetic caused by the low operating temperature. A way to resolve that is the usage of Platinum Group Materials (PGM) that have very good catalytic properties. Unfortunately, platinum and PGMs are critical raw materials: this means that their abundancy in nature is low and/or focused in specific geographic areas, so their cost is high and the supply uncertain. ^[11] For this reason the study for PEMFC is focused on the research of new no-PGM catalyts.

Alkaline Fuel Cell (AFC)

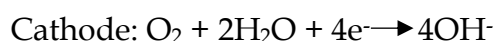
The AFCs are the first developed typology of fuel cell. NASA deployed them for the first time in the 1960s during the Apollo program, which accomplished landing the first humans on the Moon. Also, for the alkaline fuel cell, the working temperature is around 100 °C, with high efficiency (60 – 70%). The reactions are:



The electrolyte is potassium hydroxide (KOH), assure high mobility of negative charged ions (OH⁻). This electrolyte also represents the disadvantage of this technology because CO₂ reacts with it and consumes the alkaline electrolyte, reducing its concentration. In addition, KOH is highly corrosive; therefore, the device has not a long-life span. The AFCs are still used in boats and space shuttles. ^[12]

Alkaline Membrane Fuel Cells (AMFC)

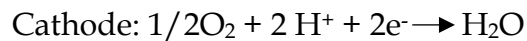
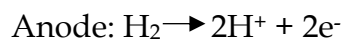
The disruptive approach of applying alkaline anion-exchange membranes (AEMs) in alkaline membrane fuel cells (AMFCs) potentially meets several of the challenges facing other approaches to low temperature fuel cells, including the otherwise high catalyst and fuel costs. Thus, the move to alkaline conditions at the electrodes opens the potential use of a range of low cost non-precious-metal catalyts. The involved reactions are:



The major issue with traditional AFCs is electrolyte and electrode degradation caused by the formation of carbonate/bicarbonate ($\text{CO}_3^{2-}/\text{HCO}_3^-$) on reaction of OH^- ions with CO_2 contamination in the oxidant gas stream. [13]

Phosphoric Acid Fuel Cell (PAFC)

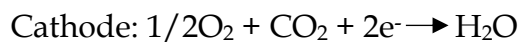
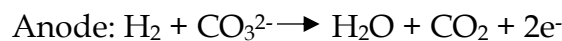
The phosphoric acid fuel cells have a very good reliability. Because of this reason, PAFCs are highly used in applications where even a short stop of electricity production represents an important economic or social issue. The relatively high electrical (37%) and total efficiency (87%) allows a reduction of fuel usage and pollution emissions compared with traditional power systems. As their name suggests, the electrolyte is phosphoric acid (H_3PO_4) and the reactions at the two electrodes are:



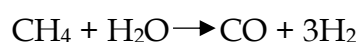
The PAFCs can operate at relative low temperatures (175-200 °C). Like the PEMFCs, the PAFCs need platinum as catalyst, and this is one of the drawbacks for this fuel cell typology in addition to the use of high concentration phosphoric acid solutions. [14]

Molten Carbonate Fuel Cell (MCFC)

This kind of fuel cell was developed starting from 1970s. It uses as electrolyte a mixture of molten carbonates in a porous, chemically inert ceramic matrix of beta-alumina solid electrolyte. The operating temperatures are higher than those needed by the previous fuel cells ($T \geq 650$ °C). At the anode side hydrogen reduces CO_3^{2-} ion to CO_2 , with the release of two electrons. At the cathode the CO_2 of the exhaust anode is oxidized by oxygen from the air.



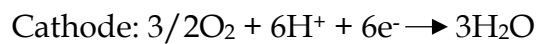
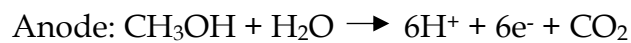
The hydrogen supply is typically generated from natural gases through steam reforming: methane, by means of a catalyst (nickel) and the heat from the fuel cell, combines with water to combust carbon releasing hydrogen.



A molten carbonate fuel cell has electrical efficiencies of 47% and a total efficiencies of more than 80%. It is typically used for medium and large power applications. The main drawback is a high intolerance to sulphurs. [15]

Direct Methanol Fuel Cell (MCFC)

The best improvement given by this kind of fuel cell is that they are not dependent on hydrogen generation, storing and transportation processes. Methanol has a relatively high volumetric theoretical energy density, and this is of core importance for small portable applications. Their electrolyte is made by a polymer, like for the PEMFCs. The occurring reactions are:



Their performances are limited by crossover of methanol from anode to cathode that lowers the system efficiency. The slow kinetic of the electrochemical oxidation of methanol is another problem to be solved. [16]

1.2.3 Solid Oxide Fuel Cell (SOFC) theory

The first fuel cell was invented in 1838 by William Grove, with the name of “Grove cell” or “wet cell battery”. The modern solid oxide fuel cell came into existence after the discovery of solid electrolytes made by Gaugain in 1853. [17]

The solid oxide fuel cell is composed by a dense electrolyte layer that is sandwiched between two porous electrodes. The electrons generated through the oxidation of fuel at the anode are accepted for oxygen reduction at cathode, which completes the external circuit. Since the diffusion of oxide ions through the electrolyte is necessary, the working temperatures are relatively high (~ 800 - 1000 °C). The solid electrolyte is an advantage for the device, because of the possibility to avoid corrosion; moreover, no noble metals are required for electrocatalysis because the kinetics is favoured by high temperatures; finally, because of the absence of liquid electrolyte, there is not a preferential orientation of the cell. In addition, the high temperatures allow to obtain a high efficiency of over 42%. [18] Because of their high temperature of operation, no noble metals are required for electrocatalysis, and natural gas fuel can be reformed within the cell stack eliminating the need for an expensive, external reformer system. Also, pressurized SOFCs can be successfully used as replacements for

combustors in gas turbines; such hybrid SOFC–gas turbine power systems are expected to reach efficiencies approaching 70%. [19] Anyway, the high operating temperatures also present some problems. The materials used for SOFCs must be durable to high temperatures without chemical and mechanical changes. Much research has been done to obtain materials useful for SOFCs applications.

SOFCs, as all the others fuel cells, present an anode, where fuel oxidation occurs, and a cathode where the main reaction is the reduction of the oxidizing species. An oxide-based electrolyte allows O^{2-} ions diffusion from the cathode to the anode; moreover, it separates the two different gases in the electrodes, in order to avoid the chemical reactions that are useless for the electrochemical process.

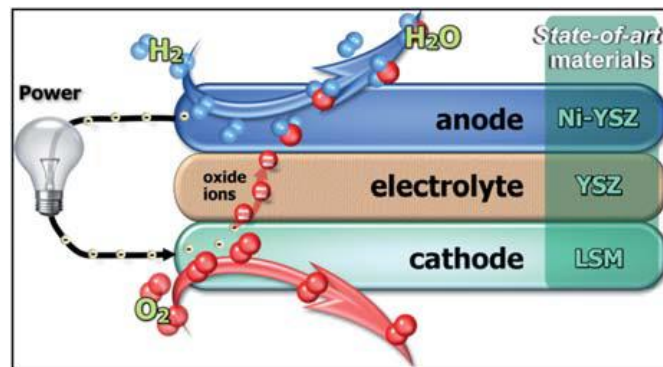
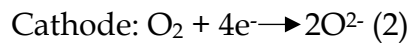
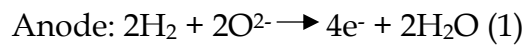


Figure 4: Solid Oxide Fuel Cell configuration and commercial state-of-art materials for H_2 applications. [20]

The state-of-art for SOFCs is represented by a cermet (i.e., Ni-YSZ, where YSZ is Yttria Stabilized Zirconia) as anode, and a manganite perovskite (Lanthanum Strontium Manganite, LSM, or Lanthanum Strontium Iron Manganite, LSFM) for the cathode. The electrolyte is usually YSZ (Yttria Stabilized Zirconia) or GDC (Gadolinium Doped Ceria); the last one has the huge advantage of being a good ionic conductor at intermediate temperature SOFCs (600 - 800 °C) but is poorly stable under reducing condition (because of the arising electrical conductivity). On the contrary, there are no problems of chemical stability for YSZ, but higher temperatures are needed and problems of interaction with the electrodes may be relevant.

Anode

The anode materials must be compatible (chemical interaction and thermal expansion) with electrolyte and interconnect; it must be a good electronic conductor and, possibly, also ionic (for oxygen anions) conductor. It must present a good porosity to allow the passage of the gas to the active regions of the electrode. The catalytic properties of the anode in fuel oxidation are mandatory; fuel flexibility, easy fabrication, and, considering the real commercial applications, the economic and environmental sustainability, are also relevant. The electrical resistance of the anode is essentially comprised of internal resistance, contact resistance, concentration polarization resistance, and activation polarization resistance. Electronic resistance and thickness of anode determine the first one. Contact resistance can be reduced by a better adhesion between electrode and electrolyte. The microstructure of the material (volume percent porosity, pore size and tortuosity factor) is responsible of concentration polarization, which is related to the transport of gaseous species through the electrode. Activation polarization is given by the charge transfer processes and depends on the electrocatalytic activity of the electrode itself and by the area of triple-phase boundaries (TPB). [21] TPBs are the confluence of sites where the oxygen ion conductor, electronic conductor, and the gas phase come in contact. The use of Mixed Ionic Electronic Conductors (MIECs) for electrodes allow to solve this problem and to reach higher efficiency.

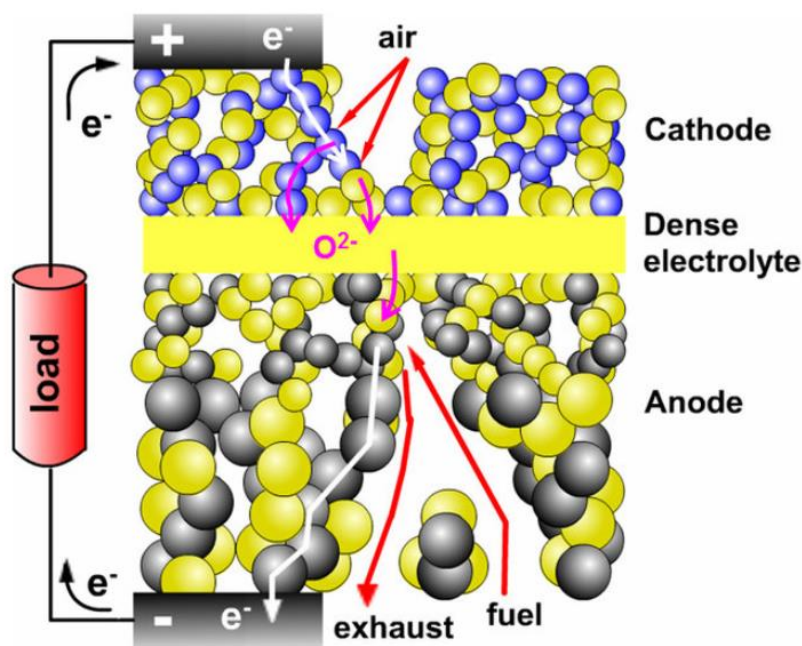


Figure 5: By implementing electrodes able to conduct both ions and electrons, it is possible to widely extend the active region of the electrodes, as presented in the above scheme.

Cathode

In SOFCs, the cathode is the electrode where electrochemical reduction of oxygen takes place. To this effect, the cathode must have: high electronic conductivity (preferably more than 100 Scm^{-1} under oxidizing atmosphere); a matched thermal expansion coefficient (TEC) and chemical compatibility with the electrolyte and interconnect materials; adequate porosity to allow gaseous oxygen to readily diffuse through the cathode to the cathode/electrolyte interface; stability under an oxidizing atmosphere during fabrication and operation; high catalytic activity for the oxygen reduction reaction (ORR); and possibly low cost.

The electrochemical reactions can only occur at the triple-phase boundaries. The elementary reactions in the overall electrode reaction are usually considered as follows: the reduction of O_2 molecules involving adsorption, dissociation, reduction, and incorporation of the oxygen anions into the lattice of the cathode materials; ionic transport through the porous cathode toward the electrolyte; and the ion jumping into the electrolyte lattice. Among all three elementary reaction steps, several steps could be rate-limiting for the oxygen reduction process. The first mechanism resistance contribution can be lowered by good catalyst material. The cathodic reaction can be summarized with three different pathways shown in **Figure 6**. It is not possible to know previously which elementary reaction will be rate-limiting step and this may depend on local conditions like temperature and oxygen partial pressure or on microstructural conditions. In addition, there may be parallel reaction pathways and a crossover of these various reaction pathways may cause interference. [22]

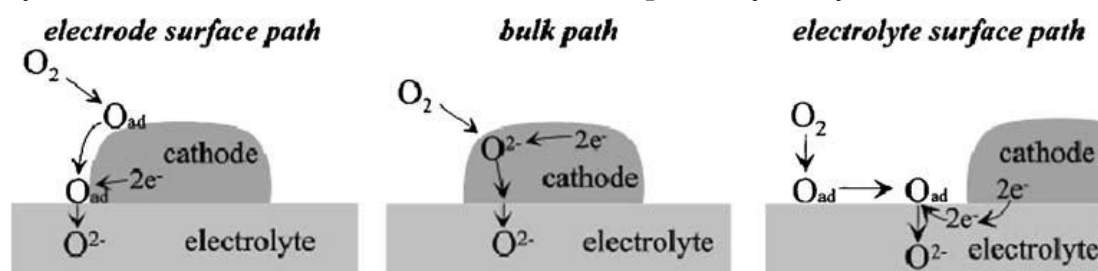


Figure 6: Three reaction paths of the oxygen reduction and incorporation reaction and some possible rate-determining steps. [22]

Electrolyte

Electrolyte, an O^{2-} ion-conducting ceramic, is a main component of SOFC. The needed properties of the oxides for using as SOFC electrolyte are:

- High oxide ion (or proton) conductivity ($0.01\text{-}0.1 \text{ Scm}^{-1}$ for the thickness $1\text{-}100 \mu\text{m}$).

- Low electronic conductivity, otherwise, there is the cell short-circuit.
- Chemical stability.
- Mechanical strength.
- Low cost (for commercial applications).

The relation between ion conductivity of state-of-art/potential materials and temperature are shown in **Figure 7**.

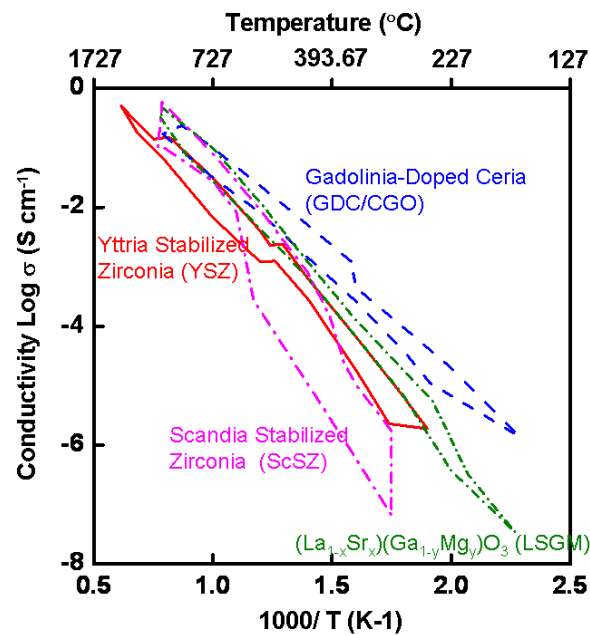


Figure 7: Ion conductivity at different temperatures for state-of-art material and new promising electrolytes. [23]

One of the main drawbacks for O^{2-} ions-conductive electrolytes are the high working temperatures, with consequent high initial and operating costs. Reducing the SOFCs operating temperatures leads to two main problems: a decrease in electrolyte conductivity and an increase in electrode polarization losses, because both the ion transport in ceramic electrolytes and the electrochemical reactions at the TPBs are thermally activated processes. It will be clear at the reader that the work presented in this thesis is focused on the research of materials able to lead the electrochemical reactions at lower temperatures, by implementing innovative materials at the electrodes. Anyway, must be mentioned that in the last decade, High Temperature Protonic Conductors (HTPCs) have been recognized as particularly suitable electrolytes for IT applications, because, compared with oxygen-ion conductors, they show lower activation energy (between 0.4 and 0.6 eV) and larger conductivity values in the IT range. [24] Moreover, for HTPC-based FCs, water is produced at the cathode rather than at the anode, avoiding fuel dilution, which reduces the cell

efficiency. The most suitable materials for this kind of electrolytes are Barium Cerate or Zirconate, with Ytria doping at the B-site. Even if this kind of SOFCs present many advantages compared to the anionic one, must be considered that the scientific research on this topic is only at the beginning. That means that there is wide room for improvements, but also that it is still very far the commercialization step for this kind of technology. Since this work would be an intermediate, but also quick and easy to implement, step towards the complete decarbonization of the energy production sector, the HTPCs were not considered.

1.2.4 Reversible SOC (R-SOC)

R-SOCs could be fundamental devices in future scenarios, thanks to their possibility to store electric power that exceeds from renewable energy sources, in chemical energy. In principle, it is possible to simplify their functionality comparing R-SOCs to rechargeable batteries. When renewable energy exceeds needs, electric power is converted in chemical energy in the electrolytic mode (recharge battery); when there is not power from the renewable energy, it is possible to use the fuel stored in the fuel cell to produce electric current (discharge battery). This strategy is also valuable when considering the intermittent character of the renewable energy sources.

The high temperatures allow low current usage for the electrolytic process. SOFC mode process is exothermal, while SOEC mode process is endothermic. If using external heating sources to promote endothermic process, a roundtrip efficiency about 20-55% can be reached and an energy cost of 3.46 €/kWh. However, higher efficiencies are possible with a heat recovery steam generator (HRSG), that consists in exploiting the heat given by an exothermic reaction (e.g., a methanation reaction) for the SOEC process. This expedient can lead to roundtrip efficiency about 70%. In this way it is possible to reach energy with a cost of 3.43 €/kWh. ^[25] There is the possibility to have a third configuration where the HRSG is implemented with a fuel recirculation. In this way the costs are lowered to 3.14 €/kWh. The system lifetime was assumed 20 years with: R-SOC stack replaced every 5 years, inflation rate of 2%, and capacity factor of 80%. ^[26] Another study, performed considering the data recorded in one year in the island of Procida (Italy) from the deployment of a real reversible SOFC, showed an important decrease in emissions and an energy self-sufficiency of at least

29% and 58% respectively, with a reachable 3 years payback period for the future. To date, in which this thesis is written, it is equivalent to the lifetime of the device. [27]

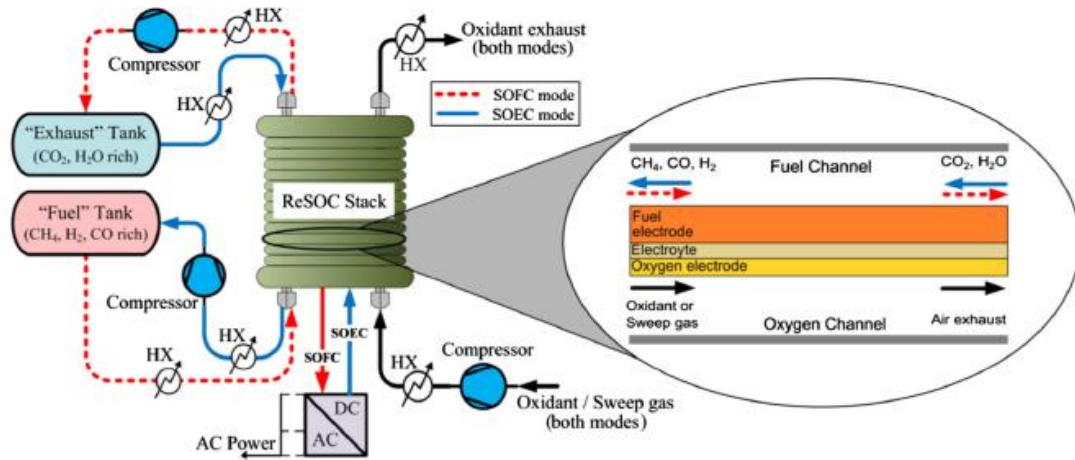


Figure 8: Simplified schematic of a reversible solid oxide cell.

R-SOCs present many advantages. For example, inverting the polarization, the effects of different degradation processes (sulphur poisoning, carbon deposition, electrodes delamination) are greatly decreased. [25] Therefore, this allows to use fuels different than pure hydrogen, like hydrocarbons. As well, electrolytic process is the purest source of hydrogen, and this is very important because less impurities mean higher efficiency and higher durability for fuel cells. An important challenge with R-SOCs is the development of electrodes stable and active both under reducing and oxidizing condition, when working in fuel cell or in electrolyser mode.

The drawbacks are related to the design of R-SOCs systems. For example, overcoming the thermal disparity between fuel cell (exothermic process) and electrolysis (endothermic or near thermoneutral) process using a unitized cell-stack and common hardware. Another problem to solve is selecting the right operating condition (T , p) that can promote high efficiency in both operating modes. In addition, because reaction products are tanked for use in the opposite mode of operation, it is requested to process them allowing the compression to storage pressure with minimal energetic costs.

1.2.5 Symmetrical SOFC (S-SOFC)

The use of the same material on the two electrodes characterizes Symmetrical SOFCs (S-SOFC).

Therefore, the cell preparation becomes easier with consequent lower fabrication costs. In addition, on the two sides of the cell there is the same interface, so originating less chemical and structural compatibility problems to the device (higher durability). Since the two electrodes can act as cathode or anode, they can be used as R-SOCs, with relative advantages. Symmetrical fuel cells are intrinsically reversible and so able to avoid sulphur poisoning or coke formation, or oxygen bubbles induced delamination. Since the anode is in a reducing environment while the cathode is in an oxidizing environment, the challenge for the electrode in a symmetrical SOFC is that it must demonstrate chemical and structural stability in both reducing and oxidizing environments while maintaining dual electrocatalytic performances for both oxygen reduction and fuel oxidation. Furthermore, it needs to show high electronic conductivity to reduce ohmic losses and appreciable oxygen ionic conductivity to promote electrochemical reactions. Different types of oxides with perovskite, fluorite and pyrochlore structures have been investigated as potential redox stable electrode materials. [28] When a proper material can satisfy all these requirements, it is possible to have lower problems related to sulphur and carbon deposition, by reversing the gases and cleaning the surfaces of the electrodes. Furthermore, the implementation of this technology for power generation (SOFC), and hydrogen production (SOEC) is possible. In other words, a symmetrical cell is the best candidate for the realization of a R-SOC. [29] .

An analysis of the literature data published in the past five years shows that iron-containing perovskites are of most interest. This is due to the ease of the change in the coordination number from 6 to 4 characteristic of iron cations in the oxygen coordination environment, resulting in the appearance of oxygen-ion conductivity in the electrode material and promoting the change in the mechanism of the electrode reaction. This leads to higher efficiency of such materials for SOFCs and, consequently, many iron-containing perovskites, e.g., $\text{La}_{0.6}\text{Sr}_{0.4}\text{Co}_{0.2}\text{Fe}_{0.8}\text{O}_{3-\delta}$ (LSCF), are used as conventional cathode materials for intermediate temperature SOFCs. [30]

1.2.6 SOFC challenges

The solid oxide fuel cells are a big opportunity for material scientists focusing their research on electrochemical conversion of energy, but in order to obtain a well-developed and commercial technology there are still many challenges. The state-of-art electrolytes operate

only at high temperatures and prevent the SOFCs capillary diffusion and utilization. Many efforts have been done to obtain a thin film electrolyte and thus to decrease the operating temperature, but in this way, there are many durability problems for the device. A possible solution can be new design and two-phase materials, especially in nanocomposites material. [31] About the electrodes is well known that eventual losses can be minimized by carefully engineering and optimization of TPBs. Development of new electrodes with those characteristics is not a straightforward and simple challenge. A possible solution can be the new wet impregnation or infiltration approach. Now, durability and reliability of the devices are the main important research fields on fuel cells. Revolutionary for fuel cells commercial competitiveness it would be the discovery of low-cost materials with very good performances. [32]

1.2.7 SOFC thermodynamic

Considering hydrogen oxidation reaction at the anode, when one mole per second of hydrogen reacts with a half mole per second of oxygen ions, two moles per second of electrons escape to an external circuit. The voltage is:

$$E = E_{\max} - E_{\text{activation}} - E_{\text{Ohm}} - E_{\text{conc}} \quad (1),$$

where E : overall cell voltage; E_{\max} : maximum voltage given by thermodynamic performance; $E_{\text{activation}}$: loss of activation processes; E_{conc} loss of non-infinity speed of reacting gases; E_{Ohm} : loss of resistance of electrolyte, electrodes, etc. Since $E_{\text{activation}}$; E_{Ohm} and $E_{\text{concentration}}$ are constants it is possible to write:

$$E = E_{\max} - E_{\text{const}} \quad (2)$$

E_{\max} is given by the following equation:

$$E_{\max} = E_0 + \frac{RT}{2F} \ln \frac{p_{H_2} \cdot p_{O_2}^{1/2}}{p_{H_2O}} \quad (3),$$

Where E_0 is the voltage under standard conditions; p_{H_2} is the hydrogen partial pressure at the anode; p_{O_2} is the oxygen partial pressure at the cathode and p_{H_2O} is the water partial pressure at the anode obtained by the process; R is the gas constant (8.31451 kJ/kgK) and F the Faraday constant (96485.309 C/mol). This equation assumes that reactants and products

partial pressures are separated, but in a SOFC the hydrogen and the water are mixed, so the previous equation can be replaced as follows:

$$E_{max}^{SOFC} = \frac{RT}{2F} \ln K + \frac{RT}{4F} \ln \frac{p_{O_2}^{cathode_inlet}}{p_{H_2}^{anode_inlet}} + \frac{RT}{4F} \ln \left(\frac{\frac{1-\eta_f}{2 \frac{o}{h}}}{1 + \frac{s}{h}} \right) + \frac{RT}{2F} \ln \left(\frac{1-\eta_f}{\frac{s}{h} + \eta_f} \right) \quad (4)$$

where η_f : fuel utilization factor; $p_{O_2}^{cathode_inlet}$: inlet oxygen partial pressure at the cathode; $p_{H_2}^{anode_inlet}$: inlet hydrogen partial pressure at the anode; $\frac{o}{h}$: oxygen to hydrogen ratio; $\frac{s}{h}$: steam to hydrogen ratio.

The previous equation defines the maximum voltage reachable by a SOFC from the electrochemical processes. However, irreversible losses must be taken into considerations as the internal resistance, which is defined as follows:

$$r = R_{cell} \cdot A_{cell} \quad (5),$$

where R_{cell} is the cell resistance and A_{cell} is the cell active area.

The associate voltage is

$$\eta_{irr} = i \cdot r \quad (6),$$

with I the current density.

The current generated by the cell (I) depends on fuel utilization factor η_f and hydrogen mass flow ($\dot{n}_{H_2}^{anode_inlet}$) fed to the anode:

$$I = 2F \dot{n}_{H_2}^{anode_inlet} \cdot \eta_f \cdot 10^3 \quad (7).$$

The internal resistance is

$$r_f = 2F \dot{n}_{H_2}^{anode_inlet} \cdot R_{cell} \cdot 10^3 \quad (8).$$

Considering the equations:

$$(4), (6), (7) \text{ and } (8)$$

the voltage of a SOFC for the anode is:

$$E_{SOFC} = E_{max}^{SOFC} - \eta_f \cdot r_f \quad (9).$$

In addition, electrolyte presents a resistance, and for its activation, $\eta_{electrolyte}$ potential must be applied, so the equation for SOFC voltage is:

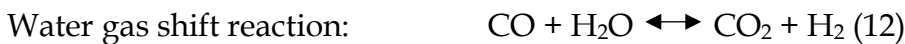
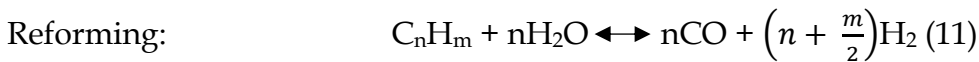
$$E = \eta_{electrolyte} \cdot E_{SOFC} \quad (10).$$

From mathematical studies on efficiency of SOFCs it is possible to determine the following parameters for one kilogram per second of inlet methane mass flow ($T = 25 \text{ }^\circ\text{C}$) and air ($T = 25 \text{ }^\circ\text{C}$ and $p = 1 \text{ atm}$) at $1000 \text{ }^\circ\text{C}$: SOFC efficiency = 32.79%; cell voltage = 0.572 V; fuel utilization factor = 74% and oxidant utilization factor = 53%. [18]

1.2.8 From Hydrogen to Methane

Nowadays, all the commercial fuel cells are based on having hydrogen as fuel, but are we sure that this is the best option for this technology in the middle term?

Hydrogen based energy will pave the way towards a more efficient and interconnected energy sector, driven by the twin goals of a cleaner planet and a stronger economy. Anyway, the high cost to produce “low carbon H_2 ” is the most significant barrier to its mass adoption for use across the global energy market. H_2 accounts for less than 2% of Europe’s present energy consumption and is primarily used to produce chemical products, such as plastics and fertilizers. 96% of this H_2 is produced by natural gas. The main process used for hydrogen production from fossil fuels is Steam Methane Reforming (SMR), which main chemical reactions are:



Of course, the scientific community is trying to find out different pathways for the transition to a carbon free and renewable H_2 production. Anyway, green hydrogen technologies are not quickly accessible with sensible effectiveness and low expense. For instance, studies on

effectiveness and cost of Photovoltaic (PV) electrolysis for large- and small-scale hydrogen production show that PV electrolysis is currently expensive (>\$5/kg for H₂) and it cannot reach high conversion efficiencies (with energy and exergy efficiencies less than 5%). [33][34] During this transition the use of methane will be necessary, and, to this purpose, the huge extension of the methane grid will play an important role. The hydrogen injection into the methane grid is another point. Under this scenario the possibility of a FC to operate efficiently with H₂, CH₄ and CH₄+H₂ as fuel does not need to be underlined.

1.2.9 Methane from Biogas: it's green!

Obviously, methane from natural gas and fossil fuels cannot be the source of methane for our devices. Biomass is unique in providing the only renewable source of fixed carbon, which is an essential ingredient in meeting many of our fuel and consumer goods requirements. The biodegradable components of municipal solid waste (MSW) and commercial and industrial wastes are also significant bio-energy resources, although particularly in the case of MSW, they may require extensive processing before conversion. Biomass is considered the renewable energy source with the highest potential to contribute to the energy needs of modern society for both the developed and developing economies worldwide. [35] Biomass fuels and residues can be converted to energy via the thermal, biological, and mechanical or physical processes summarized in **Figure 9**.

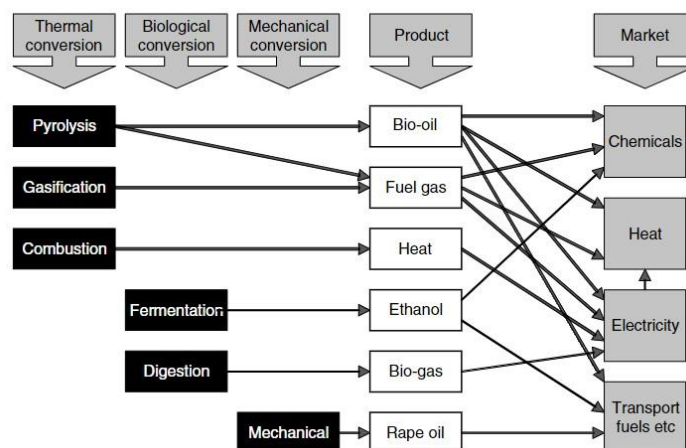


Figure 9: Conversion processes, products, and applications.

The best way to produce biogas is through biomass digestion. Anaerobic digestion is microbial conversion of organic materials to methane and carbon dioxide in the absence of oxygen. The product gas from farm digesters is typically around 60% methane, although higher levels have been reported. The typical methane content from landfill sites is lower at 50 - 55%. Digestion is particularly suitable for residues with high moisture contents, as drying is not required. The biogas can be used for heat with minimal processing, or for power generation in engines or turbines and (after upgrading to methane quality by removal of carbon dioxide and other components) in fuel cells or as gaseous fuel for transport applications. [36]

The generation of methane from biomass, could be also a possible solution to valorize food waste (FW), which is one of the major obstacles to achieving sustainable development in terms of global warming. By 2030, the global FW generation is expected to reach 3.62 Gt, which corresponds to a 2-fold increase compared to 2011 (1.95 Gt) [37]. Notably, four countries, China, India, USA, and Brazil, will contribute to over 50% of the global FW generation. [38] The conventional FW treatment technologies cause environmental pollution and waste the potential energy of FW. Notably, the production of green methane (CH₄) from FW has been proposed as a promising approach to overcome the environmental challenges associated with typical FW treatment and transportation technologies. The generated CH₄ could be utilized as a fuel for natural gas vehicles (NGVs). Additionally, the economic feasibility of the process was evaluated by considering appropriate economic parameters and assumptions. Treatment of 50 t/d of FW in China resulted in the generation of 0.3 t of green CH₄, and its minimum selling price was calculated at 0.991 \$/kWh. The benefits of scale-up as well as the developed FW treatment method were demonstrated by successful energy recovery and conversion of FW to green CH₄. Importantly, the minimum selling price could be decreased to US\$ 0.069/kWh, which is comparable to the current NGV fuel prices. [39]

1.2.10 Methane oxidation reaction

When thinking to feed a SOFC with a gas different from hydrogen, like methane in the case of the present thesis, the cathodic reaction is not involved in the gas change, since the ORR is always taking place in that side of the cell. For this reason, it is not necessary to study

dedicated cathodic material for direct methane SOFCs, but it is necessary to understand deeply only what happens to the anodic side of the cell. To figure out which one could be the best material for our purpose, it is fundamental to know and investigate the mechanism and the thermodynamic of the involved reaction, which is methane complete oxidation.



Methane oxidation is thermodynamically favorable but is kinetically hindered due to the high stability of the C-H bond (104 kcal mol⁻¹). Nonetheless, in the presence of a catalyst, the apparent activation energy can be as low as 7-10 kcal mol⁻¹. Two are the possible solutions for an efficient catalyst for methane oxidation: the development of opportune metal nanoparticle technology, preferably noble metal as Pd; or the engineering of metal oxides, like perovskites. In this work both the approaches are studied, so in this paragraph, we will try to go deeper on the understanding of the mechanisms that are involved in the two solutions.

In Pd-based catalysts, two are the stable active phases: Pd and PdO, which may or may not co-exist under reaction conditions. Over PdO a redox mechanism (Mars-van Krevelen reaction mechanism) is involved, in which the first C-H bond activation is the rate-determining step. [40] Over metallic Pd, the reactivity is controlled by competitive adsorption of methane and oxygen at the surface in a Langmuir-Hinshelwood mechanism. Anyway, it is evident from many tests that PdO is the most active phase for methane oxidation. Some studies have reported that methane oxidation over Pd-based catalysts is structure sensitive. [41],[42] According to the authors, at high dispersion and low loading the Pd phase interacts with the support and is relatively inactive, while at higher Pd loadings, where particles of >7 nm, are formed, the specific activity is higher, and the reaction becomes structure insensitive. Theoretical calculations and model catalysts studies have helped to design new catalysts aiding in the selection of promoters and in the indication of the active phases. [43], [44]

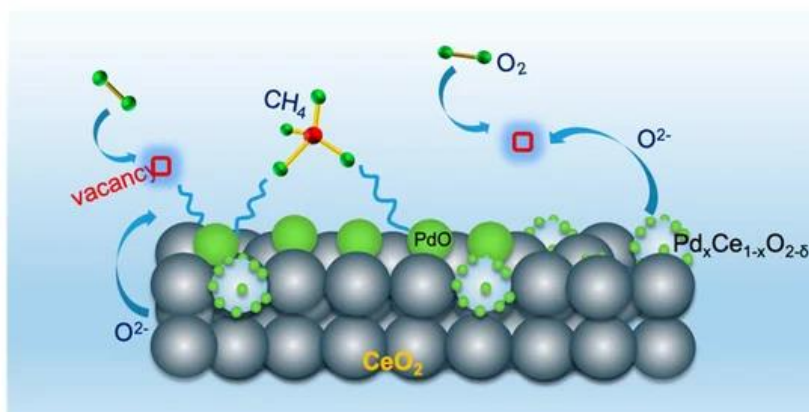


Figure 10: Schematic representation of the CH₄ oxidation following Mars-von Krevelen mechanism over the Pd/CeO₂ catalyst. [45]

Because of the high temperatures, active phase sintering and PdO complete decomposition to Pd are major causes of deactivation for Pd-based methane oxidation catalysts. A consolidated strategy to stabilize PdO against decomposition is the use of reducible oxides (promoters), such as rare earths (e.g., Ce, Pr, Eu). [46] Promoters have multiple functions: they improve PdO thermal stability against decomposition and sintering via strong interactions and oxygen transfer with the Pd phase and provide reactive oxygen species during methane combustion. Among other promoters, CeO₂ is very effective for Pd reoxidation, resulting in a strong reduction of the Pd-PdO hysteresis. This effect has been ascribed to the oxygen storage properties of CeO₂ [47], and (by DFT and molecular dynamics simulations) to a mixed oxide chemistry at the Pd/CeO₂ interface leading to the formation of Pd⁴⁺, thereby creating highly reducible sites ideal for methane activation.

Water vapor is the main poisoning agent of Pd-based catalysts under the conditions encountered in exhaust after-treatment technologies and power generation. [48] Water is ubiquitous in methane oxidation systems, being a product of the reaction itself and of combustion reactions taking place upstream in exhaust after-treatments. In most applications, the water vapor concentration varies in the range of 5-15%. This is known to cause a reversible deactivation of Pd-based catalysts at low temperatures (<450 °C) due to coverage effects and hydroxylation of the support/promoter, which inhibits O exchange.

Among the not-noble metal catalysts, the perovskite-type catalyst (ABO₃) is one of the best catalytic materials due to its special structure and properties for catalytic combustion of CH₄. Compared with the mixed metal oxide, perovskite-type catalysts have higher thermal stability properties, unusual valence states of transition metal ions in their structure, and

redox properties of high activity at low temperatures. Also, A or B zone cations are usually joined by other ions which will produce more defect sites and oxygen vacancies to improve the performance of the catalyst. [42],[50] These perovskites exhibit perfect hydrothermal stability and sulfur resistance in comparison with palladium-based catalysts. They are nominated as an alternative to noble metals used in the catalytic oxidation of CH₄ because they are relatively inexpensive.

A single mechanism cannot fully explain the oxidation kinetics of various hydrocarbons (alkanes, alkenes, aromatics,) on different perovskites. Therefore, a variety of reaction mechanisms and reaction orders are employed for different molecules and catalysts. In general, two are the possible reaction ways that can be find out: suprafacial and intrafacial reactions. Suprafacial reactions are the preferred ones at lower temperatures and consists of the reaction between the adsorbed species on the surface. Reaction rate of suprafacial reactions is related to the electronic configurations of the surface transition metal ions. On the contrary, intrafacial reactions occur at relatively high temperatures, since a high mobility of the ions in the bulk region of the catalysts is required. Reaction rate of intrafacial reactions is primarily related to the thermodynamic stability of oxygen vacancies adjacent to a transition metal ion. Still, the role of these oxygen species in complete and selective oxidation and their participation in combustion over various ceramic perovskite phases are not yet totally understood.

Suprafacial and Intrafacial ways are the two big sets, in which it is possible to find different kinetic models for hydrocarbons combustion. Many extensive computational studies have proposed four types of kinetics: Langmuir-Hinshelwood (LH), Eley-Rideal (ER), Mars-van Krevelen (MVK), and a two-term model. [51]

- For LH: Surface reaction occurs between dissociative or molecular adsorption of O₂ and CH₄.
- For ER: Surface reaction occurs between dissociative adsorption of O₂ and gaseous CH₄.
- For MVK: The reaction takes place through alternative oxidation and reduction of the catalyst surface.

- For the two-terms model: two ways of oxidation occur: via the lattice O_2 and via the adsorbed O_2 .

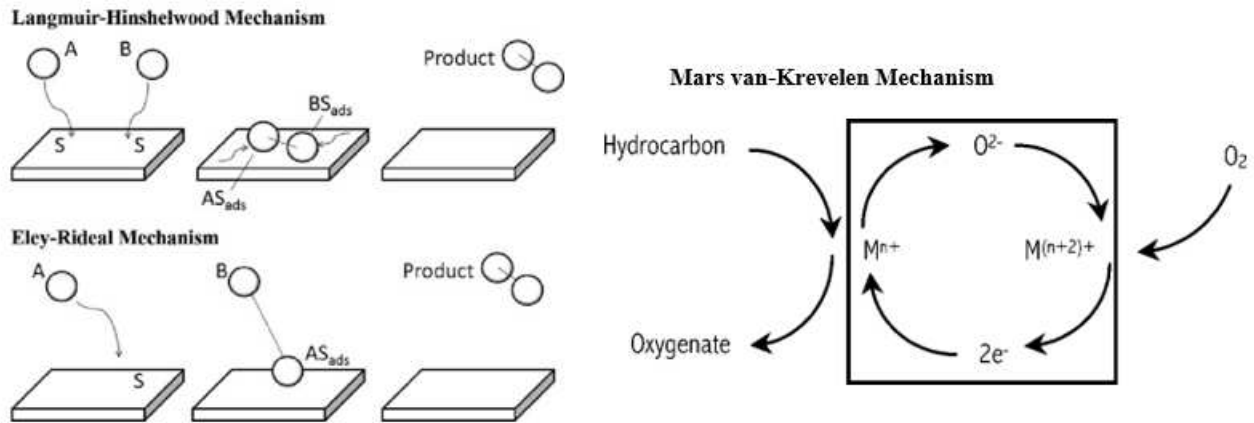


Figure 11: On the left the schematic comparison between Langmuir-Hinshelwood and Eley-Rideal mechanism. On the right the reaction scheme for the Mars van-Krevelen mechanism.

Oxidation for methane proceeds with the Eley-Rudeal (RD) mechanism, which is compatible with the difficulty of activating this molecule. [52] Ladavos and Pomonis [53] studied the catalytic combustion of CH_4 on two perovskite series $La_{1-x}Sr_xNiO_{4-\lambda}$ prepared by nitrate and citrate methods with stoichiometric oxygen content. They proposed a twin mechanism: one is a suprafacial process that uses oxygen from the gas phase and is active at low temperatures, and the other is an intrafacial process that receives oxygen from the perovskite lattice at high temperatures.

As a result of many regression analyses applied to experimental results, it is known that some mechanisms are in good harmony at certain temperature ranges but are meaningless at higher temperatures. Besides, as known, ER and MVK mechanism models mostly used for describing oxidation of organic compounds over well-known noble metals and metal oxides. The ER mechanism fulfilled the experimental kinetics for the most used perovskite for this kind of reaction: $LaMnO_3$. [54]

1.3 Lowering of the operating temperatures

The usage of methane as fuel gas for SOFC is not the only innovative aspects of this research and neither the most challenging. Indeed, one of the main purposes of this research is the operating temperature lowering. The traditional temperature range for SOFCs is in the High Temperature (HT) range, between 800 – 1000 °C. The high temperatures are a strong obstacle to the commercialization spreading of these devices. In fact, operating at 1000 °C

means high costs to maintain the temperature and materials challenge. Even if, as already said above, it is possible to use pressurized SOFCs as replacements for combustors in gas turbines, reaching efficiencies approaching 70%, must be noted that lowering the operating temperature can open new scenarios for SOFCs applications. Furthermore, there are many other aspects that must be considered. As an example, by lowering the operating temperatures, many other materials can be used as SOFCs components, allowing a cheaper fabrication, particularly in relation to interconnects and balance-of-plant (BoP) components. Obviously, start-up and shutdown can be quicker if the operating temperature to reach is lower and the corrosion rate of the metallic components is reduced too. Consequently, the reliability of the devices and the durability of the components is improved. For all these reasons, it was considered fundamental to test the studied material in the Intermediate (IT) and Low (LT) Temperature range. To be clearer the IT range is set between 600 – 800 °C, while the LT is conventionally set between 500 – 600 °C. This is completely a material science challenge, since the main problem is to find innovative anodic materials that are effective in these lower temperature ranges. Specifically, obtaining satisfactory anionic conductivity and electrochemical activity towards methane oxidation, were the main challenges since they are thermic activated processes.

For the research of the proper anodic material, it was tried to minimize the use of noble metals or compounds considered Critical Raw Materials (CRM). Their criticality can be due to their low presence or to the specific location of their extracting sites. Once more, the meaning of this constraints is to lower the fabrication costs and consequently increase the commercial spread of the SOFC technology. This goal was reached for IT-SOFCs applications, unfortunately, this was not possible for LT-SOFCs.

Therefore, in this research it is possible to find two different main pathways to reach the common main goal of an anode able to operate with methane at lower temperatures. The first pathway was focused on finding a completely CRW-free electrode operating in the IT range of temperatures.

The second one has, as main topic, the possibility to obtain LT-SOFCs fueled by methane. Since avoiding noble metals and having good performances with the actual scientific

knowledge it is not reachable, the main challenge is to lower the noble content on the electrodes. To reach this goal a new *ad hoc* deposition technique was developed.

1.4 Perovskites

In the previous [Paragraph 1.2.10](#) perovskites compounds were mentioned as possible low-cost candidate for substitution of noble metals catalysts. Thus, in this paragraph a description of this compounds will be discussed.

The name perovskite stems from the Russian mineralogist L. A. Perovski and it identifies a class of compounds with a specific structure. They find application in many research fields such as photovoltaics [\[\[55\], \[56\]\]](#), catalysis [\[\[55\], \[57\], \[58\]\]](#), optoelectronics [\[\[57\], \[59\], \[60\]\]](#) and others thanks to their physical and chemical properties, among them ferroelectricity, ferromagnetism, superconductivity, thermal and electronic conductivity. Their properties can be tuned by including different elements in the structure: perovskite can host 90% of the metals of the Periodic Table.

With the term perovskite a wide range of compounds with general formula ABX_3 are indicated. Where A and B are cations, usually with A larger than B and X could be N, C or O. For the applications considered in this work perovskite oxides will be considered. They exhibit overwhelming and flexible properties for working as electrodes in FC technology. In perovskites, ionic and electronic conductivity are strictly connected with structure and doping as well as catalytic activity.

The ideal cubic structure features B cations in a 6-fold coordination, surrounded by an octahedron of anions, and the A cation in 12-fold cuboctahedral coordination. A pictorial representation of the structure is reported in **Figure 12**.

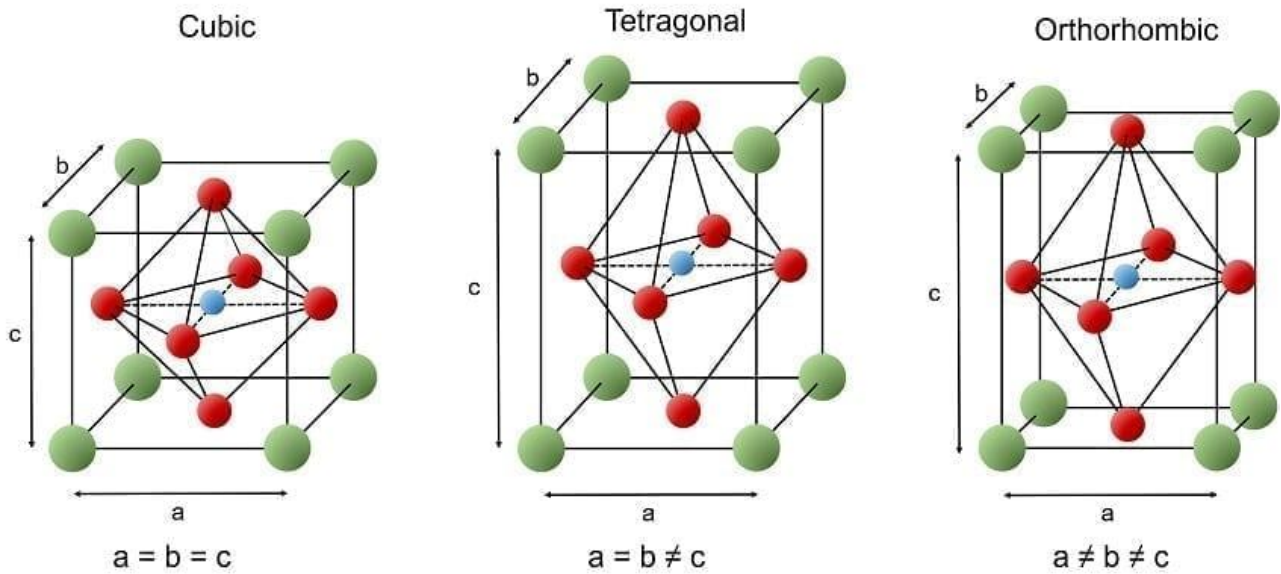


Figure 12: The cubic, tetragonal, and orthorhombic crystal structures of perovskite. The phase that the perovskite adopts depends on the temperature of the lattice.

Goldschmidt theorized the t-factor rule relating the stability of the cubic-perovskite phase to the empirical ionic radii of the ions inside the crystal structure.

$$t = \frac{r_A + r_O}{\sqrt{2}(r_B + r_O)} \quad (15)$$

Perovskite arrangement can be possible for t values oscillating from 0.75 to 1.05. Nonetheless, the perfect ideal cubic structure range is narrower: from 0.97 to 1.05. For lower t values a distorted structure can be obtained: orthorhombic, rhombohedral, monoclinic, triclinic, or tetragonal. Recent calculations prove that cubic structures may be formed even at higher t values. ^[61] Commonly, native perovskites do not show good performances in catalytic or electrochemical applications and, to enhance these features, doping is a suitable solution. Oxide can be mainly found as $A^{1+}B^{5+}O_3$, $A^{2+}B^{4+}O_3$ or $A^{3+}B^{3+}O_3$, for all of them the electroneutrality is maintained. Generally, A is a rare earth, alkaline, or alkaline earthy, while B is a transition metal of 3d, 4d or 5d group. ^[62] Challenging is to reach the more appropriate stoichiometric ratio to achieve the threshold for boosting the performances and below it is possible to find the most common strategies.

In literature, it's a common opinion that the A cation is almost inert, and its main function is to give structural stability to the crystal lattice. Anyway, that is not completely true. Indeed, must be considered that is very common a surface segregation of the A cation on the surface, with consequent formation of oxides or hydroxyls that can chemically interact

with the considered molecules of the reactions. Therefore, considering if the formation of these secondary phases is helpful or on the contrary detrimental, must be decided the stoichiometry of the compound, keeping in mind that some dopant species encourage the segregation of the A cation to the surface.

The electronic and catalytic activity is commonly attributed to the B cation. For this reason, it is very important to tune its properties through doping. A common strategy is to perform an aliovalent doping on the A site, forcing the B cation to different oxidation states to maintain the total electroneutrality. The presence of different oxidation states of the B site is very effective, for example, for the electronic conductivity given by polaron hopping. Another way it is to perform doping directly in the B site, giving new properties to the perovskite. Anyway, must be considered that generally the resultant material properties are not the perfect sum of the performances of the cations, but sometimes there is a synergic effect between the different chemical species, other times there is huge incompatibility with consequent lowering of the performances. As an example, Cu doping is generally performed to enhance the electronic conductivity of perovskites, that is generally not so high. Anyway, if it is performed directly on Sr, it is known in literature that there is the formation of a strontium segregation to the surface, with consequent formation of SrO that is completely insulating. ^[63]

1.5 Outline and aim of the thesis

To conclude, let me resume the technologies and strategies presented in the previous pages that were chosen as possible solutions to the energy demand and air pollution. First, Solid Oxide Cells (SOCs) were illustrated with the aim to show how this technique is extremely efficient to transform chemical energy into electrical energy (fuel cell mode) and vice versa (electrolyzer mode).

The innovative aspect of this research is the implementation of this technology from different aspects that can push this technology to a wider commercialization and in the meantime to realize a total green technology. This could seem a utopia, but the realization of a symmetrical and reversible SOC (Paragraph 1.2.4 - 1.2.5) fueled by biogas

([Paragraph 1.2.9](#)) with components realized through innovative materials, like perovskites ([Paragraph 1.4](#)), can be the final solution to a completely green production of energy.

In detail, the outline of the thesis:

In Chapter 2 the characterization techniques and the cell fabrication procedure are explained.

Chapter 3 illustrates the possibility to use $\text{La}_{0.6}\text{Sr}_{0.4}\text{MnO}_3$ as anode material for IT-SOFCs fuelled by methane. LSM powder and nanofibers were characterized to understand the effects of morphology on the performances.

Chapter 4 is focused on the study of $\text{La}_{0.8}\text{Sr}_{0.2}\text{MnO}_3$ and $\text{La}_{0.6}\text{Sr}_{0.4}\text{Cu}_{0.1}\text{Mn}_{0.9}\text{O}_3$ as alternatives of LSM, understanding the effects given by Sr and Cu doping on the performances.

In Chapter 5 Cu@GDC with a 2%Pd infiltration is analyzed as anode material for DM-SOFCs operating in the LT-range.

In Chapter 6 the Raman spectroscopy studies performed at Denmark Technical University (DTU) on the studied compounds and cell electrodes are discussed.

In the final Chapter 7 are presented the conclusions obtained by the research work.

References

- [1] P. V. F. Lopes, C. M. da S. B. Costa, A. K. Almeida, and I. K. de Almeida, "Sustainability assessment model for Brazilian hydroelectric projects using multicriteria analysis," *Sustainable Energy Technologies and Assessments*, vol. 51, p. 101851, Jun. 2022, doi: 10.1016/j.seta.2021.101851.
- [2] J. Zhao *et al.*, "The determinants of renewable energy sources for the fueling of green and sustainable economy," *Energy*, vol. 238, Jan. 2022, doi: 10.1016/j.energy.2021.122029.
- [3] M. Lennan and E. Morgera, "The Glasgow Climate Conference (COP26)," *The International Journal of Marine and Coastal Law*, pp. 1–15, Feb. 2022, doi: 10.1163/15718085-bja10083.
- [4] M. Ram, M. Child, A. Aghahosseini, D. Bogdanov, A. Lohrmann, and C. Breyer, "A comparative analysis of electricity generation costs from renewable, fossil fuel and nuclear sources in G20 countries for the period 2015-2030," *J Clean Prod*, vol. 199, pp. 687–704, Oct. 2018, doi: 10.1016/j.jclepro.2018.07.159.
- [5] T. Trainer, "Some problems in storing renewable energy," *Energy Policy*, vol. 110, pp. 386–393, Nov. 2017, doi: 10.1016/J.ENPOL.2017.07.061.
- [6] F. Zhang, P. Zhao, M. Niu, and J. Maddy, "The survey of key technologies in hydrogen energy storage," *Int J Hydrogen Energy*, vol. 41, no. 33, pp. 14535–14552, Sep. 2016, doi: 10.1016/J.IJHYDENE.2016.05.293.
- [7] M. Hirscher, *Handbook of Hydrogen Storage*. Wiley-VCH, 2009.
- [8] N. Khan, | Saad Dilshad, R. Khalid, | Ali, R. Kalair, and N. Abas, "Review of energy storage and transportation of energy," 2019, doi: 10.1002/est2.49.
- [9] D. Rutz, "Biofuel technology handbook," 2007.
- [10] S. M. Haile, "Materials for fuel cells," *Materials Today*, vol. 6, no. 3, pp. 24–29, Mar. 2003, doi: 10.1016/S1369-7021(03)00331-6.
- [11] M. W. Ellis, M. R. von Spakovsky, and D. J. Nelson, "Fuel Cell Systems: Efficient, Flexible Energy Conversion for the 21st Century," *Proceedings of the IEEE*, vol. 89, no. 12, pp. 1808–1817, 2001, doi: 10.1109/5.975914.
- [12] A. Kirubakaran, S. Jain, and R. K. Nema, "A review on fuel cell technologies and power electronic interface," *Renewable and Sustainable Energy Reviews*, vol. 13, no. 9, pp. 2430–2440, Dec. 2009, doi: 10.1016/J.RSER.2009.04.004.
- [13] R. C. T. Slade, J. P. Kizewksi, S. D. Poynton, R. Zeng, and J. R. Varcoe, *Encyclopedia of Sustainability Science and Technology*, vol. Chapter 2. Springer New York, 2012. doi: 10.1007/978-1-4419-0851-3.
- [14] M. Watanabe, K. Tsurumi, T. Mizukami, T. Nakamura, and P. Stonehart, "Activity and Stability of Ordered and Disordered Co-Pt Alloys for Phosphoric Acid Fuel Cells," 1994.
- [15] A. L. Dicks, "Molten carbonate fuel cells," *Curr Opin Solid State Mater Sci*, vol. 8, no. 5, pp. 379–383, Oct. 2004, doi: 10.1016/J.COSSMS.2004.12.005.
- [16] K. M. McGrath, G. K. S. Prakash, and G. A. Olah, "Direct Methanol Fuel Cells," *J. Ind. Eng. Chem.*, vol. 10, no. 7, pp. 1063–1080, 2004.
- [17] N. Mahato, A. Banerjee, A. Gupta, S. Omar, and K. Balani, "Progress in material selection for solid oxide fuel cell technology: A review," *Prog Mater Sci*, vol. 72, pp. 141–337, Jul. 2015, doi: 10.1016/J.PMATSCI.2015.01.001.
- [18] J. Milewski Andrzej Miller, "Mathematical Model of SOFC (SOLID OXIDE FUEL CELL) for Power Plant Simulations," in *ASME Turbo Expo 2004*, 2004, pp. 14–17. [Online]. Available: <http://www.asme.org/about-asme/terms-of-use>
- [19] S. C. Singhal, "Advances in solid oxide fuel cell technology," *Solid State Ion*, vol. 135, no. 1–4, pp. 305–313, Nov. 2000, doi: 10.1016/S0167-2738(00)00452-5.
- [20] J. C. Ruiz-Morales, F. Marrero-López, M. Gálvez-Sánchez, J. Canales-Vázquez, C. Savaniu, and S. N. Savvin, "Engineering of materials for solid oxide fuel cells and other energy and environmental application," *Energy Environ Sci*, vol. 3, no. 11, pp. 897–1004, 2010, doi: 10.1039/c0ee00166j.

- [21] W. Z. Zhu and S. C. Deevi, "A review on the status of anode materials for solid oxide fuel cells," *Materials Science and Engineering: A*, vol. 362, no. 1–2, pp. 228–239, Dec. 2003, doi: 10.1016/S0921-5093(03)00620-8.
- [22] C. Sun, R. Hui, and J. Roller, "Cathode materials for solid oxide fuel cells: a review," 2003, doi: 10.1007/s10008-009-0932-0.
- [23] N. Laosiripojana, W. Wiyaratn, W. Kiatkittipong, A. Arpornwichanop, A. Soottitantawat, and S. Assabumrungrat, "Reviews on solid oxide fuel cell technology," *Engineering Journal*, vol. 13, no. 1, pp. 65–83, 2009, doi: 10.4186/ej.2009.13.1.65.
- [24] E. Fabbri, D. Pergolesi, and E. Traversa, "Electrode materials: a challenge for the exploitation of protonic solid oxide fuel cells," *Sci Technol Adv Mater*, 2010.
- [25] C. H. Wendel and R. J. Braun, "Design and techno-economic analysis of high efficiency reversible solid oxide cell systems for distributed energy storage," *Appl Energy*, vol. 172, pp. 118–131, Jun. 2016, doi: 10.1016/J.APENERGY.2016.03.054.
- [26] V.-T. GIAP, Y. D. U. K. LEE, Y. S. KIM, and K. Y. AHN, "Techno-economic analysis of reversible solid oxide fuel cell system couple with waste steam," *Transactions of the Korean hydrogen and new energy society*, vol. 30, no. 1, pp. 21–28, 2019.
- [27] M. Lamagna, B. Nastasi, D. Groppi, C. Rozain, M. Manfren, and D. A. Garcia, "Techno-economic assessment of reversible Solid Oxide Cell integration to renewable energy systems at building and district scale," *Energy Convers Manag*, vol. 235, p. 113993, 2021.
- [28] Q. Liu, X. Dong, G. Xiao, F. Zhao, and F. Chen, "A novel electrode material for symmetrical SOFCs," *Advanced Materials*, vol. 22, no. 48, pp. 5478–5482, Dec. 2010, doi: 10.1002/adma.201001044.
- [29] J. Zamudio-García, L. Caizán-Juanarena, J. M. Porrás-Vázquez, E. R. Losilla, and D. Marrero-López, "A review on recent advances and trends in symmetrical electrodes for solid oxide cells," *Journal of Power Sources*, vol. 520. Elsevier B.V., Feb. 01, 2022. doi: 10.1016/j.jpowsour.2021.230852.
- [30] Sy. Istomin, N. Lyskov, G. Mazo, and E. Antipov, "Electrode materials based on complex d-metal oxides for symmetrical solid oxide fuel cells", doi: 10.1070/RCR4979.
- [31] B. Zhu, "Solid oxide fuel cell (SOFC) technical challenges and solutions from nano-aspects," *Int J Energy Res*, vol. 33, no. 13, pp. 1126–1137, 2009, doi: 10.1002/er.1600.
- [32] S. P. Jiang, "Nanoscale and nano-structured electrodes of solid oxide fuel cells by infiltration: Advances and challenges," *Int J Hydrogen Energy*, vol. 37, no. 1, pp. 449–470, Jan. 2012, doi: 10.1016/J.IJHYDENE.2011.09.067.
- [33] A. Yilanci, I. Dincer, and H. K. Ozturk, "A review on solar-hydrogen/fuel cell hybrid energy systems for stationary applications," *Progress in Energy and Combustion Science*, vol. 35, no. 3, pp. 231–244, Jun. 2009. doi: 10.1016/j.peccs.2008.07.004.
- [34] I. Dincer and C. Acar, "Review and evaluation of hydrogen production methods for better sustainability," *Int J Hydrogen Energy*, vol. 40, no. 34, pp. 11094–11111, Aug. 2014, doi: 10.1016/j.ijhydene.2014.12.035.
- [35] T. Bridgwater, "Biomass for energy," *Journal of the Science of Food and Agriculture*, vol. 86, no. 12, pp. 1755–1768, Sep. 12, 2006. doi: 10.1002/jsfa.2605.
- [36] P. Weiland, "Biomass digestion in agriculture: A successful pathway for the energy production and waste treatment in Germany," *Engineering in Life Sciences*, vol. 6, no. 3, pp. 302–309, Jun. 2006. doi: 10.1002/elsc.200620128.
- [37] J. Byun and J. Han, "Economically feasible production of green methane from vegetable and fruit-rich food waste," *Energy*, vol. 235, p. 121397, Nov. 2021, doi: 10.1016/J.ENERGY.2021.121397.
- [38] M. Herrero *et al.*, "Innovation can accelerate the transition towards a sustainable food system," *Nature Food*, vol. 1, no. 5. Springer Nature, pp. 266–272, May 01, 2020. doi: 10.1038/s43016-020-0074-1.

- [39] J. Byun and J. Han, "Sustainable development of biorefineries: integrated assessment method for co-production pathways †," *Energy Environ. Sci*, vol. 13, p. 2233, 2020, doi: 10.1039/d0ee00812e.
- [40] R. Burch, D. J. Crittle, and M. J. Hayes, "C-H bond activation in hydrocarbon oxidation on heterogeneous catalysts," *Catal Today*, vol. 47, no. 1-4, pp. 229-234, Jan. 1999, doi: 10.1016/S0920-5861(98)00303-4.
- [41] D. Ciuparu and L. Pfefferle, "Support and water effects on palladium based methane combustion catalysts," *Appl Catal A Gen*, vol. 209, no. 1-2, pp. 415-428, Feb. 2001, doi: 10.1016/S0926-860X(00)00783-3.
- [42] R. F. Hicks, H. Qi, M. L. Young, and R. G. Lee, "Structure Sensitivity of Methane Oxidation over Platinum and Palladium," 1990.
- [43] J. Nilsson *et al.*, "Methane oxidation over Pd/Al₂O₃ under rich/lean cycling followed by operando XAFS and modulation excitation spectroscopy," *J Catal*, vol. 356, pp. 237-245, Dec. 2017, doi: 10.1016/J.JCAT.2017.10.018.
- [44] H. A. Doan, M. K. Sharma, W. S. Epling, and L. C. Grabow, "From Active-Site Models to Real Catalysts: Importance of the Material Gap in the Design of Pd Catalysts for Methane Oxidation," *ChemCatChem*, vol. 9, no. 9, pp. 1594-1600, 2017, doi: 10.1002/cctc.201601333.
- [45] Y. Liu, C. Hu, and L. Bian, "Highly Dispersed Pd Species Supported on CeO₂ Catalyst for Lean Methane Combustion: The Effect of the Occurrence State of Surface Pd Species on the Catalytic Activity," *Catalysts*, vol. 11, no. 7, p. 772, 2021, doi: 10.3390/catal.
- [46] D. Ciuparu, N. Katsikis, and L. Pfefferle, "Temperature and time dependence of the water inhibition effect on supported palladium catalyst for methane combustion," *Appl Catal A Gen*, vol. 216, no. 1-2, pp. 209-215, Aug. 2001, doi: 10.1016/S0926-860X(01)00558-0.
- [47] S. Colussi, A. Trovarelli, G. Groppi, and J. Llorca, "The effect of CeO₂ on the dynamics of Pd-PdO transformation over Pd/Al₂O₃ combustion catalysts," *Catal Commun*, vol. 8, no. 8, pp. 1263-1266, Aug. 2007, doi: 10.1016/J.CATCOM.2006.11.020.
- [48] J. K. Lampert, M. S. Kazi, and R. J. Farrauto, "Palladium catalyst performance for methane emissions abatement from lean burn natural gas vehicles," *Appl Catal B*, vol. 14, no. 3-4, pp. 211-223, Dec. 1997, doi: 10.1016/S0926-3373(97)00024-6.
- [49] A. Aranzabal, B. Pereda-Ayo, M. P. González-Marcos, J. A. González-Marcos, R. López-Fonseca, and J. R. González-Velasco, "State of the art in catalytic oxidation of chlorinated volatile organic compounds," *Chemical Papers*, vol. 68, no. 9. Versita, pp. 1169-1186, 2014. doi: 10.2478/s11696-013-0505-7.
- [50] W. B. Li, J. X. Wang, and H. Gong, "Catalytic combustion of VOCs on non-noble metal catalysts," *Catal Today*, vol. 148, no. 1-2, pp. 81-87, Oct. 2009, doi: 10.1016/J.CATTOD.2009.03.007.
- [51] S. Thaicharoensutcharittham, V. Meeyoo, B. Kitiyanan, P. Rangsunvigit, and T. Rirksomboon, "Catalytic combustion of methane over NiO/Ce_{0.75}Zr_{0.25}O₂ catalyst," *Catal Commun*, vol. 10, no. 5, pp. 673-677, Jan. 2009, doi: 10.1016/J.CATCOM.2008.11.014.
- [52] P. Granger, V. I. Parvulescu, S. Kaliaguine, and Prellier W, *Perovskites and related mixed oxides: concept and applications*. John Wiley & Sons, 2015.
- [53] A. K. Ladavos and P. J. Pornonis, "Catalytic Combustion of Methane on La-,Sr,NiO,-~ Perovskites prepared via the Nitrate and Citrate Routes," 1992.
- [54] V. Bashan and Y. Ust, "Perovskite catalysts for methane combustion: applications, design, effects for reactivity and partial oxidation," *International Journal of Energy Research*, vol. 43, no. 14. John Wiley and Sons Ltd, pp. 7755-7789, Nov. 01, 2019. doi: 10.1002/er.4721.
- [55] S. il Seok, M. Jung, S.-G. Ji, and G. Kim, "Featuring work from the research group of Professor Chem Soc Rev Perovskite precursor solution chemistry: from fundamentals to photovoltaic applications," *Chem. Soc. Rev*, vol. 48, doi: 10.1039/c8cs00656c.

- [56] X. Ma, L. Yang, K. Lei, S. Zheng, C. Chen, and H. Song, "Doping in inorganic perovskite for photovoltaic application," *Nano Energy*, vol. 78, p. 105354, Dec. 2020, doi: 10.1016/J.NANOEN.2020.105354.
- [57] S. Keav, S. K. Matam, D. Ferri, and A. Weidenkaff, "Structured Perovskite-Based Catalysts and Their Application as Three-Way Catalytic Converters-A Review," *Catalysts*, vol. 4, pp. 226-255, 2014, doi: 10.3390/catal4030226.
- [58] M. Misono, "Recent progress in the practical applications of heteropolyacid and perovskite catalysts: Catalytic technology for the sustainable society," *Catal Today*, vol. 144, no. 3-4, pp. 285-291, Jun. 2009, doi: 10.1016/J.CATTOD.2008.10.054.
- [59] Q. Chen *et al.*, "Under the spotlight: The organic-inorganic hybrid halide perovskite for optoelectronic applications," *Nano Today*, vol. 10, no. 3, pp. 355-396, Jun. 2015, doi: 10.1016/J.NANTOD.2015.04.009.
- [60] P. Docampo and T. Bein, "A Long-Term View on Perovskite Optoelectronics," 2016, doi: 10.1021/acs.accounts.5b00465.
- [61] S. C. Tidrow, "Mapping comparison of goldschmidt's tolerance factor with perovskite structural conditions," *Ferroelectrics*, vol. 470, no. 1, pp. 13-27, Oct. 2014, doi: 10.1080/00150193.2014.922372.
- [62] C. J. Bartel *et al.*, "New tolerance factor to predict the stability of perovskite oxides and halides," *Sci Adv*, vol. 5, pp. 1-9, 2019, [Online]. Available: <https://www.science.org>
- [63] N. Caillol, M. Pijolat, and E. Siebert, "Investigation of chemisorbed oxygen, surface segregation and effect of post-treatments on La_{0.8}Sr_{0.2}MnO₃ powder and screen-printed layers for solid oxide fuel cell cathodes," *Appl Surf Sci*, vol. 253, no. 10, pp. 4641-4648, 2007.

Chapter 2: Characterization techniques and cell fabrication

2.1 X-Ray Diffraction (XRD)

The crystal structure of the samples was investigated by X-ray diffraction (XRD) using a diffractometer (Bruker D8 Advance) equipped with Ni filtered Cu K α radiation, variable slits, and energy sensitive line detector (LynxEye). Diffractograms were collected at an acquisition time of 0.6 s and a step size of $\Delta 2\theta = 0.02^\circ$ in the range 20-80°. Background fitting, peak parameter determination and phase identification were performed using the EVA software from Bruker. To estimate the crystal size (d) of the studied compounds, the Scherrer equation ^[1] is used:

$$d = \frac{K\lambda}{FWHM\cos\theta} \quad (1)$$

Where, K is the form factor ($K=0.9$), λ is the X-ray source wavelength ($\lambda=1.54 \text{ \AA}$ in case of Cu anode), θ is the angular reflection position and FWHM is the Full Width at Half Maximum of the correspondent diffraction reflex.

2.2 H₂-Temperature Programmed Reduction (H₂-TPR)

Temperature programmed reduction in hydrogen experiments were carried out on a bench top AutoChem 2920 instrument equipped with a Thermal Conductivity Detector (TCD) to measure H₂ consumption. The samples (~50 mg) were loaded into the quartz reactor tube. Measurements were recorded in 5 vol% H₂/Ar (30 sccm) and with a heating rate of 10 °Cmin⁻¹. TPR samples were previously outgassed with He (50 sccm) at room temperature. Single TPRs were usually conducted up to 900 °C.

2.3 Scanning Electronic Microscopy (SEM)

Scanning Electron Microscopy was used to observe the morphological changes of powder samples and the cell sections. These images are useful to verify the electrodes porosity. The instrument used to obtain the images is a field emission SEM (Zeiss ULTRA 55). The samples are deposited on sticky carbon tape on aluminum stubs before analysis. The sample were

analyzed using a 20 keV electron beam and the in-lens secondary electron detector at a working distance of 7 mm.

2.4 Specific surface area determination

Nitrogen physisorption at -196 °C was used to determine the specific surface area (SSA) based on the theory of Brunauer-Emmett-Teller (BET) using an ASAP 2020 instrument from Micromeritics. The measurements were conducted on 0.5 g of powder sample, which was outgassed at 300 °C for 6h. Seven-point adsorption isotherms were collected in the pressure range of 0.05 - 0.3 P/P₀, as typically values applied for mesoporous materials.

2.5 X-Ray Photoelectron Spectroscopy (XPS)

X-ray photoelectron spectroscopy (XPS) measurements are carried out employing a Perkin Elmer Φ 5600ci Multi Technique System. The spectrometer is calibrated by assuming that the binding energy (BE) of the Au 4f_{7/2} line is 84.0 eV with respect to the Fermi level. Both extended spectra (survey-187.85 eV pass energy, 0.5 eV/step, 0.05 s/step) and detailed spectra (La 3d, Mn 2p, Sr 3d, O 1s and C 1s -23.5 eV pass energy, 0.1 eV/step, 0.1 s/step) are collected with a standard Al Kα source. The atomic percentage is evaluated using the PHI sensitivity factors [2] after a Shirley-type background subtraction [3]. The peak positions are corrected for the charging effects by considering the C 1s peak at 285.0 eV and evaluating the BE differences [4].

2.6 Methane oxidation catalytic tests

The methane oxidation catalytic activity tests are carried out at atmospheric pressure in a quartz reactor (6 mm ID) equipped with a packed bed of powders. The temperature increased until 800 °C with a temperature ramp of 2° C min⁻¹, was monitored by a thermocouple right upstream of the bed. Two are the studied gas mixtures of methane and air. The first one with a stoichiometric ratio between methane and oxygen of 2:1; the second one with an atmosphere characterized by under-stoichiometric oxygen presence, namely with a ratio between methane and oxygen of 1:2. Flows are dosed by a Vögtlin Red-y system. Total flow of 100 ml min⁻¹ is kept constant, balancing it with He. The composition of the gas

mixture (before and after reaction) is measured by GC (Agilent 7890A), with a TCD detector and 13X (60/80 mesh, 1.8 m) and Porapak Q (1.8 m) columns.

2.7 Cells manufacturing

It was chosen to use electrolyte supported button cell as samples for electrochemical testing due to its manufacturing simplicity. In addition, between the different possible configurations, electrolyte supported guarantee the best reproducibility of the tests. In fact, the main purpose of this work is to study the synthesized catalysts as electrode materials for symmetrical solid oxide cells. To obtain the green pellet of $\text{Ce}_{0.9}\text{Gd}_{0.1}\text{O}_2$ (GDC) or yttria stabilized zirconia (8-YSZ), commercial powders (2.5 g) were compressed utilizing a pressure of 3.5 tons for 5 minutes; in the end the pellets were treated thermally at 1500 °C for 6 hours with a ramp of 5 °C/min until 1100 °C followed by a ramp of 3 °C/min up to the final temperature. The mass of GDC powder and pressure are optimized parameters to obtain a good density of the pellets, that is the most similar to the nominal ones. A good density of the electrolyte is important to avoid the O_2 gas diffusion inside the electrolytic material. The manufactured electrolytes possessed dimensions are 21 mm of diameter and 1 mm of thickness for GDC and 19 mm of diameter and 1.6 mm of thickness for YSZ. It was chosen to use the GDC pellets as electrolyte for single chamber testing, while the double chamber tests were carried out on YSZ electrolyte supported button cells. After electrolyte sintering, the pellets were cleaned in ethanol with an ultrasonic bath, and they are ready for electrode deposition. The depositions of the electrode ink were made by tape casting procedure. For the electrodes based on perovskitic compounds, the inks were made by pestering a certain quantity of perovskites with the same amount in mass of GDC in a mortar and mixing the resultant powder with a commercial polymer binder with mass ratio binder/powder 1:2. The viscosity of the ink was adjusted adding a few drops of a vehicle resin. A vehicle resin is the fluid carrier of the ink, which can be evaporated, leaving only the dry electrode material. The choice to use a composite electrode containing the electrolyte powder is given by considering the difficult adhesion of tape casted inks on the electrolyte. In addition, 3% by weight of soot was added in order to confer good porosity to the final electrode through its combustion during the electrode thermal processing. The tape casted electrodes have circular shape, with a diameter of 12 mm. After electrode deposition, a thermal treatment till 1050 °C for 2 hours with a heating ramp of 3 °C/min was carried out.

The last step consists of covering the electrode with a gold paste, that will be the electrons-collector of the cell. This gold paste is a commercial mixture of gold and organic binder. This last one is decomposed with another thermal treatment that reaches 800 °C with no steady time and with a ramp of 5 °C/min.

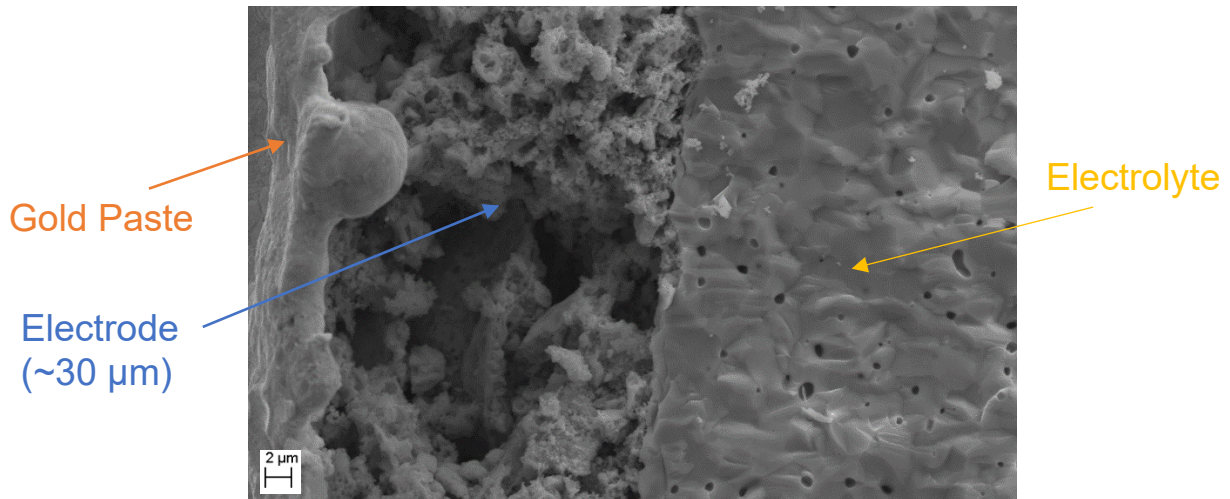


Figure 1: SEM image of cell section. From left to right is possible to see the gold paste tape casted on the surface of the electrode as current collector; in the middle is visible the electrode (in this case LSM/GDC composite electrode), with a measured thickness of about 30 μm and on the right the electrolyte (in this case GDC).

2.8 Electrochemical Impedance Spectroscopy (EIS) experimental setup

To study in a proper way the properties of a material as electrode for a solid oxide cell is the symmetrical configuration [5], [6]: both the electrodes are equal and are composed by the same materials. For symmetrical test, the cell was supported by an α -alumina DEGUSIT AL23 tube able to canalize the gases parallel to the electrode surface, as showed in **Figure 2**. Platinum wires present on the ceramic tube were connected to the golden wires on the cell in order to establish a consistent electron pathway.

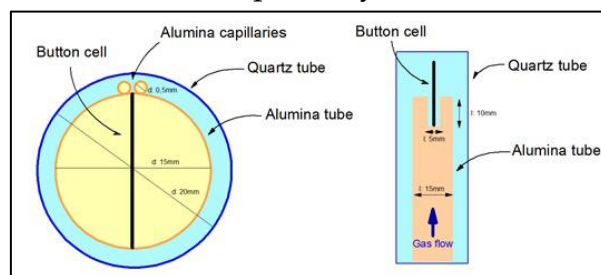


Figure 2: Representation of the symmetrical setup used for electrochemical measurements.

Electrochemical results were obtained through PGSTAT 302 Autolab Frequency Response Analyzer: the tests were carried out in steady state conditions, i.e., with no DC current in the frequency range between 10^{-2} - 10^6 Hz with a signal amplitude of 20 mV. All EIS data were fitted and analyzed through the ZView 4 software and different circuits were utilized to fit different EIS data.

2.9 Electrochemical Impedance Spectroscopy (EIS) theory

Impedance spectroscopy is one of the main techniques for SOFC materials characterization and evaluation of electrochemical performances. It is highly sensitive toward sample configuration and fabrication procedures but allows investigating the polarization processes of the material.

Some basic concepts concerning Impedance Spectroscopy are reported in the following pages.

An ideal resistor has several simplifying properties:

- It follows Ohm's Law at all current and voltage levels.
- Its resistance value is independent on frequency.
- AC current and voltage signals through a resistor are in phase with each other.

However, the real world contains circuit elements that exhibit much more complex behaviors. These elements force us to abandon the simple concept of resistance, and impedance, a more general circuit parameter, needs to be used. Like resistance, impedance is a measure of the ability of a circuit to resist the flow of electrical current, but unlike resistance, it is not limited by simplifying properties listed above. The measurements are carried out by applying a little and sinusoidal AC potential to the cell and then measuring the produced current.

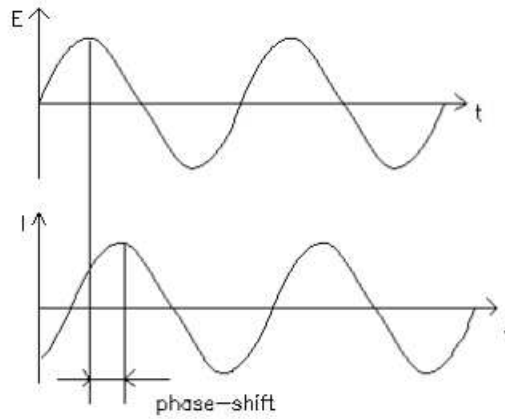


Figure 3: Sinusoidal potential signal and relative current response in a linear system

The excitation signal has the form:
$$E_t = E_0 \sin(\omega t) \quad (2)$$

with E_t the potential at the time t , E_0 is the amplitude of the signal, and ω is the radial frequency, that is linked with frequency f (expressed in Hz) as:
$$\omega = 2\pi f \quad (3)$$

Therefore, the produced current at the time t (I_t) is:
$$I_t = I_0 \sin(\omega t + \phi), \quad (4)$$

where ϕ is the phase shift.

With the analogue of the Ohm's law:
$$Z = \frac{E_t}{I_t} = \frac{E_0 \sin(\omega t)}{I_0 \sin(\omega t + \phi)} = Z_0 \frac{\sin(\omega t)}{\sin(\omega t + \phi)} \quad (5)$$

The impedance is expressed in terms of a magnitude (Z_0) and a phase shift (ϕ).

With Euler's relationship, it is possible to express the impedance as a complex function:

$$Z = \frac{E_t}{I_t} = Z_0 \exp(j\phi) = Z_0 \cos(\phi + j\sin\phi) \quad (6)$$

The data presentation is through "Nyquist plot", where the real part of Z is plotted on the X-axis, while the opposite of the imaginary part is plotted on Y-axis. With Nyquist plot is not possible to know at what frequency was recorded the point, but the Bode plot gives this information. The logarithm of the frequencies is given on the X-axis, while in the ordinate is plotted the logarithm of impedance.

The information that this technique can give are numerous, but often they are quite difficult to visualize and understand. EIS data are commonly analyzed by fitting them with an equivalent electrical circuit model. Most of the circuit elements in the model are common electrical elements such as resistors, capacitors, and inductors. To be useful, the elements in the model should have a basis in the physical electrochemistry of the system. As an example, most models contain a resistor that models the cell electrolyte resistance. So, by fitting the obtained spectra with the correct elements. Parameters characterizing the cell, like

capacitance (C) and Area Specific Resistance (ASR), can be obtained. It is also possible to be better understand the occurring processes. For example, frequency is an important parameter to identify the physical phenomenon causing a particular signal in the spectrum.

References

- [1] P. Scherrer, "Nachrichten von der Gesellschaft der Wissenschaften zu Göttingen," *Mathematisch-Physikalische Klasse*, vol. 2, pp. 98–100, 1918.
- [2] J. Chastain and R. C. King Jr, "Handbook of X-ray photoelectron spectroscopy," *Perkin-Elmer Corporation*, vol. 40, p. 221, 1992.
- [3] D. A. Shirley, "High-resolution X-ray photoemission spectrum of the valence bands of gold," *Phys Rev B*, vol. 5, no. 12, p. 4709, 1972.
- [4] S. C. Singhal, "Advances in solid oxide fuel cell technology," *Solid State Ion*, vol. 135, no. 1–4, pp. 305–313, 2000.
- [5] N. Mahato, A. Banerjee, A. Gupta, S. Omar, and K. Balani, "Progress in material selection for solid oxide fuel cell technology: A review," *Progress in Materials Science*, vol. 72. Elsevier Ltd, pp. 141–337, Jul. 28, 2015. doi: 10.1016/j.pmatsci.2015.01.001.
- [6] S. P. S. Shaikh, A. Muchtar, and M. R. Somalu, "A review on the selection of anode materials for solid-oxide fuel cells," *Renewable and Sustainable Energy Reviews*, vol. 51. Elsevier Ltd, pp. 1–8, Jun. 20, 2015. doi: 10.1016/j.rser.2015.05.069.

Chapter 3: $\text{La}_{0.6}\text{Sr}_{0.4}\text{MnO}_3$, from powder to IT-SOFCs anode fueled by CH_4

3.1 Introduction

We have seen in the previous [Chapter 1](#) that Fuel Cells are electrochemical devices that directly convert the chemical energy of the fuel into electrical energy, avoiding the Carnot cycle and allowing high efficiencies to be achieved ^{[1], [2]}. For this reason—and due to the constant increase in energy demand and, consequently, in greenhouse gas emissions—fuel cells have drawn great attention over the last few decades. Among all fuel cell configurations, solid oxide fuel cells (SOFCs) have all solid-state components, with high benefits in terms of corrosion, orientation of the stack, etc. Intermediate Temperature Solid Oxide Fuel Cells (IT-SOFCs), moreover, allow to better afford the materials requirements and thus the device cost. Moreover, these devices offer wide fuel flexibility, since they can operate with both hydrogen and light hydrocarbons ^{[3], [4]}. The latter is an interesting feature, since natural gas and methane are cheap and abundant fuels, whereas pure hydrogen is mostly produced through the hydrocarbon reforming process ^{[5]-[8]} and storage and transportation are still issues. In the SOFC anode, methane can either be electro-oxidized directly or undergo an internal reforming process in which methane is converted into hydrogen. Both options have been investigated in recent years. The internal methane reforming process is generally carried out employing nickel-based electrodes. The main challenges of this process are controlling temperature gradients across the SOFC stacks and avoiding coke deposition over the nickel catalyst, with consequent catalyst deactivation. The issue of temperature control, is due to the strong endothermicity of the methane steam reforming reaction, resulting in uneven temperature distribution over the cell, with the possible formation of cold spots ^[9]. The coke deposition issue is behind the need to operate the cell with a steam-to-carbon (S/C) ratio larger than three, which makes it difficult to achieve complete methane conversion. Due to these problems, IT-SOFCs, running internal steam methane reforming processes, require high costs and complex balance-of-plant (BoP) components. The direct electro-oxidation of methane represents an interesting alternative.

The direct utilization of methane provides high open-circuit voltage, with high efficiency and simple BoP [10], [11].

Nevertheless, the direct electrochemical oxidation of methane cannot be carried out employing standard nickel-based electrodes. Indeed, at an operating temperature above 800 °C, severe coke deposition takes place with Ni-containing catalysts. At temperatures below 800 °C, the nickel-based anode provides low power densities [12]. Nevertheless, it is possible to use innovative anode materials. Interesting improvements have been made employing anode materials containing Cu, which does not catalyze the formation of graphite [9,10]. Another option is the use of perovskite materials, which have been widely investigated in SOFC applications as both anode and cathode. The ideal perovskite, represented with the ABO_3 general formula, is a versatile metal oxide. It can be doped in both the A and B sites, affecting the oxygen stoichiometry and improving the oxygen ion mobility – as well as the electron conductivity [13]-[17].

To choose the most suitable perovskite as electrode material for symmetrical SOFC, we considered that one state-of-the-art perovskite for SOFC cathode application is the Sr-doped $LaMnO_3$. Lanthanum substitution with strontium in the A-site results in an increase of electronic conductivity from 83 S cm^{-1} for $LaMnO_3$ to 320 S cm^{-1} for $La_{0.6}Sr_{0.4}MnO_3$ (LSM), at the same operating temperature of 800 °C [18]. The same type of material ($La_{0.8}Sr_{0.2}Mn_{0.98}O_3$) has also been studied for oxidative coupling of methane in solid oxide membrane reactors [19]. The reason of high activity in $LaMnO_3$ -based materials is their ability to have fast, reversible, and nondestructive valence alternation. These features are responsible of partial charge transfer between adsorbed oxygen and the metallic sites on the perovskite surface. For this reason, the availability of Mn to have many different possible oxidation states, makes manganite perovskites suitable for these applications. Furthermore, conductive perovskites, such as $(La,Sr)(Cr,Mn)O_3/(Ce,Gd)_{2-\delta}$, have been tested in fuel cells with a direct methane configuration, reporting a polarization resistance of $0.496 \text{ } \Omega\text{cm}^2$ at 850 °C [20].

In addition to new materials, innovative electrode architectures have been investigated as well. This was possible thanks to a fruitful collaboration with Prof. Paola Costamagna and Caterina Sanna, Ph.D. candidate in Prof. Costamagna's research group, from University of

Genova. The main goal of this collaboration was to fully characterize nanofibers and compare them with powders.

The used production process for nanofibers is electrospinning. This technique involves an electrohydrodynamic process, during which a liquid droplet is electrified to generate a jet, followed by stretching and elongation to generate fibers. The nanofiber manufacture process is carried out by applying a high voltage between a metal precursor solution, injected through a syringe equipped with a metal needle, and a metal collector. The power supply can be either direct current (DC) or alternating current (AC). During electrospinning, the liquid is extruded from the spinneret to produce a pendant droplet because of surface tension. The droplet is deformed into a Taylor cone due to the electrostatic repulsion among the surface charges. The jet, stretched into thinner diameters, solidifies quickly, leading to the deposition of solid fiber(s) on the collector. Summarizing, the electrospinning process can be divided into four steps:

1. Liquid droplet charging and formation of Taylor cone.
2. Straight line extension of the charged jet.
3. Electric field promoted jet thinning.
4. Solidification and solid fiber(s) collection from the grounded collector.

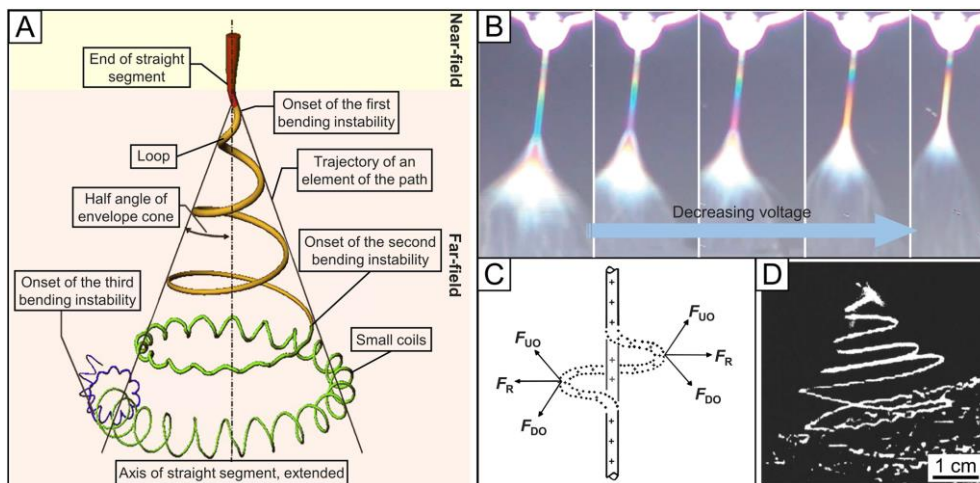


Figure 1: A) Electrospun jet path. B) Line information about jet diameter and length of straight segment as a function of the applied voltage, rendered using characteristics interference colors. C) Illustration of the forces acting on a charged jet. F_{DO} : downward and outward forces by the charges that produce perturbations on the analyzed segment. F_{UO} : upward and outward forces produced by the charges below the perturbation. F_R : net lateral electrostatic force, responsible for the bending of the jet. D) Stereographic image of the bending jet during the different stages of bending instabilities. ^[21]

Many are the materials that can be spun through this technique: organic polymers (e.g., polyvinylpyrrolidone, PVP), small molecules, colloidal particles, composites, and complex polycationic oxides (e.g., perovskites). Perovskites, usually prepared by adding sol-gel precursors, have been extensively explored for solution electrospinning. In this case, it is necessary to avoid the occurrence of sol-gel reactions, including hydrolysis, condensation, and gelation of the precursors. For this reason, one of the main factors that determine the solution electro-spinnability are precursors, as well as viscosity, electrical conductivity, and the choice of the carrier polymer. This last one must be spinnable with a high molecular weight (M_w). To this end, one of the most popular carrier polymers is PVP. It has high solubility in ethanol and water and a good compatibility with many sol-gel precursors. [22] The type of precursor affects the rates of sol-gel reactions in the jet. The blockage of the spinneret by a rapid hydrolysis must be avoided and, in the meantime, the rapid gelation that leads in a less stretchable jet and consequently fibers with a thicker diameter. As already mentioned, the viscosity plays an important role in stretching the jet. It can be controlled by varying the concentrations of the precursor and the polymer. Not only the precursor solution parameters are important to lower the thickness of nanofibers, but also the atmosphere plays an important role. In fact, a lower humidity can reduce the rates of hydrolysis and gelation and therefore give rise to continuous electrospinning. [23] Another parameter to take into consideration is the distance between the needle and the collector. Typically, electrospinning is conducted in the far-field mode ($H = 5-15$ cm) with the application of a high voltage (10-20 kV).

Electrospun nanofibers have been extensively explored for applications related to catalysis, energy, photonics, and electronics. The reasons to their large usage in these fields are their large porosity, high specific surface area, good stability. Furthermore, nanofibers can support rapid conduction of electrons and/or intercalation of ions, giving the possibility to use them as interesting materials for energy harvesting, conversion, and storage. Consequently, nanofibers are deeply studied in literature as appealing solutions for fuel cells. In fact, due to their high void degree morphology, they are able to provide a large electrode/electrolyte contact area, rapid transfer of electrons and ions, and feasibility for functionalization to improve electroactivity. In addition, the high porosity of a nonwoven mat of nanofibers and the interconnection among the pores can facilitate the mass transport

of reactants, provide extensive contact between reactants and active sites on electrocatalysts, and promote electron and proton conduction.

Over the past two decades made of polymers, metals, ceramics, and carbon have all been extensively explored for the fabrication of fuel cells in an effort to improve their efficiency and durability while reducing the cost. [24]-[26] So, one-dimensional (1D) nanomaterials, like nanofibers and nanorods, have been widely studied as promising electrode structures [27]-[31]. Moreover, once the process parameters are optimized, the results are reproducible [32]-[35]. Overall, nanofiber-based electrodes are expected to show better electrochemical performance than common powder ones.

The two different architectures were investigated through the electrochemical impedance spectroscopy test (EIS), and the nanofiber-based electrode reported lower polarization resistance. Nevertheless, the structural and microstructural origin of this behavior has, to date, received little attention. In this work, our aim was to understand how the structure and morphology of the material affects its capability in activating and oxidating methane. The specific surface area is not the only aspect that can deeply differ from powder to fibers; the surface composition can be severely modified by the synthesis procedure and can play a relevant role. Methane oxidation was selected as a model reaction because it is not easily promoted by perovskites or Ni-free catalysts. Moreover, this is a reaction of high technological impact; its application in direct methane IT-SOFCs is just one example. LSM electrospun nanofibers and powders were synthesized, and particular attention was paid to the optimization of the fiber procedure. The obtained materials were investigated using X-Ray Diffraction (XRD), Scanning Electron Microscopy (SEM), Energy Dispersive X-Ray Spectroscopy (EDX), and N₂-Physisorption. Care was devoted to the study of the surface using X-Ray Photoelectron Spectroscopy (XPS). The H₂-Temperature Programmed Reduction (TPR) and methane oxidation activity tests were carried out to investigate stability and catalytic activity.

3.2 Material synthesis

3.2.1 La_{0.6}Sr_{0.4}MnO₃ nanofibers preparation

Strontium nitrate, Sr(NO₃)₂ (Sigma-Aldrich, ACS 99+%), lanthanum nitrate, La(NO₃)₃·6H₂O (AlfaAesar, 99.9%), and manganese acetate, (CH₃COO)₂Mn·4H₂O (Sigma-Aldrich,

99.99%) are used as metal precursors for the starting solution for electrospinning. Each precursor is carefully weighted in order to achieve a molar ratio 0.6:0.4 for La:Sr, and 1:1 for (La+Sr):Mn. Prior to mixing, the metal precursors are dissolved in a solution 60%/40% water/ethanol. Polyvinylpyrrolidone ($M_w=1.3 \cdot 10^6$ g/mol) is then added to the solution, achieving a weight ratio of 1:1.3 between the polymer and the metal salts. The PVP represents the 10% wt/wt of the whole solution. Dissolution is obtained using a magnetic stirrer for one night. The solution is then fed to the electrospinning device, equipped with a temperature and relative humidity (RH) regulator, and with a flat collector (Doxa Microfluidics, Malaga, Spain). The flow rate is 1 ml/h, applied voltage is 1.7 kV/cm, RH is 40%, and temperature is 25°C. Then, the raw electrospun nanofiber tissue undergoes heat treatment. The nanofibers are heated from room temperature to 800°C at a constant heating rate of 0.5°C/m. The cooling occurs without thermal control.

3.2.2 $\text{La}_{0.6}\text{Sr}_{0.4}\text{MnO}_3$ powders preparation

$\text{La}_{0.6}\text{Sr}_{0.4}\text{MnO}_3$ powders are synthesized by citrate route [36]. Stoichiometric quantities of lanthanum nitrate ($\text{La}(\text{NO}_3)_3 \cdot 6\text{H}_2\text{O}$, Sigma-Aldrich 99.99%, powder), strontium nitrate ($\text{Sr}(\text{NO}_3)_2$, Sigma-Aldrich 99%, powder) and manganese acetate ($(\text{CH}_3\text{COO})_2\text{Mn} \cdot 4\text{H}_2\text{O}$ (Sigma-Aldrich, 99.99%) are dissolved in deionized water and nitric acid (HNO_3). Citric acid ($\text{C}_6\text{H}_8\text{O}_7$, Sigma-Aldrich $\geq 99.0\%$) is added as complexing agent (with a molar ratio of 1.9:1 with respect to the total amount of cations) under stirring and then the solution is lead to neutral pH by dropwise addition of ammonium hydroxide. At pH 7, the stirring is stopped, and the solution is heated overnight to eliminate water and to allow the formation of a gel. The gel is burned, heating it at 400 °C. The formed powders are calcined at 800°C for 6 hours using a heating and cooling ramp of 6 °C/min.

3.3 Morphological Characterization

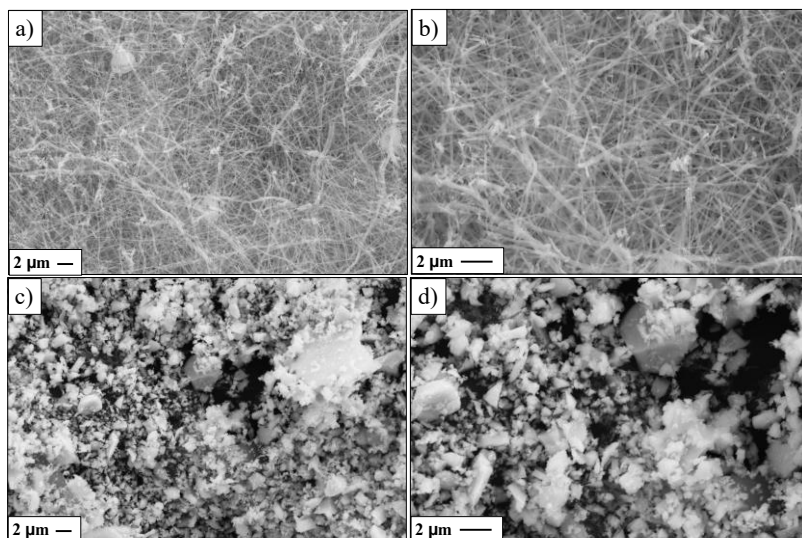


Figure 2: SEM images of LSM nanofibers (a-b) and LSM powders (c-d).

SEM images of LSM nanofibers and LSM powders are reported in **Figure 2**. **Figure 2 (a-b)** shows the LSM nanofibers after the thermal treatment. There are thin nanofibers with no detachment, which ensure a compact network. It is possible to achieve these features after an optimization of the many solution and process parameters. Indeed, in **Figure 2** the nanofibers show a preferential cylindrical shape which is the results of a correct solvent evaporation during the electrospinning process. The proper evaporation of the solution is obtained by controlling three main parameters: the type of solvent, the humidity in the electrospinning chamber and the distance between the needle tip and the metal collector. Furthermore, the nanofibers appear thin, but intact. This result is achieved by adding the suitable amount of polymer in the precursor solution, and by setting the optimized flow rate in the electrospinning process. Indeed, the lower is the amount of polymer in the solution and the higher is the flow rate, the thinner are the nanofibers. However too low polymer quantity affects the nanofibers ejection provoking detachments, and too higher flow rate values request a too high voltage which breaks the drop on the top of the needle avoiding the correct elongation. **Figure 2 (c-d)** shows the LSM powder particles after the sintering process. The images clearly show the presence of particle of different dimensions and shape. Beside well-defined polyhedral crystals of more than one micron, small particles are evident. The ImageJ analysis is carried out onto SEM images reported in **Figure 2**. The measurement result is reported in **Figure 3**.

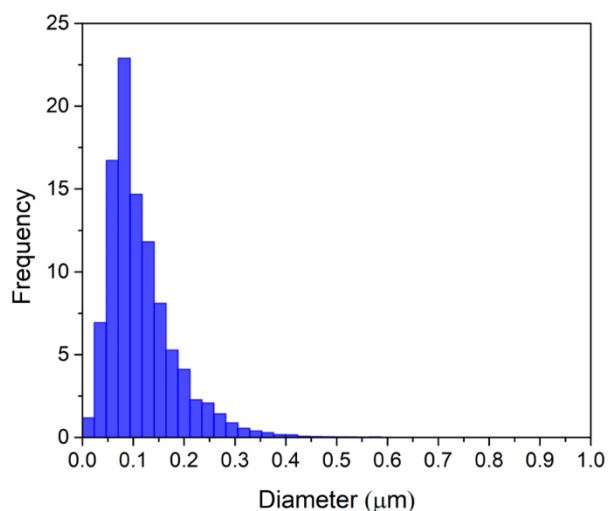


Figure 3: Diameter analysis of LSM nanofibers after thermal treatment

Figure 3 shows for each diameter range, the frequency of the nanofiber's diameter identified by the software. The highest relative frequency is found for the diameter range between 0.08 μm - 0.1 μm . On the contrary, the particles average size turned out to be around 0.7 μm .

XRD measurement is carried out on the heat treated LSM nanofibers and citrate route powders to verify the achievement of the desired crystal phase. In **Figure 4** the experimental patterns are reported together with the reference pattern. The experimental patterns contain all the signals related to the reference, without any undesired one. It confirms that the thermal treatment permits to achieve the desired crystallinity.

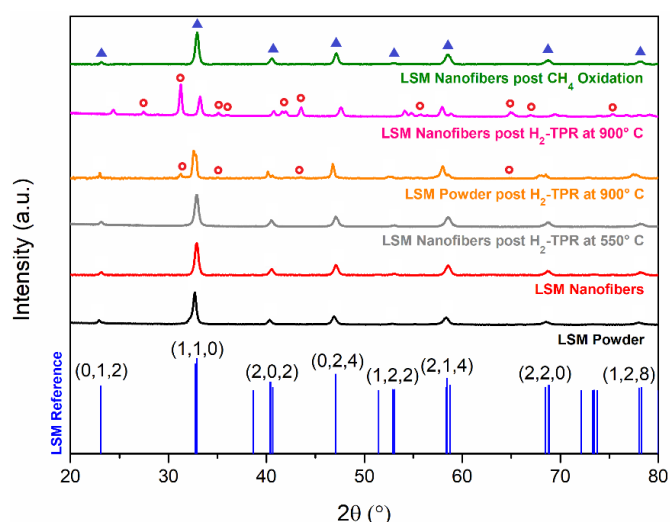


Figure 4: all the XRD performed during this work. In blue there is LSM reference pattern. The experimental pattern of LSM electrospun powders (black) and nanofibers (red) after the thermal treatment are shown. LSM nanofibers post H_2 -TPR performed up to 550° C (grey) and 900° C (pink) and powders after reduction in H_2 up to 900° C (orange). The last pattern is referred to LSM nanofibers post CH_4 oxidation lead up to 800° C (green). Blue triangles are referred to LSM peaks, while red circles to MnO phase. The patterns are normalized with respect to their maximum values.

3.4 Compositional Characterization

Extended spectra (survey) are collected in the range 0–1250 eV and reported in **Figure 5**. In the XPS survey spectra, no signals of elements other than the expected ones are detected. The atomic composition obtained from the XPS data reveals, by comparison with the nominal one determined from the weighted amounts, a good correspondence for all the elements, as reported in **Table 1**.

Element	Teorical %		XPS Experimental %		EDX Experimental %	
	Nominal %		Fibers	Powders	Fibers	Powders
O	60		58	74	62	58
La	12		15	4	12	12
Sr	8		6	7	7	7
Mn	20		21	15	19	22
Mn/(La+Sr)	1		1	1.4	1	1.2
Sr/La	0.7		0.4	1.7	0.6	0.6

Table 1: XPS and EDX quantitative results comparison between LSM powders and nanofibers. For better comprehension nominal values are present as well.

In **Table 1** the comparison between the surface (XPS) composition of powders and nanofibers is presented. The main difference is referred to the Sr/La atomic ratio. Following the nominal composition, Sr/La atomic should be 0.7. A value of 1.7 is observed on powders and of 0.4 in fibers. This suggests a marked strontium surface segregation in powders, which is not detectable in fibers. Strontium segregation with consequent formation of strontium oxide is an undesired phenomenon already well known in literature for Sr containing perovskites. Since the B-site transition metal in perovskites plays a critical role for catalytic activity it is necessary to preserve the structure and the composition on the surface. Furthermore, SrO is traceable to a lower electronic conductivity. For all these reasons, avoiding Sr-enriched layers on LSM surface is a substantial difference between the two synthesis and a preliminary important goal reached by electrospinning. Surface segregation properties of ionic solids are strongly related to their punctual defects. Assuming that, the presence or not of Sr segregation on the two sample can be seen as evidence of different presence of punctual defects in the two morphologies [37], [38]. Further work will be spent to confirm this hypothesis.

La 3d peaks positions (834.6 and 851.0 eV for La 3d_{5/2} and La 3d_{3/2}, respectively) are consistent with those expected for this element in a perovskite powder. (Refs. NIST Standard Reference Database 20, Version 3.4. [39], [40]) The La 3d level is characterized by a double peak for each spin-orbit component, attributed either to energy loss phenomena induced by intense O 2p → La 4f charge transfer events or to strong final state mixing of electronic configurations [41]. The presence of the double signals is characteristic of La (III) as reported in **Figure 5-a**.

The Mn 2p_{3/2} spectral lines are centered in 642.4 eV, a typical position of Mn in oxides and in manganites [42]. The interpretation of the Mn 2p spectrum is complicated because of the multiple splitting of the Mn 2p spectra of Mn⁴⁺, Mn³⁺, and Mn²⁺ ions. The exact oxidation state of Mn ions is difficult to evaluate but according to the references [43], the observed binding energy of Mn 2p_{3/2}, suggests that the oxidation state of Mn ions is (III) and (IV) for both LSM nanofibers and powders. Anyway, the higher binding energy for LSM nanofibers compared to powders suggests a higher presence of Mn (IV). The proved higher presence of the redox couple Mn^{4+/3+} in the nanofiber perovskite, as reported in **Figure 5-b**, confirms the Sr doping effectiveness and agrees with the absence of surface segregation. The stable insertion of Sr inside the perovskite cell is a promising indication for an improvement of the material electronic conductivity.

Sr 3d spectrum of LSM is fitted by the two components 3d_{5/2} and 3d_{3/2}. Their Binding Energies (BE) are in accordance with the typical values of Sr-O in perovskite (131.8 - 134.3 eV) [42]. While for La and Mn spectra no differences between powders and nanofibers are detectable, a small but significant difference is observed in the spectral region Sr 3d. In the spectrum referred to the powders, in fact, it is possible to observe a tail around 135-137 eV which confirms the more relevant presence of SrO **Figure 5-c**.

The O 1s spectra show the presence of two contributions centered around 530 and 531.6 eV; the contribution at lower BE is attributed to the lattice oxygen whereas the one at higher BE to surface oxygen species; this contribution is more evident in the fibers surface, **Figure 5-d**.

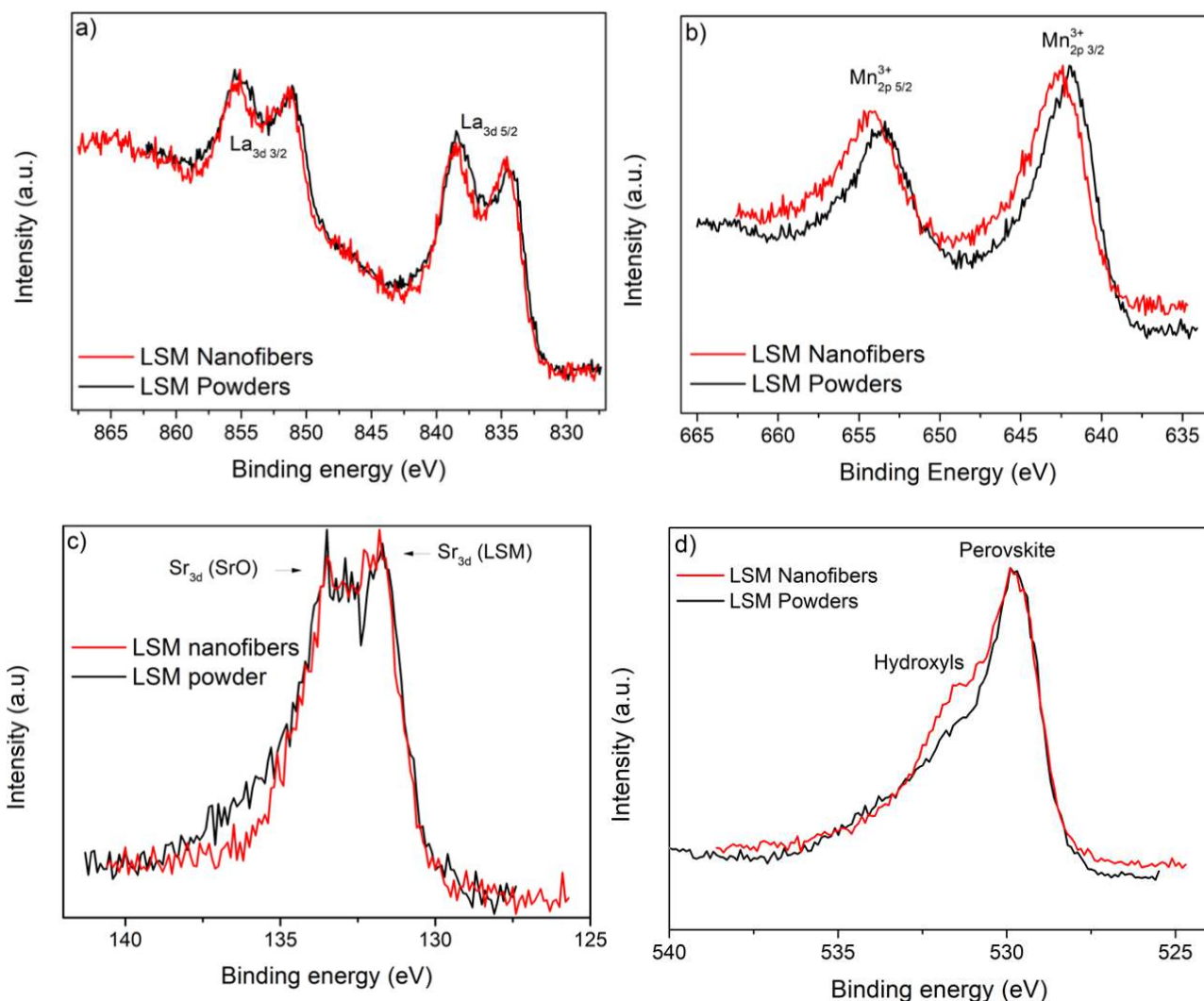


Figure 5: a) La 3d XP spectra of LSM samples prepared, respectively, by citrate gel method (black line) and electrospinning (red line). The spectra are normalized with respect to their maximum value. b) Mn 2p XP spectra of LSM samples. c) Sr 3d XP spectra of LSM samples. d) O 1s XP spectra of LSM samples.

Trying to understand the chemical composition in the inner region of the nanofibers, an EDX analysis is carried out. **Table 1** shows the comparison between the nominal and the experimental detected percentages of the two samples. No marked differences are present between fibers and powders and with the nominal values, confirming that the two syntheses are successfully realized. Furthermore, it is possible to assert that the two samples differ for the morphology and the chemical composition of the surface.

3.5 Temperature Programmed Reduction (H₂-TPR) and N₂-adsorption-desorption

The TPR profiles obtained for the fibers and the powders, compared in **Figure 6**, show two peaks, one set at 430° C and the other at higher temperature (700° C). Both are related to manganese cations reduction, since manganese is the only species that can be reduced in the

analyzed temperature range. The lower temperature peak corresponds to the reduction of Mn^{4+} , the second one is due to the reduction from Mn^{3+} to Mn^{2+} . This hypothesis, suggested in literature [44], is also confirmed by the XRD measurements performed after H_2 -TPR. In the XRD patterns obtained after TPR MnO is observed but the main part of the sample has maintained the perovskite structure. In **Figure 4** the XRD pattern obtained for the fibers sample reduced up to 550°C (hypothetically when the first reduction is finished, but the second one has still to start) underlines the absence of the MnO phase. This result confirms that the peak at higher temperature is due to the reduction to Mn^{2+} .

The experimental hydrogen consumption in the fibers is about $9 \cdot 10^{-5}$ mol, which is lower than the theoretical one ($16.7 \cdot 10^{-5}$ mol). This is calculated considering that all the Sr inserted in the sample promotes the manganese to Mn^{4+} , and all manganese is reduced to Mn^{2+} . This assumption is clearly disproved since the XRD after TPR shows LSM phase presence. Anyway, it is possible to make a simple calculation and assert that about 50% of the sample is reduced to Mn^{2+} .

In addition, trying to understand if the different morphology modifies the stability, the same reducing treatment (5% H_2 in Ar at 900°C) was performed to the powders. Significant differences were noted by the TPR profiles. The peak referred to $\text{Mn}^{4+/3+}$ reduction starts at 305°C for powders that is 35°C higher than nanofibers. Furthermore, the $\text{Mn}^{3+/2+}$ peak is much higher for nanofibers than powders. These two aspects suggest the higher reactivity of nanofibers.

The post reduction XRD is also significantly different. From **Figure 4** it is possible to note how the powder diffractogram shows after reduction the same reflexes of MnO observed in the fibers, but with a lower intensity. The different behavior observed between powders and fibers suggest a lower reducibility of the powders and can be explained considering two aspects. The first one is related to the high presence of SrO in the powders surface, that behaves like a coating for the perovskitic structure protecting it from reduction. The second feature is related to the higher surface area observed for the fibers.

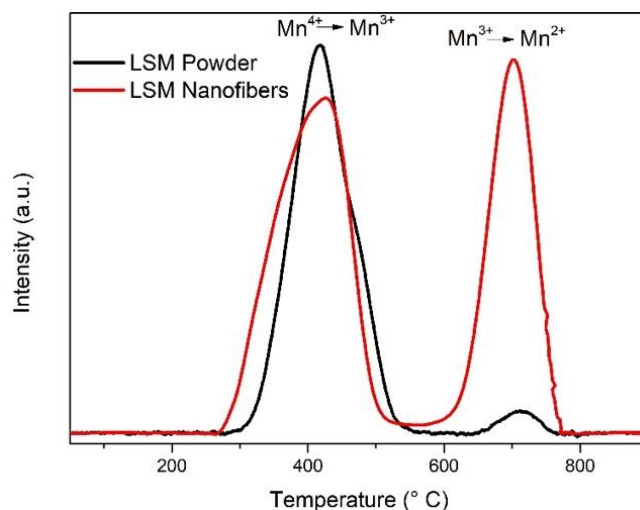


Figure 6: TPR profile of LSM nanofibers and powders. The patterns are normalized with respect to their maximum values.

Figure 7 shows the N₂-adsorption-desorption isotherms carried on LSM nanofibers, which is used in order to determine the BET surface area of the nanofibers. The calculated surface area of the sample is 16.7 m²/g. A good correspondence can be observed with other studies present in literature on this material [45]. This value is about two times the typical values for LSM perovskite synthesized by citrate route and subjected at the same temperature of calcination (800 °C), further confirmed by our measurement (5.8 m²/g). Surface area determination from BET confirms the theory of a lower hydrogen stability at high temperatures due to a higher surface area. The BET plots of the two samples are traceable to type IV isotherm: they show a hysteresis cycle between adsorption and desorption processes. So, at the same partial pressure, during the desorption more nitrogen is desorbed than the quantity of gas adsorbed in the adsorption process. The hysteresis is a signal of a mesoporous material, but the small region between adsorption and desorption curves indicates that there is a little dispersion of the average width of the pores [46].

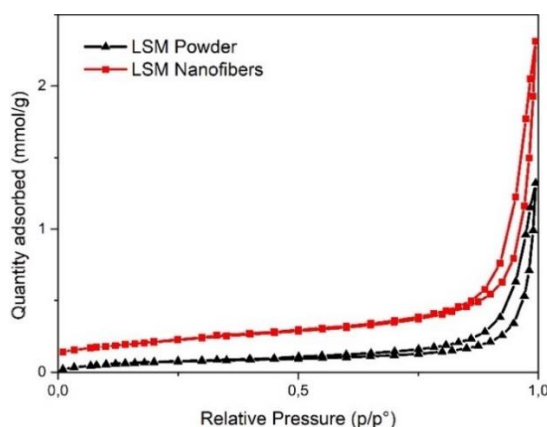


Figure 7: N₂-adsorption and desorption isotherm for LSM powders (black) and nanofibers (red).

3.6 Methane oxidation catalytic activity test

The catalytic behaviors observed in a methane/oxygen atmosphere, with a stoichiometric ratio between methane and oxygen of 2:1, are reported in **Figure 8**. The nanofibers onset temperature for methane oxidation is about 500 °C; for powders is set 100° C higher. The temperature of 50% methane conversion is lower for nanofibers (700 °C) than powders (900 °C). The maximum reached conversion for nanofibers is about 75% at 800 °C. Considering that the typical temperature range for SOFCs application is between 600 °C and 800 °C, it can be argued that this catalytic activity of nanofibers could be exploited in relationship with these devices. Taking in account this catalytic result and the previous material characterizations, the higher activity of nanofibers can have two different explanations. The first is the higher surface area of nanofibers compared to powders, with consequent higher number of active sites for the reaction. In addition, the higher performances of nanofibers can be explained by the previous XPS results. As a matter of fact, SrO in the LSM powders surface is inactive to methane oxidation and covers the underneath perovskite structure. On the contrary, electrospinning synthesis allows the maintenance of active perovskite phase till the last atomic layers.

Figure 4 compares the XRD pattern obtained for the nanofiber samples as synthesized and after the reaction. No differences are detectable considering neither the position of the peaks either their FWHM. Thus, no modification regarding the phase structure or crystallinity is attributable to the performed catalytic test.

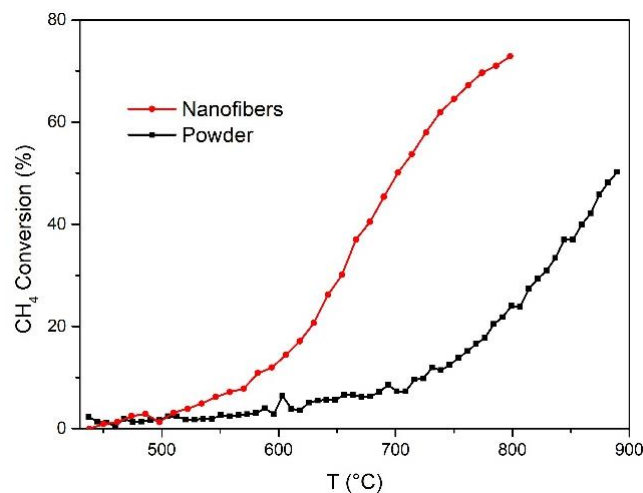


Figure 8: Catalytic activity in methane oxidation observed for LSM powders (black line) and nanofibers (red line).

3.7 Electrochemical Impedance Spectroscopy

The electrochemical measurements are performed using symmetrical cells (LSM-GDC (50:50)/GDC/LSM-GDC (50:50)) made of dense gadolinium doped ceria ceramics (theoretical density >96%) as electrolyte. Both LSM powders and nanofibers are ground with commercial GDC powders. Three symmetrical cells are prepared. The first is assembled with the nanofiber-based electrodes with 30 μm of thickness, while the second one is assembled with the powder-based electrodes with 70 μm of thickness. Furthermore, another powder-based symmetrical cell is prepared with an electrode thickness of 40 μm .

Electrochemical Impedance Spectroscopy (EIS) measurements are carried out using an Autolab Frequency Response Analyser. The frequencies scanned are from 0.003 Hz to 1 MHz and set to amplitude 0.02 V. The tests are carried out at 865 °C, 815 °C, 765 °C, 715 °C, and 665 °C. The raw experimental data are corrected by subtracting the inductance contribution of the device wires, which is one of the major sources of error is given by the stray components of the device [47].

3.8 Equivalent Circuit-Based Modeling

The EIS experimental data obtained in air and methane atmosphere are fitted through different equivalent circuit (EQVCRT) models. The EQVCRT model is a powerful tool to evaluate the electrode polarization resistance R_p , which is the difference between the intercepts of the Nyquist curve and the real impedance axes at low and high frequencies. The polarization resistance is one of the main parameters to evaluate the electrochemical performance of cathodes and anodes.

The equivalent circuits involved in this work consist of serial resistance R_s , placed in series with RQ elements, while in certain cases also the Gerischer and the FLW elements are used. These ECs are previously proposed in [48], [49] where R_s in series with RQ elements were used to fit EIS data obtained with composite LSM/GDC or LSM/YSZ electrodes.

The R_s is used to consider all the ohmic contributions of the symmetrical cell: the electrolyte ohmic resistance, as well as the electrodes ohmic resistance, and the contact resistances between the electrodes and the current collectors:

$$R_S = R_{\text{electrolyte}} + 2(R_{\text{contact}} + R_{\text{electrode}}) \quad (1)$$

The RQ element consists of a resistor and a constant phase element (CPE) placed in parallel. It is generally used to simulate electrochemical phenomena which take place at the electrode/electrolyte interface [50]. Indeed, the resistor simulates the charge transfer process, i.e., the oxygen reduction reaction (ORR), while the capacity Q of the CPE refers to the electrode/electrolyte double layer. The RQ impedance equation is:

$$Z_{\text{RQ}}(\omega) = \frac{1}{R_{\text{RQ}}^{-1} + Q(j\omega)^\alpha} \quad (2)$$

Where α is a CPE parameter, which is independent of frequency. When $\alpha = 1$, the electrode/electrolyte interface is simulated as a CPE which is become an ideal capacitor, with capacity Q and units (F) and the Nyquist plot of the RQ impedance is a semi-circle. Otherwise, when α is lower than 1, the deviations from the ideality are considered in the RQ impedance. For example, the heterogeneity which takes place at the electrode/electrolyte interface, or to continuously distributed time constants for the charge-transfer reactions is reflected in the α value [51]. In this condition, the RQ impedance representation in the Nyquist plot is a depressed semi-circle. The Q unit becomes ($F \cdot s^{\alpha-1}$), so an equivalent capacitance Q_{equiv} is calculated with units (F), and the formula is below:

$$Q_{\text{equiv}} = \frac{(QR)^{1/\alpha}}{R} \quad (3)$$

The Gerischer element is used to simulate both charge transport and charge transfer reaction in the bulk of the electrode [52]. The representing equation is:

$$Z_G(\omega) = \frac{1}{Y_G(k + j\omega)^{0.5}} \quad (4)$$

The k parameter is the oxygen surface exchange coefficient, while Y_G is referred to all the coefficients regarding the oxygen mass transport in the electrode, and all the structural parameters [53].

When the EIS tests are carried out at high temperatures, generally an additional arc appears at low frequencies due to the gas diffusion limitations [54], [55]. This additional arc is well fit with the Finite-Length-Warburg (FLW):

$$Z_{\text{FLW}}(\omega) = \frac{\tanh((Bj\omega)^{0.5})}{(Y_{\text{FLW}}j\omega)^{0.5}} \quad (5)$$

B and Y_{FLW} are phenomenological coefficients.

The EC used to fit all the experimental data obtained in air, changes within the temperature: between 665 °C and 765 °C the Rs-RQ-RQ-RQ is used, while at higher temperatures the EC is modified to Rs-RQ-RQ-FLW. For the data obtained in methane, the Rs-G is used for both the electrode and at each temperature.

Besides the Rs-G model, another option is used to fit the experimental data obtained in the methane atmosphere. The electrolyte used in this work is a pellet made with GDC, which tends to become an electronic conductor if exposed to a reducing atmosphere e.g., methane. For this reason, the second equivalent circuit involved in the fitting of the methane data considers a possible influence on the Nyquist plot given by the short-circuiting electrolyte. The second model (Mod2) consists of an RQ-G circuit with another resistance placed in parallel. The resistance placed in parallel simulates the effect of the electrolyte short-circuiting.

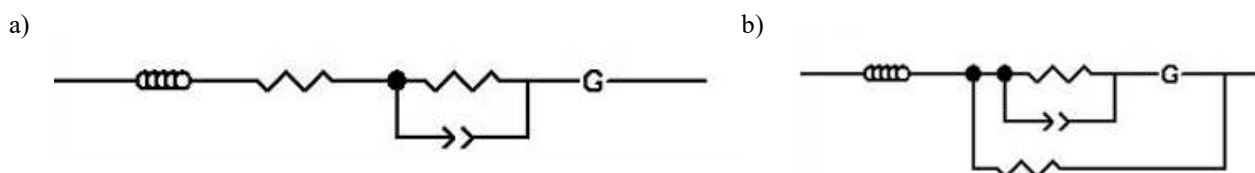


Figure 9: Schematic representation of the two models used to fit the experimental data obtained in methane. a) Rs-RQ-G model; b) RQ-G with a parallel Rs model.

3.9 Electrochemical Impedance Spectroscopy in Air

LSM is considered the state-of-the-art material for SOFC cathodes, and composite LSM/GDC electrodes have been widely investigated in the last decades. Therefore, this section aims at comparing the EIS results obtained in the air from the LSM/GDC nanofiber-based and powder-based electrodes with the available literature, to have a firm starting point for the subsequent discussions. The electrochemical characterization is carried out on the 30 μm thick nanofiber-based electrode and the 70 μm thick powder-based electrode.

Figure 10 shows the Nyquist and Bode plots of the EIS experimental data obtained in air between 665°C and 865°C with the nanofiber-based LSM/GDC electrode. The contributions of the fitting elements used in the equivalent circuit model are reported as well.

Between 665°C and 765°C, the equivalent circuit used to fit the data is the Rs-RQ-RQ-RQ. At each temperature, the experimental data display two main arcs in the Nyquist plot: the

first one is a little semicircle placed at high frequencies, while the second one is the main curve which covers the middle and low range of frequencies. The small high-frequency arc is well fitted with two RQ elements, and it is identified as RQ1. When the temperature rises, the shape of the main arc changes. Indeed, the two RQ elements modify their relative contributions to the overall polarization resistance, until 815°C where only one RQ fits the main curve.

Thus, between 815°C and 865°C, the equivalent circuit used to fit the experimental data becomes Rs-RQ-RQ-FLW. The FLW element is used to simulate the small arc which appears at low frequencies, due to the shrinkage of the main impedance arcs in the Nyquist plot. This additional contribution, fitted with the FLW element coherently with the previous works [56]-[58], is associated with the gas diffusion resistance [59]. Despite the electrode containing both LSM and GDC, which are respectively pure electronic and ionic conductors, the Nyquist plot is not associated with the Gerischer behavior, which is normally related to mixed electronic-ionic conductors. Indeed, the Nyquist shape is the sum of several semicircles in series. However, this behavior is quite common for composite electrodes investigated as cathodes, and several examples are reported in the literature. *E.P. Murray et al.* performed EIS tests on a symmetrical cell made with an LSM/YSZ composite electrode.

Despite the YSZ being considered the state-of-the-art material for HT-SOFC, the experimental data reported in the Nyquist plot do not show the common Gerischer shape. On the contrary, the spectra represent the sum of several semicircle arcs, which are fitted with an Rs-RQ-RQ equivalent circuit [60]. Other composite electrodes made with LSM and YSZ have been tested, achieving the same behavior [61]-[63]. Furthermore, *M. Zhi et al.* characterized symmetrical cells made with YSZ nanofibers infiltrated with LSM solution. The change in the electrode microstructure results in lower polarization resistance [64], but also in this case the experimental point in the Nyquist plot shows a sum of several semicircle arcs as seen in the previous cases [65]. The behavior reported for the LSM/YSZ composite electrode is also found for substituting the ionic conductor material. Indeed, *X. Luo et al.* performed an EIS test on LSM/GDC symmetrical cells and no Gerischer behavior is reported in the Nyquist plot, but the experimental data show the already discussed sum of several arcs [66]. Other LSM/GDC composite electrodes have been tested obtaining the same

behavior [67], [68]. On the contrary, several mixed ionic and electronic conductors, which have generally high electronic conductivity but low ionic conductivity, report a Gerischer behavior in the Nyquist plot after EIS characterization. One of the most studied MIEC materials is the LSCF perovskite, which is considered the state-of-the-art material for IT-SOFC. *Costamagna et al.* carried out the investigation on LSCF nanofiber electrodes, achieving the typical Gerischer shape in the Nyquist plot [58]. Furthermore, some LSCF/GDC composite electrodes have been investigated as well, reporting the same Gerischer behavior [69], [70]. *S. Sunde* and *Costamagna et al.* performed some simulations on several composite electrodes. They found out that when the electrode and the electrolyte material are randomly mixed to form a composite electrode, it is possible that one phase is not connected to its bulk phase, causing a lack of percolation of one phase [71], [72]. The problem detected by *S. Sunde* and *Costamagna et al.* may be the reason why the Nyquist plots shown in **Figure 10** do not show the Gerischer behavior. If one phase does not percolate in the electrode thickness, it is possible that the electronic and ionic pathways are not properly connected limiting the conduction of ionic or electrons, and so the reaction. On the contrary, a mixed conductor has both the pathways in the same material and the reaction can take place wherever in the electrode thickness.

According to the literature [73], when LSM/YSZ composite electrodes are tested in an air atmosphere, it is possible to identify five main processes, and each of them is associated with an RQ arc. **Figure 10** shows the presence of three well-defined processes at 665 °C, while at high temperature only two of them are reported at 815°C. In the range of temperature between these two limits the EC contributions appear shifted and overlapped, which implies a difficult interpretation of the processes related to them. For this reason, it is not possible to assign an accurate process that takes place in the cell to the EC element used to fit the data. The only contribution which is present at each investigated temperature is the little semicircle at high frequencies. This contribution is also detected in the LSM/YSZ composite electrode characterized by *E.P. Murray et al.*, who attributed this high-frequency contribution to the grain boundary resistance made by the YSZ particles inside the electrode [74]. Lastly, at 800°C a small additional arc in **Figure 10** appears at low frequencies. *Costamagna et al.* investigated this process as well, identifying this additional arc at low

frequencies and high temperatures and associating this contribution to the gas diffusion resistance [58], [70], [75].

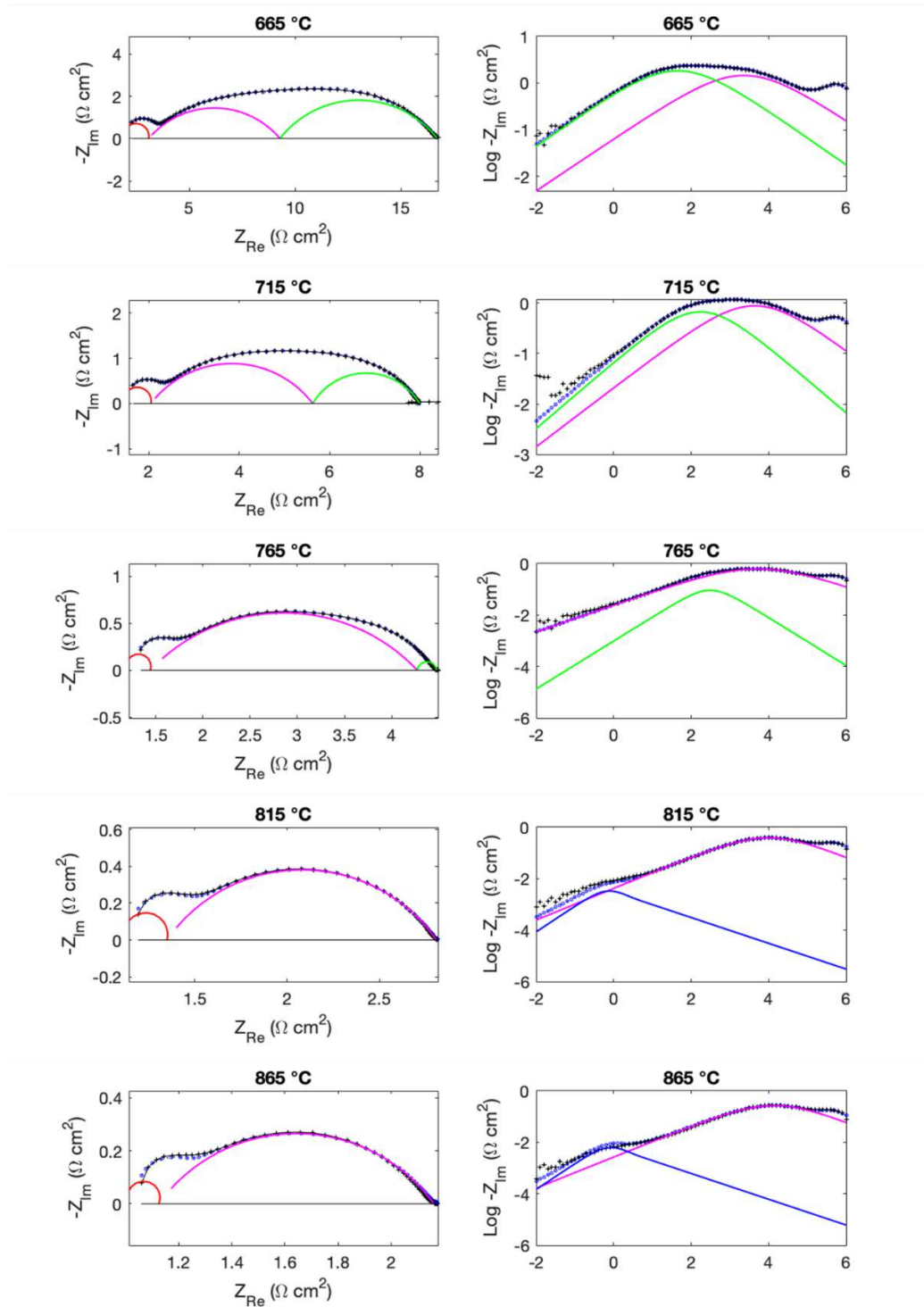


Figure 10: - Nyquist (left) and Bode (right) plots of the EIS results obtained with the nanofiber-based LSM/GDC electrode at operating temperatures from 665°C to 865°C: \bullet experimental data; \square fitting through the R_s -RQ-RQ equivalent circuit model; $---$ RQ1 contribution; $---$ RQ2 contribution; $---$ RQ3 contribution and $---$ FLW contribution.

Figure 11 shows the Nyquist plots of the EIS experimental data obtained between 665 °C and 865 °C in air with the 70 μm thick powder-based LSM/GDC electrode. The shape is slightly different from that reported in **Figure 10**. Indeed, the RQ1 contribution is only identified at 665 °C and over 765 °C the unique contribution to the overall polarization resistance is given by only one RQ element. Thus, at 665 °C the experimental data are fitted with the Rs-RQ-RQ-RQ equivalent circuit, at 715 °C the EC becomes Rs-RQ-RQ and between 765 °C and 865 °C, the EC becomes Rs-RQ. However, the correlation between the fitting elements and the electrochemical phenomena is in accordance with the discussion reported above for the LSM/GDC nanofiber electrodes. Furthermore, there is a good correlation between the electrochemical performances obtained with the nanofiber-based electrode and the powder one. The polarization resistance obtained with the nanofiber-based LSM/GDC electrode at 815 °C is 1.6 Ωcm², a value quite similar to the 1.08 Ωcm² obtained with the powder-based LSM/GDC electrode at the same operating temperature. Finally, the obtained results are consistent with the literature data found for composite electrodes based on LSM. Indeed, LSM/YSZ composite electrode shows a polarization resistance of 1.5 Ωcm² at 800 °C, while LSM/GDC electrodes reports 0.5 Ωcm² at 750°C [76], [77].

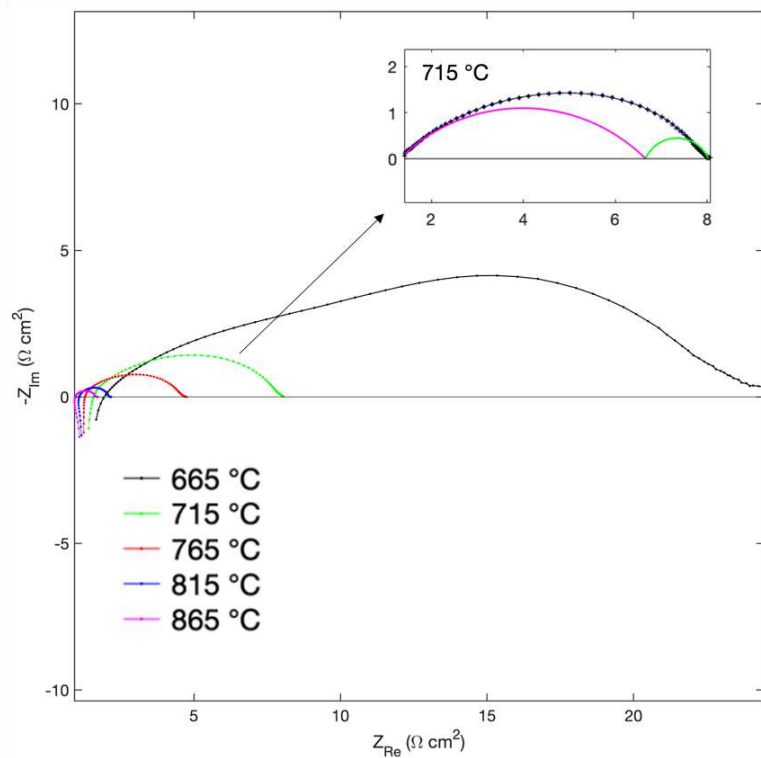


Figure 11: – Nyquist plot of EIS results obtained with the 70 μm thick powder-based LSM/GDC electrode at operating temperatures from 665°C to 865°C. In the right corner, the Nyquist acquired at 715 °C is highlighted: • experimental data; -□- fitting through the Rs-RQ-RQ equivalent circuit model; - - RQ2 contribution; - - RQ3 contribution.

In **Figure 12** the reverse of the polarization resistance (R_p^{-1}) of the LSM/GDC nanofiber-based electrode and 70 μm thick powder-based electrode are reported in an Arrhenius plot. The activation energies are respectively 115 kJ/mol and 153 kJ/mol. In particular, the value found for the nanofiber-based cathode is consistent with the activation energy reported in the literature for pure LSM electrode, which is 121 kJ/mol [78]-[80]. This may suggest that in the investigated LSM/GDC composite electrodes when used as cathodes in air atmosphere, only the LSM is electrochemically active, rather than the GDC.

In **Figure 13** the $1/R_p$ vs $1000/T$ of the RQ1 polarization resistance and the overall polarization resistance of the LSM/GDC nanofiber electrode are reported. In particular, polarization resistance of the RQ1 shows an Arrhenius behavior as compared to the temperature; furthermore, the activation energy is 90 kJ/mol, which is very similar to the 96 kJ/mol found by *E.P. Murray et al.* in [74].

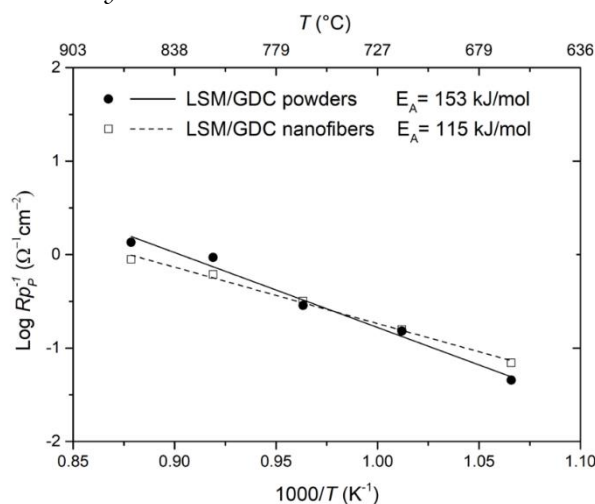


Figure 12: $1/R_p$ vs $1000/T$ of \square - LSM/GDC nanofiber-based and \bullet - LSM/GDC powder-based electrode obtained in air atmosphere.

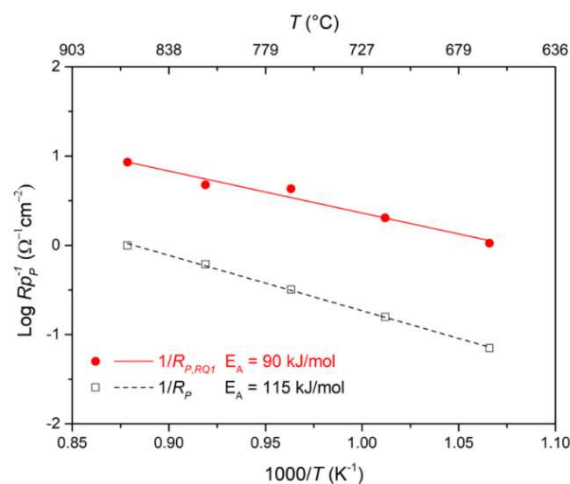


Figure 13: Arrhenius plot of the ECs elements used to fit the LSM/GDC nanofiber-based electrode. R_p obtained in air atmosphere. \square - overall R_p ; \bullet - $R_{p,RQ1}$.

3.10 Electrochemical Impedance Spectroscopy in Methane

In this section, the EIS experimental data obtained in a 97% of methane and 3% of water atmosphere with the LSM/GDC 30 μm thick nanofibers-based and the 70 μm thick LSM/GDC powder-based electrodes, are discussed. **Figure 14** and **Figure 15** show the Nyquist plots of the EIS experimental data obtained between 715 $^{\circ}\text{C}$ and 865 $^{\circ}\text{C}$ with the nanofiber-based LSM/GDC electrode. Furthermore, the Rs-G fitting result at 715 $^{\circ}\text{C}$ is reported as well.

The shape of the raw experimental data is different compared to the data reported in **Figure 10**. Indeed, the data acquired in the reducing atmosphere report a typical Gerischer behavior, instead of a sum of semicircles as reported for the data obtained in air. In both **Figure 14** and **Figure 15** serial and polarization resistance decrease, while the shape remains similar. At 715 $^{\circ}\text{C}$ it is possible to see that the Gerischer arc individuated at low frequencies, doesn't close its trajectory, but it remains open. At 765 $^{\circ}\text{C}$ the overall polarization resistance decreases its magnitude and from this temperature, the curve follows its trajectory to form a closed shape. From a quantitative point of view, the polarization resistances obtained with both the electrode configurations are extremely lower compared to the values achieved using the air atmosphere. As seen before, the nanofiber-based LSM/GDC electrode at 815 $^{\circ}\text{C}$ in the air is 1.6 Ωcm^2 , while it is 1.08 Ωcm^2 with the powder-based LSM/GDC electrode. At the same operative temperature, the polarization resistance obtained in methane with both the powder and nanofiber-based electrode is 0.15 Ωcm^2 , so ten times lower compared to the air results. At 865 $^{\circ}\text{C}$ the result is even better since with both the electrode architectures the polarization resistance is 0.04 Ωcm^2 , which is a value around twenty times lower compared to the air results of the same electrode.

The same behavior is reported by *Sandoval M.V. et al.*, where the $\text{La}_{0.5}\text{Sr}_{1.5}\text{MnO}_4$ symmetrical cell has been tested both in air and wet hydrogen, obtaining respectively a polarization resistance of 1.2 Ωcm^2 and 0.57 Ωcm^2 [81]. Furthermore, the polarization resistances reported in **Figure 14** and **Figure 15** are better also compared to literature values concerning the CH_4 as feedstock. *Wang et al.* investigated a composite anode made with GDC and Nickel, which is considered as the state-of-the-art metal for anode application, achieving a polarization resistance of 3.05 Ωcm^2 at 800 $^{\circ}\text{C}$ in a 97% of methane and 3% of water [82].

Analyzing the spectra from a qualitative point of view, the shapes of EIS experimental data reported in the Nyquist plot in **Figure 14** and **Figure 15**, remind the typical Gerischer element. This behavior is quite common for GDC-based electrodes, as confirmed by several examples reported in the literature. *Cho et al.* performed an EIS test on SrTiO_{3-δ}-GDC in a hydrogen atmosphere and the Nyquist shape reflects a Gerischer behavior [83]. *Nenning et al.* tested a Ni/GDC composite anode in a hydrogen atmosphere achieving the Gerischer arc as well [84]. The possible explanation may be found in the conductive properties of the GDC. Indeed, when the GDC is exposed to the air atmosphere, its fluorite structure allows the conduction of oxygen ions at operating temperatures even lower compared to ones generally used for the YSZ. Otherwise, when the GDC is exposed to a reducing atmosphere, poor electronic conduction is activated, and it becomes an MIEC [85].

Furthermore, as reported in **Figure 4**, the LSM modified its structure arrangement from the ABO₃ single perovskite structure, achieved after the preparation process, the Ruddlesden-Popper double perovskite after the exposition to methane atmosphere. The RP crystal structure provides a higher open framework compared to the single perovskite and due to this feature, it allows the accommodation of hyper stoichiometric oxide ions, which may permit poor ionic conduction. Thus, the LSM when exposed to a reducing atmosphere behaves like mixed ionic and electronic conductors as well [86]-[88]. The explanation just reported may explain the Nyquist shape reported in **Figure 10**, **Figure 11**, **Figure 14**, and **Figure 15**. The LSM/GDC electrodes tested as cathodes may behave as respectively pure electronic and pure ionic conductors, which are not able to extend the electrochemical reaction in the whole electrode thickness; on the contrary when the LSM/GDC electrodes are tested as anodes in methane atmosphere, both the materials achieve MIEC properties allowing the reaction process in the whole electrode volume. The different behaviors just described are reflected also in the widely lower polarization resistances achieved in anode configuration compared to cathode one.

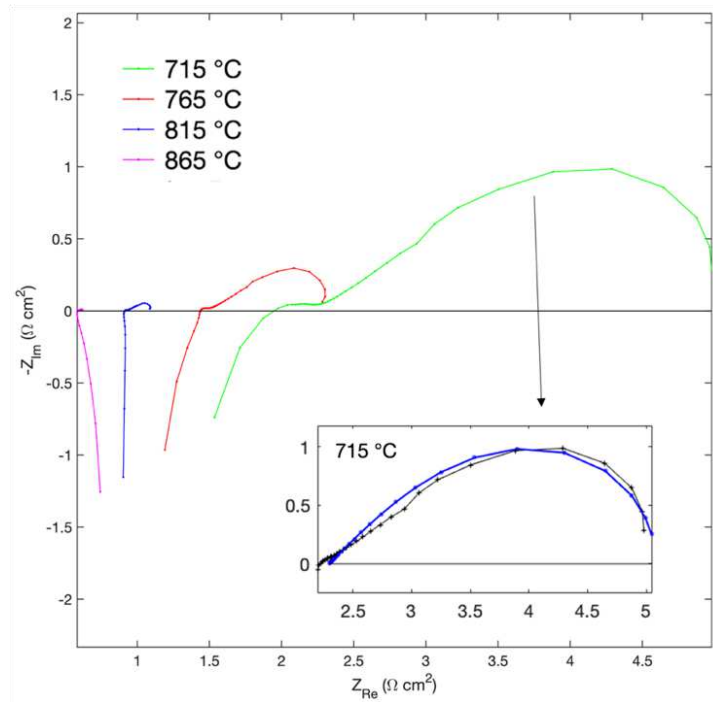


Figure 14: Nyquist plots of the EIS results obtained with the 30 μm thick nanofiber-based LSM/GDC electrode in methane atmosphere at operating temperatures from 715°C to 865°C. In the right corner, the Nyquist acquired at 715 °C is highlighted: -•- experimental data; -□- fitting through the Rs-G equivalent circuit model.

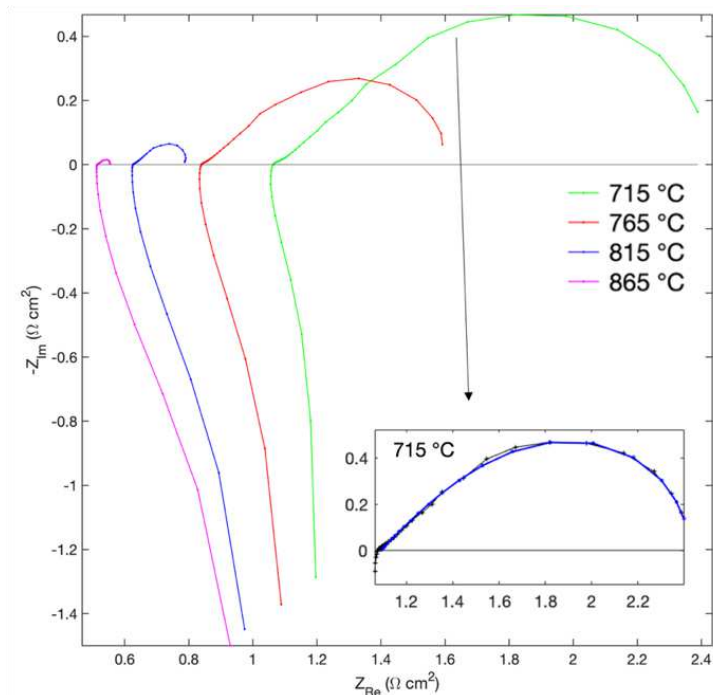


Figure 15: Nyquist plots of the EIS results obtained with the 70 μm thick powder-based LSM/GDC electrode in methane atmosphere at operating temperatures from 715°C to 865°C. In the right corner, the Nyquist acquired at 715 °C is highlighted: -•- experimental data; -□- fitting through the Rs-G equivalent circuit model.

In **Figure 16** the reverse of the polarization resistances of the LSM/GDC 30 μm thick nanofiber and 70 μm thick powder-based electrode are reported in an Arrhenius plot, within the activation energies which are respectively 297 kJ/mol and 222 kJ/mol. It is possible to

see that the major differences between the two architectures are detected at 715 °C, while at higher temperatures the results are almost overlapped which underlines the good repeatability of the results. Furthermore, compared to the results acquired in the air atmosphere, the activation energies are quite higher, while the polarization resistances are widely lower.

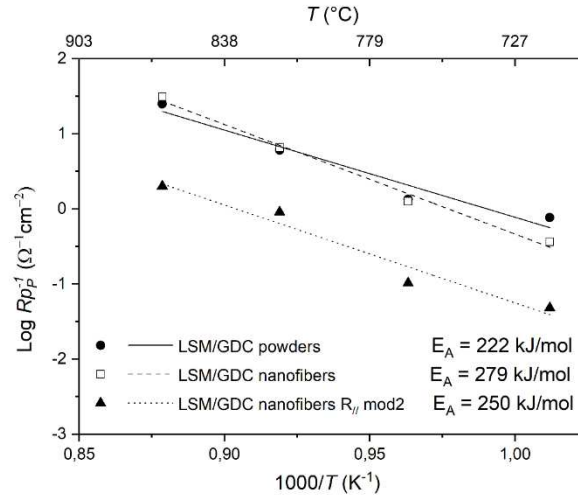


Figure 16: Arrhenius plot of polarization resistance of -□- LSM/GDC nanofiber-based; -□- LSM/GDC powder-based electrode tested in methane; ●▲● LSM/GDC nanofiber $R_{//}$ calculated through Mod2.

In **Figure 16** the reverse of the polarization resistance ($R_{p//}^{-1}$) related to the $R_{//}$ given by the Mod2 used to fit the nanofiber LSM/GDC electrode is reported as well. As reported above, the GDC acts as a mixed ionic and electronic conductor once exposed to a reducing atmosphere, so both the electrode and electrolyte start to conduct electrons.

In **Table 2** the resistances of the different EC elements as well as the total polarization resistance are reported for each investigated temperature.

Element	715 °C	765 °C	815 °C	865 °C
R_1 (Ωcm^2)	2.4	2.2	3.8	7.0
R_G (Ωcm^2)	3.6	1.1	6.0	482.0
$R_{//}$ (Ωcm^2)	20.9	9.7	1.1	0.5
R_p (Ωcm^2)	4.7	2.5	1.0	0.6

Table 2: Resistance values of the elements that appear in Mod2 and the calculated total polarization resistance. All values are normalized to the surface area. The experimental data derives from the nanofiber composite electrode measurements.

In **Figure 9** as well as **Figure 16** and **Table 2** it is possible to identify the two parallel pathways for electrons and ions which are available in the investigated cells, and which are schematized by the EC Mod2.

The first pathway is the electrochemical process, which is represented by the RQ-G elements, while the second one is the short-circuited electrolyte, described by $R_{//}$. As matter of fact, when an electric circuit is provided by different components placed in parallel, the electrical current is more favorable to flow in the pathway which offers a lower resistance. In the Mod2 EC, the relative currents through the electrochemical and short-circuited pathway are related to the value of R_1 and $R_{//}$. At lower temperatures, the resistance of R_1 is widely lower compared to $R_{//}$, and the electrochemical pathway results to be the more favorable. Furthermore, at these temperatures the GDC electronic conductivity has higher activation energy compared to the GDC ionic conductivity, thus the reduction of GDC is not sufficiently performed to generate a short-circuit. On the contrary, at the higher temperatures, the GDC reduction is at an advanced stage, and the value of R_1 is widely higher compared to $R_{//}$, so the short-circuited pathway becomes more favorable. For this reason, since the electrical current is not directed exclusively to the electrochemical activity of the electrode, the electrochemical performance cannot be considered intrinsic of the material. Furthermore, the measured activation energy is 250 kJ/mol for the electronic conductivity, which agrees with the literature value of 248 kJ/mol [89].

The very low polarization resistances measured from the impedance test may be affected by the parallel pathway, so they do not reflect the pure electrochemical activity. However, if the electronic pathway has no complex contribution to the imaginary part, it is expected that the Nyquist shape, e.g., the Gerischer element, is not affected by the short-circuit so reflects the electrode processes involved in the EC pathway. However, the results indicate the importance to employ a pure ionic conductor as an electrolyte, for example, a multilayer electrolyte based on zirconia coated with GDC on both sides.

3.11 Effect of the Electrode Thickness

Figure 17 shows the Nyquist plots acquired between 715°C and 815°C with the 70 μm thick powder-based LSM/GDC electrode (already reported in **Figure 15**) and the 40 μm thick powder-based LSM/GDC electrode. The experimental data are acquired in the methane atmosphere. In both cases, the shape reported in the Nyquist plots recalls the typical Gerischer behaviour, as seen in **Figure 14** and **Figure 15**, but it is possible to underline some differences between the two architectures. Indeed, the Gerischer arc obtained with the

70 μm thick powder electrode has a shape that is more stable with the temperature, as already reported in **Figure 15**. From 715 $^{\circ}\text{C}$ to 865 $^{\circ}\text{C}$ the polarization resistance decreases but the shape does not shrink and remains well defined. On the other hand, the 30 μm thick powder electrode reflects the Gerischer behaviour as well, but looking more deeply in the experimental data, the shape obtained is more similar to a Finite-Length-Gerischer (FLG) element. The FLG feature is individuated in electrodes which show mixed ionic and electronic properties, and so they allow the electrochemical reaction process in the whole volume of the electrode, but the electrode thickness results too thin. Thus, the thickness of the electrode is lower compared to the value needed from the electrochemical process and this limitation is reflected in the impedance spectra, which appears as a hybrid between the Gerischer and the Finite-Length-Warburg element [90], [91]. For this reason, in the 30 μm thick powder-based electrode some thickness limitations take place, reflecting this hybrid shape.

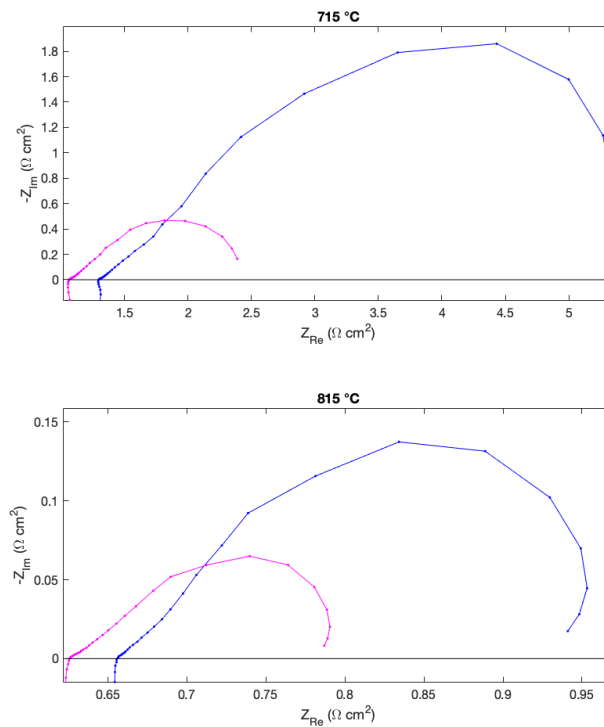


Figure 17: Nyquist plots obtained at 715 $^{\circ}\text{C}$ and 815 $^{\circ}\text{C}$ in methane atmosphere employing LSM/GDC powder-based electrodes prepared with different thicknesses. -□- 70 μm thick LSM/GDC powder electrode (already reported in **Figure 15**); -□- 30 μm thick LSM/GDC powder electrode.

3.12 Conclusions

$\text{La}_{0.6}\text{Sr}_{0.4}\text{MnO}_3$ (LSM), the SOFC cathode state-of-art material, is prepared in the form of nanofibers and powders, and is tested for direct methane intermediate temperature solid oxide fuel cell anodes. Proper synthesis and crystallinity are confirmed for both samples by XRD. In addition, the XRD measurements identify a change of the LSM crystal structure from the single perovskite obtained after the preparation process to the RP structure achieved after the exposition to the methane atmosphere. However, this transition is reversible after a re-oxidation. The X-ray photoelectron spectroscopy (XPS) measurements show that the two different synthesis routes heavily influence the surface properties, since LSM powders display strontium oxide segregation, which is not detected in nanofibers. The catalytic activity towards direct methane oxidation is investigated for the two samples, showing that the onset temperature for methane oxidation is 500 °C with nanofibers, and 600 °C with powders. Methane conversion at 800 °C is 73% with nanofibers, and 50% at 900 °C with powders. Two explanations are proposed for the superior nanofiber performance. The first is the absence of strontium oxide segregation on the surface, which exhibits perovskitic active sites till the last atomic layers. The second is the higher surface area, revealed by BET analysis.

Therefore, symmetrical cells made with nanofiber-based LSM/GDC electrodes and powder-based LSM/GDC electrodes were investigated. The LSM/GDC electrodes show a good electrochemical performance in air, consistent with literature data, reporting a polarization resistance of 1.6 Ωcm^2 at 815 °C. Furthermore, the LSM/GDC electrodes show an even better electrochemical performance once tested as an anode, in the methane atmosphere. The polarization resistance achieved at 815 °C is 0.15 Ωcm^2 , ten times lower compared to the cathode application. These very low values obtained in the methane atmosphere may find an explanation by considering the possibility of a reduction of GDC. This can lead to the presence of a parallel electron conductive pathway that may not affect the shape and the description of the electrochemical impedance phenomena, but it may influence the measured R_p .

Further investigation will be performed to better understand better this eventuality. In other cases, in fact, a contribution to the decrease of polarization resistance was attributed to the presence of C-nanoparticles whose formation was consequent to the use of methane.

References

- [1] F. S. da Silva and T. M. de Souza, "Novel materials for solid oxide fuel cell technologies: A literature review," *Int J Hydrogen Energy*, vol. 42, no. 41, pp. 26020–26036, 2017.
- [2] K. Huang and J. B. Goodenough, "Solid oxide fuel cell technology: principles, performance and operations," 2009.
- [3] A. Mehmeti, S. J. McPhail, D. Pumiglia, and M. Carlini, "Life cycle sustainability of solid oxide fuel cells: From methodological aspects to system implications," *J Power Sources*, vol. 325, pp. 772–785, 2016.
- [4] A. B. Stambouli and E. Traversa, "Solid oxide fuel cells (SOFCs): a review of an environmentally clean and efficient source of energy," *Renewable and sustainable energy reviews*, vol. 6, no. 5, pp. 433–455, 2002.
- [5] P. Kaur and K. Singh, "Review of perovskite-structure related cathode materials for solid oxide fuel cells," *Ceram Int*, vol. 46, no. 5, pp. 5521–5535, 2020.
- [6] D. Panthi, B. Choi, and A. Tsutsumi, "Direct methane operation of a micro-tubular solid oxide fuel cell with a porous zirconia support," *Journal of Solid State Electrochemistry*, vol. 21, no. 1, pp. 255–262, 2017.
- [7] P. Costamagna, P. Costa, and V. Antonucci, "Micro-modelling of solid oxide fuel cell electrodes," *Electrochim Acta*, vol. 43, no. 3–4, pp. 375–394, 1998.
- [8] B. Tu, Y. Yin, F. Zhang, X. Su, X. Lyu, and M. Cheng, "High performance of direct methane-fuelled solid oxide fuel cell with samarium modified nickel-based anode," *Int J Hydrogen Energy*, vol. 45, no. 51, pp. 27587–27596, 2020.
- [9] H. Kim, J. M. Vohs, and R. J. Gorte, "Direct oxidation of sulfur-containing fuels in a solid oxide fuel cell," *Chemical Communications*, no. 22, pp. 2334–2335, 2001.
- [10] J. Liu, B. D. Madsen, Z. Ji, and S. A. Barnett, "A fuel-flexible ceramic-based anode for solid oxide fuel cells," *Electrochemical and solid-state letters*, vol. 5, no. 6, p. A122, 2002.
- [11] C. M. Grgicak, R. G. Green, and J. B. Giorgi, "SOFC anodes for direct oxidation of hydrogen and methane fuels containing H₂S," *J Power Sources*, vol. 179, no. 1, pp. 317–328, 2008.
- [12] E. P. Murray, T. Tsai, and S. A. Barnett, "A direct-methane fuel cell with a ceria-based anode," *Nature*, vol. 400, no. 6745, pp. 649–651, 1999.
- [13] G. Yang, W. Jung, S.-J. Ahn, and D. Lee, "Controlling the oxygen electrocatalysis on perovskite and layered oxide thin films for solid oxide fuel cell cathodes," *Applied Sciences*, vol. 9, no. 5, p. 1030, 2019.
- [14] S. P. Jiang, "Development of lanthanum strontium cobalt ferrite perovskite electrodes of solid oxide fuel cells-A review," *Int J Hydrogen Energy*, vol. 44, no. 14, pp. 7448–7493, 2019.
- [15] J. Richter, P. Holtappels, T. Graule, T. Nakamura, and L. J. Gauckler, "Materials design for perovskite SOFC cathodes," *Monatshefte für Chemie-Chemical Monthly*, vol. 140, no. 9, pp. 985–999, 2009.
- [16] A. Jun, J. Kim, J. Shin, and G. Kim, "Perovskite as a cathode material: a review of its role in solid-oxide fuel cell technology," *ChemElectroChem*, vol. 3, no. 4, pp. 511–530, 2016.
- [17] M. J. Escudero, J. T. S. Irvine, and L. Daza, "Development of anode material based on La-substituted SrTiO₃ perovskites doped with manganese and/or gallium for SOFC," *J Power Sources*, vol. 192, no. 1, pp. 43–50, 2009.
- [18] S. P. Jiang, "Development of lanthanum strontium manganite perovskite cathode materials of solid oxide fuel cells: a review," *J Mater Sci*, vol. 43, no. 21, pp. 6799–6833, 2008.

- [19] B. L. Farrell and S. Linic, "Oxidative coupling of methane over mixed oxide catalysts designed for solid oxide membrane reactors," *Catal Sci Technol*, vol. 6, no. 12, pp. 4370–4376, 2016.
- [20] X. J. Chen, Q. L. Liu, K. A. Khor, and S. H. Chan, "High-performance (La, Sr)(Cr, Mn)O₃/(Gd, Ce)O₂- δ composite anode for direct oxidation of methane," *J Power Sources*, vol. 165, no. 1, pp. 34–40, 2007.
- [21] J. Xue, T. Wu, Y. Dai, and Y. Xia, "Electrospinning and electrospun nanofibers: Methods, materials, and applications," *Chemical Reviews*, vol. 119, no. 8. American Chemical Society, pp. 5298–5415, Apr. 24, 2019. doi: 10.1021/acs.chemrev.8b00593.
- [22] D. Li and Y. Xia, "Fabrication of titania nanofibers by electrospinning," *Nano Lett*, vol. 3, no. 4, pp. 555–560, Apr. 2003, doi: 10.1021/nl034039o.
- [23] D. Li, J. T. McCann, Y. Xia, and M. Marquez, "Electrospinning: a simple and versatile technique for producing ceramic nanofibers and nanotubes," *Journal of the American Ceramic Society*, vol. 89, no. 6, pp. 1861–1869, 2006.
- [24] S. T. Aruna, L. S. Balaji, S. S. Kumar, and B. S. Prakash, "Electrospinning in solid oxide fuel cells—A review," *Renewable and Sustainable Energy Reviews*, vol. 67, pp. 673–682, 2017.
- [25] C. Wang *et al.*, "Metal-organic framework-derived one-dimensional porous or hollow carbon-based nanofibers for energy storage and conversion," *Mater Horiz*, vol. 5, no. 3, pp. 394–407, 2018.
- [26] S. Agarwal, A. Greiner, and J. H. Wendorff, "Functional materials by electrospinning of polymers," *Prog Polym Sci*, vol. 38, no. 6, pp. 963–991, 2013.
- [27] P. Costamagna, C. Sanna, A. Campodonico, E. M. Sala, R. Sažinas, and P. Holtappels, "Electrochemical impedance spectroscopy of electrospun La_{0.6}Sr_{0.4}Co_{0.2}Fe_{0.8}O_{3- δ} nanorod cathodes for intermediate temperature–solid oxide fuel cells," *Fuel Cells*, vol. 19, no. 4, pp. 472–483, 2019.
- [28] C. Sanna, W. Zhang, P. Costamagna, and P. Holtappels, "Synthesis and electrochemical characterization of La_{0.6}Sr_{0.4}Co_{0.2}Fe_{0.8}O_{3- δ} /Ce_{0.9}Gd_{0.1}O_{1.95} co-electrospun nanofiber cathodes for intermediate-temperature solid oxide fuel cells," *Int J Hydrogen Energy*, vol. 46, no. 26, pp. 13818–13831, 2021.
- [29] C. Sanna, W. Zhang, P. Costamagna, and P. Holtappels, "Synthesis and electrochemical characterization of La_{0.6}Sr_{0.4}Co_{0.2}Fe_{0.8}O_{3- δ} /Ce_{0.9}Gd_{0.1}O_{1.95} co-electrospun nanofiber cathodes for intermediate-temperature solid oxide fuel cells," *Int J Hydrogen Energy*, vol. 46, no. 26, pp. 13818–13831, 2021.
- [30] Y. Jeon, J. Myung, S. Hyun, Y. Shul, and J. T. S. Irvine, "Corn-cob like nanofibres as cathode catalysts for an effective microstructure design in solid oxide fuel cells," *J Mater Chem A Mater*, vol. 5, no. 8, pp. 3966–3973, 2017.
- [31] L. Fan *et al.*, "Performance of Gd_{0.2}Ce_{0.8}O_{1.9} infiltrated La_{0.2}Sr_{0.8}TiO₃ nanofiber scaffolds as anodes for solid oxide fuel cells," *J Power Sources*, vol. 265, pp. 125–131, 2014.
- [32] W. Zhang, "Electrospinning for solid oxide fuel cells," *Electrospinning for Advanced Energy and Environmental Applications*. [Electronic resource]. (S. Cavaliere, ed.), pp. 61–76, 2015.
- [33] S. T. Aruna, L. S. Balaji, S. S. Kumar, and B. S. Prakash, "Electrospinning in solid oxide fuel cells—A review," *Renewable and Sustainable Energy Reviews*, vol. 67, pp. 673–682, 2017.
- [34] J. M. Deitzel, J. Kleinmeyer, D. E. A. Harris, and N. C. B. Tan, "The effect of processing variables on the morphology of electrospun nanofibers and textiles," *Polymer (Guildf)*, vol. 42, no. 1, pp. 261–272, 2001.
- [35] W. E. Teo and S. Ramakrishna, "A review on electrospinning design and nanofibre assemblies," *Nanotechnology*, vol. 17, no. 14, p. R89, 2006.
- [36] C. Marcilly, "Preparation of highly dispersed mixed oxides and oxide solid solutions by pyrolysis of amorphous organic precursors," *J. Am. Ceram. Soc.*, vol. 53, pp. 56–57, 1970.
- [37] G. Horvath, J. Gerblinger, H. Meixner, and J. Giber, "Segregation driving forces in perovskite titanates," *Sens Actuators B Chem*, vol. 32, no. 2, pp. 93–99, 1996.

- [38] J. Nowotny, "Interface defect chemistry of oxide ceramic materials. Unresolved problems," *Solid State Ion*, vol. 49, pp. 119–128, 1991.
- [39] M. M. Natile, E. Ugel, C. Maccato, and A. Glisenti, "LaCoO₃: Effect of synthesis conditions on properties and reactivity," *Appl Catal B*, vol. 72, no. 3–4, pp. 351–362, 2007.
- [40] A. Glisenti, A. Galenda, and M. M. Natile, "LaMnO₃: Influence of the Addition of Ba and Sr," *Surface Science Spectra*, vol. 16, no. 1, pp. 83–94, 2009.
- [41] R. P. Vasquez, "X-ray photoemission measurements of La_{1-x}Ca_xCoO₃ (x= 0, 0.5)," *Phys Rev B*, vol. 54, no. 21, p. 14938, 1996.
- [42] D. Berger, C. Matei, F. Papa, D. Macovei, V. Fruth, and J. P. Deloume, "Pure and doped lanthanum manganites obtained by combustion method," *J Eur Ceram Soc*, vol. 27, no. 13–15, pp. 4395–4398, 2007.
- [43] J. W. Murray, J. G. Dillard, R. Giovanoli, H. Moers, and W. Stumm, "Oxidation of Mn (II): Initial mineralogy, oxidation state and ageing," *Geochim Cosmochim Acta*, vol. 49, no. 2, pp. 463–470, 1985.
- [44] M. Florea *et al.*, "La_{0.75}Sr_{0.25}XO₃ (X= Fe, Mn or Cr) with coking tolerance for CH₄/H₂O reaction: effect of H₂S on catalytic performance," *Catal Sci Technol*, vol. 9, no. 9, pp. 2351–2366, 2019.
- [45] Y. Chen *et al.*, "A highly efficient and robust nanofiber cathode for solid oxide fuel cells," *Adv Energy Mater*, vol. 7, no. 6, p. 1601890, 2017.
- [46] D. Dollimore, P. Spooner, and A. Turner, "The BET method of analysis of gas adsorption data and its relevance to the calculation of surface areas," *Surface Technology*, vol. 4, no. 2, pp. 121–160, 1976.
- [47] J. R. Macdonald and a J. Wiley, *Theory, Experiment, and*.
- [48] T. Suzuki, M. Awano, P. Jasinski, V. Petrovsky, and H. U. Anderson, "Composite (La, Sr)MnO₃-YSZ cathode for SOFC," *Solid State Ion*, vol. 177, no. 19-25 SPEC. ISS., pp. 2071–2074, 2006, doi: 10.1016/j.ssi.2005.12.016.
- [49] J. R. Macdonald and a J. Wiley, *Theory, Experiment, and*.
- [50] H. Viktor. Napporn Teko W., Holade Yaovi, Kokoh Boniface, Mitsushima Shigenori, Mayer Kurt, Eichberger Bernd, "Electrochemical measurement methods and characterization on the cell level," in *Fuel Cells and Hydrogen*, 2018, pp. 175–214. doi: 10.1016/B978-0-12-811459-9.00009-8.
- [51] B. Hirschorn, M. E. Orazem, B. Tribollet, V. Vivier, I. Frateur, and M. Musiani, "Determination of effective capacitance and film thickness from constant-phase-element parameters," *Electrochim Acta*, vol. 55, no. 21, pp. 6218–6227, 2010, doi: 10.1016/j.electacta.2009.10.065.
- [52] V. Yousefi, D. Mohebbi-kalhari, and A. Samimi, "Equivalent Electrical Circuit Modeling of Ceramic-Based Microbial Fuel Cells Using the Electrochemical Impedance Spectroscopy (EIS) Analysis," *Journal of Renewable Energy and Environment*, vol. 6, no. 1, pp. 21–28, 2019.
- [53] P. Costamagna, E. M. Sala, W. Zhang, M. Lund Traulsen, and P. Holtappels, "Electrochemical impedance spectroscopy of La_{0.6}Sr_{0.4}Co_{0.2}Fe_{0.8}O_{3-δ} nanofiber cathodes for intermediate temperature-solid oxide fuel cell applications: A case study for the 'depressed' or 'fractal' Gerischer element," *Electrochim Acta*, vol. 319, pp. 657–671, 2019, doi: 10.1016/j.electacta.2019.06.068.
- [54] J. Nielsen, T. Jacobsen, and M. Wandel, "Impedance of porous IT-SOFC LSCF:CGO composite cathodes," *Electrochim Acta*, vol. 56, no. 23, pp. 7963–7974, 2011, doi: 10.1016/j.electacta.2011.05.042.
- [55] T. Jacobsen, P. V. Hendriksen, and S. Koch, "Diffusion and conversion impedance in solid oxide fuel cells," *Electrochim Acta*, vol. 53, no. 25, pp. 7500–7508, 2008, doi: 10.1016/j.electacta.2008.02.019.
- [56] P. Costamagna, C. Sanna, A. Campodonico, E. M. Sala, R. Sažinas, and P. Holtappels, "Electrochemical Impedance Spectroscopy of Electrospun La_{0.6}Sr_{0.4}Co_{0.2}Fe_{0.8}O_{3-Δ} Nanorod

- Cathodes for Intermediate Temperature – Solid Oxide Fuel Cells,” *Fuel Cells*, vol. 19, no. 4, pp. 472–483, 2019, doi: 10.1002/fuce.201800205.
- [57] C. Sanna, W. Zhang, P. Costamagna, and P. Holtappels, “Synthesis and electrochemical characterization of electrospun nanofiber cathodes for intermediate- temperature solid oxide fuel cells,” *International Journal of Hydrogen Energy*, no. xxxx, pp. 1–14, 2020, doi: 10.1016/j.ijhydene.2020.11.216.
- [58] P. Costamagna, E. M. Sala, W. Zhang, M. Lund Traulsen, and P. Holtappels, “Electrochemical impedance spectroscopy of La_{0.6}Sr_{0.4}Co_{0.2}Fe_{0.8}O_{3-δ} nanofiber cathodes for intermediate temperature-solid oxide fuel cell applications: A case study for the ‘depressed’ or ‘fractal’ Gerischer element,” *Electrochimica Acta*, vol. 319, pp. 657–671, 2019, doi: 10.1016/j.electacta.2019.06.068.
- [59] M. Cannarozzo, A. Del Borghi, and P. Costamagna, “Simulation of mass transport in SOFC composite electrodes,” *Journal of Applied Electrochemistry*, vol. 38, no. 7, pp. 1011–1018, 2008, doi: 10.1007/s10800-008-9527-1.
- [60] E. P. Murray, T. Tsai, and S. A. Barnett, “Oxygen transfer processes in (La,Sr)MnO₃/Y₂O₃-stabilized ZrO₂ cathodes: An impedance spectroscopy study,” *Solid State Ionics*, vol. 110, no. 3–4, pp. 235–243, 1998, doi: 10.1016/s0167-2738(98)00142-8.
- [61] E. Siebert, A. Hammouche, and M. Kleitz, “Impedance spectroscopy analysis of La_{1-x}Sr_xMnO₃-yttria-stabilized zirconia electrode kinetics,” *Electrochimica Acta*, vol. 40, no. 11, pp. 1741–1753, 1995, doi: 10.1016/0013-4686(94)00361-4.
- [62] M. J. L. Østergård and M. Mogensen, “ac Impedance study of the oxygen reduction mechanism on La_{1-x}Sr_xMnO₃ in solid oxide fuel cells,” *Electrochimica Acta*, vol. 38, no. 14, pp. 2015–2020, 1993, doi: 10.1016/0013-4686(93)80334-V.
- [63] M. Juhl, S. Primdahl, C. Manon, and M. Mogensen, “Performance/structure correlation for composite SOFC cathodes,” *Journal of Power Sources*, vol. 61, no. 1–2, pp. 173–181, 1996, doi: 10.1016/S0378-7753(96)02361-0.
- [64] P. Costamagna, P. Holtappels, and C. Sanna, “Metal Oxide Nanofiber-Based Electrodes In Solid Oxide Fuel Cells,” in *Metal oxide-based nanofibers and their applications*, Elsevier.
- [65] M. Zhi, N. Mariani, R. Gemmen, K. Gerdes, and N. Wu, “Nanofiber scaffold for cathode of solid oxide fuel cell,” *Energy and Environmental Science*, vol. 4, no. 2, pp. 417–420, 2011, doi: 10.1039/c0ee00358a.
- [66] X. Luo *et al.*, “Reduced-temperature redox-stable LSM as a novel symmetrical electrode material for SOFCs,” *Electrochimica Acta*, vol. 260, pp. 121–128, 2018, doi: 10.1016/j.electacta.2017.11.071.
- [67] S. P. Jiang and W. Wang, “Novel structured mixed ionic and electronic conducting cathodes of solid oxide fuel cells,” *Solid State Ionics*, vol. 176, no. 15–16, pp. 1351–1357, 2005, doi: 10.1016/j.ssi.2005.03.011.
- [68] S. Wang, X. Lu, and M. Liu, “Electrocatalytic properties of La_{0.9}Sr_{0.1} MnO₃-based electrodes for oxygen reduction,” *Journal of Solid State Electrochemistry*, vol. 6, no. 6, pp. 384–390, 2002, doi: 10.1007/s10008-001-0250-7.
- [69] S. P. Jiang, “ScienceDirect Development of lanthanum strontium cobalt ferrite perovskite electrodes of solid oxide fuel cells e A review,” *International Journal of Hydrogen Energy*, vol. 44, no. 14, pp. 7448–7493, 2019, doi: 10.1016/j.ijhydene.2019.01.212.
- [70] C. Sanna, W. Zhang, P. Costamagna, and P. Holtappels, “Synthesis and electrochemical characterization of electrospun nanofiber cathodes for intermediate- temperature solid oxide fuel cells,” *International Journal of Hydrogen Energy*, no. xxxx, pp. 1–14, 2020, doi: 10.1016/j.ijhydene.2020.11.216.
- [71] S. Sunde, “Monte Carlo Simulations of Polarization Resistance of Composite Electrodes for Solid Oxide Fuel Cells,” *Journal of The Electrochemical Society*, vol. 143, no. 6, pp. 1930–1939, 1996, doi: 10.1149/1.1836927.

- [72] P. Costamagna, P. Costa, and V. Antonucci, "Micro-modelling of solid oxide fuel cell electrodes," *Electrochimica Acta*, vol. 43, no. 3–4, pp. 375–394, 1998, doi: 10.1016/S0013-4686(97)00063-7.
- [73] M. J. Jørgensen and M. Mogensen, "Impedance of Solid Oxide Fuel Cell LSM/YSZ Composite Cathodes," 2001, doi: 10.1149/1.1360203.
- [74] E. P. Murray, T. Tsai, and S. A. Barnett, "Oxygen transfer processes in (La,Sr)MnO₃/Y₂O₃-stabilized ZrO₂ cathodes: An impedance spectroscopy study," *Solid State Ionics*, vol. 110, no. 3–4, pp. 235–243, 1998, doi: 10.1016/S0167-2738(98)00142-8.
- [75] P. Costamagna, C. Sanna, A. Campodonico, E. M. Sala, R. Sažinas, and P. Holtappels, "Electrochemical Impedance Spectroscopy of Electrospun La_{0.6}Sr_{0.4}Co_{0.2}Fe_{0.8}O_{3-Δ} Nanorod Cathodes for Intermediate Temperature – Solid Oxide Fuel Cells," *Fuel Cells*, vol. 19, no. 4, pp. 472–483, 2019, doi: 10.1002/face.201800205.
- [76] S. P. Jiang, *Development of lanthanum strontium manganite perovskite cathode materials of solid oxide fuel cells : a review*. 2008. doi: 10.1007/s10853-008-2966-6.
- [77] M. Zhi, N. Mariani, R. Gemmen, K. Gerdes, and N. Wu, "Nanofiber scaffold for cathode of solid oxide fuel cell," *Energy and Environmental Science*, vol. 4, no. 2, pp. 417–420, 2011, doi: 10.1039/c0ee00358a.
- [78] S. Wang, Y. Jiang, Y. Zhang, J. Yan, and W. Li, "Promoting effect of YSZ on the electrochemical performance of YSZ + LSM composite electrodes," *Solid State Ionics*, vol. 113–115, pp. 291–303, 1998, doi: 10.1016/S0167-2738(98)00379-8.
- [79] L. Fan *et al.*, "Performance of Gd_{0.2}Ce_{0.8}O_{1.9} infiltrated La_{0.2}Sr_{0.8}TiO₃ nanofiber scaffolds as anodes for solid oxide fuel cells," *Journal of Power Sources*, vol. 265, pp. 125–131, 2014, doi: 10.1016/j.jpowsour.2014.04.109.
- [80] J. Parbey *et al.*, "High-performance solid oxide fuel cells with fiber-based cathodes for low-temperature operation," *International Journal of Hydrogen Energy*, vol. 45, no. 11, pp. 6949–6957, 2020, doi: 10.1016/j.ijhydene.2019.12.125.
- [81] M. V. Sandoval *et al.*, "In-depth study of the Ruddlesden-Popper La_xSr_{2-x}MnO_{4±Δ} family as possible electrode materials for symmetrical SOFC," *International Journal of Hydrogen Energy*, vol. 42, no. 34, pp. 21930–21943, 2017, doi: 10.1016/j.ijhydene.2017.07.062.
- [82] W. Wang, S. P. Jiang, A. I. Y. Tok, and L. Luo, "GDC-impregnated Ni anodes for direct utilization of methane in solid oxide fuel cells," *Journal of Power Sources*, vol. 159, no. 1 SPEC. ISS., pp. 68–72, 2006, doi: 10.1016/j.jpowsour.2006.04.051.
- [83] S. Cho, D. E. Fowler, E. C. Miller, J. S. Cronin, K. R. Poeppelmeier, and S. A. Barnett, "Fe-substituted SrTiO_{3-δ}-Ce_{0.9}Gd_{0.1}O₂ composite anodes for solid oxide fuel cells," *Energy and Environmental Science*, vol. 6, no. 6, pp. 1850–1857, 2013, doi: 10.1039/c3ee23791e.
- [84] A. Nanning, C. Bischof, J. Fleig, M. Bram, and A. K. Opitz, "The relation of microstructure, materials properties and impedance of SOFC electrodes: A case study of Ni/GDC anodes," *Energies*, vol. 13, no. 4, pp. 5–9, 2020, doi: 10.3390/en13040987.
- [85] N. Mahato, A. Banerjee, A. Gupta, S. Omar, and K. Balani, "Progress in material selection for solid oxide fuel cell technology: A review," *Progress in Materials Science*, vol. 72, pp. 141–337, 2015, doi: 10.1016/j.pmatsci.2015.01.001.
- [86] G. Amow and S. J. Skinner, "Recent developments in Ruddlesden-Popper nickelate systems for solid oxide fuel cell cathodes," *Journal of Solid State Electrochemistry*, vol. 10, no. 8, pp. 538–546, 2006, doi: 10.1007/s10008-006-0127-x.
- [87] A. Manthiram, J. H. Kim, Y. N. Kim, and K. T. Lee, "Crystal chemistry and properties of mixed ionic-electronic conductors," *Journal of Electroceramics*, vol. 27, no. 2, pp. 93–107, 2011, doi: 10.1007/s10832-011-9635-x.
- [88] S. Vecino-Mantilla, P. Simon, M. Huvé, G. Gauthier, and P. Gauthier-Maradei, "Methane steam reforming in water-deficient conditions on a new Ni-exsolved Ruddlesden-Popper manganite: Coke formation and H₂S poisoning," *International Journal of Hydrogen Energy*, vol. 45, no. 51, pp. 27145–27159, 2020, doi: 10.1016/j.ijhydene.2020.07.065.

- [89] C. Chatzichristodoulou and P. V. Hendriksen, "Electronic conductivity of $\text{Ce}_{0.9}\text{Gd}_{0.1}\text{O}_{1.95-\delta}$ and $\text{Ce}_{0.8}\text{Pr}_{0.2}\text{O}_{2-\delta}$: Hebb-Wagner polarisation in the case of redox active dopants and interference," *Physical Chemistry Chemical Physics*, vol. 13, no. 48, pp. 21558–21572, 2011, doi: 10.1039/c1cp21824g.
- [90] J. Nielsen and J. Hjelm, "Impedance of SOFC electrodes: A review and a comprehensive case study on the impedance of LSM:YSZ cathodes," *Electrochimica Acta*, vol. 115, pp. 31–45, 2014, doi: 10.1016/j.electacta.2013.10.053.
- [91] J. Nielsen, T. Jacobsen, and M. Wandel, "Impedance of porous IT-SOFC LSCF:CGO composite cathodes," *Electrochimica Acta*, vol. 56, no. 23, pp. 7963–7974, 2011, doi: 10.1016/j.electacta.2011.05.042.

Chapter 4: Chemical and electrochemical characterization of $\text{La}_{0.8}\text{Sr}_{0.2}\text{MnO}_3$ and $\text{La}_{0.6}\text{Sr}_{0.4}\text{Cu}_{0.1}\text{Mn}_{0.9}\text{O}_3$

4.1 Introduction

In the previous chapter, the possibility to use $\text{La}_{0.6}\text{Sr}_{0.4}\text{MnO}_3$ (LSM) as electrode material for intermediate temperature symmetrical SOFCs was analyzed. The improvement on the performances given by the 1D morphology was studied as well by the creation of LSM nanofibers.

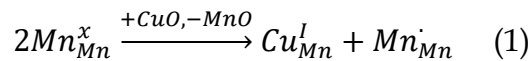
In this chapter the change of the stoichiometry is performed to understand if it affects the performances on methane oxidation. At this purpose, two are the studied compounds in this section: $\text{La}_{0.8}\text{Sr}_{0.2}\text{MnO}_3$ (L8S2M) and $\text{La}_{0.6}\text{Sr}_{0.4}\text{Cu}_{0.1}\text{Mn}_{0.9}\text{O}_3$ (LSCuM).

LSCuM was taken into consideration since the doping in the B-site can be very effective in improving the electronic conductivity. Therefore, several attempts have been made to substitute Mn with other transition elements, such as Cr, Co, Fe and Ni. [2]-[8] Cu was already studied as B-site element for possible IT-SOFCs cathodes too. *Berenov et al.* evaluated Sr,Mn-doped lanthanum copper oxide, $\text{La}_{0.8}\text{Sr}_{0.2}\text{Cu}_{1-x}\text{Mn}_x\text{O}_3$. They reported that lowering the Cu content in the perovskite, through Mn doping, resulted in a decrease in electronic conductivity. On the contrary, the thermal expansion coefficient decreased linearly with x. [9], [10]

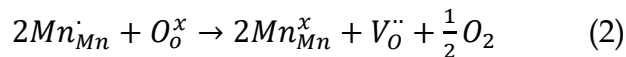
A combination of two different ions at the B-site has synergistic effects and can improve the performance of LSM as an electrode. Furthermore, Cu doping will also change the Mn^{3+} - Mn^{4+} ratio and the Mn-Mn exchange interaction. As an aliovalent doping element, the most stable state of Cu is Cu^{2+} but there is also a lower possibility of a Cu^{3+} state. The lattice parameters and crystal structure will be affected due to mismatch of the ionic radius between Mn ions and Cu ions. The most stable state of Cu is Cu^{2+} , and the Cu^{2+} (6 coordination) radius is approximately 0.73 Å. This is much larger than the radius of Mn^{3+} (0.645 Å) and Mn^{4+} (0.53 Å) [11]. Consequently, the B-site doping of Cu^{2+} should lead to an

expansion of the unit cell rather than a contraction. Anyway, it is experimentally verified that with the addition of Cu, there is a unit cell volume contraction. This discrepancy is explained assuming that Cu doping changes a part of the Mn³⁺ ions to the smaller Mn⁴⁺ ions. Therefore, an increase in Mn⁴⁺ ion concentration leads to a contraction of the unit cell volume. In addition, a change in the unit cell volume of LaMnO₃ perovskites is associated with the deformation of LaO₁₂ and MnO₆ polyhedra by variations of their bond lengths and bond/tilt angles. [12], [13]

In general, Sr-doping enhances the electronic conductivity of LaMnO₃ by the formation of Mn⁴⁺ for charge compensation. The increased Mn⁴⁺ concentration can create more Mn³⁺/Mn⁴⁺ pairs, which act as hopping sites for hole conduction. The higher conductivity increases with increasing number of hopping sites available. Similarly, an increase in the electrical conductivity with increasing Cu contents was attributed to a charge compensation generated Mn³⁺-Mn⁴⁺ redox couple. As already observed in literature, the compositions with x = 0.1 and x = 0.2 showed a higher value of electrical conductivity than that of the composition with x = 0 (LSM), which can be expressed in the Kröger-Vink notation as:



The substitution of Cu²⁺ into the B-site in La_{0.8}Sr_{0.2}MnO₃ can be compensated by formation of Mn⁴⁺. Therefore, as written above, the enhancement of performance with the addition of Cu content can be explained by the following. The additional Mn⁴⁺ promotes the formation of surface oxygen vacancies when Mn⁴⁺ is converted to Mn³⁺. At low temperatures in an oxidizing environment, these vacancies can be filled by active oxygen, while at relatively high temperatures (above 600 °C) they can be desorbed, with the formation of oxygen vacancies according to the following reaction:



A greater abundance of Mn⁴⁺ cations is beneficial for the generation of more oxygen vacancies and the presence of surface oxygen vacancies promotes the oxygen reduction reaction. Consequently, it is very relevant to consider which is the quantity of Cu to insert in the B-site. *Ryu et al.* showed as increasing the Cu content in the B-site doping improves the electronic conductivity, but this is true until there is the complete solubility of Cu atoms in the structure. Indeed, it was demonstrated that when too much copper is inserted in the

structure there is the formation of some secondary phases (SrCu_2O_2 and Cu_2O) that, being insulant, decreases the electronic conductivity of the electrode. In the same paper, the authors found that the maximum Cu content in the perovskite that gives an improvement of the material regarding the electronic conductivity is $x=0.3$. [14]

In this work, the amount of Cu inserted in the perovskite structure at the B-site is $x=0.1$. The choice to insert a lower quantity of Cu, is related to its high mobility. The high mobility is a phenomenon that happens especially under reducing atmosphere, which is exactly the environment the material will be subjected to, when it is used as fuel electrode.

The addition of copper as B-site dopant is not the only strategy considered and discussed in this chapter. Indeed, one of the challenges consists in finding the appropriate chemical composition of the electrode powder to get the best compromise between, on the one hand, excellent transport properties, and, on the other hand, mechanical and chemical stability, suitable for a long life of the electrolyte-electrode interface in SOFCs operating conditions.

The amount of Sr doping in LSM can affect many properties of the material, among which the crystalline structure: the lattice contraction, as an example, occurs over a 0.2 mol Sr. [15] These changes in the structure are relevant since they significantly affect the electronic conductivity that increases in proportional to the Sr content. In fact, the polaron hopping mechanism occurs easily between the Mn-O-Mn combinations, with an enhancing of the hopping rate by an increase in the valence of the transition metal located in the B-site. In literature, the effect of strontium doping level on magnetic properties is well studied. [16]-[18] One of the results of this study is that T_p (insulator-metal transition temperatures) and T_c (Curie temperatures: temperature above which certain materials lose their permanent magnetic properties) increase systematically in proportion to the strontium doping level in $\text{La}_{1-x}\text{Sr}_x\text{MnO}_3$ nanoparticles and the maximum values of T_p and T_c occur at $x = 0.3$.

Other research demonstrates that the morphological and the structural properties can be affected by Sr doping too. In literature was observed that maintaining the same synthesis procedure, the results of SEM measurements of the studied compounds indicate that the particle size can vary from 40 to 80 nm. [19], [20] Furthermore, the XRD patterns indicate that

the symmetry of crystal structure is improved with the increased amount of Sr doping. This behavior is attributed to the role of Sr, which, having a larger ionic radius than that of La^{3+} ($r_{\text{La}^{3+}} = 0.106 \text{ nm}$, $r_{\text{Sr}^{2+}} = 0.112 \text{ nm}$), increase the average ionic radius $\langle r_A \rangle$ (where, $\langle r_A \rangle = (1 - x)r_{\text{La}^{3+}} + xr_{\text{Sr}^{2+}} = (r_{\text{Sr}^{2+}} - r_{\text{La}^{3+}})x + r_{\text{La}^{3+}}$); meanwhile, Sr-doping, inducing the change $\text{Mn}^{3+} \rightarrow \text{Mn}^{4+}$, contributes to the decrease of $\langle r_B \rangle$ (where, $\langle r_B \rangle = (1 - x)r_{\text{Mn}^{3+}} + xr_{\text{Mn}^{4+}} = (r_{\text{Mn}^{4+}} - r_{\text{Mn}^{3+}})x + r_{\text{Mn}^{3+}}$). Consequently, the tolerance factor increases, and the crystal structure of the samples is modified, by the Jahn-Teller effect, from rhombohedral to tetragonal [21], i.e., the crystal distortion diminishes, and the symmetry of crystal structure is improved. The final effect is that the conduction band is enlarged, and the double exchange effect is enhanced in direct proportion to the e_g bandwidth. In other words, as a function of Sr doping, the valence state of Mn^{3+} ionic will be changed to Mn^{4+} , causing the 3d e_g electrons to “cruise” between these two ions through an oxygen atom, and the e_g electrons, called itinerant electrons, are responsible of the conductivity of the material. [22]

In the previous chapter, LSM showed all the characteristics to become an electrode for symmetrical SOFCs fueled directly by methane. Indeed, it shows acceptable catalytic activity towards methane oxidation, good electronic and ionic conductivity. However, it was considered that could be useful to investigate the possibility to increase these three material features by performing different Sr doping and introducing Cu as aliovalent doping in the B-site. In fact, there are many studies in literature that assert the possibility to enhance the electronic conductivity varying the Sr content as dopant in the A site of LSM perovskite. Not only that, but also Cu doping can be responsible of important improvements on electronic conductivity and, due to its easy movability, diffusion of Cu cations through the surface can become effective catalytic sites towards methane oxidation reaction. For all these reasons, $\text{La}_{0.8}\text{Sr}_{0.2}\text{MnO}_3$ (L8S2M) and $\text{La}_{0.6}\text{Sr}_{0.4}\text{Cu}_{0.1}\text{Mn}_{0.9}\text{O}_3$ (LSCuM) were investigated as innovative anodic materials for IT-SOFC fueled by methane.

4.2 XRD

As usual, XRD is the first characterization to be shown, as it is fundamental to certify the correct synthesis of the desired materials and excluding the presence of secondary phases.

(Figure 1)

These two goals were reached for both the samples, confirming that the sol gel method is a consistent procedure that guarantees the correct synthesis of compounds and allows obtaining the exact composition (which, as mentioned in the previous Paragraph 4.1, is fundamental to obtain the electrocatalytic behavior). It is important to underline the complete absence of any copper oxide reflex (main peak should be at 36°) in the LSCuM XRD pattern: this supports the expected insertion of the Cu cations in the perovskitic crystalline structure. Another confirmation of the successful insertion of copper in the perovskitic structure is the significant shift of the LSCuM peaks at higher 2θ values, as can be observed, as an example, from reflex (110) enlarged in **Figure 1**. Reflexes shifting to larger Bragg's angles confirm the volume reduction of the crystalline unit cell due to the lower ionic radius of Cu^{2+} compared to Mn^{3+} , (the expected species in the un-doped perovskite). The presence of the Cu^{2+} ions in the structure, induces the formation of Mn^{4+} cations, characterized by a smaller radius of Mn^{3+} , thus contributing to the volume reduction (and to the XRD reflexes shift). When LSM and L8S2M are compared, a reflex shift of L8S2M reflexes towards larger Bragg's angles is observed as well, but less evident compared to the LSCuM shift. This can be explained since the difference between Sr^{2+} and La^{3+} ionic radii is lower than between Cu^{2+} and Mn^{3+} (the Sr^{2+} cation radius is only slightly larger than the La^{3+} one [23],[24]) and thus, by introducing a smaller amount of Sr cations in the structure, the free volume of the unit cell is reduced with respect to LSM, but the shift is lower compared to LSCuM.

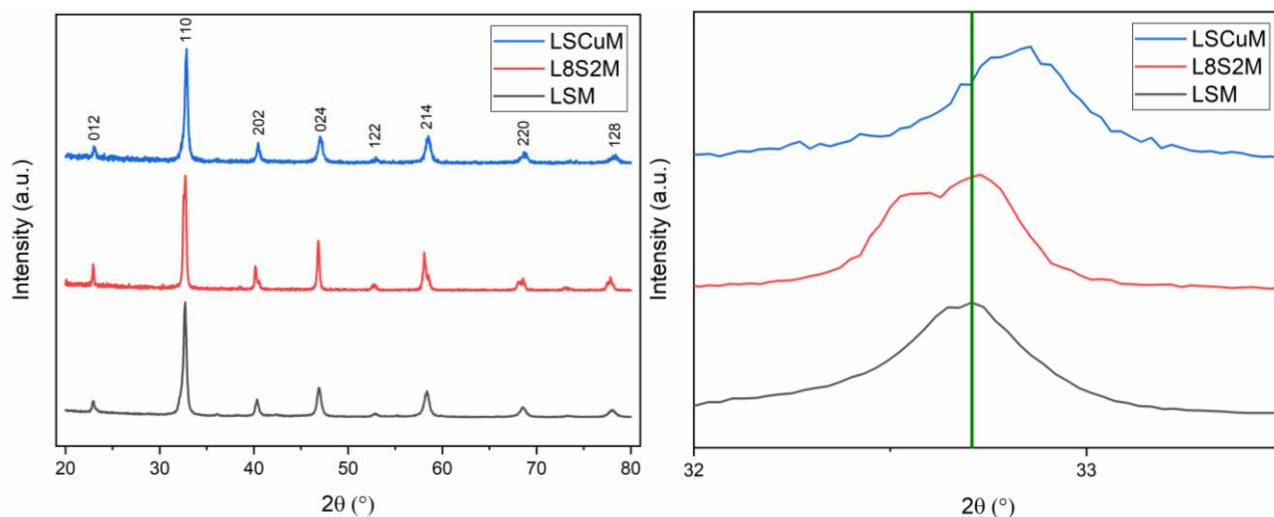


Figure 1: On the left the XRD patterns for the synthesized LSM, L8S2M and LSCuM. The Miller index for every reflex is indicated. On the right: the zoom of the main peak is presented. The green line is set on the maximum of the LSM main peak.

The second step is to verify the stability of these compounds under reducing atmospheres, since they will be used not only as cathode material, but also in the anodic side, to reach the final goal of a symmetric cell.

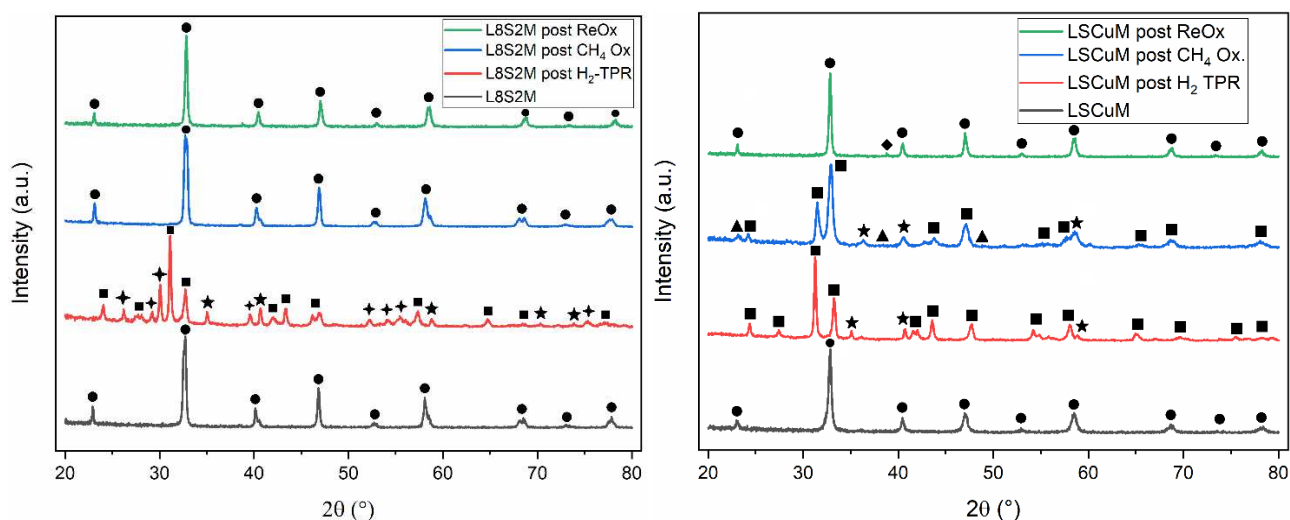


Figure 2: On the left the stability test XRD for L8S2M and on the right the one for LSCuM. In black the diffractogram patterns of the compounds as synthesized; in red after the exposition to H_2 at $900\text{ }^\circ\text{C}$; in blue after the CH_4 oxidation tests and in green after the exposition to CH_4 at $800\text{ }^\circ\text{C}$ and consequent reoxidation in air. ●L8S2M (on the left) and LSCuM (on the right); ■ Ruddlesden-Popper phase: $La_{1.2}Sr_{0.8}MnO_4$ (on the left) and $La_{1.2}Sr_{0.8}Cu_{0.1}Mn_{0.9}O_4$ (on the right); † La_2O_3 ; ★ MnO; ▲ Mn_2O_3 ; ◆ CuO.

On **Figure 2**, the behavior of the L8S2M (left) and LSCuM (right), crystalline structure under different atmospheres, is shown:

- after a reducing treatment until $900\text{ }^\circ\text{C}$ with a ramp of $10\text{ }^\circ\text{C}$ in H_2 (red line) - (for more details see [Paragraph 4.3](#))

- after the methane oxidation reaction (blue line). The CH₄ catalytic tests on oxidation reaction were led introducing in the test chamber the stoichiometric ratio between methane and air and heating the samples till 900 °C. (for more details see [Paragraph 4.4](#))
- after the methane oxidation reaction followed by reoxidation (green line). Reoxidation was performed by introducing a controlled flow of air (100 sccm) at 900 °C for 30 minutes and cooling down the sample in air.

From the red XRD pattern referred to L8S2M, it is evident that the material, subjected to a high reductive atmosphere (900 °C in H₂), is not stable. The perovskite stoichiometry is reduced to the Ruddlesden-Popper one (A₂BO₃). This confirms, as already mentioned for LSM, that the RP phase is more stable in reducing atmospheres. Anyway, this is not the only change that hydrogen leads to the sample. Indeed, it is observed the presence of two new phases in the diffractogram that confirms the degradation of the perovskite crystal structure into a mixture of La₂O₃ and MnO. It is quite interesting to note that the formation of lanthanum oxide was not detected for LSM (see [Paragraph 3.5](#)), even after the same treatment in hydrogen. This is true also for LSCuM. Indeed, looking at its diffractogram after LSCuM exposition to H₂ (red line on the right of **Figure 2**), the diffractogram carried out after the hydrogen exposition, presents only MnO as secondary phase. These data seem to suggest that Sr can be seen as a stabilizing agent of lanthanum in the crystal structure.

The behavior of L8S2M when exposed to methane is completely different. The blue line (XRD carried out on the exhaust sample of the catalytic test towards methane oxidation) does not show any modification compared to the XRD referred to the as synthesized material. The same result was obtained for the material reduced in CH₄ and then oxidized again in air (green line). Indeed, the material does not show any modification or formation of new phases.

As mentioned before, the LSCuM crystal structure is subjected to degradation because of the exposition to hydrogen. Even if there is not formation of lanthanum oxides, the presence of MnO is evident. Besides, even for this sample the transition of the perovskite structure to the RP structure is verified. Contrarily to what observed for LSM and L8S2M, for the Cu doped material, the catalytic test leads to the formation of secondary phases as MnO and

Mn₂O₃. The formation of the manganese oxide can be referred to the presence of Cu doping, that has a destabilizing effect on the perovskite crystal structure. Another observed difference between LSM and L8S2M is highlighted by XRD post catalytic test. While the two materials without copper have maintained the perovskite structure after the exposition to the catalytic atmosphere, for LSCuM the perovskite structure is reduced to the RP one.

Treatment	LSM	L8S2M	LSCuM
After H ₂ -TPR	RP	RP	RP
After CH ₄ Ox.	Perovskite	Perovskite	RP
After ReOx.	Perovskite	Perovskite	Perovskite

Table 1: Crystal structure of the main studied compounds after the different treatments.

In the end, it is significant to observe the XRD of LSCuM after methane exposition till 800 °C and the consequent reoxidation in air. Indeed, even if the perovskite structure was not maintained after the exposition to the methane-air mixture during the catalytic test, the perovskite structure is reobtained after the atmosphere switching to pure air. Anyway, there is an important difference between the diffraction patterns collected on the sample “as synthesized” and after the reoxidation. Indeed, at about $2\theta = 38^\circ$ a small peak is present for the re-oxidized material, but this is not observed for the pristine LSCuM. This peak is the main reflex of CuO. So, the treatment in methane at 800 °C seems to be able to induce the exsolution of Cu nanoparticles on the surface of the perovskite structure. This is an important feature of the material, since the presence of small Cu nanoparticles on the surface is a booster of the electronic conductivity of the material. An improved electronic conductivity is fundamental to obtain smaller resistances of the material and consequently better performances from the entire cell. The presence of this peak after the reoxidation means that the exsolution of the Cu cation towards the surface is not reversible, at least with a simple exposition of the material to air.

Finally, let's try to explain the reason why there are not clear evidence of copper exsolution after LSCuM exposition to methane. We cannot exclude that in the XRD pattern carried out after the catalytic tests, the CuO peak is present. Anyway, due to a more complex diffractogram and the very small quantity of Cu inserted in the structure (that lead to a very small intensity of the peak), the peak at 38° it is not clearly visible. On the other side, in the XRD pattern after the reduction of the material in hydrogen, the main expected peak caused by the nanoparticles should set at 44° . Indeed, at this Bragg angle is set the main peak for

metallic copper. [25] Most probably, even here the high signal-noise ratio does not allow to see distinctly the presence of this peak.

4.3 H₂-TPR

To better understand the reducibility properties of the two compounds, a Temperature Programmed Reduction in hydrogen (H₂-TPR) was carried out. The material is heated with a controlled thermal ramp of 10 °C/min and subjected to a hydrogen flux (5% H₂ in Ar). By means of this experimental procedure, it is possible to better understand the reduction behavior of the catalyst by distinguishing the contribution of each cation. Furthermore, the results of this reducing treatment are a fundamental preliminary step to confirm the suitability of these materials to be used as anode for SOFCs.

The H₂-TPRs of L8S2M and LSCuM are presented in the following **Figure 3**.

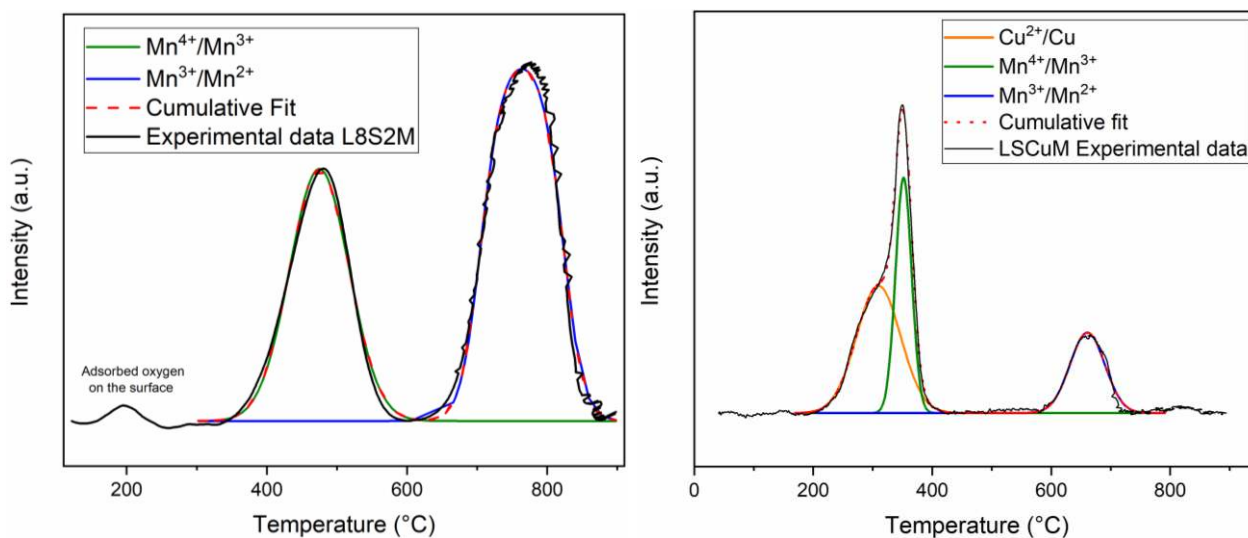
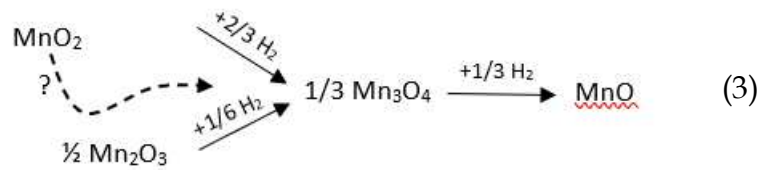


Figure 3: H₂-TPR experimental profiles (black solid line) and cumulative fit (red dot line) for L8S2M (on the left) and LSCuM (on the right). In green there is the fitting curve for Mn³⁺/Mn²⁺ reductive process; in blue the Mn²⁺/Mn⁰ process; in orange there is the fitted contribution for the Cu²⁺/Cu⁰ reductive process.

The TPR profile for L8S2M (on the left of **Figure 3**) shows two main peaks, one set at 475 °C and the other one set at 770 °C. These two peaks are related to manganese cations reduction, since is the only species that can be reduced in the analyzed temperature range. As described in the graph above, the first one is referred to the reduction of Mn⁴⁺ cations present in the structure due to Sr doping. The second one is given by the reduction of Mn³⁺ to Mn²⁺. This attribution is confirmed not only by literature [26], [27], but also from what

observed (and discussed in the previous [Paragraph 3.5](#)) for LSM. This result agrees with the mechanism proposed by Kapteijn et al. [28]:



Anyway, by comparing the reduction temperatures obtained for L8S2M and LSM, it is possible to observe (**Table 2**) a significant increment of the temperatures for both the reductive processes in L8S2M. This behaviour was expected, since the increasing of the Sr doping amount lowers the Mn-O bonding energy, consequently enhancing the reducibility of alkaline-earth substituted manganites. Infact, increasing the Sr amount in the perovskite it is enhanced the formation of more reducible Mn⁴⁺ species, if compared to the original Mn³⁺ ones present in the undoped manganite lathanum. [26]

These two reductive processes, referred to the Mn reduction, are not the only signals detected by the TPR. Indeed, at about 200 °C, it is possible to observe a smaller peak, that does not correspond to any reductive processes for manganite oxides. The most plausible explanation of this signal is the presence of surface oxygen, due to the air exposition of the sample before the analysis. This chemisorption is favoured in aliovalent doped LaMnO₃ perovskites. As already mentioned, the Sr²⁺ ions are responsible for the shifting of manganese from a Mn³⁺ to a Mn⁴⁺ oxidation state. This situation promotes the reaction of the oxygen close to Mn⁴⁺ with a reducing agent, like methane in our case, with contemporary regression of manganese to the Mn³⁺ state. Fresh oxygen can then chemisorb on the generated oxygen vacancies, thus restoring the original situation. [29]

The TPR profile for LSCuM (**Figure 3** on the right) is characterized, similarly for the one referred to L8S2M, by two main peaks, but it is not present the small peak at low temperatures referred to surface oxygen. Unlike L8S2M, the peak set at lower temperature (352 °C) presents an evident shoulder attributed to the Cu²⁺/Cu⁰ reduction process. This shoulder reaches its maximum at 310 °C, a temperature slightly higher than what is expected for CuO on alumina, meaning the presence of a stabilizing effect of the perovskite structure on Cu²⁺ cations. [30] Concerning the two steps for the Mn cations reduction, it is possible to observe a significant lowering of the processes temperatures. This could be considered in agreement with the theory explained in the previous Paragraph 4.2, underlying how an higher amount of Sr doping, corresponds to an easier reducibility of the Mn cations present in the structure. However, the reductive temperatures do not correspond to those detected for LSM, even if the Sr doping is the same. This indicates that the Mn-O bond reducibility is increased as a consequence of Cu doping in the B-site. It has been observed in different perovskites that copper, under reducing conditions, migrates toward the surface forming metal nanoparticles capable of activating hydrogen and enhancing the reducibility of the other cations.

Peak attribution	LSM	L8S2M	LSCuM
Mn ⁴⁺ /Mn ³⁺	430 °C	475 °C	352 °C
Mn ³⁺ /Mn ²⁺	700 °C	770 °C	661 °C
Cu ²⁺ /Cu ⁰	/	/	310 °C

Table 2: Reduction temperatures for the reducing processes detected by H₂-TPRs for LSM, L8S2M and LSCuM. A quantitative analysis for the two H₂-TPRs was also carried out. In the following **Table 3** the experimental and theoretical values of hydrogen consumption for the two studied compounds are shown.

Hydrogen consumption	L8S2M		LSCuM	
	Experimental	Theoretical	Experimental	Theoretical
Mn ⁴⁺ /Mn ²⁺	0.0016 mol	0.0043 mol	0.0019 mol	0.0040 mol
Cu ²⁺ /Cu ⁰	/	/	0.0004 mol	0.0004 mol

Table 3: Quantitative analysis of H₂-TPR for L8S2M and LSCuM with a comparison with theoretical consumption.

The theoretical consumption calculated for the manganese reduction from the Mn⁴⁺ state to the Mn²⁺ is significantly higher compared to the experimental one. This is verified both for LSCuM and L8S2M. The theoretical value is calculated by considering that all the Mn in the perovskite structure is reduced, while the experimental results are given by the peaks area

obtained through the fitting of the TPR profiles. The lower value of experimental hydrogen consumption compared to the theoretical one can be explained by the stabilizing effect of the perovskitic structure on manganese. This consideration is not only supported by literature data [31], but also from the XRD shown in **Figure 2**. Indeed, the red diffractograms show that the perovskitic crystal structure is not completely disrupted in lanthanum and manganese oxides because of the reduction. On the contrary, a well-distinct signal is given by the Ruddlesden-Popper structure. From a simple calculation is possible to determine that almost one third of the manganese for L8S2M and a half for LSCuM is reduced and it is not anymore present in the perovskite.

The LSCuM H₂-TPR profile shows the signal for the reduction of copper from Cu²⁺ state to Cu⁰. In this case, there is correspondence between experimental and the theoretical values, meaning that all the copper in the structure is reduced and therefore exsolved to the surface. The presence of the copper nanoparticles on the surface is confirmed, as already discussed in the previous Paragraph 4.2, from XRD carried out after reducing treatments and significantly contribute to increase the reducibility of the catalyst.

4.4 Methane oxidation catalytic tests

Each sample has been tested for CH₄ oxidation both with a stoichiometric ratio between methane and oxygen of 1:2, and under-stoichiometric conditions (ratio of 2:1 between methane and air) (**Figure 4**). The main purpose of this test in non-stoichiometric condition is to better understand the mechanism of methane oxidation.

The methane oxidation catalytic activity tests are carried out at atmospheric pressure in a quartz reactor (6 mm ID) equipped with a packed bed of powders. The temperature was increased until 900 °C with a temperature ramp of 2 °C · min⁻¹, monitored by a thermocouple right upstream of the bed. Flows are dosed by a Vögtlin Red-y system. Total flow of 100 ml · min⁻¹ is kept constant, balancing it with He. The composition of the gas mixture (before and after reaction) is measured by GC (Agilent 7890A), with a TCD detector and 13X (60/80 mesh, 1.8 m) and Porapak Q (1.8 m) columns.

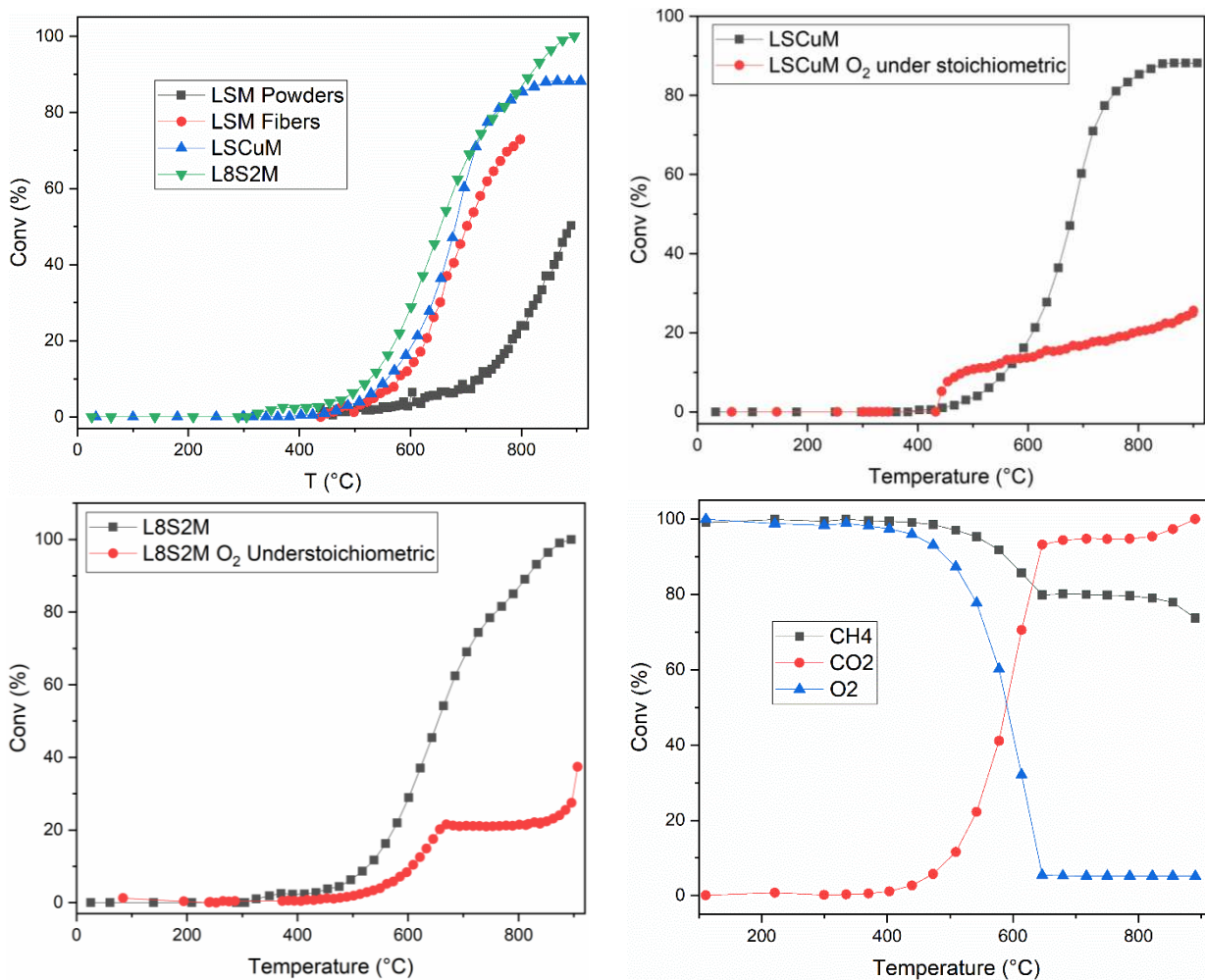


Figure 4: CH₄ oxidation reactivity for sample LSM powders, LSM fibers, LSCuM and L8S2M. Up left: comparison between the different compounds. Up right: comparison between stoichiometric mixture (black line) and under-stoichiometric in oxygen (red line) for LSCuM. Bottom left: comparison between stoichiometric mixture (black line) and under-stoichiometric in oxygen (red line) for L8S2M. Bottom right: CH₄, CO₂ and O₂ conversion for L8S2M in under-stoichiometric conditions.

The light-off temperature for CH₄ oxidation is in accordance with the typical values for oxides catalysts, approximately about 500 °C [32], [33], and is slightly lower for L8S2M; this is the best sample being able to approach full conversion of CH₄ below 900 °C. Both LSCuM and L8S2M behave very similarly, despite the different doping and the differences highlighted by the chemical characterization. These preliminary results suggests that the catalyst characterized by higher activity, despite also the slightly lower specific surface area (see Paragraph 3.5), is L8S2M. For comparison also the catalytic tests carried out for LSM in both the studied morphologies (powders and nanofibers) are shown. The performances obtained from L8S2M and LSCuM are almost equivalent to the LSM fibers, and widely better if compared with the LSM powders. Indeed, the methane conversion for L8S2M and LSCuM starts approximately 100 °C before the one for LSM (600 °C). In addition, the

reached conversion at 900 °C is much lower for LSM ($\approx 50\%$) if compared with those obtained for LSCuM ($\approx 90\%$) and for L8S2M ($\approx 100\%$).

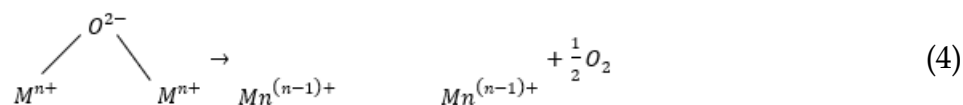
The kinetic models presented for methane combustion in the literature are mainly categorized into four types: Langmuir–Hinshelwood (LH) models, Eley-Rideal (ER) models, Mars-van Krevelen (MvK) models, and a two-term model (TT). [34] The details of each model are summarized in the **Table 4** below.

Model	Assumption	Reaction mechanism	Rate determining step
LH1	Surface reaction between dissociative adsorption of oxygen and adsorption of methane	$\frac{1}{2}O_2 + X \xrightleftharpoons{K_1} O - X$ $CH_4 + X \xrightleftharpoons{K_2} CH_4 - X$ $CH_4 - X + O - X \xrightleftharpoons{K_3} \text{product} - x + x$ $\text{product} - X \xrightleftharpoons{K_4} \text{product} + x$	$\frac{1}{2}O_2 + X \leftrightarrow O - X$ $CH_4 + X \leftrightarrow CH_4 - X$ $CH_4 - X + O - X \leftrightarrow \text{product} - x + x$
LH2	Surface reaction between molecular adsorption of oxygen and adsorption of methane	$O_2 + X \xrightleftharpoons{K_1} O_2 - X$ $CH_4 + X \xrightleftharpoons{K_2} CH_4 - X$ $CH_4 - X + O - X \xrightleftharpoons{K_3} \text{product} - x + x$ $\text{product} - X \xrightleftharpoons{K_4} \text{product} + x$	$O_2 + X \leftrightarrow O_2 - X$ $CH_4 + X \leftrightarrow CH_4 - X$ $CH_4 - X + O - X \leftrightarrow \text{product} - x + x$
ER	Surface reaction between dissociative adsorption of oxygen and gaseous methane	$\frac{1}{2}O_2 + X \xrightleftharpoons{K_1} O_2 - X$ $CH_4 + O - X \xrightleftharpoons{K_2} \text{product} - x + x$ $\text{product} - X \xrightleftharpoons{K_3} \text{product} + x$	$CH_4 + O - X \leftrightarrow \text{product} - x + x$
MvK	The reaction takes place through alternative oxidation and reduction of the catalyst surface	$\frac{[O]_{\text{lattice}} + CH_4 \xrightleftharpoons{k_{\text{red}}} [\text{intermediate}]}{(2\gamma-1)[O]_{\text{lattice}} \rightarrow \text{product} + 2\gamma[VS]_{\text{lattice}}}$ $[VS]_{\text{lattice}} + O_2 \xrightarrow{k_{\text{ox}}} [O_2] \xrightarrow{[VS]_{\text{lattice}}} 2[O]_{\text{lattice}}$	/
TT	The oxidation on catalyst surface by two roots: via the lattice oxygen and via the adsorption oxygen	$[O]_{\text{lattice}} + CH_4 \rightarrow k_1 \text{product} + [VS]_{\text{lattice}}$ $[O - X] + CH_4 \rightarrow k_1 \text{product} + x$	/

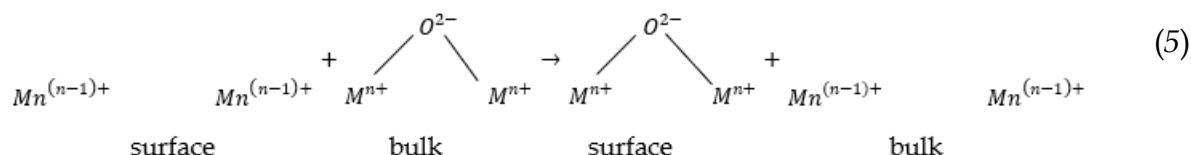
Table 4: Typical kinetic models reported in the literature concerning methane combustion for metal oxide catalysts. [35]

It must however be noted that two possible mechanisms, respectively suprafacial and intrafacial, were proposed since long time by Voorhoeve et al. [36] and are now still widely accepted for oxidation reactions over metal oxides catalysts, especially when considering the reactions over perovskite oxides. The former mechanism involves oxygen coming from the gaseous phase or located at the surface oxygen vacancies of the catalysts (α -oxygen) and it is believed to proceed at relatively low temperature. The latter is effective at higher temperature and involves a MvK redox cycle. In this case, bulk oxygen (intrafacial oxygen or β -oxygen, desorbed at high temperature) migrates towards the surface, becoming available for the oxidation of the adsorbed substrate and it is quickly replaced by oxygen

coming from the gaseous phase. This process can be expressed as equations (4) and (5). The desorption of β -oxygen requires the formation of oxygen desorption site:



This step is followed by the diffusion of oxygen ion from the bulk to the desorption site at the surface of the structure.



An interesting accordance between the model proposed by *Voorhoeve* and the experimental results were highlighted by the tests carried out in the oxygen under-stoichiometric mixture. Considering the test carried out for L8S2M (bottom left of **Figure 4**), it is possible to observe as the methane is initially converted in CO₂ using the oxygen present in the test chamber. This is also confirmed by the O₂ complete consumption around 650 °C (bottom right of **Figure 4**). At this temperature, the methane conversion is stopped and restarts only at higher temperature. Around 900 °C, even if no more oxygen is present in the chamber, the CH₄ combustion restarts and the only source of oxygen is the bulk oxygen. Therefore, it is possible to consider this test as an experimental confirmation of the suprafacial and intrafacial mode. At lower temperature the main contribution is given by the oxygen adsorbed on the surface from the reaction atmospheres, while at higher temperatures there is enough energy for the mobility process of oxygen ions towards the surface. In other words, at lower temperatures the suprafacial process is the only process that is possible, while at higher temperatures the contribution from the intrafacial mechanism becomes consistent. This evident transition between the two mechanisms is not so evident for LSCuM. Indeed, the methane conversion never stops completely, on the contrary continues slowly till the maximum conversion of $\approx 30\%$ at 900 °C. A possible explanation for that can be given considering the H₂-TPRs shown in the previous [Paragraph 4.3 Figure 3](#). Indeed, it is possible to observe a slightly higher reducibility for LSCuM, that can correspond to an easier mobility of oxygen ions towards the surface.

4.5 Morphological characterization

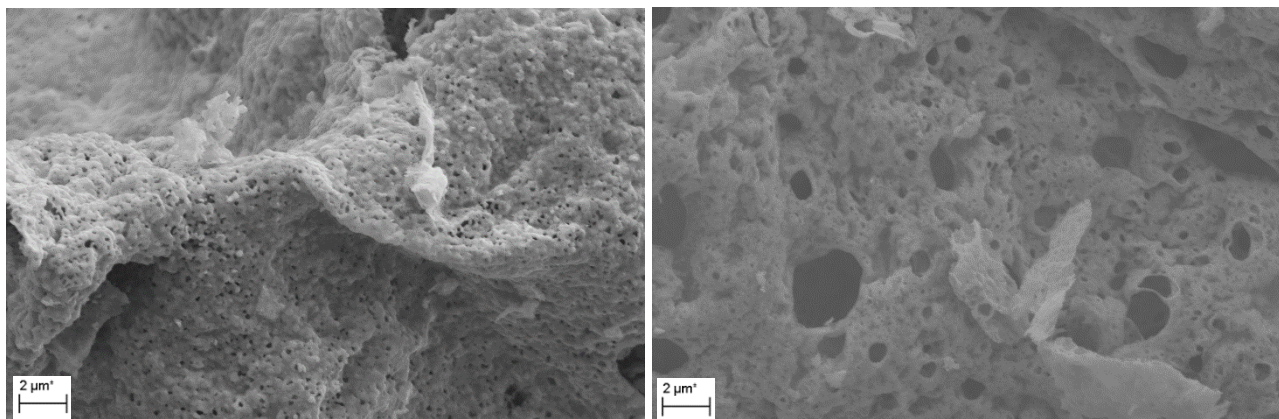


Figure 5: SEM images for L8S2M (on the left) and LSCuM (on the right) powders.

An electrode material must present many different properties. In fact, not only the fundamental electronic and ionic conductivity or the catalytic activity are required. To have the best electrode material for fuel cells, other parameters are required. As an example, the morphology is an aspect that must be considered to increase the performances. If the electrode is characterized by high surface area, the active sites are present in higher amount and, consequently, the material can convert more gas, enhancing the efficiency of the device. To check the morphology properties of the material, SEM was used to observe the porosity of the materials, while N_2 -adsorption/desorption isotherm was carried out to calculate the surface area through BET theory.

From the two images in **Figure 5**, it is possible to observe as the two materials presents significant differences regarding the porosity, where the porosity for LSCuM appears much larger compared to L8S2M one. On the contrary, the flakes-like morphology seems substantially the same for the two compounds. Unfortunately, these images do not give many other information and N_2 -adsorption/desorption is fundamental for a deeper study.

For this reason, N_2 -adsorption/desorption isotherm was carried out on L8S2M and LSCuM powders with an ASAP 2020 Plus. A BET analysis was performed on these data to obtain the surface area value. Usually, perovskites and brownmillerites synthetized by citrate route do not have high specific surface area, especially if the calcination temperature is above 800 °C. Typical values of specific surface area for $LaSr_{0.2}MnO_3$ in literature is $36.4 \text{ m}^2 \cdot \text{g}^{-1}$ with a calcination temperature of 600 °C. If this temperature is carried out at 850 °C, the surface

area decreases to $8.2 \text{ m}^2\cdot\text{g}^{-1}$.^[37] However, it is possible to reach higher surface areas changing the pH of the solution or varying the amount of citric acid.^{[38], [39]}

The BET equation (6) uses the information from the isotherm to determine the surface area of the sample, where X is the weight of nitrogen adsorbed at a given relative pressure (P/P_0), X_m is monolayer capacity, which is the volume of gas adsorbed at standard temperature and pressure (STP), and C is constant. STP is defined as 273 K and 1 atm.

$$\frac{1}{X\left[\left(\frac{P_0}{P}\right)-1\right]} = \frac{1}{X_m C} + \frac{C-1}{X_m C} \left(\frac{P}{P_0}\right) \quad (6)$$

The BET analysis gave surface areas in accordance with these values: $5.51 \text{ m}^2\cdot\text{g}^{-1}$ for L8S2M and $5.92 \text{ m}^2\cdot\text{g}^{-1}$ for LSCuM.

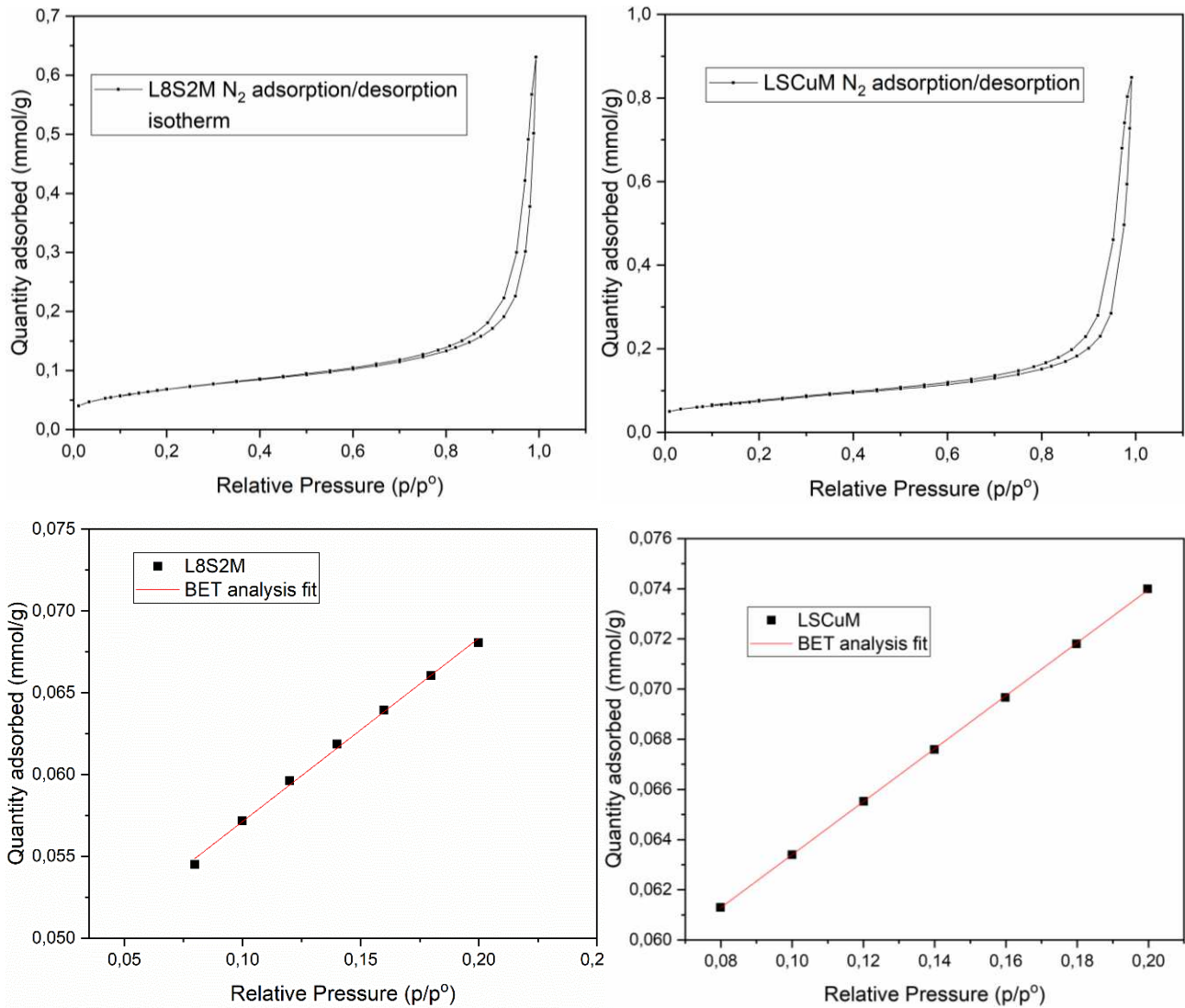


Figure 6: N_2 adsorption-desorption isotherm plot and BET fittings for L8S2M and LSCuM.

The two isotherms are almost identical: this is easily justified by considering that the morphology and the specific surface area are strongly influenced by the synthesis, which is the same for these two samples. On the contrary, neither the different Sr doping in the A-site, nor the Cu doping in the B-site are responsible of any modification. The two plots show a hysteresis cycle between adsorption and desorption processes. Therefore, at the same partial pressure, during the desorption more nitrogen is desorbed than the quantity of gas adsorbed in the adsorption process. The hysteresis is a signal of a mesoporous material, but the small region between adsorption and desorption curves indicates that there is a little dispersion of the average width of the pores. [40]

To determine the pores average width, the Barrett-Joyner-Halenda (BJH) method was used. This method and density functional theory (DFT) allow estimating pore size distribution

(PSD) based on the physisorption equilibrium isotherms. The BJH theory implements two fundamental assumptions; first the shape of pore is cylindrical, and second the adsorbed amount results from both physical adsorption on the pore walls and capillary condensation in mesopores. [41] BJH, thus, considers the radius of pore as the sum of the multilayer thickness (t) and the meniscus radius obtained from the Kelvin equation:

$$\ln \frac{P}{P_0} = \frac{2\gamma V_M}{rRT} \quad (7)$$

where P/P_0 is the relative pressure in equilibrium with a meniscus; γ is the surface tension of the adsorbate in the liquid form; V_M is the molar volume of the liquid; R is the universal gas constant; r is the radius of the meniscus formed in the mesopore; and T is temperature. BJH calculates the change in the thickness of adsorbed film from the decrease of relative pressure in the desorption branch. Each decrement is considered to result from evacuation of the largest pores from the capillary condensate, as well as a reduction in thickness of the physically adsorbed layer. This theory yields a particular equation correlating pore volume and radius, which is solved by numerical iteration. [42]

The determined pore volumes from BJH are in accordance with the meso-porosity suggested by the N_2 -adsorption/desorption hysteresis cycles. Indeed, the value for L8S2M is $w_{av} = 19,4 \pm 0.01$ nm, while for LSCuM is $w_{av} = 23,2 \pm 0.01$ nm. These results are in accordance with what observed by the SEM images.

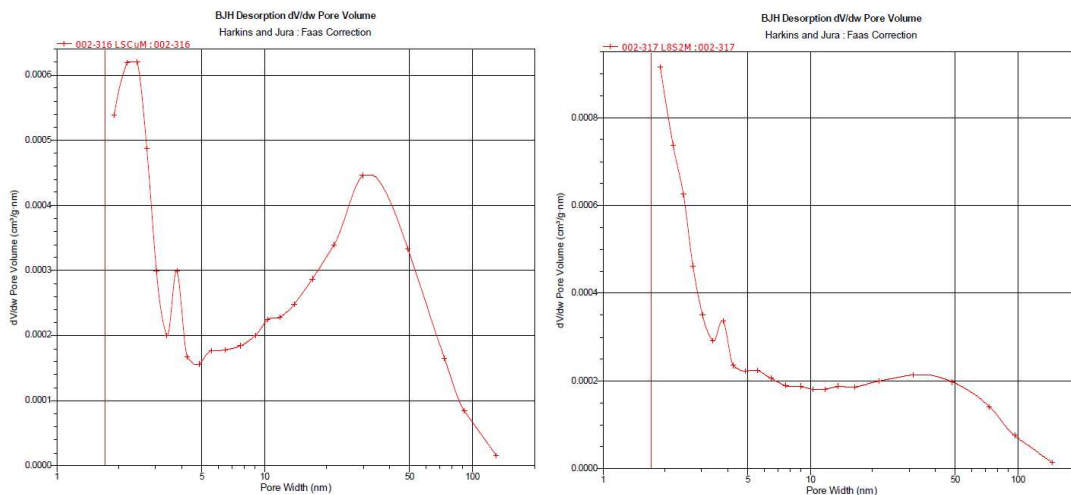


Figure 7: BJH Desorption dV/dw Pore Volume for L8S2M on the left and LSCuM on the right.

4.6 EDX – XPS

The bulk and the surface compositions of the two considered compounds were investigated through EDX and XPS respectively. Starting from this second technique, the obtained spectra are presented below.

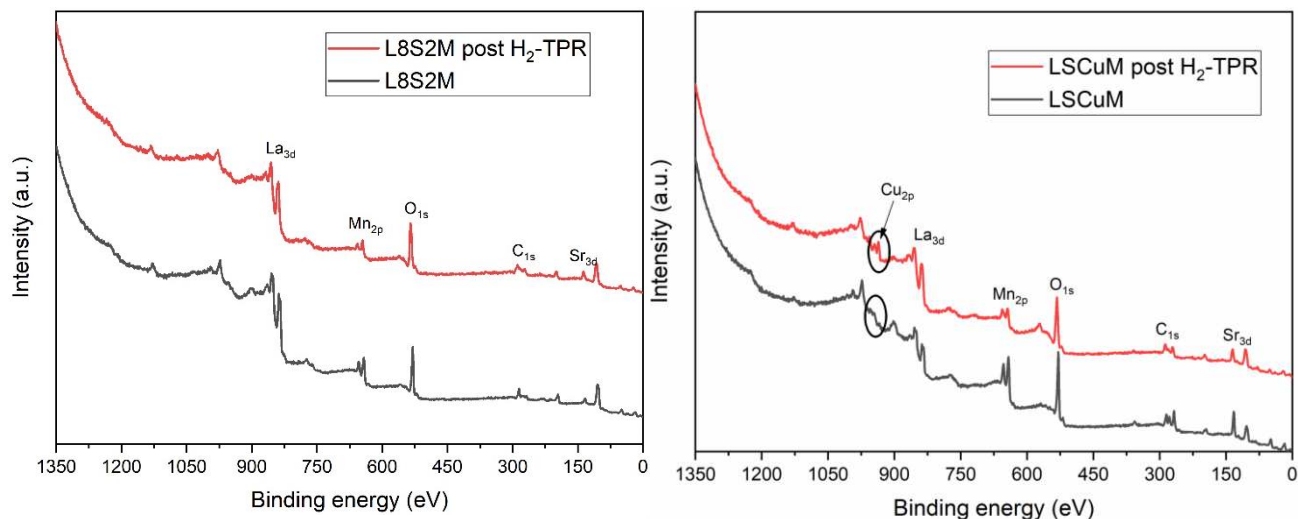


Figure 8: XPS spectra for L8S2M on the left and LSCuM on the right. In black the spectra carried out on the as synthesized material and in red the spectra carried out after H₂-TPR.

Focusing the discussion on the spectra carried out on the two as synthesized materials it is possible to observe the correspondence of the signals between them. Moreover, the XPS spectra highlight the same peaks obtained by the spectrum for LSM, that are listed in the following **Table 5**.

	L8S2M	XPS		EDX	LSCuM	XPS		EDX
	Nominal	Exp. L8S2M	Exp. Post H ₂ -TPR	Exp. L8S2M	Nominal	Exp. LSCuM	Exp. Post H ₂ -TPR	Exp. LSCuM
La 3d	16.0	17.4	9.2	12.9	12.0	10.0	8.3	11.5
Sr 3d	4.0	2.5	5.5	3.5	8.0	7.9	5.5	7.9
Mn 2p	20.0	15.6	10.7	18.9	18.0	20.7	18.1	16.4
Cu 2p	0.0	0.0	0.0	0.0	2.0	0.5	3.0	2.5
O 1s	60.0	64.6	74.6	64.8	60.0	60.9	65.1	61.7
La/Sr	4.0	7.0	1.7	3.7	1.5	1.3	1.5	1.4
La/Mn	0.8	1.1	0.9	0.7	0.7	0.5	0.5	0.7
Mn/Sr	5.0	6.3	2.0	5.4	2.3	2.6	3.3	2.1
Mn/Cu	n.a.	n.a.	n.a.	n.a.	9.0	41.4	6.0	6.6

Table 5: XPS and EDX quantitative analyses for L8S2M and LSCuM. The ratio between the different cations were calculated as well. XPS analysis was performed also for the powders subjected to H₂-TPR analysis.

The quantitative analysis for the as synthesized materials does not show big deviances between the nominal and the experimental values. Therefore, the Sr segregation on the surface of the compounds seems to be avoided. A consistent segregation of Sr on the surface

would be detrimental for the catalytic activity and the electronic conductivity of the compounds, due to the formation of SrO, an insulating and inert phase. [43]

Must be mentioned the very low detection of copper in LSCuM. A possible explanation of this incongruity between theoretical and experimental values can be justified by the small quantity of copper inserted during the synthesis; that becomes even more smaller considering that, statistically, only a very restrict part of it find place on the surface. Anyway, the presence of copper on LSCuM was confirmed by EDX, that having a larger sampling depth, it allows to analyze the bulk region of the powders. Comparing the two techniques, the results are mostly in accordance, indeed as for the XPS quantitative analyses, also for EDX not big discrepancies were highlighted between theoretical and experimental values.

It is interesting to observe the results given by the XPS analyses performed on LSCuM after the exposition to hydrogen during the H₂-TPR. In fact, in addition to the peaks referred to La, Sr, Mn, O and C (given by the formation of carbonates due to the interactions of the compounds with the CO₂ in the air), it is possible to easily recognize the peak given by Cu_{2p} orbital. Its signal is given by a doublet set at 934 and 936 eV. Due to the low quantity of Cu present in the compound, its intensity is not so high, but anyway it is quite evident. This is even more true, comparing it with the XPS spectrum carried out on the as synthesized material. The signal intensity is not the only difference regarding the copper peak between the two spectra. Indeed, looking at the XPS spectrum carried out on LSCuM before H₂-TPR, it is possible to recognize a peak set at 934 eV; a typical value for CuO. Differently for the reduced sample, it is evident a doublet set at 934 and 936 eV, which peaks could be referred to CuO and Cu₂O. The presence of Cu(I) is confirmed by the Auger peak set at 915 eV.

Anyway, the higher presence of copper after the reducing treatment carried out by the H₂-TPR, could be seen as first evidence of the possible exsolution of Cu cations to the surface. If this will be confirmed, it can be expected that the electronic conductive properties of this material could be very enhanced compared to LSM and L8S2M. A much-detailed explanation of this phenomenon will be given in the following Paragraph 6.5.2, when second evidence of this exsolution will be shown through the *in situ* Raman spectroscopy.

Passing to the quantitative analyses of the samples after H₂-TPR, it is observable an evident Sr segregation on the surface for L8S2M. Indeed, the value obtained for the ratio between La and Sr is equal to 1.7 against an expected value of 4.0, suggesting a higher presence of Sr on the surface. On the contrary, there is no discrepancy between theory and experimental values for LSCuM. These results are in accordance with literature. In fact, it is confirmed by literature that a Sr segregation should be expected when LSM type perovskite are exposed to oxygen poor atmosphere. [44] Furthermore, the Sr segregation is much more favored for samples containing low percentages of Sr in their stoichiometry as discussed by *Yu et al.* [44]

4.7 Symmetrical cell characterization

In this and in the following paragraphs the performances of L8S2M and LSCuM as electrodes for symmetrical methane fueled SOFCs will be inspected. In this section, the results obtained in a single chamber setup, will be discussed.

The electrodes are composite materials, since L8S2M and LSCuM are both mixed with GDC, that is also the electrolyte material for these tests, to assure a good adhesion. Since, these materials will be used in symmetrical cells, the tests were carried out in air and in pure methane. Both the tests were carried out in wet conditions (3% of H₂O) and with a total flux of 100 sccm. To investigate the electrocatalytic performances of the two electrodes the tests have been carried out at the following temperatures: 665, 715, 765, 815 and 865 °C.

4.7.1 L8S2M EIS in air

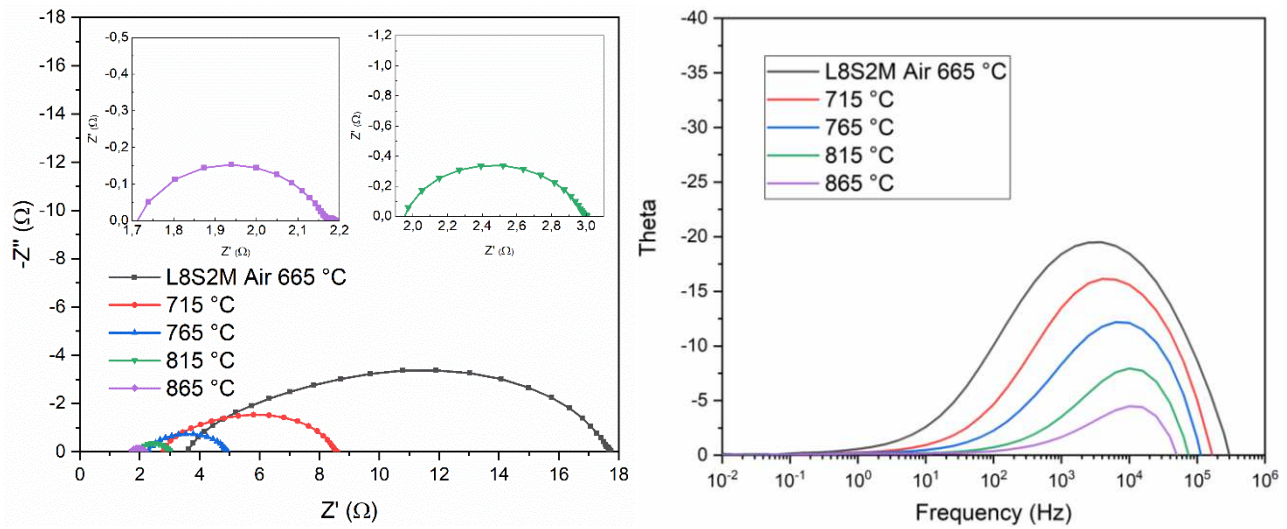


Figure 9: On the left it is shown the Nyquist plot for L8S2M/GDC composite electrode in wet air in the intermediate temperature range between 665 and 865 °C. On the right: the correspondent Bode plot.

In the graph on the left of **Figure 9**, the impedance spectra obtained for L8S2M:GDC (50:50)/GDC/L8S2M:GDC (50:50) are presented. All the spectra were fitted with a model circuit. This kind of analyses is necessary not only to obtain a proper estimation of the total polarization resistance (R_p) of the electrode, but also to understand which physical phenomena are involved and their contributions to the total resistance. The used model circuit differs on dependance by the temperature. In fact, in the temperature range between 665 and 765 °C the model circuit consists in a resistance in series with two RQs (R_s -RQ-RQ). These two processes are indicated in **Table 6** as High Frequency (HF) and Low Frequency (LF) process, depending by their stimulating frequency. Whereas, when the temperature reaches the 815 °C, the LF process disappears and becomes evident at low frequencies the process referred to the gas diffusion resistance. This physical phenomenon is represented with a Final Length Warburg (FLW) element. [45] Therefore, the resultant best model circuit is R_s -RQ-FLW. Since the gas diffusion on the electrode is not drastically dependent on temperature, its resistance is almost the same in the two temperatures where it is observable. On the contrary the two RQ elements correspond to thermo-activated processes: in fact, their resistances and capacitances decrease when the temperature increases. The process at high frequencies, as shown in the Bode plot (top right graph of **Figure 9**), does not present a fixed frequency, but there is a shift of the stimulating frequency towards higher values, from 10^3 to 10^4 Hz. This shifting on the frequencies can be referred to an increasing of the processes rate given by the higher temperatures. The calculated

values of the capacitance associated with the two processes are about 10^{-5} and 10^{-4} F, consistent with the electrochemical reaction mechanisms that occur on electrode. [46], [47]

	665 °C	715 °C	765 °C	815 °C	865 °C
	Capacitance (F)				
HF process (10^3 - 10^4 Hz)	$6.0 \cdot 10^{-5}$	$9.0 \cdot 10^{-5}$	$1.4 \cdot 10^{-4}$	$2.0 \cdot 10^{-4}$	$3.7 \cdot 10^{-4}$
LF process (10^{-2} Hz)	$4.6 \cdot 10^{-4}$	$4.0 \cdot 10^{-4}$	$6.4 \cdot 10^{-4}$		

Table 6: Process capacitances for L8S2M:GDC composite electrode in wet air conditions.

Most probably the electrochemical process (HF) is the oxygen adsorption and dissociation on the active region of the electrode. [48] The second RQ element at lower frequencies (LF) becomes evident at $T \leq 765$ °C and is referred to oxygen reduction process. [49] In order to understand which is the Rate Determining Step (RDS) of the process, it is fundamental to verify the presence or the absence of a Warburg element after the first resistance of the model circuit. If the RDS is given by the diffusion of O^{2-} ions through the electrode, a straight line with a 45° slope, easily attributable to a Warburg element, should characterize the Nyquist plot. This is not observed in the obtained spectra. In this case, it is possible to conclude that the RDS of the process is the adsorption and dissociation of O_2 at the gas/film interface. If O_2 exchange at the gas-exposed surface is rate limiting step, the relatively fast transport of oxygen ions in the electrode will cause the electrode to act as a uniformly concentrated and electrically neutral reservoir for oxygen vacancies and associated electrons/holes. [50]

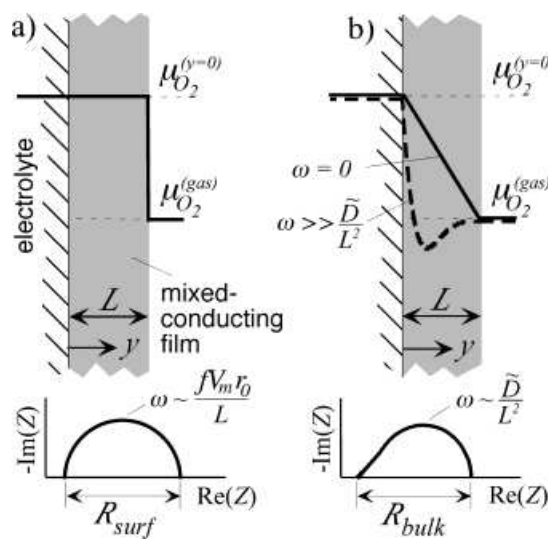


Figure 10: Models illustrating the RDS for thin film mixed conducting electrodes. a) Oxygen adsorption and dissociation; b) O^{2-} ions transport.

The total Area Specific Resistance (ASR) has been calculated for each temperature giving the following results. As already explained before, the ASR reduces with the increment of temperature, suggesting the presence of one, or more, temperature dependent process.

Temperature (°C)	665	715	765	815	865
ASR(Ωcm^2)	8.04	3.28	1.49	0.59	0.25

Table 7: ASR values for L8S2M/GDC composite electrode obtained using a single chamber setup in wet air conditions.

4.7.2 LSCuM EIS in air

In this paragraph, the results obtained using a symmetrical cell with LSCuM:GDC (50:50)/GDC/LSCuM:GDC (50:50) in a single chamber testing setup in wet (3% H₂O) air, will be discussed. The Nyquist and Bode plot are shown in **Figure 11**.

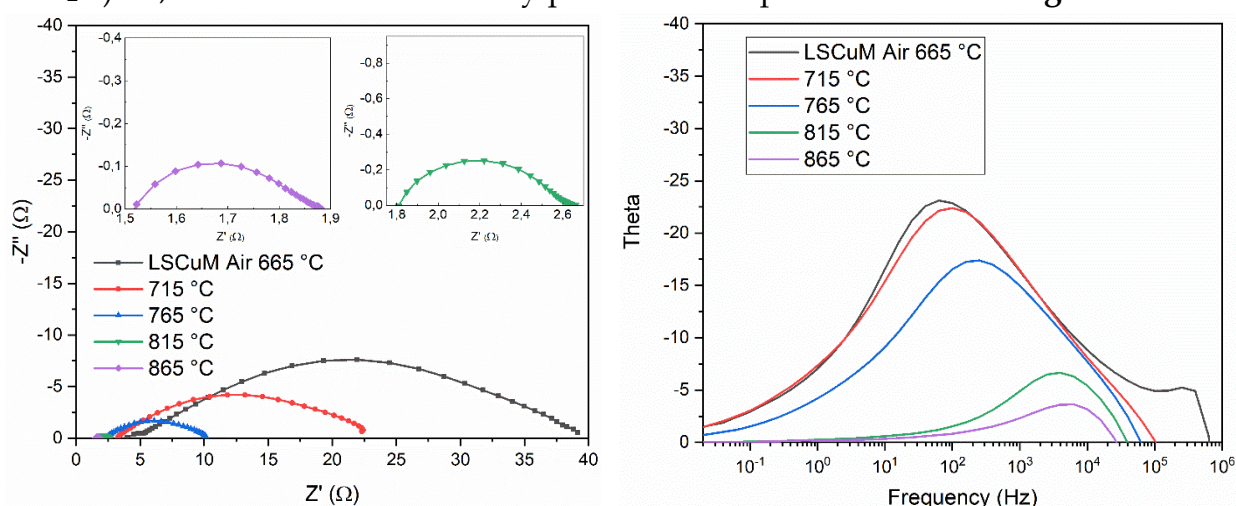


Figure 11: On the left: the Nyquist plot for LSCuM/GDC composite electrode performed in wet air. On the right: the correspondent Bode plot.

Almost all the considerations taken in account in the previous paragraph can be referred to the LSCuM:GDC (50:50) composite electrode, too. In fact, the used model circuits are the same: R_s -RQ-RQ for measurements performed below 765 °C, whereas when the temperature is increased till 815 and 865 °C the best model circuit is R_s -RQ-FLW, with the disappearance of the process at low frequencies and the simultaneous appearance of the small signal given by the gas diffusion at very low frequencies (10⁻¹ Hz).

The only significant difference between L8S2M and LSCuM can be observed from the Bode plot on **Figure 11**, where the stimulating frequencies for the process at high frequencies at low temperature (665, 715 and 765 °C) move at lower values (10² - 10³ Hz) compared to L8S2M (10³ - 10⁴ Hz). A possible explanation of this significant difference can be referred to

the presence of copper oxide nanoparticles on the surface that un-favor the oxygen reduction capability of the material. At higher temperature this difference of process frequency becomes less evident, suggesting that the limiting effect of CuO nanoparticles became lower compared to the reducing properties of the perovskitic substrate.

Regarding the process capacitances (**Table 8**), the values are quite similar to those obtained for L8S2M, so the attribution to the same electrochemical processes (the oxygen adsorption and dissociation for the HF process, oxygen reduction process for the LF process) is confirmed also in this case.

	665 °C	715 °C	765 °C	815 °C	865 °C
	Capacitance (F)				
HF process	$7.1 \cdot 10^{-4}$	$1.0 \cdot 10^{-3}$	$1.4 \cdot 10^{-3}$	$7.3 \cdot 10^{-5}$	$8.9 \cdot 10^{-5}$
LF process	$6.4 \cdot 10^{-4}$	$9.6 \cdot 10^{-4}$	$5.2 \cdot 10^{-4}$		

Table 8: Process capacitances for LSCuM:GDC composite electrode in wet air conditions.

The lower efficiency of LSCuM compared to L8S2M in air is confirmed also from the ASRs obtained and presented in the following **Table 9**.

Temperature (°C)	665	715	765	815	865
ASR(Ωcm^2)	22.66	12.48	5.88	1.46	1.05

Table 9: ASR values for LSCuM/GDC composite electrode obtained using a single chamber setup in wet air conditions.

An Arrhenius plot has been performed in order to determine the resultant activation energy of the involved processes.

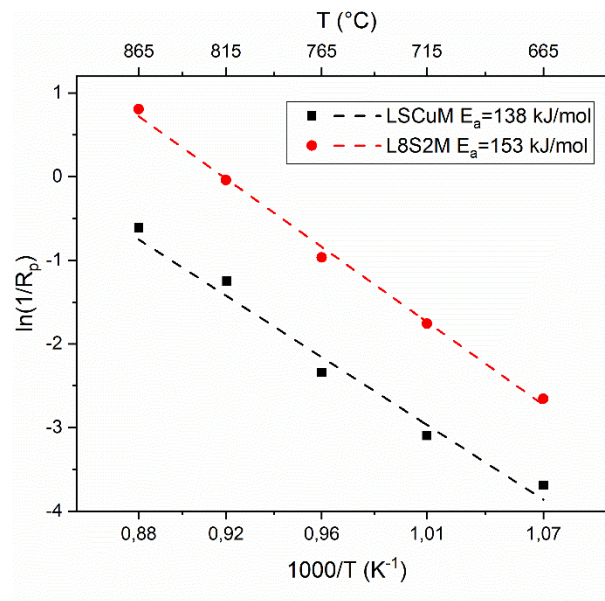


Figure 12: Arrhenius plot obtained for L8S2M -●- and for LSCuM -■- obtained in wet air atmosphere.

In **Figure 12**, the activation energies are shown. The obtained values are 138 kJ/mol and 153 kJ/mol for LSCuM and L8S2M, respectively. These values are comparable with the activation energy obtained for LSM powder electrode (153 kJ/mol, see [Paragraph 3.9](#)). This value is consistent with values for LSM/GDC composite electrode reported in literature by *Zhang et al.* [51] (146 kJ/mol). Looking forward in literature, the limiting step presenting values similar to those found in this study, is the O₂ dissociation and subsequent oxygen atom reduction. [52]-[54]. Therefore, not only the processes capacitance suggests the attribution of the signals obtained from the Nyquist plot to the electrochemical reactions, but also the activation energy obtained from the Arrhenius plot.

4.7.3 L8S2M EIS in CH₄

Since the studied materials will be used as fuel electrodes in symmetrical SOFCs, the performances in CH₄ were studied performing tests in a single chamber setup with wet methane atmosphere (3% H₂O, 97% CH₄) on symmetrical cells.

Below, it is possible to find the Nyquist and Bode plots for L8S2M:GDC (50:50) /GDC/L8S2M:GDC (50:50) symmetrical cell performed in methane.

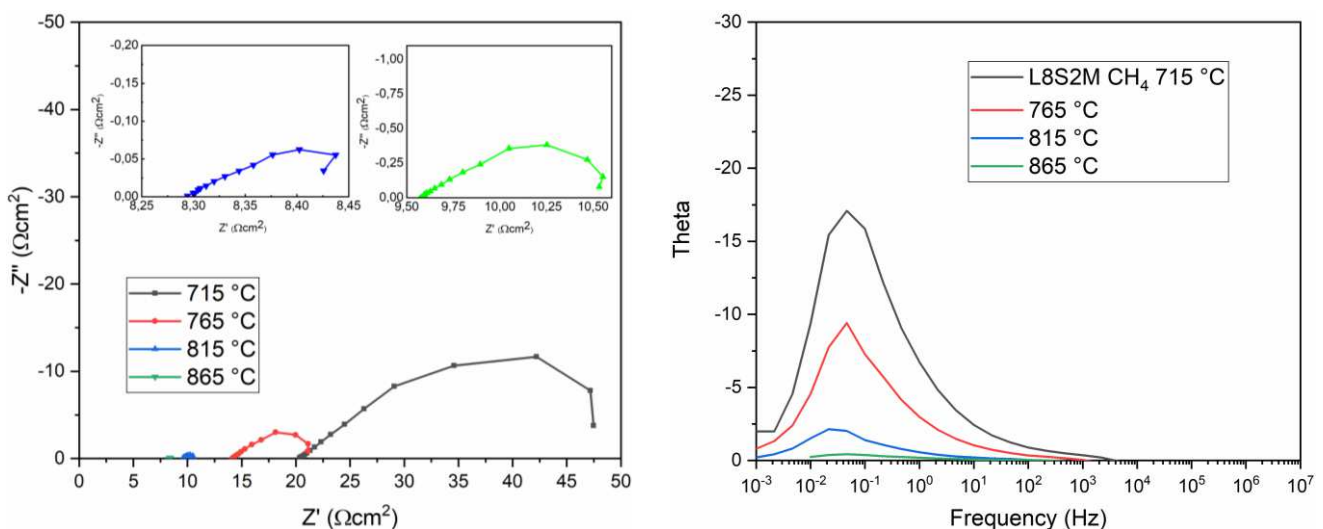


Figure 13: On the left it is shown the Nyquist plot for L8S2M/GDC composite electrode in wet CH₄ in the intermediate temperature range between 665 and 865 °C. On the right: the correspondent Bode plot.

All the Nyquist plots performed in methane for L8S2M/GDC composite electrode were fitted with the same R_s-G circuit. Indeed, similarly to what observed for the LSM, the plots show a typical Gerischer behavior, and not the typical shape of a sum of semicircles as seen in air tests. The usage of a Gerischer element to fit anodic Nyquist plot is quite spread and

consolidated in literature. [55]-[57] Modelling EIS data with a Gerischer element implies a diffusion process coupled to a 'chemical reaction'. Two can be the most interesting interpretation for this element. The first is the combination of surface diffusion with a slow ambient/surface exchange or distributed charge transfer step. Otherwise, a possible explanation could be the formation of immobile complexes that limit the mobility for one of the mobile species. This is typically observed in literature for bulk processes in mixed conducting materials. The mixed conductivity (ionic and electronic) is guaranteed by the formation of Ruddlesden-Popper phase in L8S2M, observed by XRD after exposition to methane (see [Paragraph 4.2](#)). The correlation of this process with the ionic diffusion is confirmed also by the slow stimulating frequencies (10^{-1} Hz) suggested by the Bode plot on the right graph of **Figure 13**. The absence of a frequencies shifts towards higher values with the temperature increasing, should also be noted.

On the contrary, ASR values present a significant reduction of their values with temperature, with interesting values starting from 765 °C. The good performances starting from this temperature can be related with the partial reduction of the perovskite and the formation of RP phase.

Temperature (°C)	715	765	815	865
ASR(Ωcm^2)	17.81	4.43	0.59	0.09

Table 10: ASR values for L8S2M/GDC composite electrode obtained using a single chamber setup in wet methane conditions.

As already mentioned in the previous chapter for LSM powders and nanofibers, these ASRs values are outstanding, since they are significant lower of the typical values found in literature. ($3.05 \Omega\text{cm}^2$ at 800 °C in wet methane, with the state-of-art material for methane applications that is Ni impregnated GDC [58]).

4.7.4 LSCuM EIS in CH₄

In this paragraph the results in single chamber setup for LSCuM:GDC (50:50)/GDC/LSCuM:GDC (50:50) using wet methane (3% H₂O, 97% CH₄) are presented.

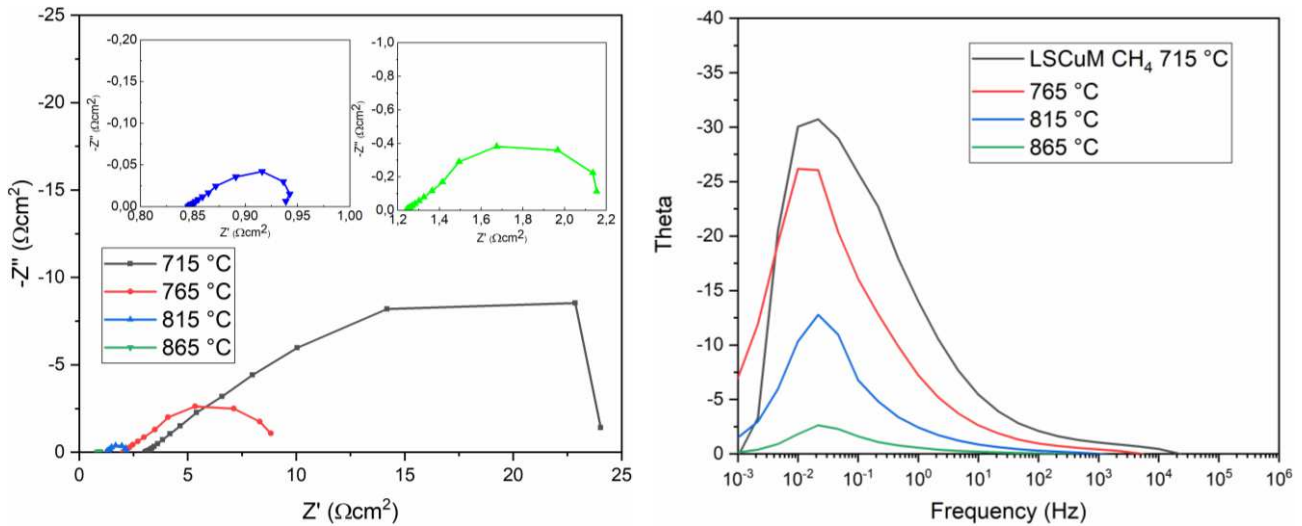


Figure 14: On the left: the Nyquist plot for LSCuM/GDC composite electrode performed in wet methane. On the right: the correspondent Bode plot.

The Nyquist plot discussion is completely analogue to that one made for L8S2M:GDC. The used model circuit is made up by the usual electrolyte resistance with a Gerischer element in series. In addition, the Bode plot does not present significant differences between the two electrode materials. The stimulating frequencies are set at 10⁻¹ Hz and does not change their values on dependence of temperature. Since, the experimental data are completely similar between the two compounds, also the physical interpretation given to the Gerischer element is the same. Therefore, the main contribution to the resistance should be referred to the ionic conduction.

Temperature (°C)	715	765	815	865
ASR(Ωcm ²)	12.05	4.06	0.56	0.06

Table 11: ASR values for LSCuM/GDC composite electrode obtained using a single chamber setup in wet methane conditions.

The determination of the ASRs confirms values remarkable lower to the state-of-art Ni-GDC. Not only that, but the obtained ASRs values are lower than those found for L8S2M and LSM, with an outstanding value of 0.06 Ωcm² at 865 °C. Anyway, even in this case the performances become significant for SOFC applications only after 765 °C. Most probably because of the transition of the crystal structure from perovskite to RP.

Considering that between L8S2M and LSM, the best solution is the first compound, with a lower amount of Sr doping; and considering that LSCuM presents the same Sr doping of LSM, two are the assessment that can be made. The first one is that the increase of the performance must be related to the presence of copper nanoparticles on the surface of the perovskite, that are naturally exsolved due to the reducing atmosphere. The second one is that should be studied the performances of a material that presents a copper doping, but with a 20% of Sr doping, as in the case for L8S2M.

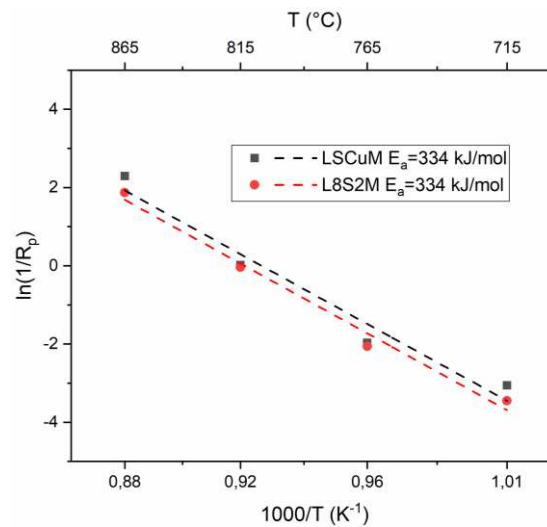


Figure 15: Arrhenius plot obtained for L8S2M -●- and for LSCuM -■- obtained in wet methane atmosphere.

The analysis of the Arrhenius plots gives an interesting result. Indeed, the activation energy for the two electrodes are the same. This confirms the consideration made from the Nyquist plot, where we assumed that the main contribution to the resistance is given by the same process, the ionic conductivity of the material. In addition, it is possible to conclude that the better performances obtained for LSCuM are not given by a higher catalytic activity given by copper, but for the higher conductivity given by the presence of the nanoparticles on the surface.

4.8 Complete cell test

In the previous paragraphs the electrochemical performances of the two considered compounds were studied separately, to better understand the behavior of the electrocatalyst under oxidizing and reducing conditions. Obtained all the information required about electrochemical performances in air and in methane, the next step is to test the complete symmetrical cell. To do that, it was necessary to change the used setup from the single chamber to the double chamber one.

This setup is made up of two concentric α -alumina tubes (DEGUSSIT AL23). The concentric position of the tubes was chosen in order to allow the double flux of the gases: in the smaller one reactant gases are fluxed and led to the cell electrode; after that, the exhaust gases are guided to the space between the two tubes and in this way out from the setup.

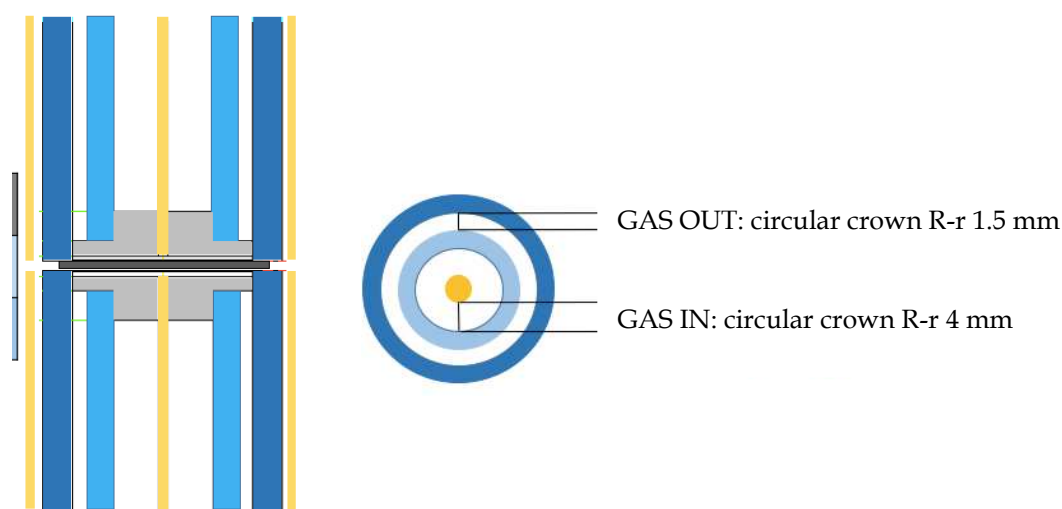


Figure 16: Double chamber setup scheme.

In these tests the electrolyte was changed passing from GDC to Yttria-Stabilized Zirconia (YSZ). This compound was chosen to understand if the studied material can be used with the commercial electrolyte. Furthermore, is preferable to not use GDC as electrolyte for high temperatures, due to its reducibility that can lead to a cell short-circuiting. Therefore, as first step the compatibility of the two materials with YSZ was studied. L8S2M and LSCuM were grinded together with YSZ powder and calcinated in air at 1200 °C for 6 hours, with a heating and cooling ramp of 3 °C/min. After that an XRD was performed looking for the appearance of new phases in the diffractogram.

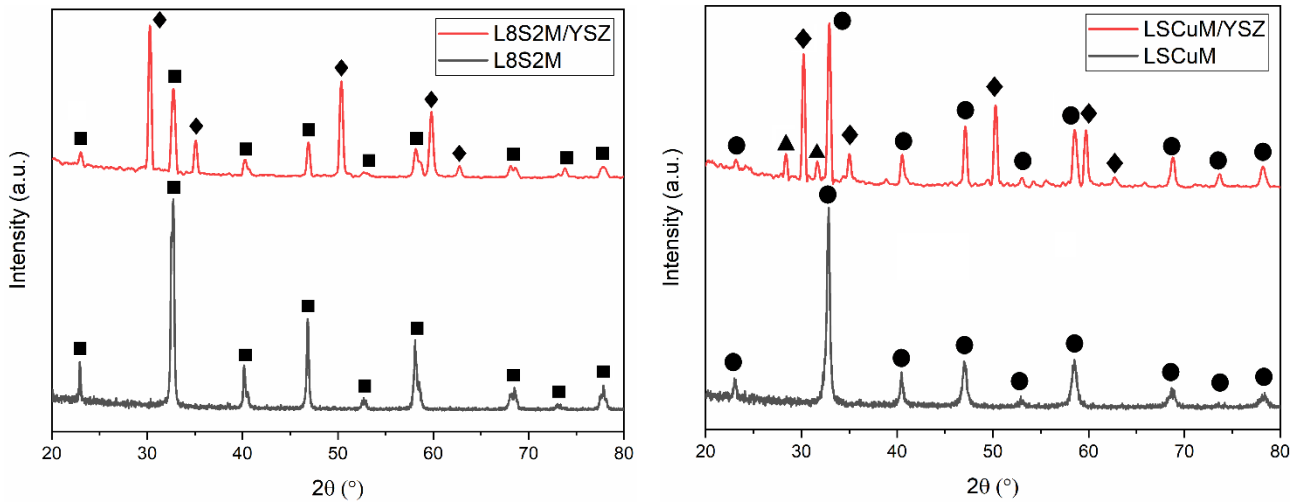


Figure 1: Compatibility test for L8S2M (on the left) and LSCuM (on the right). XRD performed after calcination at 1200 °C for 6 hours of L8S2M and LSCuM with YSZ. L8S2M ◆ YSZ LSCuM ▲ SrZrO₃. ■

As it possible to observe from the graph on the left of **Figure 17**, the diffractogram for L8S2M after calcination with YSZ does not show any new phase. The only reflexes are given by YSZ and the perovskitic compound. This is an important feature for this studied electrode, since it allows to use the commercial material as electrolyte, giving the possibility to lower remarkably the cell fabrication costs. Unfortunately, this is not true for LSCuM (right graph of **Figure 17**). Indeed, at 28° and 32° are set two peaks referred to strontium zirconate. The formation of this insulating phase for lanthanum manganite doped strontium is well known in literature. [59] To avoid this problem, a buffer layer is usually placed between the two materials. Therefore, for the electrochemical tests carried out on LSCuM:GDC, a GDC layer is placed between electrode and YSZ electrolyte. This layer is prepared by creating an ink, like those used for the electrode materials, and tape casting it directly in the YSZ electrolyte.

4.8.1 Complete cell L8S2M

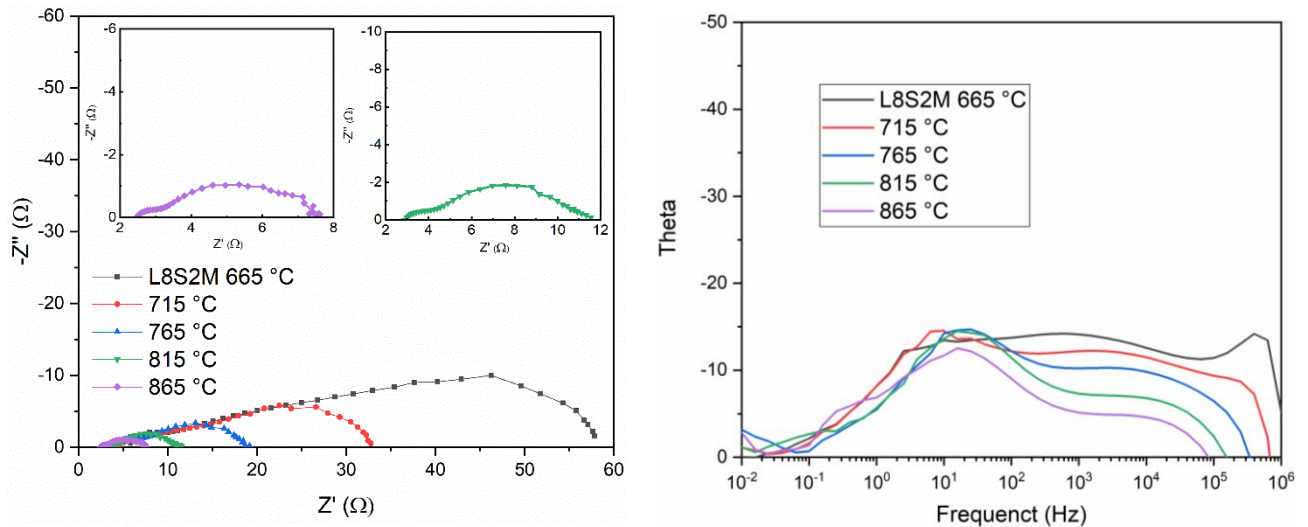


Figure 18: On the left: Nyquist plot for L8S2M/GDC symmetrical complete cell. At the anodic side the cell is fueled with wet methane, at the cathodic side with air. On the right: the correspondent Bode plot.

In **Figure 18** the Nyquist and Bode plots for L8S2M:GDC (50:50)/YSZ/ L8S2M:GDC (50:50) complete cells are shown. The complete symmetrical cell was fueled by wet methane (3% H₂O, 97% CH₄), while at the cathodic side the used oxidant is air.

The used model circuit is made up by one resistance with two RQs and a Warburg element in series (R_s-RQ₁-RQ₂-W). As for the single chamber tests, the first resistance corresponds to the electrolyte resistance. As expected, the electrolyte resistances of YSZ are higher than those obtained at the same temperature for GDC in air. In the previous paragraphs the electrolyte resistances were not mentioned, since the focus was the study of the electrode performances, and the electrolyte resistance does not influence them. On the contrary, this focus on electrolyte resistances, shown in **Table 12**, is fundamental since in the complete cell tests all the components influence the performances. The most important point to figure out is that the YSZ resistances are not only higher to those for GDC, but they are more than 10 times higher to the state-of-art YSZ thin film electrolyte resistances. ^{[60]-[62]} This discrepancy between the tested electrolytes and the commercial one is given by the thickness. As already mentioned in Paragraph 2.7, the tested cells are electrolyte supported. Furthermore, the electrolytes used for these tests are pellets made by pressing the powders with a press. To have a good reproducibility and output the used powder produces a thickness of 1.5 mm. On the other side, the commercial cells are anode supported and the electrolyte thickness is

about 5 μm .^[63] As we will see, this discrepancy will have detrimental effects on the power density output of the tested cells.

Electrolyte	Temperature ($^{\circ}\text{C}$)	665	715	765	815	865
YSZ	$R_s(\Omega)$	6.72	4.85	3.75	2.85	2.48
GDC	$R_s(\Omega)$	3.54	2.78	2.29	1.95	1.72

Table 12: Resistance values for YSZ and GDC electrolyte. For the first one the values are obtained from the complete cell tests, while the GDC resistance values are obtained by the analysis of the Nyquist plot for single chamber tests performed in air on L8S2M electrode.

Going further with the discussion of the Nyquist plots, let's consider the two RQs elements. The process capacitances have values that correspond with those typical for electrochemical processes.^[46] Furthermore, they find correspondence also with those obtained for the single chamber tests in air and in methane. The stimulating frequencies for these two processes, obtained from the Bode plot (right graph of **Figure 18**), are 10^4 and 10^3 Hz. The first process has the same stimulating frequencies of the process observed in the single chamber tests performed in air, suggesting that this process is referred to the cathode side. Consequently, even if the stimulating frequencies do not correspond with those observed in the single chamber tests performed in methane, the process at lower frequencies should be referred to the anodic side of the cell.

	665 $^{\circ}\text{C}$	715 $^{\circ}\text{C}$	765 $^{\circ}\text{C}$	815 $^{\circ}\text{C}$	865 $^{\circ}\text{C}$
	Capacitance (F)				
RQ1	$1.4 \cdot 10^{-6}$	$3.4 \cdot 10^{-5}$	$2.1 \cdot 10^{-5}$	$6.1 \cdot 10^{-4}$	$1.2 \cdot 10^{-4}$
RQ2	$5.5 \cdot 10^{-5}$	$3.0 \cdot 10^{-5}$	$2.6 \cdot 10^{-5}$	$1.7 \cdot 10^{-5}$	$1.2 \cdot 10^{-5}$

Table 13: Process capacitances for L8S2M:GDC composite electrode in complete cell tests.

There is another main difference between the Nyquist plot obtained from the complete cell tests and those obtained in the single chamber setup, and it is the presence of a Warburg element at low frequencies (10^1 Hz). The Warburg element, W , is used in the equivalent circuit to represent linear diffusion under semi-infinite conditions. This also assumes the diffusion layer to possess an infinite thickness.^[64] This element is often found in the discussion of Nyquist plot for cells fueled by methane and the typical attribution to a physical phenomenon of this element is the gas diffusion. When this element is well recognized in the Nyquist plot means that there are some problems for the gas to reach the electrode active sites.^{[65]-[67]} The contribution of this element to the total resistance of the cell is quite high. As it possible to see on Percentual contribution of the process resistance to the total one for L8S2M:GDC complete cell. **Table 15**, the resistances due to the gas diffusion are responsible

of almost half of the total electrodes resistances. Since CH_4 has a steric hindrance higher than O_2 , it is possible to assert that this gas diffusion problems are present at the anodic side of the cell. It is not clear why this problem was not so evident in the single chamber tests. A possible explanation could be found considering that in the single chamber tests, the electrode area exposed to methane is double compared to the double chamber one.

Anyway, coming back to the RQs elements it is possible to observe in **Table 14** that the resistances for the process referred to the anode side are lower compared to those for the cathode side of the cell.

Process	Temperature (°C)	665	715	765	815	865
RQ1	R (Ω)	14.6	7.6	5.7	2.5	2.2
RQ2	R (Ω)	8.9	4.5	2.7	1.3	0.4
W	R (Ω)	30.3	20.2	6.9	4.4	2.9
Rp Tot	R (Ω)	53.8	32.3	15.3	8.1	5.4
ASR	Ωcm^2	60.80	36.53	17.30	9.20	6.16

Table 14: Process and total resistances for the L8S2M:GDC complete cell tests in wet methane.

Process	Temperature (°C)	665	715	765	815	865
RQ1	% R _{Tot}	27.1	23.4	37.2	30.5	40.6
RQ2	% R _{Tot}	16.5	14.1	17.7	15.4	6.7
W	% R _{Tot}	56.4	62.5	45.1	54.1	52.7

Table 15: Percentual contribution of the process resistance to the total one for L8S2M:GDC complete cell.

4.8.2 Complete cell LSCuM

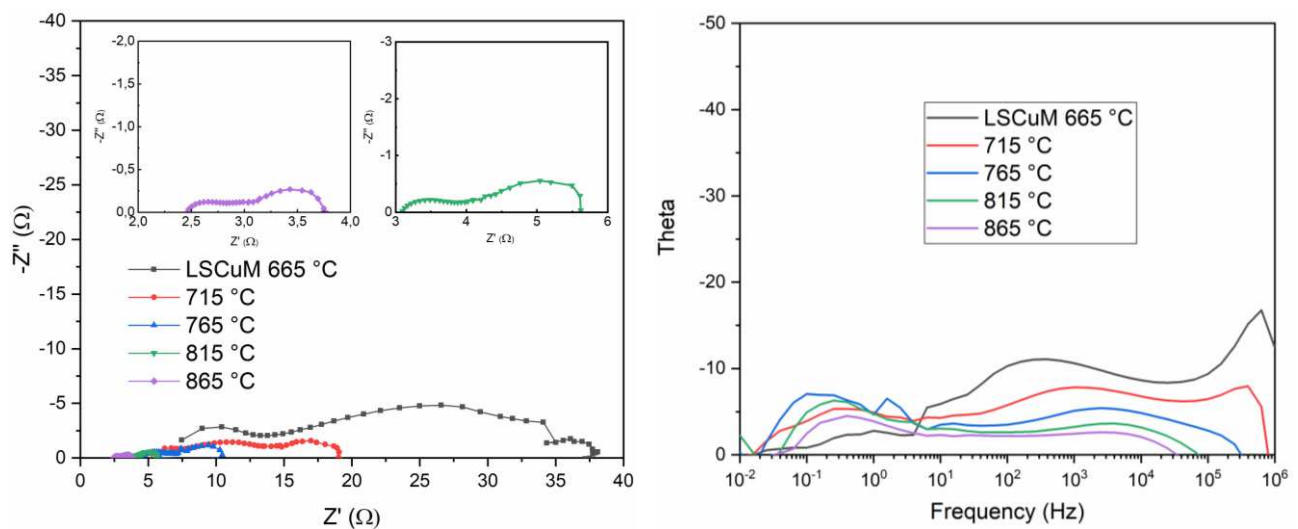


Figure 19: On the left: Nyquist plot for LSCuM/GDC symmetrical complete cell. At the anodic side the cell is fueled with wet methane, at the cathodic side with air. On the right: the correspondent Bode plot.

In this paragraph, the tests performed on LSCuM:GDC symmetrical cell with the double chamber setup are discussed. The testing conditions are the same used in the previous paragraph: wet methane at the anode side and air at the cathode.

The model circuit used to fit the experimental data in the Nyquist plot is different with respect to that used for L8S2M. Indeed, in the low frequencies range a Gerischer shaped curve trend is visible instead of a Warburg one. Anyway, at high frequencies the model circuit presents the typical electrolyte resistance and then two RQs elements in series. Therefore, the total model circuit can be represented as follows: R_s -RQ-RQ-G. The stimulating frequencies (10^3 - 10^4 Hz) and the capacitances (see **Table 16**) of the two RQ elements are consistent with the values found for the L8S2M:GDC.

This good correspondence suggests the same physical interpretation to the two elements: the first element should be referred to the electrochemical reaction occurring at the cathode, while the second semicircle is provoked by the anodic one.

	665 °C	715 °C	765 °C	815 °C	865 °C
	Capacitance (F)				
HF process	$8.2 \cdot 10^{-5}$	$7.6 \cdot 10^{-5}$	$6.8 \cdot 10^{-5}$	$1.6 \cdot 10^{-4}$	$2.7 \cdot 10^{-4}$
LF process	$2.4 \cdot 10^{-5}$	$1.6 \cdot 10^{-5}$	$7.7 \cdot 10^{-4}$	$6.3 \cdot 10^{-4}$	$1.7 \cdot 10^{-4}$

Table 16: Process capacitances for LSCuM:GDC composite electrode in complete cell tests.

The absence of the Warburg element in the Nyquist plots means that for this cell, there are not problems related to gas diffusion. Looking at the resistances in **Table 17**, it is evident that in this case the main contributions to the total resistance are given by the electrochemical reactions at the lower temperatures. At higher temperatures, the ionic conduction, expressed by the Gerischer element, becomes the most affecting to the total resistance of the electrodes.

Process	Temperature (°C)	665	715	765	815	865
RQ1	R (Ω)	11.2	1.0	0.8	0.6	0.3
RQ2	R (Ω)	11.6	9.9	3.0	0.4	0.3
RG	R (Ω)	8.8	3.5	3.0	1.6	0.7
Rp Tot	R (Ω)	31.5	14.4	6.8	2.6	1.3
ASR	Ωcm ²	35.7	16.3	7.7	3.0	1.5
RQ1	% R _{Tot}	35.3	7.1	11.5	23.7	21.4
RQ2	% R _{Tot}	36.6	68.8	44.5	16.7	21.6
W	% R _{Tot}	28.0	24.1	44.0	59.6	57.0

Table 17: Process and total resistances for the L8S2M:GDC complete cell tests in wet methane. In the last three rows are presented the percentual contribution of every element referred to the total resistance.

Finally, like for the tests performed in the single chamber setup, the contribution of copper to reduce the resistance of the anodic side and, consequently, the total resistance should be recognized. This is evident from the ASR values shown in **Table 18**. The values for LSCuM:GDC are almost two times lower between 665 and 765 °C, becoming three times lower at 815 °C and the difference becomes even higher at 865 °C.

Electrode	Temperature (°C)	665	715	765	815	865
LSCuM:GDC	ASR(Ωcm ²)	35.7	16.3	7.7	3.0	1.5
L8S2M:GDC	ASR(Ωcm ²)	60.8	36.5	17.3	9.2	6.2

Table 18: ASRs comparison between the two studied electrodes in the double chamber setup tests.

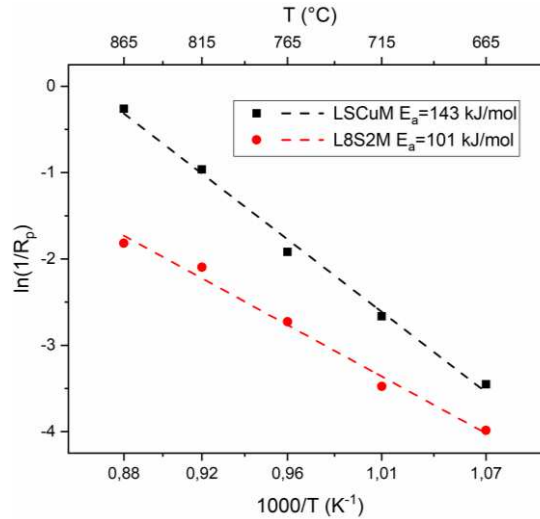


Figure 20: Arrhenius plot obtained for L8S2M -●- and for LSCuM -■- obtained for the complete cell tests.

The different behavior of the two electrodes is highlighted once more by the Arrhenius plots (**Figure 20**). In fact, the activation energy for LSCuM corresponds to the values found in air and typical for the electrochemical reactions. On the other side, for L8S2M:GDC electrode, where the gas diffusion gives a huge contribution to the total resistance, the activation

energy is significantly different and with a good correspondence with the diffusion regime as reported in literature. [68]

Finally, let's see the performances of the two symmetrical cells in terms of Open Circuit Potential (OCP) power density output.

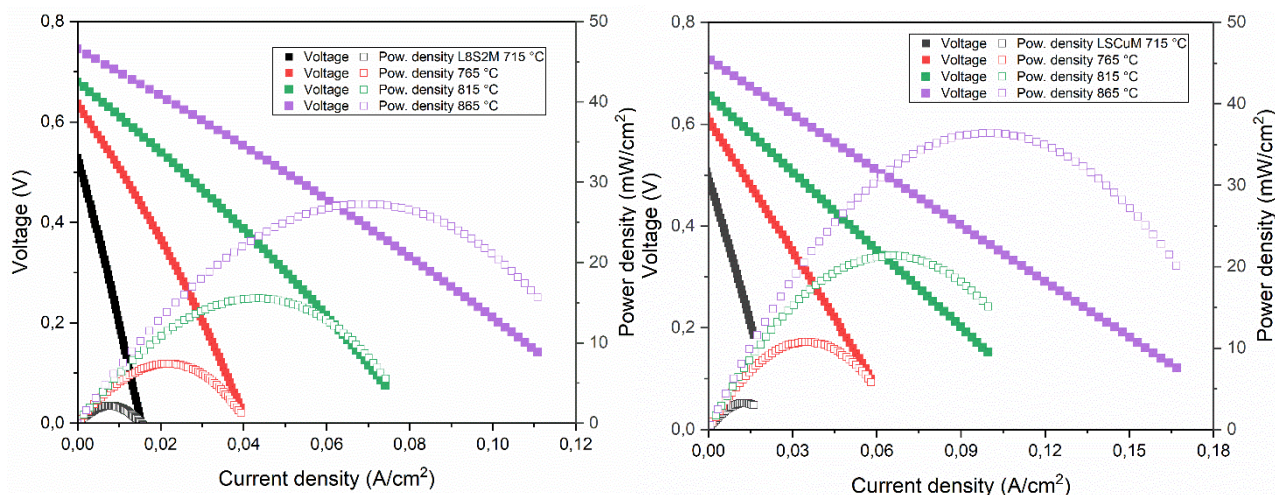


Figure 21: LSVs and power output for L8S2M:GDC electrode (on the left) and for LSCuM:GDC electrode (on the right).

Electrode	Temperature (°C)	715	765	815	865
L8S2M	Power density (mW/cm ²)	2.2	7.4	15.5	27.3
LSCuM	Power density (mW/cm ²)	3.2	10.7	21.4	36.4

Table 19: Power densities for the two studied symmetrical cells.

The open circuit potential (OCP) of the L8S2M/GDC and LSCuM/GDC composites anodes was recorded at different temperature in a testing mixture composed by 97% CH₄/3% H₂O (wet CH₄).

Taking in analysis the OCPs of the two electrodes at 765 °C, their values are quite similar and near to 0.6 V. For comparison, let's consider that the theoretical value of OCP at 750 °C is 1.2 V. [69] It is evident that the experimental values are significant lower to the theoretical ones. The very low observed OCP as compared to the theoretical one is most likely due to the low conversion of methane. [70] The low values of OCP, the electrolyte supported cell configuration and the very high thickness of the electrolyte (already discussed at the beginning of this paragraph) are the most suitable reasons of the low power density output obtained from the two cells (**Table 19**).

Anyway, must be considered as a success the generation of power output by fueling these cells with methane in the intermediate temperature range. In fact, this can be view as a clue of the possibility to obtain satisfying results, by simply working on the cell construction parameters. As an example, by reducing the electrolyte thickness and switching from an electrolyte supported cell to anode supported configuration.

Furthermore, must be considered that these cells are completely symmetrical. This not only means that their production costs should be considerably lower to the commercial cells, but that they can be used also as Reversible SOCs (R-SOC). When renewable energy exceeds needs, electric power is converted in chemical energy in the electrolytic mode; when there is not power from the renewable energy, it is possible to use the fuel stored in the fuel cell to produce electric current. This strategy is also valuable when considering the intermittent character of the renewable energy sources. For their development is fundamental to find a material that can be used in both the sides of the cell, for this reason the studied material of this chapter can be serious candidates as electrode materials for R-SOCs.

4.9 Conclusions

L8S2M and LSCuM, perovskite materials, were proposed as active and stable electrodes for symmetrical SOFCs fueled by methane.

In this chapter, the correct synthesis of the desired compounds was verified by different materials characterization techniques (XRD, XPS and EDX). Further investigations on the electrode morphology were carried out by SEM and BET analyses; this last one performed using the experimental data obtained from N₂-adsorption/desorption isotherm.

The reducing properties of the compounds were studied by H₂-TPR, and their stability in reducing conditions was verified by XRDs performed after reduction in hydrogen and methane. Furthermore, their catalytic activity towards methane oxidation was verified by GC. In the second part of this chapter, the electrochemical performances of the materials were discussed.

Symmetrical cells were made using L8S2M/GDC and LSCuM/GDC as composite electrodes. The single chamber tests in air and in methane confirm the good electrochemical

performances as cathode and very low resistances in methane. Unfortunately, due to the electrolyte supported configuration of the cell, together with the very high thickness of the electrolyte, these very good performances were not confirmed by the EIS and linear polarization tests performed on the double chamber tests.

References:

- [1] A. K. Sahu, A. Ghosh, and A. K. Suri, "Characterization of porous lanthanum strontium manganite (LSM) and development of yttria stabilized zirconia (YSZ) coating," *Ceram Int*, vol. 35, no. 6, pp. 2493–2497, Aug. 2009, doi: 10.1016/j.ceramint.2008.11.012.
- [2] R. v. Wandekar, B. N. Wani, and S. R. Bharadwaj, "Effect of Ni substitution on the crystal structure and thermal expansion behaviour of $(\text{La}_{0.8}\text{Sr}_{0.2})_{0.95}\text{MnO}_3$," *Mater Lett*, vol. 59, no. 22, pp. 2799–2803, Sep. 2005, doi: 10.1016/j.matlet.2005.03.062.
- [3] S. Kuharungrong, T. Dechakupt, and P. Aungkavattana, "Effects of Co and Fe addition on the properties of lanthanum strontium manganite," *Mater Lett*, vol. 58, no. 12–13, pp. 1964–1970, May 2004, doi: 10.1016/j.matlet.2003.12.011.
- [4] A. Berenov, J. Wei, H. Wood, R. Rudkin, and A. Atkinson, "Effect of aliovalent doping on the transport properties of lanthanum cuprates," *Journal of Solid State Electrochemistry*, vol. 11, no. 4, pp. 482–489, Apr. 2007, doi: 10.1007/s10008-006-0184-1.
- [5] S. Kuharungrong, T. Dechakupt, and P. Aungkavattana, "Effects of Co and Fe addition on the properties of lanthanum strontium manganite," *Mater Lett*, vol. 58, no. 12–13, pp. 1964–1970, May 2004, doi: 10.1016/j.matlet.2003.12.011.
- [6] Y. Zheng, C. Zhang, R. Ran, R. Cai, Z. Shao, and D. Farrusseng, "A new symmetric solid-oxide fuel cell with $\text{La}_{0.8}\text{Sr}_{0.2}\text{Sc}_{0.2}\text{Mn}_{0.8}\text{O}_{3-\delta}$ perovskite oxide as both the anode and cathode," *Acta Mater*, vol. 57, no. 4, pp. 1165–1175, Feb. 2009, doi: 10.1016/j.actamat.2008.10.047.
- [7] A. Berenov, H. Wood, and A. Atkinson, "Evaluation of $\text{La}_{0.8}\text{Sr}_{0.2}\text{Cu}_{1-x}\text{Mn}_x\text{O}_y$ Double Perovskite for Use in SOFCs," *J Electrochem Soc*, vol. 154, no. 12, p. B1362, 2007, doi: 10.1149/1.2792193.
- [8] A. Berenov, J. Wei, H. Wood, R. Rudkin, and A. Atkinson, "Effect of aliovalent doping on the transport properties of lanthanum cuprates," *Journal of Solid State Electrochemistry*, vol. 11, no. 4, pp. 482–489, Apr. 2007, doi: 10.1007/s10008-006-0184-1.
- [9] T. Noh, J. Ryu, J. Kim, Y. N. Kim, and H. Lee, "Structural and impedance analysis of copper doped LSM cathode for IT-SOFCs," *J Alloys Compd*, vol. 557, pp. 196–201, Apr. 2013, doi: 10.1016/j.jallcom.2013.01.002.
- [10] M. S. Kim, J. B. Yang, J. Medvedeva, W. B. Yelon, P. E. Parris, and W. J. James, "Electronic structure of $\text{La}_{0.7}\text{Sr}_{0.3}\text{Mn}_{1-x}\text{Cu}_x\text{O}_3$ ($0.0 \leq x \leq 0.30$)," *Journal of Physics Condensed Matter*, vol. 20, no. 25, Jun. 2008, doi: 10.1088/0953-8984/20/25/255228.
- [11] R. K. Gupta, I. J. Choi, Y. S. Cho, H. L. Lee, and S. H. Hyun, "Characterization of perovskite-type cathode, $\text{La}_{0.75}\text{Sr}_{0.25}\text{Mn}_{0.95-x}\text{Co}_x\text{Ni}_{0.05}\text{O}_{3+\delta}$ ($0.1 \leq x \leq 0.3$), for intermediate-temperature solid oxide fuel cells," *J Power Sources*, vol. 187, no. 2, pp. 371–377, Feb. 2009, doi: 10.1016/j.jpowsour.2008.10.136.
- [12] R. K. Gupta, E. Y. Kim, Y. H. Kim, and C. M. Whang, "Effect of strontium ion doping on structural, thermal, morphological and electrical properties of a co-doped lanthanum manganite system," *J Alloys Compd*, vol. 490, no. 1–2, pp. 56–61, Feb. 2010, doi: 10.1016/j.jallcom.2009.10.095.
- [13] J. Ryu, T. Noh, Y.-N. Kim, and H. Lee, "Structural analysis and electrical conductivity of $\text{La}_{1-x}\text{Sr}_x\text{Mn}_{0.8}\text{Cu}_{0.2}\text{O}_{3-\delta}$ ($0.1 \leq x \leq 0.4$) for IT-SOFCs."

- [14] M. Gaudon, C. Laberty-Robert, F. Ansart, P. Stevens, and A. Rousset, "Preparation and characterization of La_{1-x}Sr_xMnO_{3+δ} (0 < x < 0.6) powder by sol-gel processing," 2002. [Online]. Available: www.elsevier.com/locate/ssscie
- [15] Y. Li, H. Zhang, X. Liu, Q. Chen, and Q. Chen, "Electrical and magnetic properties of La_{1-x}Sr_xMnO₃ (0.1 ≤ x ≤ 0.25) ceramics prepared by sol-gel technique," *Ceram Int*, vol. 45, no. 13, pp. 16323–16330, Sep. 2019, doi: 10.1016/j.ceramint.2019.05.159.
- [16] P. van Cuong and D. H. Kim, "Effect of strontium doping level on electrical transport and magnetic properties of La_{1-x}Sr_xMnO₃ perovskite nanoparticles," in *Journal of Physics: Conference Series*, 2009, vol. 187. doi: 10.1088/1742-6596/187/1/012090.
- [17] K. P. Shinde, S. S. Pawar, P. M. Shirage, and S. H. Pawar, "Studies on morphological and magnetic properties of La_{1-x}Sr_xMnO₃," *Appl Surf Sci*, vol. 258, no. 19, pp. 7417–7420, Jul. 2012, doi: 10.1016/j.apsusc.2012.04.052.
- [18] S. Piskunov, E. Spohr, T. Jacob, E. A. Kotomin, and D. E. Ellis, "Electronic and magnetic structure of La_{0.875}Sr_{0.125}MnO₃ calculated by means of hybrid density-functional theory," *Phys Rev B*, vol. 76, no. 1, p. 012410, 2007.
- [19] S. Piskunov, E. Heifets, T. Jacob, E. A. Kotomin, D. E. Ellis, and E. Spohr, "Electronic structure and thermodynamic stability of LaMnO₃ and La_{1-x}Sr_xMnO₃ (001) surfaces: Ab initio calculations," *Phys Rev B*, vol. 78, no. 12, p. 121406, 2008.
- [20] J. Hemberger *et al.*, "Structural, magnetic, and electrical properties of single-crystalline (formula presented) (formula presented)," *Phys Rev B Condens Matter Mater Phys*, vol. 66, no. 9, pp. 1–8, 2002, doi: 10.1103/PhysRevB.66.094410.
- [21] K. L. Yan *et al.*, "Perovskite (La,Sr)MnO₃ with tunable electrical properties by the Sr-doping effect," *Journal of Alloys and Compounds*, vol. 628. Elsevier Ltd, pp. 429–432, Apr. 15, 2015. doi: 10.1016/j.jallcom.2014.12.137.
- [22] A. A. B. Baloch, "Extending Shannon's Ionic Radii Database Using Machine Learning," 2021.
- [23] A. A. B. Baloch, S. M. Alqahtani, F. Mumtaz, A. H. Muqaibel, S. N. Rashkeev, and F. H. Alharbi, "Extending Shannon's ionic radii database using machine learning," *Phys Rev Mater*, vol. 5, no. 4, Apr. 2021, doi: 10.1103/PhysRevMaterials.5.043804.
- [24] T. Theivasanthi and M. Alagar, "X-Ray Diffraction Studies of Copper Nanopowder," 2010.
- [25] F. C. Buciuman, F. Patcas, and J. Zsakó, "TPR-STUDY OF SUBSTITUTION EFFECTS ON REDUCIBILITY AND OXIDATIVE NON-STOICHIOMETRY OF La_{0.8}A'_{0.2}MnO_{3+d} PEROVSKITES," 2000.
- [26] W. Wang, F. Yuan, X. Niu, and Y. Zhu, "Preparation of Pd supported on La(Sr)-Mn-O Perovskite by microwave Irradiation Method and Its Catalytic Performances for the Methane Combustion," *Sci Rep*, vol. 6, Jan. 2016, doi: 10.1038/srep19511.
- [27] F. Kapteijn, L. Singoredjo, A. Andreini, and J. A. Moulijn, "Activity and selectivity of pure manganese oxides in the selective catalytic reduction of nitric oxide with ammonia," *Appl Catal B*, vol. 3, no. 2–3, pp. 173–189, Feb. 1994, doi: 10.1016/0926-3373(93)E0034-9.
- [28] G. Saracco, F. Geobaldo, and G. Baldi, "Methane combustion on Mg-doped LaMnO₃ perovskite catalysts," *Appl Catal B*, vol. 20, pp. 277–288, 1999.
- [29] W.-P. Dow, Y.-P. Wang, and T.-J. Huang, "TPR and XRD studies of yttria-doped ceria/-alumina-supported copper oxide catalyst," 2000.
- [30] Z. Sihaib *et al.*, "The effect of citric acid concentration on the properties of LaMnO₃ as a catalyst for hydrocarbon oxidation," *Catalysts*, vol. 9, no. 3, Mar. 2019, doi: 10.3390/catal9030226.
- [31] J. Chen, H. Arandiyani, X. Gao, and J. Li, "Recent Advances in Catalysts for Methane Combustion," *Catalysis Surveys from Asia*, vol. 19, no. 3. Springer New York LLC, pp. 140–171, Sep. 01, 2015. doi: 10.1007/s10563-015-9191-5.
- [32] J. Yang and Y. Guo, "Nanostructured perovskite oxides as promising substitutes of noble metals catalysts for catalytic combustion of methane," *Chinese Chemical Letters*, vol. 29, no. 2. Elsevier B.V., pp. 252–260, Feb. 01, 2018. doi: 10.1016/j.ccllet.2017.09.013.

- [33] S. Thaicharoensutcharittham, V. Meeyoo, B. Kitiyanan, P. Rangsunvigit, and T. Rirkosomboon, "Catalytic combustion of methane over NiO/Ce_{0.75}Zr_{0.25}O₂ catalyst," *Catal Commun*, vol. 10, no. 5, pp. 673–677, Jan. 2009, doi: 10.1016/j.catcom.2008.11.014.
- [34] J. Chen, H. Arandiyana, X. Gao, and J. Li, "Recent Advances in Catalysts for Methane Combustion," *Catalysis Surveys from Asia*, vol. 19, no. 3. Springer New York LLC, pp. 140–171, Sep. 01, 2015. doi: 10.1007/s10563-015-9191-5.
- [35] R. J. H. Voorhoeve, J. P. Remeika, P. E. Freeland, and B. T. Matthias, "Rare-Earth Oxides of Manganese and Cobalt Rival Platinum for the Treatment of Carbon Monoxide in Auto Exhaust," 1972.
- [36] H.-M. Zhang, Y. Teraoka, and N. Yamazoe, "Preparation of perovskite-type oxides with large surface area by citrate process," *Chem Lett*, vol. 16, no. 4, pp. 665–668, 1987.
- [37] A. Osti, J. P. Dacquin, A. Glisenti, and P. Granger, "Interaction strength between Pd and perovskite according to the method for Pd incorporation in NGV catalysts: Impact of thermal aging," *Top. Catal.*, vol. In press, 2022.
- [38] S. Specchia, A. Civera, and G. Saracco, "In situ combustion synthesis of perovskite catalysts for efficient and clean methane premixed metal burners," in *Chemical Engineering Science*, Nov. 2004, vol. 59, no. 22–23, pp. 5091–5098. doi: 10.1016/j.ces.2004.08.028.
- [39] D. Dollimore, P. Spooner, and A. Turner, "The bet method of analysis of gas adsorption data and its relevance to the calculation of surface areas," Elsevier Sequoia S.A, 1976.
- [40] M. Glazer, G. Burns, and Glazer A N, *Space groups for solid state scientists.*, no. 8. ACS Publications, 2012.
- [41] H. A. Jahn, Teller E, and S. Kaliaguine, "Stability of polyatomic molecules in degenerate electronic states - I—Orbital degeneracy," *Proceedings of the Royal Society of London*, pp. 220–235, Nov. 1937, doi: 10.1002/cjce.23632.
- [42] V. R. Choudhary, A. M. Rajput, and A. S. Mamman, "NiO-Alkaline Earth Oxide Catalysts for Oxidative Methane-to-Syngas Conversion: Influence of Alkaline Earth Oxide on the Surface Properties and Temperature-Programmed Reduction/ Reaction by H₂ and Methane," 1998.
- [43] N. Caillol, M. Pijolat, and E. Siebert, "Investigation of chemisorbed oxygen, surface segregation and effect of post-treatments on La_{0.8}Sr_{0.2}MnO₃ powder and screen-printed layers for solid oxide fuel cell cathodes," *Appl Surf Sci*, vol. 253, no. 10, pp. 4641–4648, 2007.
- [44] M. Cannarozzo, A. del Borghi, and P. Costamagna, "Simulation of mass transport in SOFC composite electrodes," *J Appl Electrochem*, vol. 38, no. 7, pp. 1011–1018, Jul. 2008, doi: 10.1007/s10800-008-9527-1.
- [45] J. T. S. Irvine, D. C. Sinclair, and A. R. West, "Electroceramics: Characterization by Impedance Spectroscopy," *Adv. Mater.*, vol. 3, pp. 132–138, 1990.
- [46] H. Zhao, L. Huo, and S. Gao, "Electrochemical properties of LSM-CBO composite cathode," *J Power Sources*, vol. 125, no. 2, pp. 149–154, Jan. 2004, doi: 10.1016/j.jpowsour.2003.07.009.
- [47] M. J. Jørgensen and M. Mogensen, "Impedance of Solid Oxide Fuel Cell LSM/YSZ Composite Cathodes," *J Electrochem Soc*, vol. 148, no. 5, p. A433, 2001, doi: 10.1149/1.1360203.
- [48] H. Shi *et al.*, "High performance tubular solid oxide fuel cells with BSCF cathode," *Int J Hydrogen Energy*, vol. 37, no. 17, pp. 13022–13029, Sep. 2012, doi: 10.1016/j.ijhydene.2012.05.061.
- [49] S. B. Adler, "Factors governing oxygen reduction in solid oxide fuel cell cathodes," *Chem Rev*, vol. 104, no. 10, pp. 4791–4843, Oct. 2004, doi: 10.1021/cr020724o.
- [50] X. Zhang *et al.*, "Insight into the oxygen reduction reaction on the LSM|GDC interface of solid oxide fuel cells through impedance spectroscopy analysis," *Catal Sci Technol*, vol. 6, no. 13, pp. 4945–4952, 2016, doi: 10.1039/c5cy02232k.
- [51] X. Liu, D. Han, H. Wu, X. Meng, F. Zeng, and Z. Zhan, "Mn_{1.5}Co_{1.5}O_{4-δ} infiltrated yttria stabilized zirconia composite cathodes for intermediate-temperature solid oxide fuel cells," *Int J Hydrogen Energy*, vol. 38, no. 36, pp. 16563–16568, Dec. 2013, doi: 10.1016/j.ijhydene.2013.04.106.

- [52] X. J. Chen, K. A. Khor, and S. H. Chan, "Identification of O₂ reduction processes at yttria stabilized zirconia | doped lanthanum manganite interface," *J Power Sources*, vol. 123, no. 1, pp. 17–25, Sep. 2003, doi: 10.1016/S0378-7753(03)00436-1.
- [53] J. D. Kim, G. D. Kim, and J. W. Moon, "Y. i. Park, WH Lee, K. Kobayashi, M. Nagai and CE Kim," *Solid State Ion*, vol. 143, pp. 379–389, 2001.
- [54] B. A. Boukamp and H. J. M. Bouwmeester, "Interpretation of the Gerischer impedance in solid state ionics," *Solid State Ion*, vol. 157, pp. 29–33, 2003, [Online]. Available: www.elsevier.com/locate/ssi
- [55] B. A. Boukamp, M. Verbraeken, D. H. A. Blank, and P. Holtappels, "SOFC-anodes, proof for a finite-length type Gerischer impedance?," *Solid State Ion*, vol. 177, no. 26-32 SPEC. ISS., pp. 2539–2541, Oct. 2006, doi: 10.1016/j.ssi.2006.03.002.
- [56] H. Gerischer, "The Impact of the Semiconductors on the Concepts of Electrochemistry," *Electrochimica Acta*, vol. 35, pp. 1677–1699, 1990.
- [57] W. Wang, S. P. Jiang, A. I. Y. Tok, and L. Luo, "GDC-impregnated Ni anodes for direct utilization of methane in solid oxide fuel cells," *J Power Sources*, vol. 159, no. 1 SPEC. ISS., pp. 68–72, Sep. 2006, doi: 10.1016/j.jpowsour.2006.04.051.
- [58] G. Stochniol, E. Syskakis, and A. Naoumidis, "Chemical Compatibility between Strontium-Doped Lanthanum Manganite and Yttria-Stabilized Zirconia," *J. Am. Ceram. Soc.*, vol. 78, pp. 929–932, 1995.
- [59] A. Tarancón, "Strategies for lowering solid oxide fuel cells operating temperature," *Energies*, vol. 2, no. 4. MDPI AG, pp. 1130–1150, 2009. doi: 10.3390/en20401130.
- [60] Q. Ma, J. Ma, S. Zhou, R. Yan, J. Gao, and G. Meng, "A high-performance ammonia-fueled SOFC based on a YSZ thin-film electrolyte," *J Power Sources*, vol. 164, no. 1, pp. 86–89, Jan. 2007, doi: 10.1016/j.jpowsour.2006.09.093.
- [61] L. Besra, S. Zha, and M. Liu, "Preparation of NiO-YSZ/YSZ bi-layers for solid oxide fuel cells by electrophoretic deposition," *J Power Sources*, vol. 160, no. 1, pp. 207–214, Sep. 2006, doi: 10.1016/j.jpowsour.2005.12.090.
- [62] Fuelcell Materials.com, "Anode supported commercial cells." <https://fuelcellmaterials.com/products/cells/anode-supported-cells/anode-supported-planar-cell/> (accessed Oct. 07, 2022).
- [63] V. S. Muralidharan, "Introduction Warburg impedance-basics revisited Contributed papers," *Corrosion Methods and Materials*, vol. 44, pp. 26–29, 1997.
- [64] M. A. Buccheri and J. M. Hill, "Methane Electrochemical Oxidation Pathway over a Ni/YSZ and La 0.3 Sr 0.7 TiO 3 Bi-Layer SOFC Anode," *J Electrochem Soc*, vol. 159, no. 4, pp. B361–B367, 2012, doi: 10.1149/2.001204jes.
- [65] H. Zhu and R. J. Kee, "Modeling Electrochemical Impedance Spectra in SOFC Button Cells with Internal Methane Reforming," *J Electrochem Soc*, vol. 153, no. 9, p. A1765, 2006, doi: 10.1149/1.2220065.
- [66] T. Hibino, A. Hashimoto, K. Asano, M. Yano, M. Suzuki, and M. Sano, "An intermediate-temperature solid oxide fuel cell providing higher performance with hydrocarbons than with hydrogen," *Electrochemical and Solid-State Letters*, vol. 5, no. 11, Nov. 2002, doi: 10.1149/1.1508551.
- [67] E. N. Armstrong, K. L. Duncan, D. J. Oh, J. F. Weaver, and E. D. Wachsman, "Determination of Surface Exchange Coefficients of LSM, LSCF, YSZ, GDC Constituent Materials in Composite SOFC Cathodes," *J Electrochem Soc*, vol. 158, no. 5, pp. B492–B499, May 2011, doi: 10.1149/1.3555122.
- [68] S. P. Jiang, X. J. Chen, S. H. Chan, J. T. Kwok, and K. A. Khor, "(La_{0.75}Sr_{0.25})(Cr_{0.5}Mn_{0.5})O₃/YSZ composite anodes for methane oxidation reaction in solid oxide fuel cells," *Solid State Ion*, vol. 177, no. 1–2, pp. 149–157, Jan. 2006, doi: 10.1016/j.ssi.2005.09.010.
- [69] J. Sfeir *et al.*, "Lanthanum chromite based catalysts for oxidation of methane directly on SOFC anodes," *J Catal*, vol. 202, no. 2, pp. 229–244, 2001, doi: 10.1006/jcat.2001.3286.

Chapter 5: Cu@GDC 2% Pd as Anode Material for Direct Methane LT-SOFCs

5.1 Introduction

To become climate-neutral by 2050, Europe needs to transform its energy system, which accounts for 75% of the EU's greenhouse gas (GHG) emissions. Hydrogen (H₂) based energy will pave the way towards a more efficient and interconnected energy sector, driven by the twin goals of a cleaner planet and a stronger economy. The high cost to produce “low carbon H₂” is the most significant barrier to its mass adoption for use across the global energy market. H₂ accounts for less than 2% of Europe’s present energy consumption and is primarily used to produce chemical products, such as plastics and fertilizers. 96% of this H₂ is produced from natural gas. The transition to a C-free economy will require long time and investments.

Anyway, there are three main pillars that should be followed to reach this goal:

- 1) A more “circular” energy system, with energy efficiency at its core. There is significant potential in the reuse of waste heat from industrial sites, data centers, or other sources, and energy produced from bio-waste or in wastewater treatment plants.
- 2) Direct electrification of end-use sectors. We should increasingly use electricity where possible: for example, for heat pumps in buildings, electric vehicles in transport or electric furnaces in certain industries.
- 3) Clean fuels, including renewable hydrogen and sustainable biofuels and biogas. ^[1]

It is evident that this transition cannot be done using methane supplied from natural gas. The methane supply for EU from alternative sources is even more necessary considering the international crisis caused by the Russian invasion of Ukraine at the beginning of 2022.

The possible solution for green, cheap, and selfish production of hydrocarbons is the biomethane. In fact, second-generation biofuels (first generation are wide available, but suffer from low climate benefit) can be produced from low-value forest residues and they approach zero emissions if one assumes that the entire biomass supply chain is climate-neutral. Bio-methane can be distributed both in compressed form (bio-CNG) and liquefied

form (bio-LNG). [1]

Going deeper into the discussion of first and second generation of biofuel, three are the main types of first-generation biofuels used commercially: biodiesel, ethanol, and biogas. Nowadays, these three products are produced from commodities that are also used for food. The main production processes are transesterification, ethanol conversion processes, fermentation, and anaerobic digestion of biomass. Second generation biofuels are produced from biomass in a more sustainable way, which is truly carbon neutral or even carbon negative in terms of its impact on CO₂ concentrations. Most of all this new generation fuel is produced using “plant biomass” that is largely lignocellulosic material, in other words cheap and abundant nonfood materials available from plants. At present, the production of such fuels is not cost-effective because there are several technical barriers that need to be overcome before their potential can be realized. Lignocellulosic materials are a collection of feedstocks for advanced biofuels and can be obtained either through hydrolysis and fermentation or through gasification (e.g., Fischer-Tropsch, FT). Indeed, the most important possibility for the application studied in this work, is given by the syngas production obtained by gasified biomasses. Later, syngas can be transformed into completely green methane. Another significant feature of second generation biomethane is the low sulphur content in the produced gas.

As last consideration must be noted that recent publications indicate the use of FT process technology for biomass conversion to synthetic hydrocarbon may be promising and carbon neutral alternative to conventional fuels. [2], [3]

What is explained above it is not an academic theoretical speculation of what can be done in the next decades, but it is a nowadays reality. Indeed, the work in this chapter was made in collaboration with Pietro Fiorentini S.p.A, an Italian company that is leader on the entire natural gas supply chain. It is fundamental and significant that an important company, as Pietro Fiorentini is, is expanding its horizons towards the development of technologies and solutions for a sustainable world, with a particular focus on renewable energy projects. The research activity proposed us from Pietro Fiorentini S.p.A was the creation of a methane fueled SOFC able to operate at low temperatures. This project was lead also with a collaboration with Prof. Alessandro Donazzi and Prof. Stefano Campanari from Politecnico

of Milano.

The main core of our work was to develop an anode material for methane fueled SOFCs operating at low temperature range (500-600 °C); the temperature requirement was very relevant because of the desire of remaining below the auto-ignition temperature of methane. The auto-ignition temperature is the minimum temperature at which a fuel (methane in this case) will ignite without a spark or a flame being present. It is fundamental to know this temperature and to operate below it. Especially, for the industrial operations since it is the major source of industrial fires. [4] However, the minimum auto-ignition temperature (MAIT) it is not a fundamental property of a fuel since its value depends on the means of measurement. As an example, if the experiment is carried out inside a metal vessel the MAIT is higher than the one obtained in a glass vessel. This discrepancy is due to the reactions that occur on the walls, that destroy reactive species necessary for the proceeding of the fuel oxidation. It is for this reason that in literature it is difficult to find a unique, well-accepted value. The considered temperature range, at atmospheric pressure and in presence of air, goes from 537 °C [5], [6] to 600 °C [4]. In addition, must be considered that these values highly vary in dependance with the stoichiometric ratio between methane and air. The presented values were obtained with a mixture methane/air, where the fuel is the 7% of the total composition of the atmosphere. For our applications, this specific atmosphere composition is unlikely reached, since the flow of methane is very low, and a possible leak will not create an atmosphere with a so high presence of CH₄. Anyway, to be completely aware and out of any risk, it was decided to fix the target operating temperature below these values, so at 500 °C.

In the meantime, prof. Donazzi research group worked on the development of new possible cathodic materials and of the realization of thin layer electrolyte (about 100 μm). While prof. Campanari research group studied the perfect anodic operating conditions. Indeed, the hydrogen injection into the methane grid is another point. The transition to a completely hydrogen fueled world will require long timing, due to the difficulty of hydrogen transport in our cities and in our houses. These difficulties are related to hydrogen high inflammability, which forces to a complete adaptation of the gas transport implants of our cities. That reasonably will take a long time and with a strong opposition from the

governments of the poorest countries due to the high costs of a complete modification of the gas transport implants.

Under this scenario the possibility of a Fuel Cell to operate efficiently with H_2 , CH_4 and CH_4+H_2 as fuel does not need to be underlined. And the studies made from the Prof. Campanari's research group suggested that the best composition, in terms of efficiency and safety, between hydrogen and methane is given by a 2:3 ratio. For this reason, this composition was used as reference atmosphere for the cell testing, together with pure methane and 20% of hydrogen.

Traditional Ni-based technology is not compatible with the direct use of methane due to excessive catalytic activity of traditional Ni-based anodes towards the methane cracking reaction. [7] On the other hand, the need to operate at temperature between 500 °C-600 °C is a requirement not fulfilled by commercial anodes due to the high C-H bond energy of CH_4 among alkanes, requiring highly active catalysts for its conversion and/or high temperatures (not compatible with the safety use of methane).

All these required features for the anodes of methane fueled SOFCs makes very difficult the development of carbon-tolerant and conversion-efficient materials. However, the scientific community is making very strong efforts in the research of materials able to directly use methane as fuel.[8] The state-of-the-art materials, if it is possible to call them in this way, since there is not yet sufficient performance for a commercial development of the technology, can be divided into two classes: Mixed Ionic and Electronic Conductors Materials (MIEC) and cermets (a composite material made ceramic and metal).

The most promising in the first class are doped $LaCrO_3$ doped $SrTiO_3$ [9],[10],[11]. Their lower activity towards methane oxidation, compared to Ni-based materials, is balanced by a lower performances decay due to carbon deposition on the electrode surface.

The second chance is to develop a cermet material, like Ni-YSZ, the commercial anodes for H_2 fueled SOFCs, but trying to avoid the carbon deposition. To enhance the carbon resistance, without affecting the electrochemical activity of Ni, through ionic conducting oxides as, for example, gadolinium-doped ceria (GDC), scandium-stabilized zirconia (ScDC) and samarium-doped ceria (SDC).[12],[13],[14] Otherwise it is useful to create an alloy

with metals poorly active towards methane cracking, like Cu, Co, Mn or Fe.^{[15],[16]}

In this work the main idea is to combine the high electronic conductivity and low activity towards methane cracking of copper, with the very good oxidative properties of GDC, by synthesizing a nanocomposite material of copper nanoparticles on a GDC substrate. We decide to focus on nanosized electrocatalysts, since nano-dimensions can help adding relevant functionality allowing to enhance the specific surface area (and thus the number of active sites and the reactivity) but can also stabilize faces not usual in massive materials and capable of specific reactivity. This material has been designed starting from GDC, taking into consideration the required compatibility with the electrolyte and the good activity in methane oxidation. ^{[17],[18],[19]} Cerium oxide, in fact, is a good catalyst for oxidation and the use of ceria doped as an Intermediate Temperature (IT)-SOFC electrolyte is well known. ^[20] Starting from doped ceria already assures catalytic activity in oxidation and ionic conductivity. The oxygen exchange capability, moreover, un-favors the electrode surface coking. It was observed that catalytic activity in electrooxidation and the absence of coking are also due to the electro-activated oxygen extraction from the anode.^{[12],[13]}

To create a new GDC based material, the first consideration must concern the electronic conductivity which is a missing property. To solve this problem a composite of the type of Cu@GDC was prepared with the idea to add the electronic conductivity assured by copper, to the catalytic activity and ionic conductivity of GDC. To enhance the contribution of copper it was decided to create dispersed nanoparticles through an innovative wet impregnation technique. In this preparation method it is expected to insert a complexing agent. In this way, the copper cations can interact chemically with the surface of GDC giving rise to highly dispersed copper clusters, thanks also to the steric hindrance of the complexing agent.^[14] The choice of citric acid as a complexing agent is given by its non-toxicity and its low cost.

To enhance electrode performance at the lower operating temperatures, palladium nanoparticles are added to the internal surfaces of the porous electrodes.^{[15],[16],[17]} Infiltration allows to obtain a uniform and continuous network of nanoparticles. Importantly, the infiltration can be completed in a single processing step on both electrodes. Additionally, since the method is independent of all other processing steps, it can be pre-formed at lower

temperatures, allowing for the use of otherwise reactive nanoparticle catalysts.

The polarization resistance of the state-of-art material, Ni-YSZ, will be considered as a reference for the material evaluation. *Zhu et al.* obtained a polarization resistance of about $0.1 \Omega\text{cm}^2$ for the pristine material. [18]

As made for the MIEC materials studied in the previous chapters for the realization of a Direct Methane fueled SOFC at intermediate temperature, Cu@GDC material and the cells have been characterized by means of X-Ray Diffraction (XRD), X-Ray Photoelectron Spectroscopy (XPS), Energy Dispersed X-Ray Analysis (EDX) and Scanning Electron Microscopy (SEM). The electrochemical behavior was studied by Electrochemical Impedance Spectroscopy (EIS) and Linear Sweep Voltammetry (LSV).

5.2 Material synthesis

5.2.1 Cu@GDC nanopowders synthesis

Cu@GDC (molar ratio 3:2 between Cu and GDC) powders were prepared by citrate method [19] starting from a dispersion of gadolinium doped ceria ($\text{Ce}_{0.9}\text{Gd}_{0.1}\text{O}_2$ Fuelcellmaterials, powder) in deionized water, where copper nitrate trihydrate ($\text{Cu}(\text{NO}_3)_2$ Sigma Aldrich, puriss. p.a., 99-104%) is dissolved. Citric acid ($\text{C}_6\text{H}_8\text{O}_7$ Sigma-Aldrich $\geq 99.0\%$) is added as complexing agent (with a molar ratio of 1.9:1 with respect to the total amount of cations) under stirring and then the solution is lead to neutral pH by dropwise addition of ammonium hydroxide. At pH 7, the stirring has been stopped and the solution was heated overnight to eliminate water and allow the formation of a gel. The gel was burned, heating it at $400 \text{ }^\circ\text{C}$. The formed powders were calcined at $800 \text{ }^\circ\text{C}$ for 6 hours using a heating and cooling ramp of $6 \text{ }^\circ\text{C}/\text{min}$.

5.2.2 Synthesis of the nanocomposite electrode

The electrochemical measurements of the anode were performed using symmetric cells (Cu@GDC Pd 2% wt./GDC/Cu@GDC Pd 2% wt.) made of dense gadolinium doped ceria ceramics (theoretical density $>96\%$) as electrolyte on which electrode materials based on the as prepared Cu@GDC powder were deposited. The electrode was deposited by tape casting. The used ink is composed by a vehicle liquid, whose viscosity is adjusted by a thinner solution. Both vehicle and thinner are based on α -terpineol polymer. After deposition, the

electrodes were treated at 1050 °C for 2 h (3 °C/min heating ramp). After this thermal treatment the electrode thickness was about 30 μm (evaluated with SEM). The chemical compatibility with GDC was also evaluated by XRD. The electrolyte was produced in form of pressed pellet calcined at 1500 °C for 5 h (3 °C/min heating ramp).

The electrode infiltration of Pd oxide (II) was obtained by adding, drop by drop, a certain amount of an aqueous solution containing tetraamminepalladium (II) nitrate ((NH₃)₄Pd(NO₃)₂, Sigma-Aldrich, solution 10 wt. % in H₂O), on the already deposited electrode. The electrode was then dried under vacuum and finally placed in an oven at 450 °C. This thermal treatment is necessary to achieve the formation of the oxide on the surface of the electrode. Following this procedure, two nanocomposite anodes were prepared, with 0.5 and 1 wt.% Pd amount.

A different method was also developed. In this new method, the used infiltrated solution was set to correspond to the estimated free-pore volume. This estimation was performed by observing the amount of distilled water adsorbed by the electrode. After this estimation, the infiltrated solution was prepared in order to have the desired amount of Pd in that volume. Three different infiltrations were carried out (1%, 2%, and 3 wt. %) to understand the effect of the amount of Pd on the electrochemical performance.

To understand the performances of the entire device, a complete cell was realized (Cu@GDC Pd 2% wt./GDC/LSCF:GDC (50:50)). The cathodic ink was realized with the same procedure already explained for the anode. The used powder is a composite LSCF:GDC (50:50) (Sigma-Aldrich, composite cathode powder) and it was chosen to increase the chemical compatibility and adhesion between electrode and electrolyte.

5.3 Structural, Chemical and Morphological Characterization of the electrode

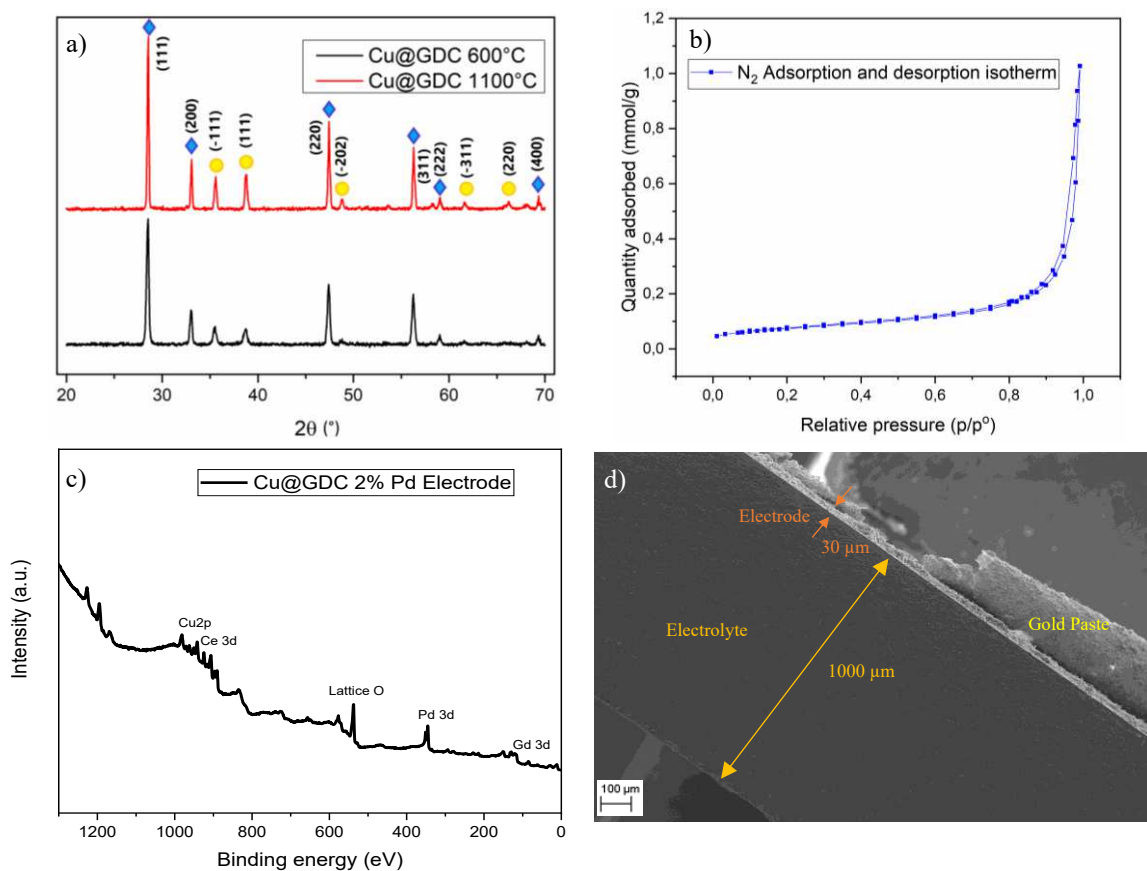


Figure 1: a) XRD diffractogram of Cu@GDC after the calcination and after thermal treatment at 1100 °C; b) N₂ adsorption and desorption isotherm on Cu@GDC powder sample. c) XPS survey for Cu@GDC 2% Pd electrode; d) SEM image of the cell section.

The nanocomposite was successfully obtained, as evident from the results reported in **Figure 1-a**. XRD pattern indicates the presence of CuO cubic crystals in addition to the supporting GDC. The nanoparticles size was estimated by means of the Scherrer equation; nanocrystals average size is around 21 ± 1 nm when the heat treatment is carried out at 600 °C and around 34 ± 1 nm for a calcination treatment at 1100 °C. The modest increment of mean diameter when increasing of 450 °C the calcination temperature, is a good result that allows to define the thermal treatment of the electrode without to be afraid to significantly loose the nanostructure.

The N₂ adsorption and desorption isotherm carried out on powders is shown in **Figure 1-b**. Even if it is very small, the isotherm presents a hysteresis that is typical for type IV isotherm. Type IV describes a mesoporous material where the gas desorption is less preferred

compared to the adsorption. On this isotherm a BET analysis was carried out in order to quantify the Specific Surface Area (SSA). The obtained SSA is $5.888 \pm 0.002 \text{ m}^2/\text{g}$. This value is small but similar to the typical values of specific surface area reported in literature for the state-of-art anode cermet Ni-YSZ. [23]

The XPS spectrum survey of the final electrode, after Pd infiltration, is shown in **Figure 1-c**. All the expected species are present. The Ce 3d level has a complicated structure: six peaks corresponding to three pairs of spin-orbit doublets [usually noted as (V, U), (V'', U''), and (V''', U''')] can be identified in the Ce 3d spectrum of Ce(IV) oxide, [30], [31], [32]. While four peaks due to two pairs of doublets characterize the Ce 3d spectrum of Ce(III) oxide. The Ce 3d peak positions (signals V, V'', U, U'' and U''') agree with literature data for CeO₂ (**Table 1**). XPS analysis does not reveal reduction, as expected for stabilized cerium oxide.

	GDC	Cu/GDC	Pd/Cu/GDC	CeO ₂	Ce ₂ O ₃
Ce 3d V	882.6	882.4	882.6	882.9	
V'					885.4
V''	888.8	888.7	889.0	889.0	
V'''	898.4	898.6	898.6	898.7	
Ce 3d U	900.9	900.9	899.2	900.8	
					903.9-904.1
	907.5	907.2	907.4	907.4	
	916.8	916.6	916.2	916.8	
Gd 4d	141.5	141.5	142.6	142.7	
Cu 2p		933.5	933.8	933.6-933.9	932.2-932.8
		942.2	942.6		(Cu, Cu ₂ O)
Cu 2p		953.9	953.8	953.7	952.5 (Cu ₂ O);
		962.1	961.8		952.4 (Cu)
Pd 3d			337.0	337.9 (PdO ₂)	335.3-335.5
				333.6-333.9	
			342.6	(PdO)	339.3-340.3
				342.2-342.5	
O 1s	529.5	529.4	529.0	529.5-530.0	530.2-530.7
	531.6	531.7		(CeO ₂ , Ge ₂ O ₃ , CuO)	(Cu ₂ O)

Table 1: XPS peaks position obtained starting from GDC and after successive deposition to reach the final anode.

Consistently, Gd 3d signal is observed a 142.6 eV, [24], [25] the position expected for this element in oxide. The Cu 2p_{3/2} and _{1/2}, 933.8 and 953.8 eV respectively, are consistent with how expected for this element in CuO, as confirmed by the shake-up structure at 942.6 and 961.8 eV. This result underlines the need of the preliminary reducing treatment. The Pd 3d peak positions suggest the presence of Pd oxide.

Since the electrodes were treated at 1050 °C, PdO should decompose and only metallic nanoparticles should be present [26], [27]. Probably the exposure to air of the nanoparticles greatly favors the metal oxidation. A quantitative analysis was carried out too.

		O	Ce	Gd	Cu	Pd	Gd/Ce
GDC	XPS	65.8	31.5 92.1	2.7 7.9	-	-	0.1
	EDX	57.5	39.5 92.8	3.0 7.2	-	-	0.1
	Nominal	66.7	30.0 90.0	3.0 10.0	-	-	0.1
Cu/GDC	XPS	53.4	16.3 35.0	8.8 18.9	21.5 46.1	-	0.5
	EDX	58.4	22.9 55.1	2.4 5.7	16.3 39.2	-	0.1
	Nominal	58.1	15.4 36.7	1.7 4.1	24.8 59.2	-	0.1
Pd/Cu/GDC	XPS	63.8	19.8 54.7	2.1 5.8	11.8 32.6	2.5 6.9	0.1
	EDX	67.5	17.5 53.8	1.7 5.2	13.1 40.3	0.2 0.6	0.1
	Nominal	59.1	17.2 42.1	1.9 4.6	20.8 50.9	1.0 2.4	0.1

Table 2: XPS and EDX quantitative analyses (at. 2% Pd) results.

Two quantitative analyses are presented in **Table 2**. The quantitative obtained from XPS spectra can be considered representative of the surface of the samples, while the EDX one represents an analysis of the chemical composition of the inner regions of the cermet nanoparticles. From the two quantitative analyses the expected ratio between gadolinium and cerium (1:10) is confirmed. Cu is present in slightly lower amount with respect to the expected one and its presence is more relevant in the subsurface layers. The recorded Pd quantity is not the same from the two techniques. While in the XPS analysis, the Pd presence, given by infiltration, is higher than expected (2%), this is not true for EDX, where the determined quantity is much lower than nominal one. This result allows to confirm that Pd is present on the surface as nanoparticle and it is not diffused inside the electrode cermet structure, consistently with how desired when selecting this deposition procedure.

5.4 Symmetrical cells EIS characterizations

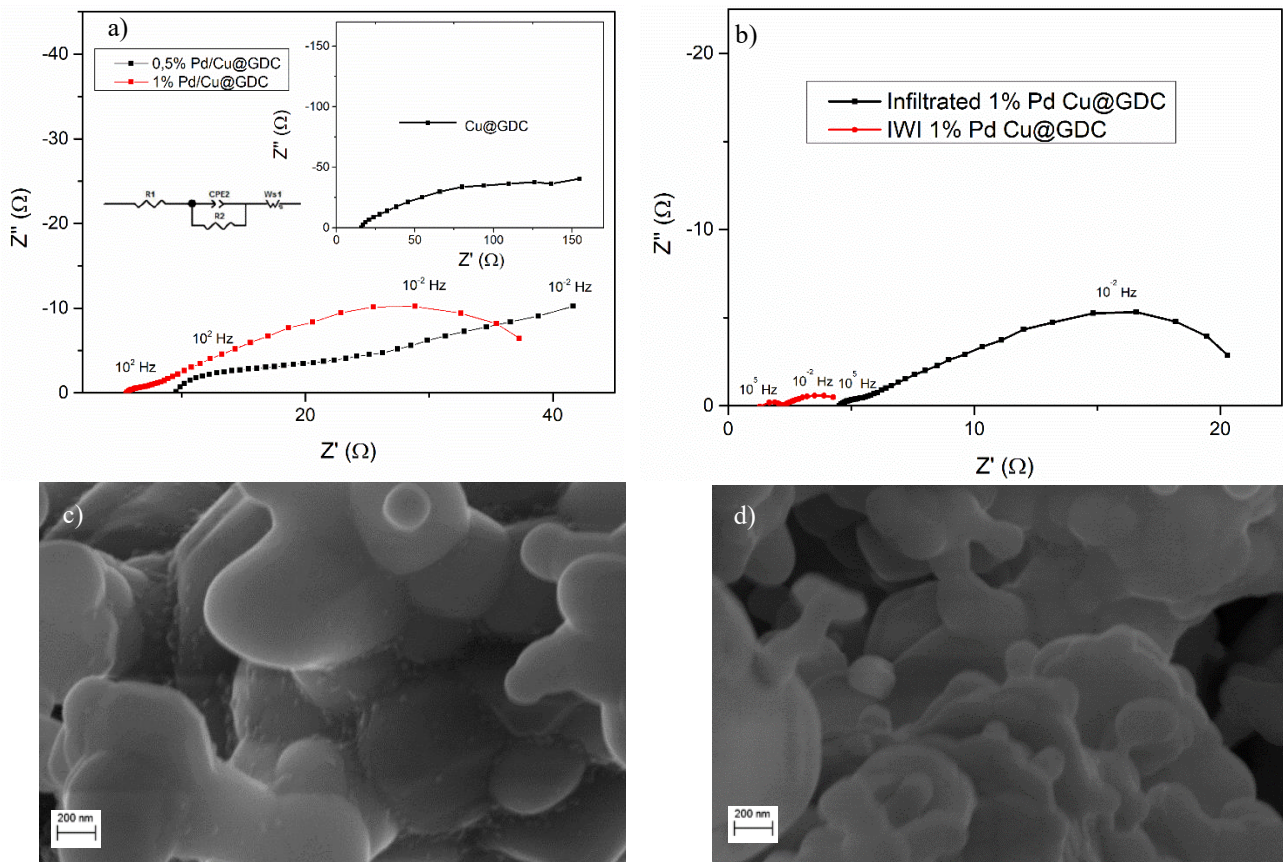


Figure 2: a) EIS for Cu@GDC with 0%, 0.5% and 1% wt. Pd infiltration electrodes. The measurements were performed in 50% CH₄ in Ar at 620 °C. b) EIS for Cu@GDC 1% wt. Pd infiltrated and with Incipient Wetness Infiltration (IWI). The measurements were performed in 50% CH₄ in Ar at 650 °C. c) SEM image for Cu@GDC with 1% wt. Pd infiltration. d) SEM image for Cu@GDC with 1% wt. Pd with IWI.

In **Figure 2-a**, the Nyquist plots of Cu@GDC and Cu@GDC with 0.5 and 1% Pd infiltration, are shown. A significant decrease in the polarization resistance (R_p) is evident between the infiltrated electrodes compared with the one tested without Pd. Furthermore, another substantial improvement of the performances is given by increasing the Pd weight percentage on the electrode surface. (**Table 3**)

The EIS spectra highlight the presence of two different contributions to the total resistance of the electrodes. The first one is set at frequencies about 10² Hz, while the second one is set at lower frequencies (10⁻² Hz). The second process, considering the frequencies and the good fitting of the experimental signal with the Warburg element, can be attributed to the gas diffusion. In addition, the resistance decreases with the temperature increasing has good correspondence with this phenomenon.^[28] On the contrary, it can be more difficult to understand the nature of the high frequencies (HF) process, that was fitted with a R//CPE

element. This resistance takes into consideration the contribution of the ionic grain boundary transportation and charge transfer resistance. In other words, this process represents the real resistance of the oxidative process.

T (°C)	Cu@GDC			Cu@GDC 0.5% Pd			Cu@GDC 1% Pd		
	1 st process (Ωcm^2)	2 nd process (Ωcm^2)	Total (Ωcm^2)	1 st process (Ωcm^2)	2 nd process (Ωcm^2)	Total (Ωcm^2)	1 st process (Ωcm^2)	2 nd process (Ωcm^2)	Total (Ωcm^2)
710	2.70	13.40	16.10	0.66	1.15	1.81	0.03	1.80	1.83
680	3.79	29.94	33.73	1.17	4.27	5.44	0.15	6.31	6.46
650	15.91	80.00	95.91	2.76	10.31	13.07	0.26	10.68	10.94
600	66.00	107.00	173.00	3.00	58.81	61.81	0.48	20.87	21.36

Table 3: ASR determination for symmetrical cell tests performed with Cu@GDC and the 0.5 and 1% wt. Pd infiltrated electrodes. The different contribution to the total R_p from the two different processes revealed from the Nyquist plots is shown.

The aggregation of the nanoparticles is a problem that characterizes wet impregnation procedure and that has been solved, in impregnation, by means of an accurate selection of the solution of the precursors. The main idea is to use a volume of solution equal to the volume of the pores present in the support (Incipient Wetness Infiltration, IWI). This strategy should bring to the complete penetration of the precursor into the pores. The successive solvent evaporation should leave nanoparticles of Pd deposited inside the pores of the electrode materials so avoiding the nanoparticles coalescence. The procedure was carried out with a solution characterized by a concentration of palladium cations enough to reach the 1, 2 and 3% wt. amount in a volume corresponding to the pore volume. The successive thermal treatment was carried out using the same conditions already mentioned for infiltration.

The SEM images obtained by infiltration and IWI are compared in **Figure 2 (c-d)**. As it can be observed there is no trace, in the new electrode, of agglomeration of Pd particles. The Pd particles are highly dispersed and not visible with SEM but the presence of Pd in the surface is underlined by X-Ray Photoelectron Spectroscopy (XPS).

In **Figure 2-b** the Nyquist plots comparison between 1% wt. Pd infiltration and IWI is shown. The presence of two processes is confirmed also with the new deposition and the attributions could be the same discussed before. Significant is the resistance lowering of both oxidation and diffusion processes given by the new deposition technique. At 650 °C in a 50% CH_4 atmosphere in Ar, the ASR is reduced from 10.63 Ωcm^2 of the infiltrated electrode

to $2.42 \Omega\text{cm}^2$ with IWI. The decrease of the resistance is obtained maintaining the same quantity of Pd (1% wt.).

To verify the best anode composition several symmetric cells characterized by increasing amounts of Pd have been realized and tested. The ASR values and the corresponding Nyquist plots obtained in methane have been compared in **Table 4** and **Figure 3-a**, respectively.

The comparison among data clearly shows that the best composition is 2% wt. Pd/Cu@GDC. Even if a higher amount of infiltrated Pd (3% wt.) is supposed to give a higher catalytic activity to the electrodes, this does not correspond to a lower ASR. The causes of this inconsistency could be the formation of big particles that brings to the cancellation of the beneficial effects of the noble metal on catalytic activation of methane.

Once optimized the electrode composition the successive step is the evaluation of the durability of the electrode. To this purpose we carried out several tests for prolonged time, also considering intermittence. The results are summarized in **Figure 3-b** and **Table 4**. Of course, the test cannot be considered a probative test for the long-term reliability of the material, but certainly can be indicative of its behavior in the first operating hours, that are widely known in literature to be the most affected by a decadence of the performance. After a first decrease of the ASR due to the stabilization of the testing conditions, there is an increase of the resistance. Anyway, no significant ASR variation was detected between the 10th and the 30th hour. A great temporary decrease of the ASR is present after the second switch off. A possible explanation can be found in the positive effect to the electronic conductivity that carbon coking can give. Unfortunately, the benefits are obtained only for a very narrow window of carbon deposition quantity. After that, the negative effects given by the surface coking of the electrodes take over.

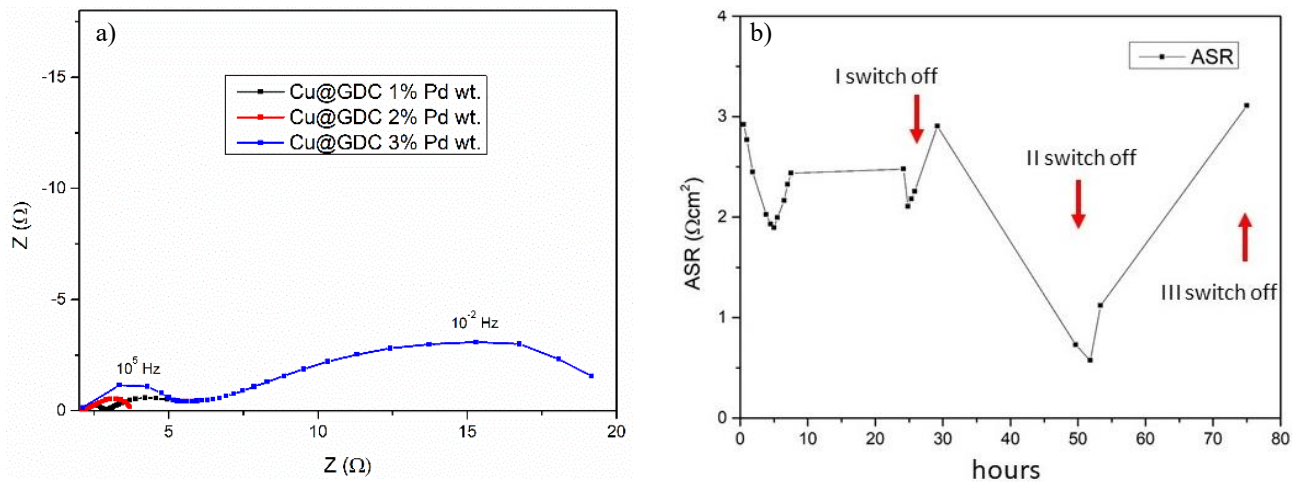


Figure 3: a) Nyquist plots of symmetrical cells with Cu@GDC 1-2-3% Pd wt. as electrodes. The measurements were performed at 650 °C in a testing atmosphere composed by a gas mixture of 50% CH₄ in Ar. b) Cu@GDC 2% Pd wt.: ASR values determined as a function of the permanence under measure conditions and after 3 switch off.

Cu@GDC		50% CH ₄	
Amount of Pd (wt %)	Catalytic process (Ωcm ²)	Total (Ωcm ²)	
1	0.39	3.02	
2	0.16	1.04	
3	0.33	2.92	

Table 4: ASR values for the catalytic process and total electrode in correspondence of Pd percentage infiltrated by IWI on the electrode surface.

Once developed, optimized, and tested the electrode, the successive step is the development and optimization of the complete cell. The device was realized following the sample procedure already mentioned. The cell is: Pd 2% wt. - Cu@GDC/GDC/LSCF:GDC.

5.5 Full cell electrochemical characterization

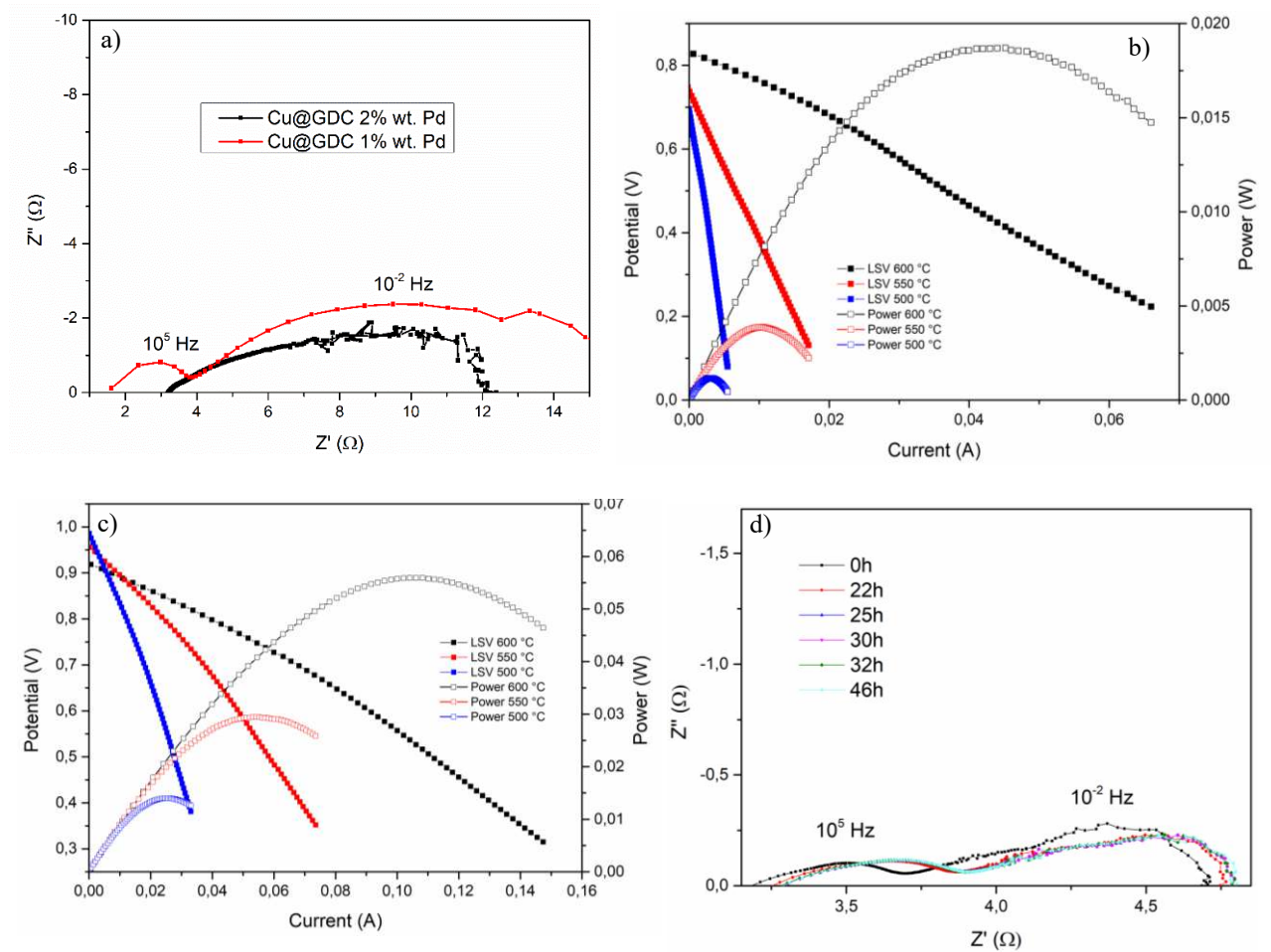


Figure 4: a) Nyquist plots of full cells. The cathode is LSCF:GDC (50:50), while the anode is composed by Cu@GDC with IWI of Pd (1-2% wt. comparison). The tests were performed at 650 °C with 50% CH₄ in Ar. b) LSV results obtained fueling 100% CH₄ at the anodic side as a function of the temperature. c) LSV results obtained fueling a gas mixture of 20% CH₄, 30% H₂, balancing with Ar, as a function of the temperature. d) Nyquist plot observed for the cell Pd 2% wt. - Cu@GDC/GDC/LSCF:GDC operating at 600 °C in the model fuel mixture for increasing time and after switching off and on.

Time (h)	ASR (Ωcm^2)	OCP (V)	Power (mW/cm ²)	CH ₄ Power (mW/cm ²)	20% H ₂ Power (mW/cm ²)
0	2.27	0.92	56	17	44
22 (after switch-off and on)	1.95	0.91	50		
25	1.95	0.91	50		
30	1.89	0.91	50		
32	1.86	0.91	49		
46	1.81	0.91	48		
50	1.84	0.90	48		

Table 5: Performances (ASR, OCP, Power) observed for the cell Pd 2% wt. - Cu@GDC/GDC/LSCF:GDC operating at 600 °C in the model fuel mixture for increasing time and after switching off and on. For comparison, the maximum power obtained in pure methane and 20% hydrogen at 600 °C are shown.

The total resistance of the complete cell with the anode infiltrated with 2% wt. of Pd is better than the one obtained using 1% Pd (**Figure 4-a**) as expected by the symmetrical cell tests. This is confirmed also by the power/potential curves (34 mW/cm² and 29 mW/cm² for 2% and 1% Pd wt. respectively).

As a general comment it needs to be considered that rather low powers are expected because of the specific cell architecture (electrolyte thickness is very high, about 1000 μm). The complete cells, that we usually test, are the so-called “button cell”: this cell typology is chosen since easier to realize with common laboratory equipment. This is a good choice for tests on a laboratory scale, but it is not the cell architecture that guarantees the best performances. In addition, the cells are electrolyte supported, while the commercial ones are anode supported. The anode supported cell combines a thin electrolyte and a larger availability of active sites: two fundamental properties to achieve better performances. In the present work the aim was in comparing electrode materials but, for sure, the next step toward application, will be the optimization of the cell architecture.

The linear polarization curves of the designed cell in pure methane are shown in **Figure 4-b**. The OCP, the indicator of the correct functioning of the cell, is rather high and reproducible. This means that the electrode is well performing, and good device performances can be obtained by decreasing the electrolyte thickness and optimizing the cell realization procedure.

Another interesting consideration concerns the working capability of the developed electrode under 100% methane: a very good result if compared with the scientific literature. Moreover, this is confirmed also at the very low goal temperature of 500 °C. Honestly, it is difficult to compare the power density obtained in this work, with those found in literature, since their values are highly influenced by the experimental setup. Anyway, the relevance of the results just presented can be easily understood considering that the main part of the contribution shows anode materials able to work starting from 600 °C. [38] Actually, it was possible to find one work published on Nature Energy by *Chen et al.* attesting the incredible result of 370 mW in dry methane, where the anode is a BaZr_{0.1}Ce_{0.7}Y_{0.1}Yb_{0.1}O_{3-δ}-based multifunctional anode coated with Ce_{0.90}Ni_{0.05}Ru_{0.05}O₂ (CNR). [39] It is of easy comprehension that, considering the complex stoichiometry of the compounds, the usage

of CRMs like Ru and Yb, and the “Baroque” material morphology, will be very difficult the exploitation of this material in the industrial sector.

The performance of the newly developed cell has been investigated, finally, with the fuel mixture suggested by modelling to be the better performing one in $H_2 + CH_4$. This mixture is composed by the 20% of hydrogen and 30% CH_4 . Ar is used for balance. The Nyquist plots and the power/potential curves obtained for the model mixture are compared in **Figure 4-b**; the comparison among the obtained results suggests that the model mixture allows to reach better performance with respect to both hydrogen (20%) and methane (100 %) (**Table 5**).

To evaluate the stability, the cell was tested in a two days campaign and the results are summarized in **Figure 4-d** and **Table 5**. There is a contrast between the slight decrease of the ASR and the opposite lowering of maximum power. The first one is probably to be attributed to the formation of some carbon particles that help enhancing the electronic conductivity. On the contrary, the carbon presence on the surface electrode reduces the catalytic activity, with the consequent recorded lower performances. Anyway, no significant detrimental effects are observed in the first operating hours that can be aware for the application of this new anodic material. To better understand this phenomenon, which is relevant in terms of cell performance vs time, the deposition of carbon during cell operation was studied in a in situ Raman equipment.

5.6 Measurements in NH_3

In the last years another solution in terms of green energy production through SOFC technology was investigated by the scientific community. And this possible solution consists in the usage of ammonia as fuel. Indeed, ammonia is a good indirect hydrogen storage compound, and it does not contain carbon atoms in the molecule, so there is no possibility to generate CO_2 emissions by its oxidation. Furthermore, it is highly less inflammable compared to hydrogen, and possible leaks in industrial implants are easily detectable since human nose can notice just few hundreds ppm of NH_3 .

The availability of ammonia is quite high. It is commonly produced through Haber-Bosch (HB) process for many and different applications: from fertilizer in the agriculture sector to the industrial one, where it was used as a refrigerant. Furthermore, Italy is one of the biggest producers of ammonia with an annual production of 2365k tons.

As just said Haber-Bosch is the commonly used process for ammonia production, where the overall occurred reaction is:



Even though HB is a well consolidated and widely used process, it is not highly sustainable, due to the required high pressures and needed to promote the desired reaction. The difficult green synthesis of ammonia could be seen as an important obstacle for the effective utilization of NH_3 fueled SOFC in the next years. For this reason, the scientific community is making great efforts in the research for sustainable ammonia production. Especially, being inspired by nature. Indeed, there are microorganisms able to convert N_2 , taken from the atmosphere, in NH_3 , using hydrogen present in water. They can do that thanks to a metalloenzyme called nitrogenase, which contains iron and molybdenum. [40]

Anyway, coming back to the NH_3 fueled SOFCs, two are the main reactions that an anode material should be able to catalyze: the ammonia cracking into nitrogen and hydrogen; and the following use of the H_2 as fuel. The most studied material, since it is not possible to use the term state-of-art for a technology at this preliminary stage, is Ni-YSZ, the same material used for the more common hydrogen fueled SOFCs. Even though the possibility to use perovskites, like Ni exsolved lanthanum titanate, are well investigated too. [41]

Since Cu@GDC 2% wt. Pd showed very good performances in hydrogen, the only step that should be a problem for this material is the ammonia cracking at low temperature. Indeed, this is not a problem at high temperatures since the ammonia cracking occurs spontaneously over 800 °C. Once verified the efficiency of the material towards this reaction, the possibility to use this electrode material not only for hydrogen and methane, but also for ammonia as fuel could be theorized.

To confirm that a symmetrical cell Cu@GDC 2% Pd wt./GDC/ Cu@GDC 2% Pd wt. was tested in a single chamber setup. The tests were carried out in wet conditions (3% of H_2O)

and with a total flux of 100 sccm of a gas mixture $\text{NH}_3:\text{Ar}$ (40:60) . To investigate the electrocatalytic performances of the two electrodes the tests have been carried out at the following temperatures: 650 °C, 600 °C, 550 °C, and 500 °C (**Figure 5**).

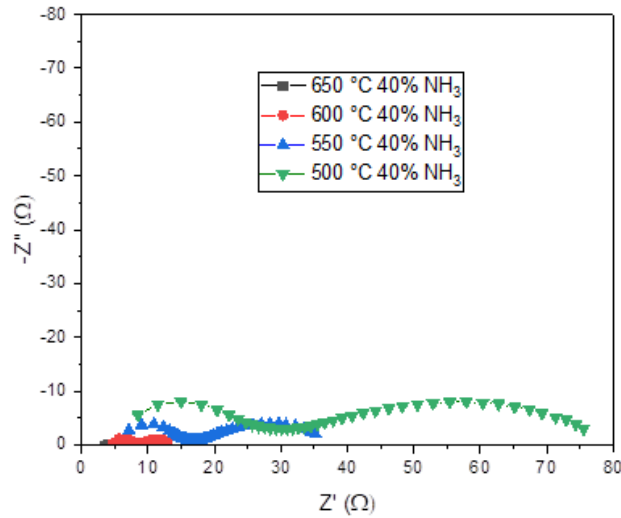


Figure 2: Nyquist plots for Cu@GDC 2% Pd wt. tests carried out in a 40% NH_3 atmosphere, in a temperature range between 500 °C and 650 °C.

	40% NH_3	50% CH_4
T (°C)	ASR (Ωcm^2)	ASR (Ωcm^2)
500	47.08	
550	20.28	
600	6.02	
650	1.08	1.04

Table 6: ASR values obtained in NH_3 for Cu@GDC 2% Pd wt. The value of ASR obtained in a 50% CH_4 in Ar atmosphere is presented for comparison.

The obtained results attest that the material can give similar performances to methane over 600 °C. On the contrary, below this temperature, the resistances are quite high. A possible explanation for this behaviour can be given considering that the activity of copper about ammonia cracking is not enough.

Therefore, these preliminary results, should not discourage the usage of this kind of material for ammonia fuelled SOFCs. On the contrary, it is evident that this material could be very promising if optimized, for example by introducing Ni nanoparticles impregnation that could enhance the performances about ammonia cracking.

This measurement was made since it was not possible to ignore the great hype that this kind of technology has created to the scientific community working in the SOFCs field. Anyway,

even though these encouraging results, no further tests were made, giving the priority to the tests carried out in methane, that is the main topic of this research work.

5.7 Conclusions

In this study are discussed the performances of a new designed anode electrode material for Direct Methane Intermediate to Low Temperatures Solid Oxide Fuel Cell (DM-ILT SOFC). The main goal is to obtain anodes capable to directly use methane, trying to limit the source gas processing and to reduce the working temperature till 500 °C (LT-SOFC). The activity in gas mixture of H₂ and CH₄ is studied as well, since the transition to green hydrogen energy production will pass through an intermediate step of coexistence of the two gases in the transport implants of our cities.

A possible anodic solution is a cermet material composed by GDC on which copper nanoparticles are deposited trough citrate method, starting through CuO then treated in a reduction atmosphere. The first tests made on symmetrical cells have suggested the necessity of a noble metal (Pd) in order to enhance the catalytic activity at lower temperatures. Palladium nanoparticles were infiltrated through an aqueous solution, containing the noble metal precursor, on the surface of the electrode. EIS impedance spectra demonstrate that this solution allows to decrease significantly the total ohmic resistance of the anode and the best performances are obtained with 2% Pd wt. After the anode material optimization, the complete cell LSCF:GDC(50:50)/GDC/Cu@GDC-2%Pd(wt), was tested in pure methane and a gas mixture of CH₄:H₂ 3:2. Cell operation is confirmed till 500 °C in pure methane and a good performance of 14 mW/cm² is obtained with the gas mixture at the same temperature. In the end, the summary of the results obtained in this study are shown in **Table 7**. The possibility to use this material as anode for ammonia fueled SOFCs was investigate as well. Good results above 600 °C were obtained, while should be considered the implementation of a Ni nanoparticles impregnation, in order to improve the ammonia cracking at low temperatures.

Temperature (°C)	Atmosphere	OCP (V)	Power (mW/cm ²)
650	20% H ₂	0.84	71
600	20% H ₂	0.90	44
	20% H ₂ / 30% CH ₄	0.92	52
	100% CH ₄	0.83	17
550	20% H ₂	0.96	27
	20% H ₂ / 30% CH ₄	0.96	29
	100% CH ₄	0.74	4
500	20% H ₂	0.98	12
	20% H ₂ / 30% CH ₄	0.98	14
	100% CH ₄	0.70	1

Table 7: Summary table of all the results obtained during this study in function of atmosphere and temperature for the LSCF:GDC (50:50)/GDC/Cu@GDC 2% Pd wt. complete cell.

References

- [1] A. Alamia, I. Magnusson, F. Johnsson, and H. Thunman, "Well-to-wheel analysis of bio-methane via gasification, in heavy duty engines within the transport sector of the European Union," *Appl Energy*, vol. 170, pp. 445–454, May 2016, doi: 10.1016/j.apenergy.2016.02.001.
- [2] M. Balat, "Sustainable transportation fuels from biomass materials," *Energy Education Science and Technology*, vol. 17, no. 1/2, p. 83, 2006.
- [3] S. N. Naik, V. v. Goud, P. K. Rout, and A. K. Dalai, "Production of first and second generation biofuels: A comprehensive review," *Renewable and Sustainable Energy Reviews*, vol. 14, no. 2, pp. 578–597, Feb. 2010. doi: 10.1016/j.rser.2009.10.003.
- [4] C. Robinson and D. B. Smith, "The Auto-ignition Temperature of Methane," *J Hazard Mater*, vol. 8, pp. 199–203, 1984.
- [5] M. G. Zabetakis, "Flammability characteristics of combustible gases and vapors," Bureau of Mines Washington DC, 1965.
- [6] Mass. Boston, "Properties of Flammable Liquids, Gases, and Solids," *Ind Eng Chem*, vol. 32, no. 6, pp. 880–884, Jun. 1940, doi: 10.1021/ie50366a030.
- [7] J.-H. Koh, Y.-S. Yoo, J.-W. Park, and H. C. Lim, "Carbon deposition and cell performance of Ni-YSZ anode support SOFC with methane fuel," *Solid State Ion*, vol. 149, pp. 157–166, 2002, [Online]. Available: www.elsevier.com/locate/ssi
- [8] N. Shi *et al.*, "Anode in Direct Methane-Fueled Solid Oxide Fuel Cells," 2021, doi: 10.1021/acsami.0c17339.
- [9] C. Aliotta, L. F. Liotta, F. Deganello, V. La Parola, and A. Martorana, "Applied Catalysis B : Environmental Direct methane oxidation on La 1 – x Sr x Cr 1 – y Fe y O 3 – 1 perovskite-type oxides as potential anode for intermediate temperature solid oxide fuel cells," *Appl Catal B*, vol. 180, pp. 424–433, 2016, doi: 10.1016/j.apcatb.2015.06.012.
- [10] J. Sfeir *et al.*, "Lanthanum Chromite Based Catalysts for Oxidation of Methane Directly on SOFC Anodes," vol. 244, pp. 229–244, 2001, doi: 10.1006/jcat.2001.3286.
- [11] A. Ovalle, J. C. Ruiz-morales, J. Canales-vázquez, D. Marrero-lópez, and J. T. S. Irvine, "Mn-substituted titanates as efficient anodes for direct methane SOFCs," vol. 177, pp. 1997–2003, 2006, doi: 10.1016/j.ssi.2006.06.014.
- [12] M. Li, B. Hua, J. Luo, P. Jiang, J. Pu, and L. Jian, "doped barium cerates for direct methane solid oxide fuel cells," pp. 21609–21617, 2015, doi: 10.1039/c5ta06488k.
- [13] A. Ideris, E. Croiset, M. Pritzker, and A. Amin, "Direct-methane solid oxide fuel cell (SOFC) with Ni-SDC anode-supported cell," *Int J Hydrogen Energy*, vol. 42, no. 36, pp. 23118–23129, 2017, doi: 10.1016/j.ijhydene.2017.07.117.
- [14] H. Sumi, P. Puengjinda, H. Muroyama, T. Matsui, and K. Eguchi, "Effects of crystal Structure of yttria- and scandia-stabilized zirconia in nickel-based SOFC anodes on carbon deposition and oxidation behavior," *J Power Sources*, vol. 196, no. 15, pp. 6048–6054, 2011, doi: 10.1016/j.jpowsour.2011.03.092.

- [15] H. Chang, H. Chen, Z. Shao, J. Shi, J. Bai, and S. Li, "nanoparticles as an independent catalyst layer for direct methane-based solid oxide fuel cells with," pp. 13997–14007, 2016, doi: 10.1039/c6ta04639h.
- [16] J. Zhao, X. Xu, and Z. Zhu, "An in situ formed MnO–Co composite catalyst layer over Ni–Ce_{0.8}Sm_{0.2}O_{2-x} anodes for direct methane solid oxide fuel cells," pp. 6494–6503, 2017, doi: 10.1039/c6ta10473h.
- [17] M. Haneda, T. Mizushima, and N. Kakuta, "Synergistic Effect between Pd and Nonstoichiometric Cerium Oxide for Oxygen Activation in Methane Oxidation," *J. Phys. Chem. B*, vol. 102, pp. 6579–6587, 1998, [Online]. Available: <https://pubs.acs.org/sharingguidelines>
- [18] K. Otsuka, Y. Wang, E. Sunada, and I. Yamanaka, "Direct Partial Oxidation of Methane to Synthesis Gas by Cerium Oxide," *J Catal*, vol. 175, no. 2, pp. 152–160, 1998.
- [19] A. Tschöpe, W. Liu, M. Flytzanistephanopoulos, and J. Y. Ying, "Redox Activity of Nonstoichiometric Cerium Oxide-Based Nanocrystalline Catalysts," *J Catal*, vol. 157, no. 1, pp. 42–50, 1995.
- [20] Y. J. Leng, S. H. Chan, S. P. Jiang, and K. A. Khor, "Low-temperature SOFC with thin film GDC electrolyte prepared in situ by solid-state reaction," *Solid State Ion*, vol. 170, no. 1–2, pp. 9–15, May 2004, doi: 10.1016/j.ssi.2004.02.026.
- [21] T. Huang and M. Huang, "Electrochemical promotion of bulk lattice-oxygen extraction for syngas generation over Ni-GDC anodes in direct-methane SOFCs," vol. 135, pp. 216–223, 2008, doi: 10.1016/j.cej.2007.03.015.
- [22] Y. Lin, Z. Zhan, J. Liu, and S. A. Barnett, "Direct operation of solid oxide fuel cells with methane fuel," vol. 176, pp. 1827–1835, 2005, doi: 10.1016/j.ssi.2005.05.008.
- [23] G. Carollo, A. Garbujo, A. Bedon, D. Ferri, and M. M. Natile, "ScienceDirect Cu / CGO cermet based electrodes for Symmetric and Reversible Solid Oxide Fuel Cells," *Int J Hydrogen Energy*, pp. 1–7, 2018, doi: 10.1016/j.ijhydene.2018.01.201.
- [24] J. Nilsson *et al.*, "Chemistry of Supported Palladium Nanoparticles during Methane Oxidation," 2015, doi: 10.1021/cs502036d.
- [25] P. Velin *et al.*, "Water Inhibition in Methane Oxidation over Alumina Supported Palladium Catalysts," 2019, doi: 10.1021/acs.jpcc.9b07606.
- [26] S. P. Jiang, Y. Ye, T. He, and S. B. Ho, "anodes for direct methane and ethanol solid oxide fuel cells," vol. 185, pp. 179–182, 2008, doi: 10.1016/j.jpowsour.2008.06.099.
- [27] H. Zhu, J. E. Soc, H. Zhu, R. J. Kee, and V. M. Janardhanan, "Modeling Elementary Heterogeneous Chemistry and Electrochemistry in Solid-Oxide Fuel Cells and Electrochemistry in Solid-Oxide Fuel Cells," 2005, doi: 10.1149/1.2116607.
- [28] C. Marcilly, P. Courty, and B. Delmon, "Preparation of highly dispersed mixed oxides and oxide solid solutions," *Journal of the American Ceramic Society*, vol. 53, no. 1, p. 56, 1970, doi: 10.1111/j.1151-2916.1970.tb12003.x.
- [29] M. Ojeda, T. Zhao, H. Wang, and J. Xuan, "Ni-YSZ Nanocomposite Synthesis: Mechanochemical vs Novel Sol-Gel Method for Solid Oxide Electrolysers," *Energy Procedia*, vol. 142, pp. 1095–1099, Dec. 2017, doi: 10.1016/J.EGYPRO.2017.12.362.
- [30] D. R. Mullins, S. H. Overbury, and D. R. Huntley, "Electron spectroscopy of single crystal and polycrystalline cerium oxide surfaces," *Surf Sci*, vol. 409, no. 2, pp. 307–319, Jul. 1998, doi: 10.1016/S0039-6028(98)00257-X.
- [31] E. Paparazzo, G. M. Ingo, and N. Zacchetti, "X-ray induced reduction effects at CeO₂ surfaces: An x-ray photoelectron spectroscopy study," *Journal of Vacuum Science & Technology A*, vol. 9, p. 1416, 1991, doi: 10.1116/1.577638.
- [32] K. Wandelt, "Photoemission studies of adsorbed oxygen and oxide layers," *Surf Sci Rep*, vol. 2, no. 1, pp. 1–121, Sep. 1982, doi: 10.1016/0167-5729(82)90003-6.
- [33] D. Raiser and J. P. Deville, "Study of XPS photoemission of some gadolinium compounds."

- [34] D. Tyagi, P. K. Rao, and B. N. Wani, "XPS studies of Mg doped GDC (Ce_{0.8}Gd_{0.2}O_{2-δ}) for IT-SOFC," in *AIP Conference Proceedings*, Apr. 2018, vol. 1942. doi: 10.1063/1.5028951.
- [35] R. J. Farrauto, J. K. Lampert, M. C. Hobson, and E. M. Waterman, "Thermal decomposition and reformation of PdO catalysts; support effects," *Appl Catal B*, vol. 6, no. 3, pp. 263–270, Aug. 1995, doi: 10.1016/0926-3373(95)00015-1.
- [36] M. Brun, A. Berthet, and J. C. Bertolini, "XPS, AES and Auger parameter of Pd and PdO," *J Electron Spectros Relat Phenomena*, vol. 104, no. 1–3, pp. 55–60, Jul. 1999, doi: 10.1016/S0368-2048(98)00312-0.
- [37] A. Flura *et al.*, "Identification and modelling of the oxygen gas diffusion impedance in SOFC porous electrodes: application to Pr₂NiO_{4+d}," *Electrochim Acta*, vol. 174, pp. 1030–1040, 2015, doi: 10.1016/j.electacta.2015.06.084.
- [38] P. Qiu *et al.*, "A review on anode on-cell catalyst reforming layer for direct methane solid oxide fuel cells," *Int J Hydrogen Energy*, vol. 46, no. 49, pp. 25208–25224, 2021.
- [39] Y. Chen *et al.*, "A robust fuel cell operated on nearly dry methane at 500 °C enabled by synergistic thermal catalysis and electrocatalysis," *Nat Energy*, vol. 3, no. 12, pp. 1042–1050, 2018, doi: 10.1038/s41560-018-0262-5.
- [40] A. Afif, N. Radenahmad, Q. Cheok, S. Shams, J. H. Kim, and A. K. Azad, "Ammonia-fed fuel cells: a comprehensive review," *Renewable and Sustainable Energy Reviews*, vol. 60, pp. 822–835, 2016.
- [41] J. Cavazzani, E. Squizzato, E. Brusamarello, and A. Glisenti, "Exsolution in La and Ni co-doped strontium titanate: a suitable anode for running SOFCs on ammonia as alternative fuel," in *E3S Web of Conferences*, 2022, vol. 334, p. 04008.

Chapter 6: Raman *ex situ* and *in situ* spectroscopy characterization

During my PhD, I have spent almost 4 months, between September and December 2021 in Denmark, as visiting student in the Prof. Peter Holtappels research group at the Technical University of Denmark (DTU). The main goal of my stay at DTU was the possibility to perform *ex situ* and *in situ* Raman Spectroscopy on the studied powders and cell electrodes.

6.1 Raman theory

To derive the Raman effect, it is better to consider the classical interpretation, where light is seen as an electromagnetic wave. This, containing an oscillating electrical field, can interact with molecules through its polarizability. If we use the classical approach, a diatomic molecule should be considered as two masses on a spring, as presented in the following figure.

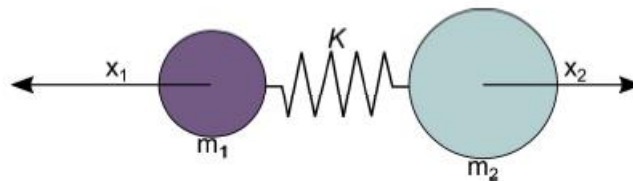


Figure 1: Representation of a diatomic molecule as two masses on a spring.

Based on this hypothesis, it is possible to express the molecule displacement, through Hook's law.

$$\frac{m_A m_B}{m_A + m_B} \left(\frac{d^2 x_A}{dt^2} + \frac{d^2 x_B}{dt^2} \right) = -k(x_A + x_B) \quad (1)$$

Where, m , is the atomic mass, x , the displacement, and k , is the elastic constant, that represents the bond strength. If the reduced masses are replaced with μ and the total displacement with q , the equation ^[1] can be simplified to:

$$\mu \frac{d^2 q}{dt^2} = -kq \quad (2)$$

Solving this last equation for q , it is obtained that:

$$q = q_0 \cdot \cos(\omega t) \quad (3)$$

Where ω stands for the molecular vibration and can be defined as:

$$\omega = \sqrt{\frac{k}{\mu}} \quad (4)$$

From the last two equations, [3] and [4], it is possible to extrapolate that the molecule vibrates with a cosine pattern and its frequency is proportional to the bond strength. In addition, it is inversely proportional to the reduced masses. Therefore, every molecule is characterized by its unique vibrational signature, that is not only determined by the molecule atoms, but by the individual bonds too. These vibrational frequencies can be determined and measured by the Raman effect, since the polarizability of a molecule (α) is correlated with the displacement q . When the molecule is illuminated, the incident light induces a dipole moment (P). The dipole moment is defined as:

$$P = \alpha \cdot E_0 \cdot \cos(\omega_0 t) \quad (5)$$

Where, E_0 is the intensity and ω_0 is the frequency of the incident electric field. By using the Taylor expansion, and considering the small amplitude approximation, it is possible to describe the polarizability as a linear function of the displacement:

$$\alpha = \alpha_0 + q \left(\frac{\partial \alpha}{\partial q} \right)_{q=0} + \dots \quad (6)$$

If the equation (6) is combined with (3) and (4), is it possible to obtain:

$$P = \alpha_0 E_0 \cdot \cos(\omega_0 t) + E_0 \cdot \cos(\omega_0 t) \cdot q_0 \cdot \cos(\omega_0 t) \cdot \left(\frac{\partial \alpha}{\partial q} \right)_{q=0} \quad (7)$$

By expanding the second term, that corresponds to the Raman scatter component, there is a shift of the incident light, in correspondence with the frequency of the molecular vibration. This is the change of frequency that is measured by Raman spectroscopy.

Obviously, it is possible to describe better this phenomenon by the quantum interpretation. Following this interpretation, the Raman effect can be viewed as a phonon inelastic scattering. This view can be visualized by the diagram in **Figure 2**.

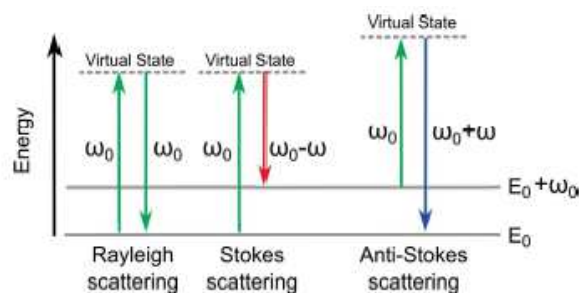


Figure 2: Jablonski diagram. The quantum energy transitions for Rayleigh and Raman Scattering are represented.

When the incident light reaches the molecule, it is excited into a virtual state and three situations can be observed. The first, and most probable, is that the molecule relaxes elastically to the ground state and emits a photon with the same energy of the incident one. This process it is also called Rayleigh scattering. The second scenario consists in the relaxation of the molecule to a real phonon state and thereby a less energetic photon, compared to the exciting light, is emitted. This is known as Stokes shifted Raman scattering. The third possibility is that the molecule is already in an excited state when the photon hits it. In this case, when the molecule relaxes down to the ground state, a photon with a higher energy, compared to the exciting one, is emitted. This scattering is called Anti-Stokes.

Raman spectroscopy is a technique where the light, usually from a laser, is used to illuminate the material and the resulted backscattered Raman radiation is detected and consequently, the vibrational modes of molecules are detected. Lasers are used since many photons can be concentrated in one spot. This is important since the Stokes and Anti-Stokes scattering are less probable than the Rayleigh one, so it is important to excite a lot of molecules, to obtain a good signal for these Raman scattering. Signal given by the backscattered light and visualized in an intensity spectrum, where the material-specific vibrational modes appear as peaks as a function of the Raman shifts, which is expressed in cm^{-1} . Typically, the used lasers have a wavelength between the ultraviolet (UV) and infrared (IR) region. In this chapter, the tests are carried out with a visible laser light with a wavelength of 532 nm.

It must be known that not all the vibrational modes are Raman active, and it is possible to determine which ones are active by looking at a classic macroscopic example. Let's consider a water molecule (**Figure 3**). This molecule will have $3N-6$ vibrational modes, with N is the number of atoms in the molecule. $3N$ are the number of degrees of freedom, excluding the

three translational and the three rotational modes. Therefore, three are the Raman active vibrational modes for water.

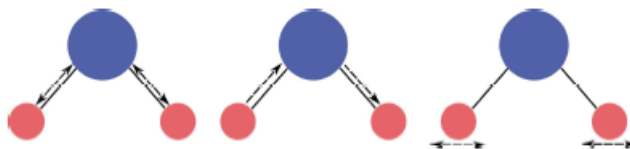


Figure 3: Water molecule vibrational modes.

Since this rule is not true for all the molecules (let's consider CO₂ that presents 3 vibrational modes, but only one is Raman active), selection rules have been devised to determine which vibrations are Raman active and which are not. If the polarizability tensor α change with displacement during the vibration, this vibrational mode is Raman active. Mathematically description can be written as:

$$\frac{\partial \alpha}{\partial q} \neq 0 \quad (8)$$

α behavior depends on the molecule symmetry. Therefore, only vibrational modes of certain symmetries are Raman active. For molecules with an inversion point, the Raman and IR active modes are mutually exclusive, meaning that if a vibration is Raman active, it cannot be also IR active and vice versa. On the contrary, if a molecule does not present an inversion point, this mutual exclusivity rule does not apply.

Let's take the water molecule as an example. For water all vibrational modes are both Raman and IR active. In general, if there is a change in α with displacement, the vibration is Raman active and if there is a change in the dipole moment, the molecule will be IR active. This can be represented in mathematical terms as:

$$\underbrace{\frac{\partial d}{\partial q} \neq 0}_{IR \text{ active}} \quad \text{or} \quad \underbrace{\frac{\partial \alpha}{\partial q} \neq 0}_{Raman \text{ active}} \quad (9)$$

Since, for more complex molecules it is very difficult to understand which vibration is Raman or IR active. For this reason, the group theory is normally used to understand the Raman active modes. Fortunately, in literature it is possible to easily find the Raman active

vibrational modes for different molecules. One of the most used databases for solid-state Raman spectroscopy are the Ruff database or the work by George Socrates. [1], [2]

6.2 *Ex situ* and *in situ* Raman spectroscopy experimental setup

The synchronous *in situ* Raman studies were performed using a Linkam TS1500 heating stage. This stage allows for temperature control from room temperature and up to 1500 °C under ambient pressure. The sample is placed directly into a ceramic crucible so it can be heated uniformly from underneath and from the sides. The stage body and large diameter quartz lid window are kept at a safe temperature by scaled circulating water. Furthermore, precision quick-release gas valves at the sides of the stage body are used to purge the sample chamber with the desired gases. For enabling electrochemical measurements, internal electrical connectors are feed through Lemo connectors on the outside of the stage. Since the Linkam stage is a commercial product, no detailed description on the stage will be done since this information is available from the manufacturer. [3] The *in situ* Raman data were obtained using a Renishaw InVia Raman spectrometer system coupled with the Linkam heat-stage. The Raman spectrometer was equipped with a 532 nm diode laser, with laser power in the 1 μm diameter beam spot was less than 8 mW, when using a 50X long working distance objective. The Stokes scattered Raman light from the sample was collected and dispersed onto the CCD detector of the spectrometer, The spectral resolution of the Raman equipment has under standard settings, using the 532 nm diode-laser, been found to be 1 cm^{-1} .

Ex situ measurements were performed on the powders and cells. For *ex situ* we mean measurements performed in air at room temperature. The experimental procedure is quite easy and consists of putting the samples on the microscope slide and determining the correct focus distance. This one is detectable by checking the intensity of the signal and determining for which distance the Stokes peaks reaches the highest intensity.

6.3 Experimental test protocols

The studied atmosphere is 3% H₂O, 97 % CH₄. The 3% of steam is added for two reasons: first of all, it is a mild oxidizer, and it reduces the undesired reduction of the backbone material. Secondly, the addition of 3% steam also increases the exchange current density and thereby decreases the polarization resistance. [4] The experimental test protocol starts with the sample heating in humidified air till the first measurement temperature (650 °C). After that the atmosphere is switched to Ar for 5 minutes and finally to methane. The testing atmosphere is maintained for one hour. After that, the sample chamber is switched again in Ar for 5 minutes and again in methane for the measurements. This is repeated for all the tested temperatures: 700 °C, 750 °C, 800 °C and 850 °C.

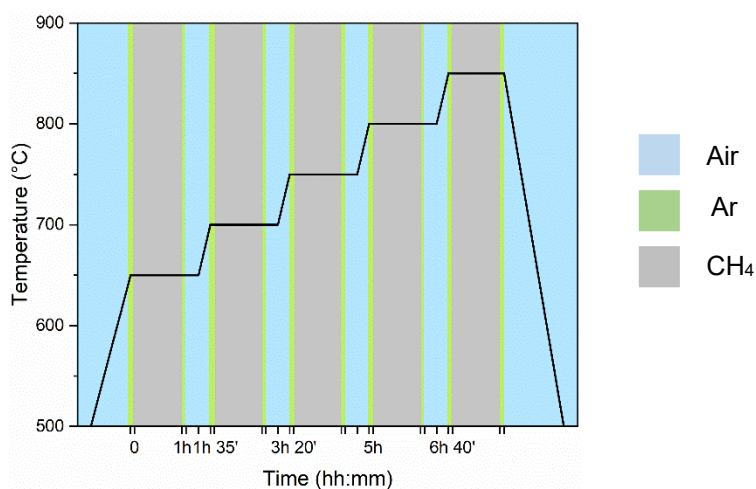


Figure 4: Schematic representation of the test protocol used for all cells in the present chapter.

Before starting with the discussion of the Raman spectra shown in **Figure 6**, let's consider why it is possible to observe Raman signals from perovskite. Indeed, the ideal perovskite ABO₃ structure consists of corner-linked BO₆ octahedra with the A cation in the center of the space between the octahedra. All five atoms of the unit cell occupy centrosymmetrical sites and none of the Γ -point phonon modes ($4F_{1u}$ C F_{2u}) is Raman active. Anyway, many of the real ABO₃ compounds have a distorted perovskite-like structure. As a rule, the ionic radii do not match exactly ($t \neq 1$), which is compensated for either by displacements of the cations along certain directions and/or by tilting of the oxygen octahedra (**Figure 5**). It turns out that there are 23 possible structures that can be formed by tilting alone. [5]

Another source of distortion of the perovskite structure can be the Jahn–Teller (J–T) effect. Following the Jahn–Teller theorem: “for a non-linear molecule in an electronically degenerate state, distortion must occur to lower the symmetry, remove the degeneracy and lower the energy.” [6] The BO_6 octahedra can be considered as non-linear molecules and it depends on the type of cations at the B-sites whether J–T distortions will occur. The J–T effect causes in this case extension or compression of Mn–O bond pairs as shown at the bottom of **Figure 5**. In contrast, Mn^{4+} in octahedral coordination has a singlet (A_{2g}) ground state and no J–T distortions occur. All six $\text{Mn}^{4+} - \text{O}^{2-}_6$ bonds can be of equal length.

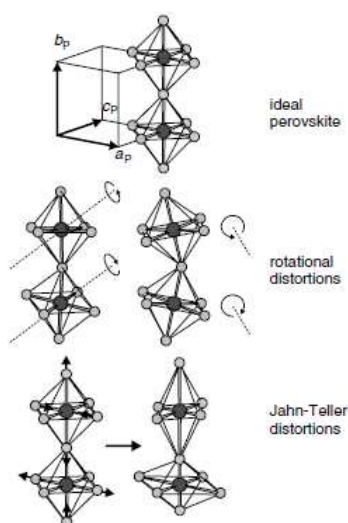


Figure 5: graphical representation of rotational and Jahn-Teller distortion compared to ideal perovskite.

6.4 *Ex situ* measurements

As shown in **Figure 6** (left), the main contribution to the total Raman scattering intensity in $\text{La}_{1-x}\text{Sr}_x\text{MnO}_3$ powders crystal, is related to a band set at about 650 cm^{-1} . This band is mainly due to second-order Raman scattering arising in the rhombohedral (pseudocubic or cubic O_h^1) perovskite disordered structures so far reported for doped $\text{La}_{1-x}\text{Sr}_x\text{MnO}_3$ materials. More precisely it is related to the stretching in the xz plane of Mn–O bond in the BO_6 octahedra of the perovskite lattice. [7] Anyway, looking at the Raman spectrum carried out on the LSM/GDC composite electrode, it is possible to observe as this band is significantly less intense of the main peak set at 461 cm^{-1} , given by the presence of GDC in the composite electrode. The Raman-active mode in GDC is attributed to a symmetrical stretching mode of the Ce–O₈ vibrational unit of cubic ceria. Therefore, this mode should be very sensitive to any disorder in the oxygen sublattice resulting from thermal and/or grain size induced

non-stoichiometry. The influence of the microstructure on the shape of the Raman spectrum was observed through the Raman shift and the width of the Raman mode. [8], [9]

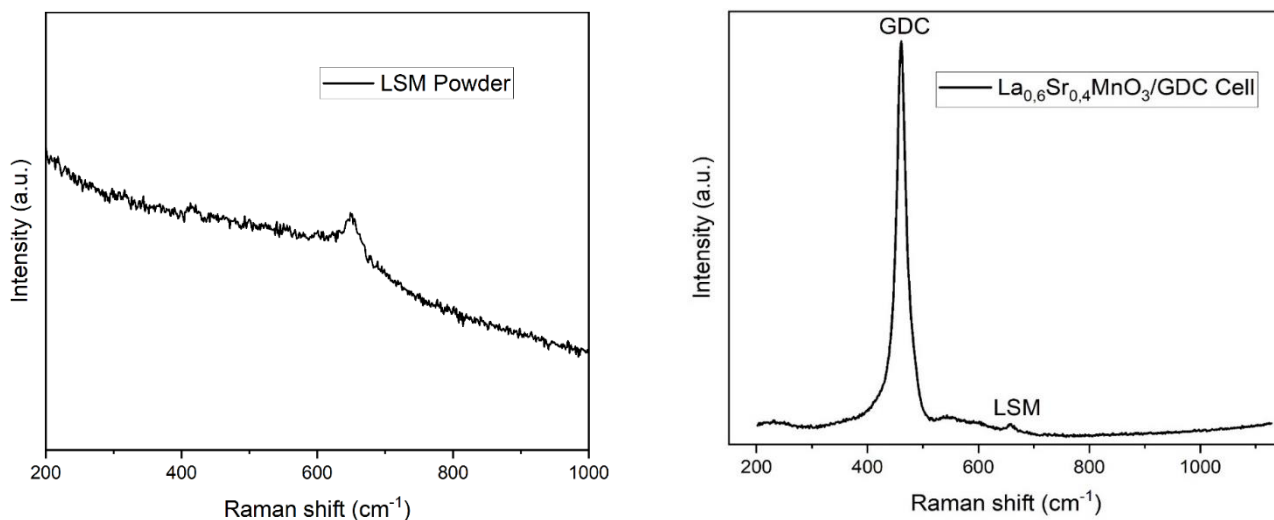


Figure 6: Ex situ Raman spectroscopy on LSM powder (left) and LSM/GDC composite electrode cell (right).

Returning to the discussion of the perovskite peak signal, there is a discrepancy between the experimental data and what it was expected. Indeed, in literature is possible to find a progressive lowering of the Stokes band intensity with the increasing of the Sr quantity inserted inside the structure. This may be explained by the gradual relative decrease of the orthorhombic lattice distortion due to reduction of the Jahn-Teller effect in doped materials, when most $\text{La}_{1-x}\text{Sr}_x\text{MnO}_3$ compounds tend to a cubic structure. In particular, in the spectrum of $\text{La}_{1-x}\text{Sr}_x\text{MnO}_3$ the intensities of the bands at 650 cm^{-1} , typical for the D_{2h}^{16} orthorhombic symmetry, are weak, but still stronger than those in highly doped crystals. In other words, the doping of LaMnO_3 by substitution of Sr^{2+} for La^{3+} has the same effect as the cation deficiency in $\text{La}_{1-x}\text{Mn}_{1-y}\text{O}_3$, namely the number of non-J-T Mn^{4+} ions increases in favor of the J-T Mn^{3+} ions. In particular, the Mn^{3+} at a B-site has an electronically degenerate (T_{1g}) ground state. In contrast, Mn^{4+} in octahedral coordination has a singlet (A_{2g}) ground state and no J-T distortions occur. All six $\text{Mn}^{4+} - \text{O}^{2-}_6$ bonds can be of equal length. The decrease of J-T distortions due to reduction of the $\text{Mn}^{3+}/\text{Mn}^{4+}$ ratio and charge delocalization through $\text{Mn}^{3+} \rightarrow \text{Mn}^{4+}$ transfer, should decrease the intensity of the density-of-state bands. [10]

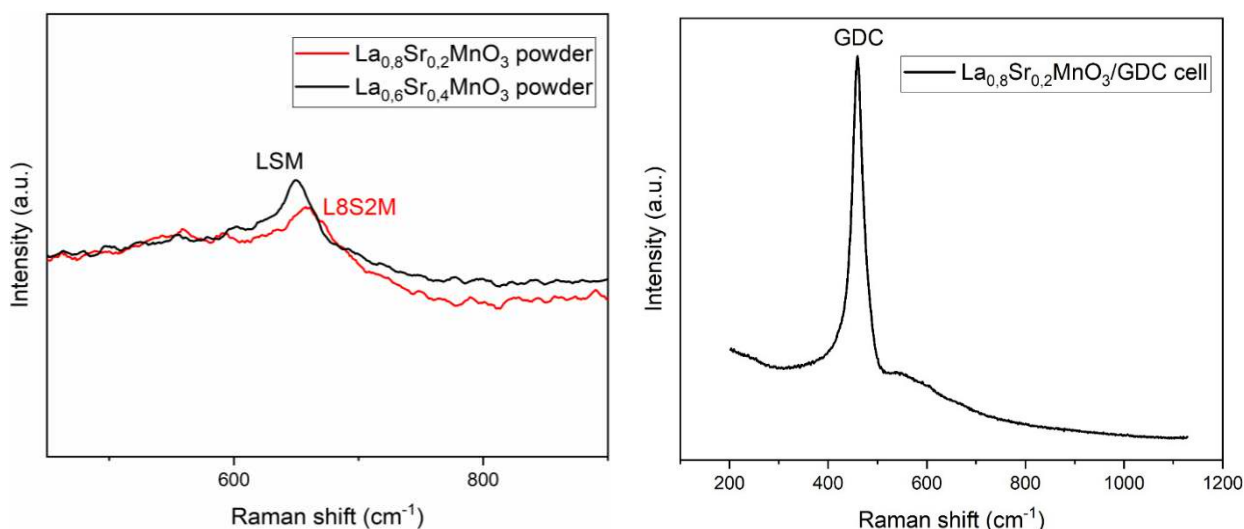


Figure 7: Ex situ Raman spectroscopy on L8S2M powder (left) and L8S2M/GDC composite electrode cell (right).

On the contrary, looking at the *ex situ* Raman spectra for L8S2M powders and for the cell composite electrode (**Figure 7**), the Mn-O stretching band set at 650 cm^{-1} has a lower intensity if compared to the LSM one. The intensity is so low that is not possible to observe the peak in the Raman spectrum carried out on the electrode (right graph of **Figure 7**). It is difficult to explain this marked discrepancy from experimental data and theory, but it deserves to try. This anomaly can be explained by assuming that L8S2M perovskite structure is compatible with the J-T distortions and consequently, the J-T effect does not result in the appearance of Raman spectral features. Otherwise, it is possible to explain this by considering the small penetration depth of the excitation radiation. Indeed, from the XPS analysis shown in the previous [Paragraph 4.6](#), the presence of Mn in the surface is lower compared to LSM and the nominal one. This lower presence of Mn can be responsible of a lower Raman signal. A possible confirm of that could be found by further investigations using a laser with a lower wavelength, for example 488 nm. Indeed, a lower wavelength, corresponds to a higher energy of the laser and consequently a deeper penetration length. On the contrary, The Mn-O bond stretching peak is visible and quite intense for LSCuM in both the spectra. (**Figure 8**)

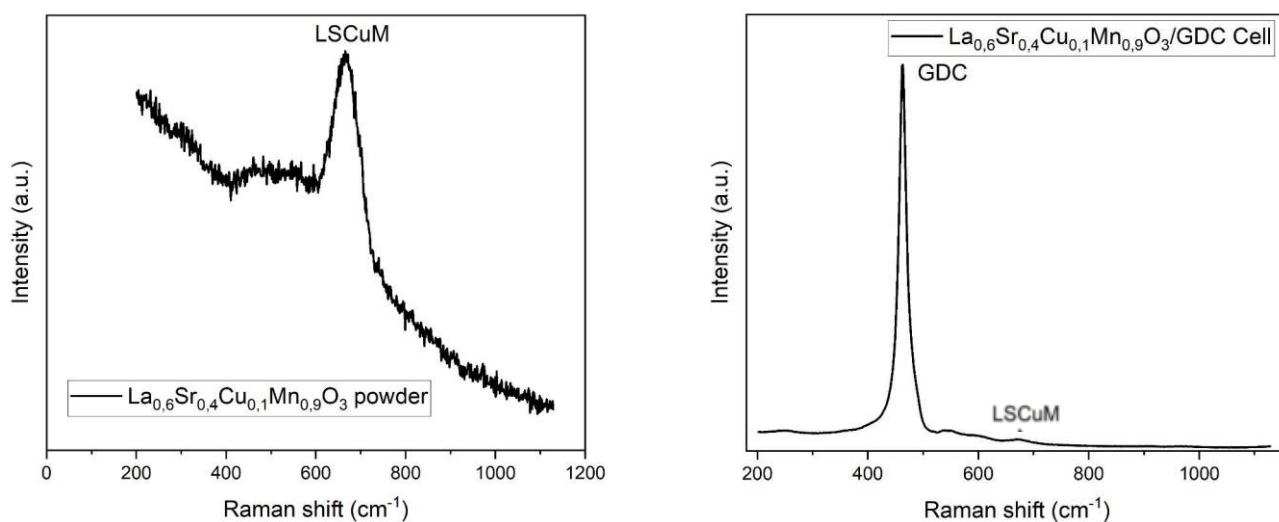


Figure 8: Ex situ Raman spectroscopy on LSCuM powder (left) and LSCuM/GDC composite electrode cell (right).

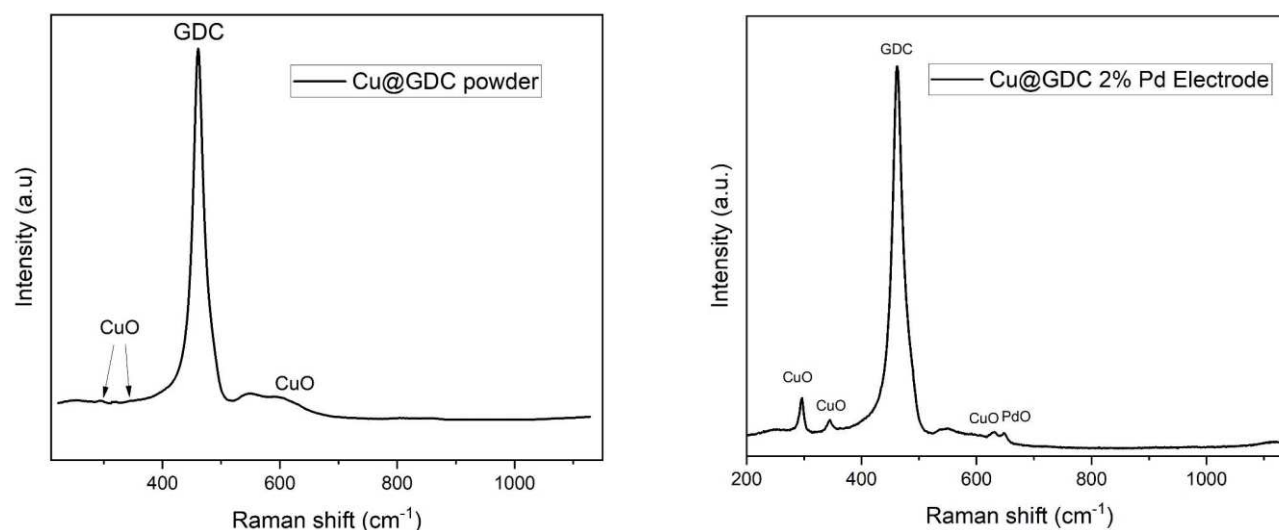


Figure 9: Ex situ Raman spectroscopy on Cu@GDC powder (left) and Cu@GDC 2% Pd composite electrode cell (right).

Finally, let's present the *ex situ* Raman spectra for Cu@GDC powder and Cu@GDC with 2% Pd infiltrated electrode. In these spectra, it is possible to see the usually highly intense band at 461 cm⁻¹ due to the Ce-O vibrational mode. While, for CuO there are three different bands, at 295 cm⁻¹, 344 cm⁻¹ and 611 cm⁻¹, with the second one much weaker than the first one. This is perfectly in accordance with data found in literature. [11] Copper (II) oxide (CuO) belongs to the C_{2h}⁶ space group with two molecules per primitive cell. There are nine zone-center optical phonon modes with symmetries 4A_u + 5B_u + A_g + 2B_g; only three A_g + 2B_g modes are Raman active. The peak at 295 cm⁻¹ in sample A to the A_g and the peaks at 330 and 621 cm⁻¹ to the B_g modes.

In the Raman spectrum for the electrode cell, also a peak set at 648 cm^{-1} referred to PdO infiltration is present. PdO has a tetragonal structure based on the space group D_{4h}^9 with two molecular units per primitive unit cell. The palladium atoms are in D_{2h} sites and the oxygen atoms in D_{2d} sites. Following the nuclear site group analysis of Rousseau et al., [12] the D_{2h} sites give rise to vibrations of species $A_{2u}+B_{1g}+2E_u$ and the D_{2d} sites to $A_{2u}+B_{1g}+E_g+E_u$. There should thus be two Raman-active modes with irreducible representations $B_{1g}+E_g$. The strongest one, and the only one visible in the Raman spectrum presented in **Figure 9**, is the B_{1g} set at 650 cm^{-1} . [13]

6.5 *In situ* measurements

6.5.1 LSM powders

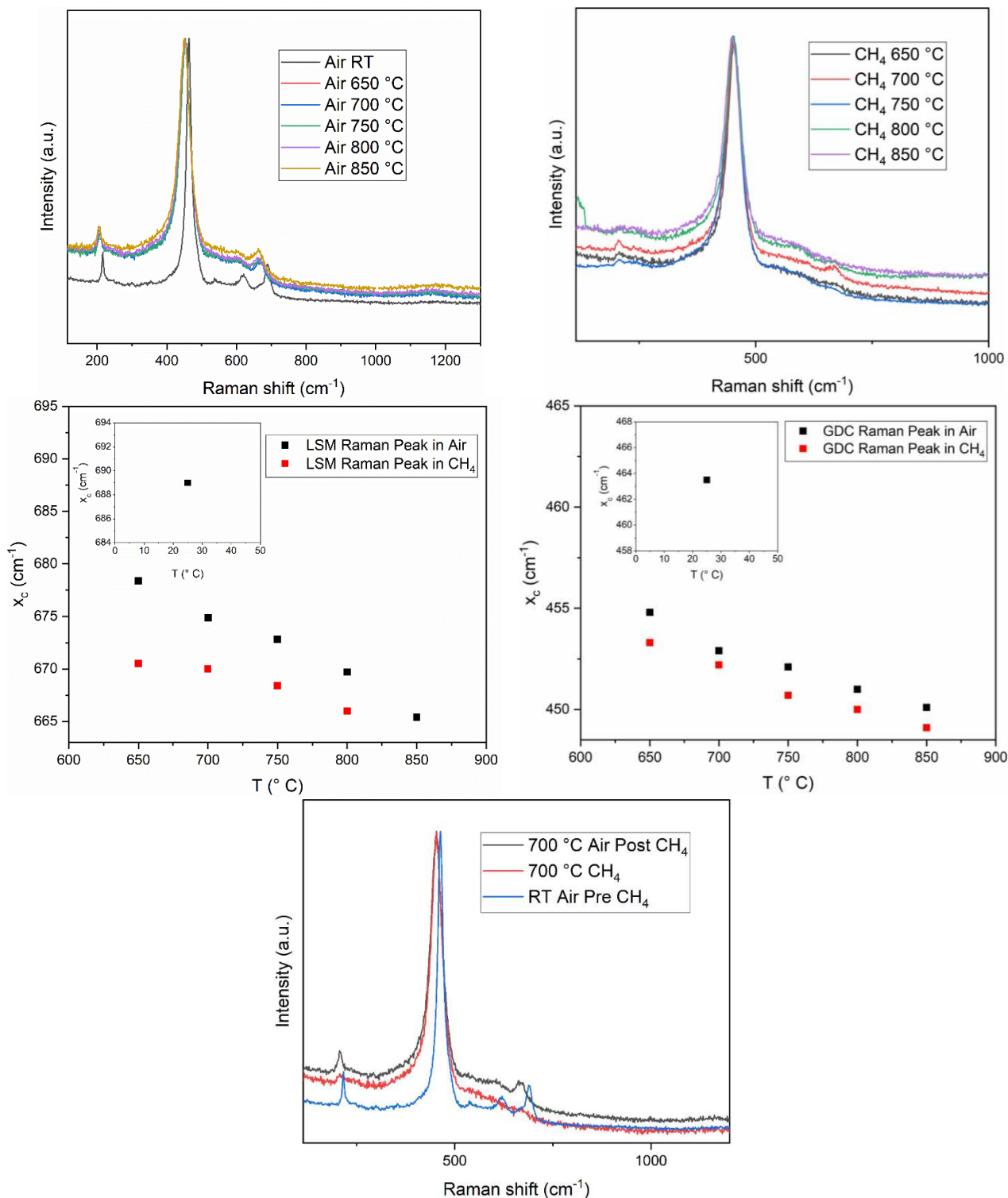


Figure 10: On the top there are presented the *in situ* Raman spectra in air (top left) and in CH₄ (top right). Are also shown the LSM Raman band position in air and in CH₄ in accordance with temperature (middle left); GDC Raman band position in air and CH₄ in accordance with temperature (middle right). The *in situ* Raman spectra for LSM/GDC composite electrode in air at room temperature (blue line), in CH₄ at 700 °C (red line) and in air, after exposition to methane, at 700 °C (black line) are presented.

As it will be easy to understand, *in situ* Raman spectroscopy is a very powerful tool for the material characterization, especially when material modifications are induced by changing the environment as temperature and atmosphere. For this reason, *in situ* Raman spectroscopy was carried out on LSM/GDC composite electrode. The complete set of spectra in air and in methane at the tested temperatures (between 650 and 850 °C) are shown on the top left and right graph of **Figure 10** respectively.

As first consideration, it is possible to observe from the graph on top right of **Figure 10** that GDC peak position presents an almost linear shift towards lower values of wavenumber by increasing the temperature. As the substrate temperature increases, oxygen desorption from the substrate increases as well as oxygen non-stoichiometry. This may lead to a slight increment in the Ce-O and Gd-O bond lengths, which would result in a Raman peak red shift. For the same reason, the Raman shifts for GDC band in methane are set at lower wavenumber compared to those in air, since even at 650 °C the methane atmosphere can reduce partially the sample. In addition, the GDC reduction is confirmed also by a decrease of the signal intensity.

For LSM the description is almost similar. In air the Raman shifts for the Mn-O stretching mode band are set at higher values of wavenumber. This is in accordance with the correspondence between partial reduction and consequent red shift of the band, explained before for GDC. Anyway, must be noted the small but visible change of slope of the Raman shift between 700 °C and 750 °C. Most probably this change of slope can be related to the LSM reduction from cubic perovskite to Ruddlesden-Popper phase. Indeed, this temperature range corresponds with this reduction observed through XRD and the performances improvement already discussed in [Paragraph 3.5](#). Finally, the LSM large reduction that occurs at 850 °C does not allow to observe any LSM peak in the Raman spectrum. The linear dependence between temperature and phonon wavenumber shifts under constant pressure, consist of two parts: the first part is due to the volume effect, which reflects the change in the equilibrium interatomic spacings with temperature caused by thermal expansion. The second part is due to the pure temperature (or explicit) effects, resulting from the change in vibrational amplitudes (e.g., the phonon occupation numbers at fixed equilibrium positions).

In the bottom graph of **Figure 10**, the reversible LSM reduction and oxidation suggested by XRD (see [Paragraph 3.5](#)) is confirmed. Indeed, it is possible to see as the LSM band in air at RT (blue line), is difficult to observe, due to its very low intensity, in the spectrum carried out at 700 °C in methane (red line). Anyway, when the cell is exposed to air at 700 °C there is a remarkable increase of the peak intensity.

6.5.2 L8S2M and LSCuM

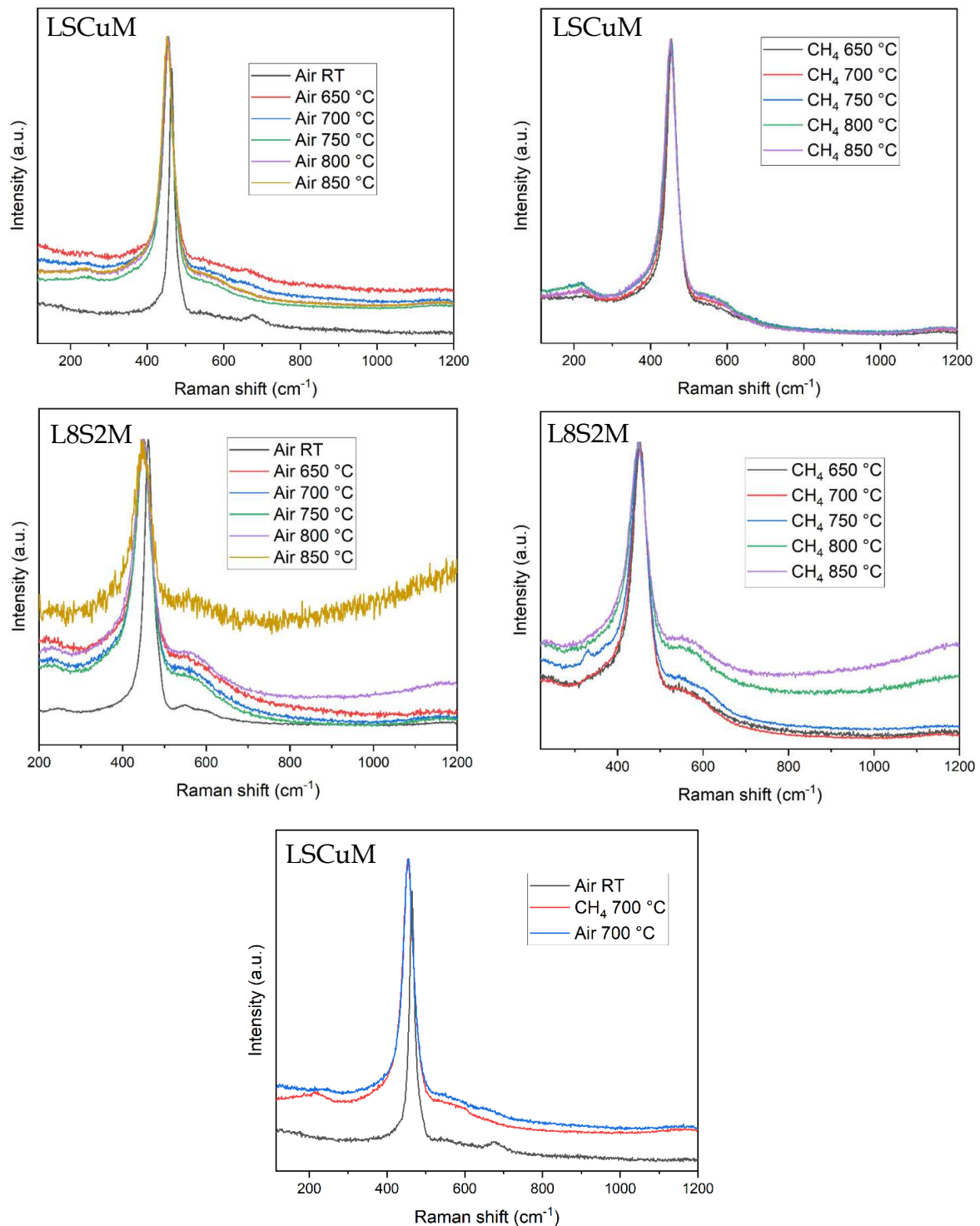
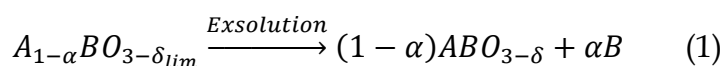


Figure 11: On top left are shown Raman spectra carried out on GDC:LSCuM composite electrode in air in the temperature range between 650 and 850 °C; on top right the Raman spectra for GDC:LSCuM electrode carried out in methane. On bottom left a comparison between GDC:LSCuM electrode Raman spectra performed in air at RT (black line); in methane at 700 °C (red line) and in air at 700 °C (blue line). On bottom right graph the L8S2M *in situ* Raman spectra performed in methane.

In the upper left graph of **Figure 11** the Raman spectra performed in air in the temperature range between 650 °C and 850 °C are shown. As already discussed in the previous paragraphs, the Raman band referred to Mn³⁺-O stretching and set at about 680 cm⁻¹ presents a red-shifting and an intensity lowering with the temperature increase. The significant difference between the Raman spectra of LSCuM and LSM was highlighted by the measurement carried out in methane. In fact, in the graph on the top right of **Figure 11**, where the Raman spectra carried out in methane are presented, the peak set at 680 cm⁻¹ is absent in all the spectra. On the contrary a new peak set at about 220 cm⁻¹ is present. The comparison with literature, reveals that the only species that can be referred to this peak is Cu₂O, whose more intense peak, caused by Γ₁₅ mode, is set exactly at this frequency. [14], [15] The presence of this copper species detected by Raman can be the proof of a spontaneous exsolution of copper cations towards the surface.

Exsolution is a novel, but at the same time well-known process, that is massively used in material science to enhance the catalytic activity of the materials with applications in catalysis ranging from automotive emission control to solid oxide fuel/electrolysis cells. Catalytically active transition metals can be substituted on the B-site of perovskite oxides in oxidizing conditions and released (exsolved) on the surface as metal particles following reduction.



What makes exsolution fundamental in the nowadays material science research, is the possibility to create particles that are more resilient to agglomeration and coking as compared to deposited analogues. Exsolved particles generally behave as if pinned to their original location, showing a level of stability beyond metal-oxide interfaces produced through conventional means on a similar A-site-deficient perovskite.

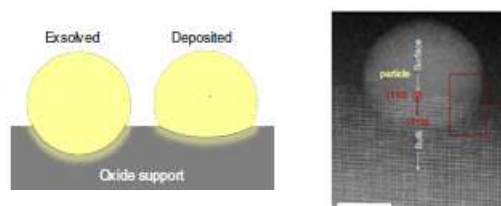


Figure 12: On the left it is presented a schematic illustration of the interface between nanoparticle and substrate, comparing deposition and exsolution. On the right a TEM image (dark field) of an exsolved nanoparticle on (110) surface facet.

The second consequence of particle-substrate interaction is in relation to the tendency of transition metals, as Ni and Cu, to grow carbon fibers in a hydrocarbon environment, which is detrimental in methane fueled SOFC applications. A more intimate interaction of the nanoparticle with the supporting oxide can avoid the C-poisoning, particularly if the oxygen exchange capability of the support is adequate.

Coming back to the discussion of the bottom left graph of **Figure 11**, it is possible to observe as the Cu₂O peak, even if with a significant lower intensity, is still visible after the gas environment transition from methane to air. The non-reversible exsolution of Cu nanoparticles is further confirmed by the XRD performed after CH₄ oxidation test and already discussed in Paragraph 4.2. On the other side, the reversible transition from RP phase to perovskite in oxidant atmosphere is confirmed also for this sample.

Unfortunately, a proper discussion on L8S2M *in situ* Raman spectroscopy is not possible, since, as already said in the previous Paragraph 6.4, the Mn-O stretching band is not visible in air and consequently even in methane. Anyway, an important consideration derives from the *in situ* Raman spectroscopy performed in methane for L8S2M and also for the other material just presented. Indeed, no carbon deposition was detected by Raman, suggesting that carbon passivation of the electrode surface is avoided in this kind of samples. A possible explanation for the missing surface passivation, can be found considering the soot oxidizing capability of the perovskite surface, being able to oxidize the carbon into CO₂, starting from 400 °C. [16], [17] When these species are formed, they can be easily removed from the surface.

The electrode carbon passivation is prevented in all these sample based on La_{1-x}Sr_xMnO₃ perovskite. On the contrary, on the following paragraph, we will observe that this is not true for all the tested temperatures on the Cu@GDC cermet.

6.5.3 Cu@GDC 2% Pd wt. electrode

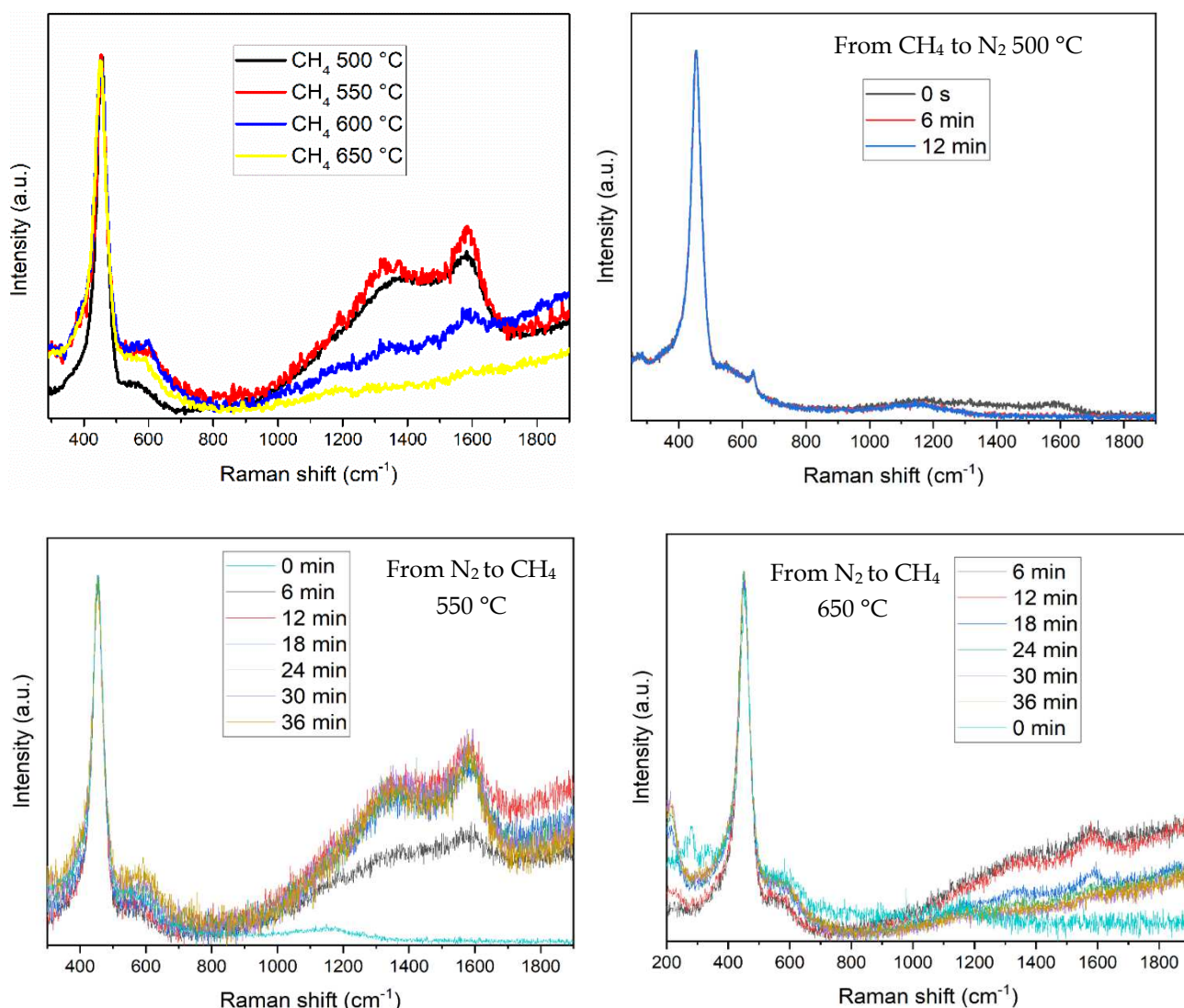


Figure 13: Top left: Temperature dependent Cu@GDC 2% Pd wt. Raman spectrum in methane. Top right: time dependent Raman spectra after electrode exposition to methane and consequent atmosphere switch to nitrogen at 500 °C. Bottom left: time dependent Raman spectra after electrode exposition to methane at 550 °C. Bottom right: time dependent Raman spectra after electrode exposition to methane at 650 °C.

Due to the reduction occurred by methane on the material, the *in situ* Raman spectra for Cu@GDC 2% Pd wt. do not present the peaks referred to CuO and PdO observed in the ex situ measurements. Anyway, from these spectra it is possible to observe the electrode behavior regarding the carbon passivation. One of the main problems for methane fueled SOFCs is the carbon deposition on the electrode surface. This can lead to several problems as gas transport inhibition, blockage of the Triple Phase Boundary (TPB) and metal catalyst breakage. Since Pd is a good catalyst not only for methane oxidation reaction, but also for carbon cracking, this can be a serious problem. On the contrary, if carbon deposition is

under control, this can enhance the cell performance adding electron conductivity. The key aspect is the possibility to tune this behavior.

On top left graph of **Figure 13**, it is possible to see that the GDC band at 450 cm^{-1} , present a reduction of its intensity, but is still visible after the reduction in methane. This change in the Raman spectra of GDC before and after the reducing treatment is consistent with a partial reduction of the electrolyte. Carbon deposition can give rise to both ordered and disordered form, consistently the signals referred to carbon are two. The first one is the dirty (D), or amorphous, band at about 1300 cm^{-1} , while at 1600 cm^{-1} is centered the peak corresponding to the Graphitic (G) ordered structure. As it possible to observe, both the D and G bands decrease their intensity with the increasing temperature. This can be related to the oxidative properties of GDC, that are enhanced with the temperature increment. Obviously, this feature is another important achievement of this material in considering the commercial application for methane fueled SOFCs. In addition, it was proved that the signal after few minutes stabilize its intensity, suggesting that there is a limit on the carbon coking.

On the top right graph of **Figure 13** it is possible to observe as few minutes in nitrogen are enough to remove all the carbon deposition. Usually air it is used to oxidize the carbon coke and remove it from the surface, but this would have detrimental effects on the mechanical stability of the electrodes due to the strong oxidation of Cu and Pd. So, the possibility to use N_2 as carrier to remove the carbon on the surface can improve the reliability of this material. In the two graphs on the bottom of **Figure 13**, are presented the Raman spectra carried out in methane and as a function of time at $550\text{ }^\circ\text{C}$ (on the left) and $650\text{ }^\circ\text{C}$ (on the right). As reported in literature, GDC is a strong catalyst towards the soot oxidation. [18], [19]. Oxygen vacancy creation due to methane reduction influences the width and position of the F_{2g} peak. Intrinsic and extrinsic oxygen vacancies are indicated from the peak at around 600 cm^{-1} . This peak is present in all the samples tested in methane, and moreover, for those carried out at higher temperature. The ratio of the intensity of CeO_2 peak (F_{2g}) to oxygen vacancy peak (O_v) provides an idea about the relative oxygen defects available in the system. For soot oxidation reaction, specifically, surface oxygen is critical in controlling the activity.

The primary step involving soot oxidation reaction is the spillover of oxygen onto active carbon sites and their desorption, subsequently. Soot oxidation reaction occurs at the interface of soot and catalyst surface. The spillover mechanism can be related to the ease of active oxygen species formation, oxygen mobility within the lattice, and redox sites. [20]

Coming back to the description of the Raman spectra, it is possible to observe as the soot oxidation is highly dependent on temperature. Indeed, in the Raman spectra carried out at 550 °C, D and G bands are stable with time. This indicates that the conversion capability of GDC is limited and in a dynamic equilibrium with the surface passivation. On the contrary, when the cell is tested at 650 °C, the intensity of the two peaks referred to carbon decreases with time: this suggests that the GDC is more efficient in the soot oxidation and this process is prevalent compared to carbon coking.

References

- [1] G. Socrates, "Infrared and Raman Characteristics Frequencies of Organic Molecules." John Wiley & Sons, Hoboken, NJ, 2001.
- [2] B. Lafuente, R. T. Downs, H. Yang, and N. Stone, "1. The power of databases: The RRUFF project," in *Highlights in mineralogical crystallography*, De Gruyter (O), 2015, pp. 1–30.
- [3] "Linkam Scientific Instruments".
- [4] A. Leonide, Y. Apel, and E. Ivers-Tiffée, "SOFC Modeling and Parameter Identification by Means of Impedance Spectroscopy," *ECS Trans*, vol. 19, no. 20, pp. 81–109, Oct. 2009, doi: 10.1149/1.3247567.
- [5] M. Glazer, G. Burns, and A. N. Glazer, *Space groups for solid state scientists*. Elsevier, 2012.
- [6] H. A. Jahn and E. Teller, "Stability of polyatomic molecules in degenerate electronic states—I—Orbital degeneracy.," *Proceedings of the Royal Society of London*, pp. 220–235, 1937, [Online]. Available: <https://royalsocietypublishing.org/>
- [7] M. v Abrashev *et al.*, "Comparative study of optical phonons in the rhombohedrally distorted perovskites LaAlO₃ and LaMnO₃."
- [8] H. Inaba and H. Tagawa, "Ceria-based solid electrolytes," *Solid State Ion*, vol. 83, pp. 1–16, 1996.
- [9] J. B. Goodenough, "Solid electrolytes," 1995.
- [10] R. L. Frost, J. Kristóf, E. Horváth, and J. T. Kloprogge, "Raman phonons and Raman Jahn-Teller bands in perovskite-like manganites," *Journal of Raman Spectroscopy*, vol. 32, no. 10, pp. 805–811, 2001. doi: 10.1002/jrs.770.
- [11] J. F. Xu *et al.*, "Raman Spectra of CuO Nanocrystals," *J. Raman Spectrosc.*, vol. 30, pp. 413–415, 1999.
- [12] D. L. Rousseau, R. P. Bauman, and S. P. S. Porto, "Normal mode determination in crystals," *J. Raman Spectroscopy*, vol. 253, no. 10, 1981.
- [13] J. T. Remillard, W. H. Weber, J. R. McBride, and R. E. Soltis, "Optical studies of PdO thin films," *J Appl Phys*, vol. 71, no. 9, pp. 4515–4522, 1992, doi: 10.1063/1.350797.
- [14] P. Y. Yo, Y. R. Shen, and Y. Petroff, "Resonance Raman scattering in Cu₂O at the blue and indigo excitons," *Solid State Commun*, vol. 12, pp. 973–975, 1973.
- [15] M. Balkanski, M. A. Nusimovici, and J. Reydellet, "First order Raman spectrum of Cu₂O," *Solid State Commun*, vol. 7, pp. 815–818, 1969.

- [16] A. A. Khaskheli, L. Xu, and D. Liu, "Manganese Oxide-Based Catalysts for Soot Oxidation: A Review on the Recent Advances and Future Directions," *Energy and Fuels*, vol. 36, no. 14. American Chemical Society, pp. 7362–7381, Jul. 21, 2022. doi: 10.1021/acs.energyfuels.2c01492.
- [17] P. Zhao *et al.*, "Self-templating construction of mesopores on three-dimensionally ordered macroporous La_{0.5}Sr_{0.5}MnO₃ perovskite with enhanced performance for soot combustion," *Catal Sci Technol*, vol. 9, no. 8, pp. 1835–1846, 2019, doi: 10.1039/c9cy00096h.
- [18] A. P. Anantharaman *et al.*, "Effect of synthesis method on structural properties and soot oxidation activity of gadolinium-doped ceria," *Chemical Papers*, vol. 72, no. 12, pp. 3179–3188, Dec. 2018, doi: 10.1007/s11696-018-0532-5.
- [19] M. G. Werhahn, O. Schneider, and U. Stimming, "Thin Film Gadolinia Doped Ceria (GDC) Anode for Direct Conversion of Carbon Black Particles in a Single Planar SOFC," *ECS Trans*, vol. 50, no. 27, pp. 73–87, Apr. 2013, doi: 10.1149/05027.0073ecst.
- [20] D. H. Prasad *et al.*, "Structural characterization and catalytic activity of Ce_{0.65}Zr_{0.25}RE_{0.10}2- δ nanocrystalline powders synthesized by the glycine-nitrate process," *Journal of Physical Chemistry C*, vol. 116, no. 5, pp. 3467–3476, Feb. 2012, doi: 10.1021/jp207107j.

Chapter 7: Conclusions and outlook

At the end of this work, I would like to resume the main proposed goals and the achievements obtained by my research.

To fight the climate change is our own responsibility to try to reduce the emissions of greenhouse gases in the atmosphere. We are convinced that the transition to a “0 Carbon world”, with the energy production completely fueled by hydrogen is the key to stop the detrimental effects of climate change on our planet. Anyway, we also believe that this transition will require time and strong economical efforts, that in this period, affected by many economic crises, are not so easy to apply by the governments. For these reasons, we think that the first step is to reach at least a “carbon neutrality”, where there is still usage of hydrocarbons, but the emissions of carbon are balanced by its removal.

Our idea to reach the “carbon neutrality” midterm step is to use green methane to fuel Low or Intermediate Temperature Solid Oxide Fuel Cells (SOFC). A Fuel Cell is an electrochemical device able to convert the chemical energy contained in a fuel (typically hydrogen) into electrical energy. SOFCs are characterized by the usage of a ceramic electrolyte, high operating temperatures and higher efficiency compared to other fuel cells. The main idea of this work is using methane directly as fuel; in fact, methane can be obtained from the organic waste produced by human activities, like farming and agriculture, and, in general, it can be produced from biomasses. In addition, methane fueled SOFCs can be implemented quite immediately in our cities, since it is possible to use the pre-existing gas implants, on the contrary of what should be needed in the case of hydrogen fueled ones.

To reach these goals, the main challenge is to find the right material that can be used in the anodic side of the cell. Indeed, the cathode and the electrolyte are not involved by the fuel changing. On the contrary it is necessary to find a material that is stable, able to electrochemically oxidize methane, and possibly able to prevent carbon coking on the electrode surface. This last property is missing for Ni-YSZ (where YSZ stands for Yttria-Stabilized Zirconia), the state-of-art material for the commercial SOFCs, fueled by hydrogen. For this reason, and due to many detrimental effects on the mechanical stability given by the carbon coking, it is not possible to use Ni based materials. The use of Ni-containing

anodes requires, at least, a reforming step to obtain hydrogen (the real fuel) and C-containing residues (that are discarded). This step increases the complexity of the plant and device and decreases the efficiency. In this thesis the attempt is to develop anodes sustainable from the economic and environmental point of view capable to operate directly with methane.

Two are the main challenges of this work; the first one consists of developing an anodic material, which should be Critical Raw Materials (CRMs) free, and efficient in the Intermediate temperature range (600 – 800 °C). In addition, with the aim of reducing the production costs, it was tried to create a symmetrical cell, i.e., a cell with the same material both in the anodic and cathodic compartment. The second challenge was to try to decrease the operating temperature below 600 °C for safety reasons connected with the use of methane.

To face the first challenge, the studied materials were three different perovskites based on $\text{La}_{1-x}\text{Sr}_x\text{MnO}_3$. The choice of this material as starting point, was given considering that $\text{La}_{0.6}\text{Sr}_{0.4}\text{MnO}_3$ (LSM) is the state-of-art material for SOFCs cathode; moreover, as attested in literature, Mn-containing compounds should be active in methane oxidation. The substitution of La and Mn with aliovalent cations can, in principle, increase both mixed ionic and electronic conductivity and reactivity. To understand the effects of Sr doping and Cu doping in the B site, other two materials $\text{La}_{0.8}\text{Sr}_{0.2}\text{MnO}_3$ (L8S2M) and $\text{La}_{0.6}\text{Sr}_{0.4}\text{Mn}_{0.9}\text{Cu}_{0.1}\text{O}_3$ (LSCuM) were tested. Not only different compositions for LSM were studied, but also the effects of different morphologies were investigated, by comparing powders with nanofibers. This work was carried out in collaboration with the University of Genova. In Genova LSM nanofibers were synthesized and later characterized and tested in Padova, to understand the effects of 1D morphology on performances.

So, in Chapter 3, the full characterization of LSM powder and nanofibers was presented. The Scanning Electronic Microscopy (SEM) images confirmed the correct formation of nanofibers and the ImageJ analyses performed on those images attested a diameter range between 0.08 μm – 0.1 μm . It was fundamental to evaluate the material stability under reducing condition, peculiar of anodic atmosphere. Both powders and nanofibers were stable till 550 °C, temperature at which, the reduction of manganese from Mn^{3+} to Mn^{2+}

starts (as confirmed by hydrogen Temperature Programmed Reduction, H₂-TPR), while after that temperature there is a reversible phase change from perovskite to Ruddlesden-Popper crystal structure (well-known in literature as active phase towards methane oxidation). The methane oxidation catalytic tests attested much higher performances for nanofibers (75% of conversion at 800 °C, compared to 50% at 900 °C for powders).

The main reason of these better performances was suggested by X-Ray Photoelectron Spectroscopy (XPS) analyses. Indeed, a lower Sr segregation on the surface was detected for nanofibers, with consequent lower presence of SrO as secondary phase. Since SrO is inert to the methane oxidation, it has a passivating effect on the perovskite active sites when present in high quantities on the surface.

The electrochemical performances of LSM, as electrode for symmetrical SOFCs fueled directly by methane, were studied for the two morphologies by Electrochemical Impedance Spectroscopy (EIS). The used electrodes are composite electrodes with gadolinium doped ceria (GDC), the electrolyte material, enhancing the adhesion between electrode and electrolyte. Since this material should be used as cathodic and anodic material, in order to create a symmetrical SOFC, the tests were performed in humidified air and in humidified methane. The obtained spectra were fitted by a model circuit to confer at every signal the correct physical explanation.

Starting from the tests carried out in air, the spectra were quite similar between the two morphologies, with three processes in the temperature range between 665 °C and 765°C, that become two over this temperature range. The missing signal at high temperature is given by a thermo-activated process (i.e., adsorption/desorption process) that becomes negligible at high temperatures.

In methane the spectra are similar at all the temperatures, and they are formed by a Gerischer element. This behavior is quite common for GDC-based electrodes, as confirmed by several examples reported in the literature. The possible explanation may be found in the conductive properties of the GDC. Indeed, when the GDC is exposed to the air atmosphere, its fluorite structure allows the conduction of oxygen ions at operating temperatures even lower compared to ones generally used for the YSZ. Otherwise, when

the GDC is exposed to a reducing atmosphere, poor electronic conduction is activated, and it becomes an MIEC.

Passing to the quantitative analyses, the obtained Area Specific Resistances (ASR) are presented in the following **Table 1**. The values in air are in perfect accordance with literature, while outstanding results are obtained in methane, with values four times lower to those reported in literature. The very low polarization resistances measured from the impedance tests may be affected by a parallel pathway given by a short-circuit of the GDC electrolyte exposed to methane. Therefore, it was considered the possibility that those results may not reflect the pure electrochemical activity. However, if the electronic pathway has no complex contribution to the imaginary part, it is expected that the Nyquist shape, e.g., the Gerischer element, is not affected by the short-circuit so reflects the electrode processes involved in the EC pathway. However, the results indicate the importance to employ a pure ionic conductor as an electrolyte, for example, a multilayer electrolyte based on zirconia coated with GDC on both sides.

Air	665 °C	715 °C	765 °C	815 °C	865 °C
Powders	22.1 Ωcm ²	6.4 Ωcm ²	3.3 Ωcm ²	1.1 Ωcm ²	0.7 Ωcm ²
Nanofibers	14.1 Ωcm ²	5.9 Ωcm ²	2.8 Ωcm ²	1.6 Ωcm ²	0.8 Ωcm ²
CH ₄		715 °C	765 °C	815 °C	865 °C
Powders		4.1 Ωcm ²	0.8 Ωcm ²	0.1 Ωcm ²	0.04 Ωcm ²
Nanofibers		5.4 Ωcm ²	2.4 Ωcm ²	0.1 Ωcm ²	0.04 Ωcm ²

Table 1: ASR values obtained in air and in methane for LSM powders and nanofibers.

In chapter 4 the full characterization for L8S2M and LSCuM was presented. The correct synthesis of the two compounds was confirmed by X-Ray Diffraction (XRD), including the insertion of Cu inside the perovskite structure. Even for these two compounds the stability in reducing atmospheres was investigated. The main result was the confirmation of the reversible phase change of the two compounds into the Ruddlesden-Popper crystal structure when exposed to methane and the reformation of the perovskite structure when exposed to air. The stability of the three LSM-based perovskite is resumed in the following **Table 2**. It is relevant that none of the materials is subjected to detrimental effects due to the exposition to reducing atmospheres. Much more interesting, considering that their low resistance to reducing atmosphere was the reason why they were not commonly considered as anode materials for SOFCs.

Treatment	LSM	L8S2M	LSCuM
After H ₂ -TPR (900 °C)	RP	RP	RP
After CH ₄ Ox. (800 °C)	Perovskite	Perovskite	RP
After ReOx.	Perovskite	Perovskite	Perovskite

Table 2: Crystal structure of the main studied compounds after the different treatments.

The XPS performed on LSCuM pre and post the H₂-TPR highlighted a higher presence of copper on the catalyst surface after the exposition to the reducing atmosphere. This was considered the first evidence of a copper nanoparticles exsolution (later confirmed also by Raman *in situ* spectroscopy). The presence of exsolved copper nanoparticles highly improves the electronic conductivity of the material, and consequently lower resistances are expected. It is relevant to consider that exsolution is a novel and innovative technique that consists of an

The catalytic tests about methane oxidation attested that the most performant material is L8S2M since it is able to fully oxidize methane at 900 °C (LSCuM shows an 90% conversion at the same temperature). The mechanisms involved in the reaction were observed by some tests performed in under-stoichiometric atmosphere of oxygen. At lower temperatures the suprafacial process (where the oxidation is promoted by the oxygen present in the anodic atmosphere) is the main mechanism, while at higher temperatures the intrafacial one is preferred, i.e., the oxygen is provided from the bulk lattice of the perovskite.

XPS performed on LSCuM before and after H₂-TPR highlighted a remarkable enrichment of copper on the surface after the reducing treatment. This was considered as first evidence of a possible exsolution of copper nanoparticles on the catalysts surface (later also confirmed by Raman *in situ* spectroscopy). The presence of exsolved nanoparticles is very useful to enhance the electronic conductivity of the materials. Must be considered that exsolution is a novel and innovative techniques that in many cases requires an *ad hoc* treatment for the materials, with the possible necessity of high temperatures and long times. On the contrary, for LSCuM this phenomenon is spontaneous and appears when the electrode is operative.

Then the two compounds were electrochemically tested in air and in methane. Even in this case the tested electrodes were composites 50:50 with GDC. The obtained results are shown in the following **Table 2**.

Air	665 °C	715 °C	765 °C	815 °C	865 °C
L8S2M	8.04 Ωcm^2	3.28 Ωcm^2	1.49 Ωcm^2	0.59 Ωcm^2	0.25 Ωcm^2
LSCuM	22.66 Ωcm^2	12.48 Ωcm^2	5.88 Ωcm^2	1.46 Ωcm^2	1.05 Ωcm^2
CH4	715 °C		765 °C	815 °C	865 °C
L8S2M	17.81 Ωcm^2		4.43 Ωcm^2	0.59 Ωcm^2	0.09 Ωcm^2
LSCuM	12.05 Ωcm^2		4.06 Ωcm^2	0.56 Ωcm^2	0.06 Ωcm^2

Table 2: ASR values obtained in air and in methane for L8S2M and LSCuM powders.

In air, the used model circuit is the same for the two compounds but differs on dependence by the temperature. In fact, in the temperature range between 665 °C and 765 °C the model circuit consists in a resistance in series with two RQs (R_s -RQ-RQ). Whereas, when the temperature reaches the 815 °C, the process at low frequencies disappears and becomes evident in the same region of frequencies the process referred to the gas diffusion resistance. This physical phenomenon is represented with a Final Length Warburg (FLW) element. Therefore, the resultant best model circuit is R_s -RQ-FLW. Since the gas diffusion on the electrode is not drastically dependent on temperature, its resistance is almost the same in the two temperatures where it is observable. Most probably the electrochemical process at high frequencies is the oxygen adsorption and dissociation on the active region of the electrode. While the second RQ element at lower frequencies that becomes evident at below 765 °C is referred to oxygen reduction process.

Let's pass to the tests carried out in methane. Since also for L8S2M and LSCuM there is the formation of the Ruddlesden Popper phase, with consequent presence of a mixed ionic/electronic conductor, the model circuit composed by a Gerischer element, find justification in literature.

The ASR values are quite in accordance with those obtained for LSM, so comparable with literature in air and much lower in methane, in which atmosphere the best results were obtained with LSCuM, confirming the relevance of exsolved nanoparticles on the catalyst surface.

The two materials were also tested through Linear Sweep Voltammetry (LSV) in a double chamber complete tests obtaining the following power densities.

Electrode	Temperature (°C)	715	765	815	865
L8S2M	Power density (mW/cm ²)	2.2	7.4	15.5	27.3
LSCuM	Power density (mW/cm ²)	3.2	10.7	21.4	36.4

Table 3: Power densities values for L8S2M and LSCuM electrodes.

The second part of the work was made in collaboration with Pietro Fiorentini S.p.A, an Italian leader company in the gas supply sector. The main idea of this work was to study a material suitable as anode for SOFCs fueled by methane with operating temperature in the range between 500 °C and 600 °C. This temperature range was considered to reduce the costs, enhance the lifetime of the materials, but most of all to operate below the methane auto-ignition temperature (commonly set about 580 °C). This is a fundamental feature to guarantee high safety standards.

The chosen compound was a cermet, where the substrate is constituted by GDC (that guarantees good ionic conductivity and high methane oxidation activity) on which copper nanoparticles were deposited by impregnation in order to guarantee a proper electronic conductivity to the electrode. XRD confirmed that Cu@GDC nanocomposite was successfully obtained, and from Scherrer equation it was possible to determine an average diameter for Cu nanoparticles of 21 ± 1 nm.

Performing EIS measurements on Cu@GDC, an interesting result has been obtained with this electrode but always at higher temperatures than the required one. The very low working temperatures don't allow to completely avoid CRM, and to enhance the catalytic activity towards methane oxidation an infiltration of Pd nanoparticles was performed. The cell performance suggested that this traditional procedure for Pd deposition was not adequate to this specific application: in fact, by impregnation rather big Pd clusters have been obtained, so vitiating the effect of nanosized metal particles realization through infiltration. In order to improve the activity of Pd containing electrode (and, incidentally, to reduce the noble metal quantity), a new infiltration method (Incipient Wetness Infiltration, IWI) was studied *ad hoc*. IWI was performed directly on the electrode and consists of determining the electrode free volume and using it as maximum volume for the infiltrating solution. In this way the Pd nanoparticles are much more dispersed, and it is inhibited their tendency to aggregate, obtaining small nanoparticles and therefore increasing their specific surface area and consequently their catalytic activity.

The smaller dimensions for Pd nanoparticles and the higher dispersion was confirmed by SEM. It was tried to obtain better performances by increasing the Pd load on the electrodes from 0.5% to 3%, and, by EIS measurements, it was determined that the best one is 2% of Pd by weight.

Once determined the best composition (Pd 2% wt. - Cu@GDC/GDC/LSCF:GDC), complete cell tests were performed in hydrogen, pure methane and in a gas mixture of CH₄:H₂ 3:2. This particular mixture is the one that should, following computational modelling carried out by Prof. Campanari of University of Milan, be the one capable of warranting the best performance. In **Table 4** it is possible to see the results obtained through LSV in terms of power density and Open Circuit Potential (OCP). Even if with a very low power output, it is noteworthy to observe that the SOFC was working also at 500 °C in pure methane.

Temperature (°C)	Atmosphere	OCP (V)	Power density (mW/cm ²)
650	20% H ₂	0.84	71
600	20% H ₂	0.90	44
	20% H ₂ / 30% CH ₄	0.92	52
	100% CH ₄	0.83	17
550	20% H ₂	0.96	27
	20% H ₂ / 30% CH ₄	0.96	29
	100% CH ₄	0.74	4
500	20% H ₂	0.98	12
	20% H ₂ / 30% CH ₄	0.98	14
	100% CH ₄	0.70	1

Table 4: Summary table of all the results obtained during this study in function of atmosphere and temperature for the Pd 2% wt. - Cu@GDC/GDC/LSCF:GDC complete cell.

Since in the last years the scientific community is putting a lot of efforts in the research of ammonia fueled SOFCs, a symmetrical test was carried out with 40% NH₃ in Ar, in order to understand the possibility to use this compound also with ammonia. Good results were obtained above 600 °C, while the low ammonia cracking below this temperature does not allow to reach satisfactory resistances. The possibility to optimize the electrode through Ni nanoparticles impregnation should be considered.

Finally, in Chapter 6 were presented the *in situ* and *ex situ* Raman spectroscopy measurements carried out at Danmarks Tekniske Universitet (DTU), in the Prof. Holtappels research group.

The *ex situ* experiments carried out on the considered perovskites (LSM, L8S2M and LSCuM) were able to determine the presence of perovskite. In fact, it was possible to observe a peak set at 650 cm^{-1} given by the stretching in the xz plane of Mn-O bond in the BO_6 octahedra of the perovskite lattice. Besides, for Cu@GDC the Raman spectrum is characterized by the peak set at 461 cm^{-1} , given by the symmetrical stretching mode of the Ce-O₈ vibrational unit of cubic ceria. In addition, there are three different bands, at 295 cm^{-1} , 344 cm^{-1} and 611 cm^{-1} given by CuO and a peak set at 648 cm^{-1} referred to PdO infiltration.

Much more interesting considerations were made from the *in situ* experiments. It was possible to observe the reversible transition from cubic perovskite to Ruddlesden-Popper, obtaining a strong confirmation of what suggested by the XRD analyses on LSM; LSCuM and L8S2M. From the measurements performed on LSCuM it was also highlighted a Cu exsolution when the perovskite is exposed to methane over $700\text{ }^\circ\text{C}$. This change could be very effective for the electronic conduction enhancement of the material. The carbon deposition on the different electrodes was evaluated as well. No formation of carbon was detected on the three perovskites electrodes, pushing further the possibility to use these materials for SOFCs directly fueled by methane. On the contrary, carbon deposition was determined in the Cu@GDC 2% Pd wt. electrode. Anyway, this deposition is significantly reduced when the working temperature is above $550\text{ }^\circ\text{C}$, and it is possible to eliminate this passivating layer just exposing the electrode for few minutes in nitrogen, avoiding the needing of an oxidant, that could lead to mechanical problems related to continuous cycles of reduction and oxidation of the material.

Finally, this thesis could be taken as a demonstration of the possibility to realize a symmetrical SOFC directly fueled by methane in the low and intermediate temperature range. Obviously, further improvements must be taken in account. First of all, a detailed and complete study about the device engineering must be done. As an example, passing from electrolyte supported to anode supported cell is a simple and needed step that should be done to understand which are the realistic performances of these materials. Anyway, the possibility to use these materials in a device is not the only result of this work. A complete characterization of the different compounds was fulfilled, highlighting their strength points

and their limitations. I am convinced that this last point is the most important one, since starting from this material knowledge, it is possible to achieve much more important goals on the development of this world to a more sustainable one.




Appendix:

List of papers published during my Ph.D.

- 1) Squizzato, E., Sanna, C., Glisenti, A., & Costamagna, P. (2021). Structural and catalytic characterization of $\text{La}_{0.6}\text{Sr}_{0.4}\text{MnO}_3$ nanofibers for application in direct methane intermediate temperature solid oxide fuel cell anodes. *Energies*, 14(12), 3602.
- 2) Sanna, C., Squizzato, E., Costamagna, P., Holtappels, P., & Glisenti, A. (2022). Electrochemical study of symmetrical intermediate temperature-solid oxide fuel cells based on $\text{La}_{0.6}\text{Sr}_{0.4}\text{MnO}_3/\text{Ce}_{0.9}\text{Gd}_{0.1}\text{O}_{1.95}$ for operation in direct methane/air. *Electrochimica Acta*, 409, 139939.
- 3) Squizzato, E., Carollo, G., & Glisenti, A. (2021). $\text{Ca}_2\text{Fe}_{1.95}\text{Mg}_{0.05}\text{O}_5$: Innovative low cost cathode material for intermediate temperature solid oxide fuel cell. *International Journal of Hydrogen Energy*, 46(48), 24555-24566.
- 4) Cavazzani, J., Squizzato, E., Brusamarello, E., & Glisenti, A. (2022). Exsolution in Ni-doped lanthanum strontium titanate: a perovskite-based material for anode application in ammonia-fed Solid Oxide Fuel Cell. *International Journal of Hydrogen Energy*, 47(29), 13921-13932.
- 5) d'Andrea, G., Squizzato, E., & Glisenti, A. (2022). Comparison of different infiltration amounts of CeO_2 inside Ni-YSZ anodes to improve stability and efficiency of Single-Chamber SOFCs operating in methane. In *E3S Web of Conferences* (Vol. 334, p. 04009). EDP Sciences.
- 6) Cavazzani, J., Squizzato, E., Brusamarello, E., & Glisenti, A. (2022). Exsolution in La and Ni co-doped strontium titanate: a suitable anode for running SOFCs on ammonia as alternative fuel. In *E3S Web of Conferences* (Vol. 334, p. 04008). EDP Sciences.

Article

Structural and Catalytic Characterization of $\text{La}_{0.6}\text{Sr}_{0.4}\text{MnO}_3$ Nanofibers for Application in Direct Methane Intermediate Temperature Solid Oxide Fuel Cell Anodes

Enrico Squizzato ¹, Caterina Sanna ², Antonella Glisenti ¹ and Paola Costamagna ^{2,*}

¹ Department of Chemical Sciences, University of Padova, Via F. Marzolo 1, 35131 Padova, Italy; enrico.squizzato.1@phd.unipd.it (E.S.); antonella.glisenti@unipd.it (A.G.)

² Department of Chemistry and Industrial Chemistry, University of Genoa, Via Dodecaneso 31, 16146 Genoa, Italy; caterina.sanna@edu.unige.it

* Correspondence: paola.costamagna@unige.it; Tel.: +39-(0)10-3532922; Fax: +39-(0)10-3538733

Abstract: In the present work, structural and catalytic characterization was performed on $\text{La}_{0.6}\text{Sr}_{0.4}\text{MnO}_3$ (LSM) nanofibers. The LSM nanofibers were obtained using the electrospinning technique. For comparison, LSM powders with identical composition were characterized as well. The LSM powders were prepared through a self-combustion citrate-based procedure. SEM, EDX, XRD, and BET investigations were carried out on both LSM nanofibers and powders, pointing out the different structural features. The LSM nanofibers showed a higher surface area than the LSM powders and a lower presence of strontium oxide on the surface. Results of the H_2 -Temperature Programmed Reduction (TPR) tests showed evidence of a higher reactivity of the nanofibers compared to the powders. The catalytic characterization was performed utilizing a methane oxidation activity test, revealing a better catalytic performance of the LSM nanofibers: at 800 °C. The methane conversion achieved with the LSM nanofibers was 73%, which compared well with the 50% obtained with powders at 900 °C.

Keywords: electrospinning; nanofibers; fuel anode; H_2 -Temperature Programmed Reduction (TPR); Intermediate Temperature-Solid Oxide Fuel Cell (IT-SOFC)



Citation: Squizzato, E.; Sanna, C.; Glisenti, A.; Costamagna, P. Structural and Catalytic Characterization of $\text{La}_{0.6}\text{Sr}_{0.4}\text{MnO}_3$ Nanofibers for Application in Direct Methane Intermediate Temperature Solid Oxide Fuel Cell Anodes. *Energies* **2021**, *14*, 3602. <https://doi.org/10.3390/en14123602>

Academic Editor: Vladislav A. Sadykov

Received: 27 May 2021

Accepted: 10 June 2021

Published: 17 June 2021

Publisher's Note: MDPI stays neutral with regard to jurisdictional claims in published maps and institutional affiliations.



Copyright: © 2021 by the authors. Licensee MDPI, Basel, Switzerland. This article is an open access article distributed under the terms and conditions of the Creative Commons Attribution (CC BY) license (<https://creativecommons.org/licenses/by/4.0/>).

1. Introduction

Fuel cells are electrochemical devices that directly convert the chemical energy of the fuel into electrical energy, avoiding the Carnot cycle and allowing high efficiencies to be achieved [1,2]. For this reason—and due to the constant increase in energy demand and consequently in greenhouse gas emissions—fuel cells have drawn great attention over the last few decades. Among all fuel cell configurations, intermediate temperature solid oxide fuel cells (IT-SOFCs) have solid-state components. These offer wide fuel flexibility, since they can operate with both hydrogen and light hydrocarbons [3,4]. The latter is an interesting feature, since natural gas and methane are cheap and abundant fuels, whereas pure hydrogen is mostly produced through the hydrocarbon reforming process [5–7]. In the SOFC anode, methane can either be electro-oxidized directly or undergo an internal reforming process in which methane is converted into hydrogen. Both options have been investigated in recent years [8,9]. The internal methane reforming process is generally carried out employing nickel-based electrodes. The main challenges of this process are controlling temperature gradients across the SOFC stacks and avoiding coke deposition over the nickel catalyst, with consequent catalyst deactivation. The previous issue is due to the strong endothermicity of the methane steam reforming reaction, resulting in uneven temperature distribution over the cell, with the possible formation of cold spots [6]. The latter issue is behind the need to operate the cell with a steam-to-carbon (S/C) ratio larger than three, which makes it difficult to achieve complete methane conversion [9]. Due to these problems, IT-SOFCs running internal steam methane reforming processes require



Electrochemical study of symmetrical intermediate temperature - solid oxide fuel cells based on $\text{La}_{0.6}\text{Sr}_{0.4}\text{MnO}_3$ / $\text{Ce}_{0.9}\text{Gd}_{0.1}\text{O}_{1.95}$ for operation in direct methane / air

Caterina Sanna^a, Enrico Squizzato^b, Paola Costamagna^{a,*}, Peter Holtappels^c, Antonella Glisenti^b

^a Department of Chemistry and Industrial Chemistry, University of Genoa, Via Dodecaneso 31, Genoa 16146, Italy

^b Department of Chemical Sciences, University of Padova and ICMATE, Via F. Marzolo 1, Padova 35131, Italy

^c Department of Energy Conversion and Storage, Technical University of Denmark, Elektrovej, 375, 234, 2800 Kgs. Lyngby, Denmark

ARTICLE INFO

Article history:

Received 29 October 2021

Revised 3 January 2022

Accepted 16 January 2022

Available online 20 January 2022

Keywords:

Direct methane fuel cell (DMFC)

Electrochemical impedance spectroscopy (EIS)

(EIS)

Equivalent circuit modeling (ECM)

Gerischer

Intermediate temperature - solid oxide fuel cell (IT-SOFC)

(IT-SOFC)

$\text{La}_{0.6}\text{Sr}_{0.4}\text{MnO}_3$ (LSM), Mixed

ionic-electronic conductor (MIEC)

ABSTRACT

$\text{La}_{0.6}\text{Sr}_{0.4}\text{MnO}_3$ (LSM), which is considered a state-of-the-art solid oxide fuel cell (SOFC) cathode, is investigated for application as an anode in direct methane intermediate temperature - solid oxide fuel cells (IT-SOFCs). $\text{Ce}_{0.9}\text{Gd}_{0.1}\text{O}_{1.95}$ (CGO) is used as the electrolyte. The characterized electrode is a composite LSM/CGO, prepared in two different configurations: LSM crushed electrospun nanofibers / GDC powders, and LSM powders / GDC powders. The electrodes are tested in both air and direct methane conditions. At 815 °C, the polarization resistance $R_p = 1.6 \Omega\text{cm}^2$ in air, and $R_p = 0.15 \Omega\text{cm}^2$ in methane. Since perovskite-type manganites may show poor stability in reducing atmosphere, electrode stability is investigated. It is found that LSM shows a reversible modification of the crystal structure, assuming a Ruddlesden-Popper (RP) structure when exposed to methane. The RP structure is expected to be more stable compared to the LSM single perovskite. Furthermore, the composite electrode is expected to benefit from the presence of CGO, which is stable in reducing conditions.

© 2022 Elsevier Ltd. All rights reserved.

1. Introduction

The possibility of feeding the anode side of a fuel cell directly with methane is attracting wide interest. This would be the first step towards a direct utilization of the natural gas capillary distributed by the gas grid, without the intermediate steam methane reforming (SMR) reactor, which is present in all the fuel cell systems currently under study [1]. The overall system would benefit in terms of reduction in complexity and cost. Furthermore, the SMR reactor is particularly prone to faults related to carbon deposition, due to the capability of the traditional Ni catalyst to catalyze also the methane cracking reaction, which produces coke which is then deposited on the catalyst, hindering its activity. It has been demonstrated that these SMR faults are particularly dangerous for the integrity of the downstream fuel cell and the whole system [2].

Direct utilization of methane is possible only in high-temperature fuel cells (molten carbonate fuel cells, MCFCs, and solid oxide fuel cells, SOFCs) and has been widely investigated for

SOFCs. In SOFCs, internal methane utilization can proceed through two different pathways. The first relies on the direct electrochemical oxidation of methane by the oxygen ions coming from the electrolyte. The second pathway is based on the internal steam reforming process, which produces hydrogen and carbon monoxide, which are then oxidized electrochemically. The two pathways can take place simultaneously [3].

Ni, which is the typical electrocatalyst used at the SOFC anode for the electrochemical hydrogen oxidation reaction (HOR), is also the traditional catalyst for the SMR reaction, which seems an ideal conjuncture to implement internal SMR. Nevertheless, from an engineering point of view, this is not a practically viable option with traditional high-temperature SOFCs, because, at their typical temperatures of about 1000 °C, the internal SMR reaction is very fast. Since the SMR reaction is strongly endothermic, this causes a dramatic temperature decrease at the cell inlet, associated with severe mechanical tensile stresses in the solid structure, which easily cause fractures and ultimately break down of the cell. On the other hand, it has been demonstrated on theoretical ground, through SOFC simulation models, that the milder temperature of Intermediate Temperature-Solid Oxide Fuel Cells (IT-SOFCs),

* Corresponding author.

E-mail address: paola.costamagna@unige.it (P. Costamagna).

Available online at www.sciencedirect.com

ScienceDirect

journal homepage: www.elsevier.com/locate/he

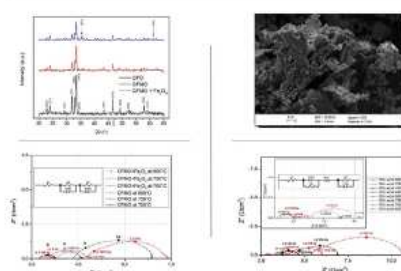
Ca₂Fe_{1.95}Mg_{0.05}O₅: Innovative low cost cathode material for intermediate temperature solid oxide fuel cell

E. Squizzato ^{a,*}, G. Carollo ^a, A. Glisenti ^{a,b}^a Department of Chemical Sciences, University of Padova, Via F. Marzolo 1, Padova, 35131, Italy^b CNR-ICMATE, Via F. Marzolo 1, Padova, 35131, Italy

HIGHLIGHTS

- Cheap Brownmillerite based nanocomposites successfully synthesized by citrate route.
- Ca₂Fe_{1.95}Mg_{0.05}O₃ activated by deposition of FeO_x nanoparticles by coprecipitation and wet impregnation.
- Fe induced chemical capacitance observed and studied vs T and P_{O2}.
- ASR comparable to State-of-Art cathode (0.19 Ωcm² at 800 °C) is obtained.
- The best performance was achieved by 15% wt. Fe₂O₃ infiltration (0.17 Ωcm² at 800 °C).

GRAPHICAL ABSTRACT



ARTICLE INFO

Article history:

Received 24 February 2021

Received in revised form

3 May 2021

Accepted 4 May 2021

Available online 28 May 2021

Keywords:

Brownmillerite

SOFC

Cathode

Iron oxide on Brownmillerite

EIS

Nanocomposites

ABSTRACT

The good oxygen ion conductivity makes brownmillerites suitable as electrode materials for SOFCs. In this contribution, we focus on Ca₂Fe_{1.95}Mg_{0.05}O₅ (CFMO) with the idea of evaluating this brownmillerite as a promising innovative and low-cost cathode material. The synthesis was made through citrate route, where a magnesium doping was carried out to emphasize Fe³⁺/Fe⁴⁺ redox couple and thus the electronic conductivity. The chemical and physical properties of the material were verified by XRD, H₂-TPR, XPS, BET and SEM techniques. The material was electrochemically characterized as a cathode by EIS, obtaining promising ASR values (0.19 Ωcm² at 800 °C). Furthermore, CFMO stability under different atmosphere conditions was confirmed by EIS investigation at different oxygen partial pressures. The material was activated by deposition of FeO_x nanoparticles through co-deposition and infiltration; the effect of increasing amount (10 and 15 wt %) was also studied. The Ca₂Fe_{1.95}Mg_{0.05}O₅ based nanocomposites well perform as cathode materials and the electrocatalytic reduction of oxygen is enhanced by iron oxide. This is confirmed

* Corresponding author.

E-mail address: enrico.squizzato.1@phd.unipd.it (E. Squizzato).<https://doi.org/10.1016/j.ijhydene.2021.05.020>

0360-3199/© 2021 Hydrogen Energy Publications LLC. Published by Elsevier Ltd. All rights reserved.

Available online at www.sciencedirect.com

ScienceDirect

journal homepage: www.elsevier.com/locate/hydro

Exsolution in Ni-doped lanthanum strontium titanate: a perovskite-based material for anode application in ammonia-fed Solid Oxide Fuel Cell

Jonathan Cavazzani^{a,*}, Enrico Squizzato^a, Elena Brusamarello^a, Antonella Glisenti^{a,b}

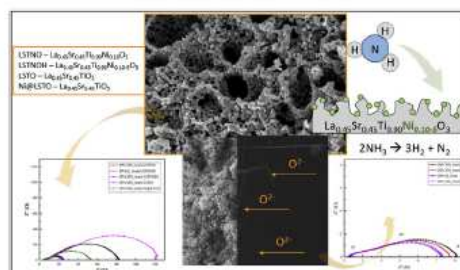
^a Department of Chemical Sciences, University of Padova, Via F. Marzolo 1, 35131, Padova, Italy

^b ICMATE - Department of Chemical Sciences, University of Padova, Via F. Marzolo 1, 35131, Padova, Italy

HIGHLIGHTS

- Successful Ni exsolution in Lanthanum Strontium Titanate confirmed by XRD, SEM, XPS.
- Powder morphology not affected by Ni doping and exsolution.
- Ni nano-decoration of LaSrTiO₃ by exsolution boosts electrochemical performances.
- Exsolution is much more effective than infiltration in decreasing polarization.
- Increasing the temperature, the cell performances using NH₃ or H₂ become similar.

GRAPHICAL ABSTRACT



ARTICLE INFO

Article history:

Received 29 November 2021

Received in revised form

4 February 2022

Accepted 15 February 2022

Available online 15 March 2022

Keywords:

Ammonia

Hydrogen

SOFC

Anode

ABSTRACT

Hydrogen represents the most conventional fuel to feed Solid Oxide Fuel Cells (SOFCs) for green energy production. However, hydrogen has some drawbacks which prevent the large-scale implementation. Research identified ammonia as promising hydrogen vector. Hereby, highly dispersed Ni nanoparticles are deposited on La-doped strontium titanate by exsolution, greatly affecting the electrochemical performance. The exsolved Ni-doped lanthanum strontium titanate ($\text{La}_{0.45}\text{Sr}_{0.45}\text{Ti}_{0.90}\text{Ni}_{0.10}\text{O}_3$ – LSTNOH) was largely characterized. XRD analysis detected 10 mol% of Ni doping has been successfully incorporated in to the perovskite structure and then released when exposed in reducing environment. SEM images show Ni nanoparticles highly dispersed on the surface. XPS confirms the presence of Ni on the surface after the exsolution and allows to exclude other detrimental diffusion towards the bulk. A LSTNOH derived composite based anode has been investigated through impedance spectroscopy using ammonia and hydrogen as fuel. It demonstrates best performances compared to the one obtained by Ni infiltration on LSTO ($\text{La}_{0.45}\text{Sr}_{0.45}\text{TiO}_3$)

* Corresponding author.

E-mail address: jonathan.cavazzani@phd.unipd.it (J. Cavazzani).

<https://doi.org/10.1016/j.ijhydene.2022.02.133>

0360-3199/© 2022 Hydrogen Energy Publications LLC. Published by Elsevier Ltd. All rights reserved.

Comparison of different infiltration amounts of CeO₂ inside Ni-YSZ anodes to improve stability and efficiency of Single-Chamber SOFCs operating in methane

Giovanni d'Andrea^{1,*}, Enrico Squizzato¹, and Antonella Glisenti^{1,2}

¹ Department of Chemical Sciences, University of Padova, Via F. Marzolo 1, 35131, Padova, Italy

² ICMATE - Department of Chemical Sciences, University of Padova, Via F. Marzolo 1, 35131, Padova, Italy

Abstract. Electrochemically active oxide-based anodes capable of working in Single-Chamber Solid Oxide Fuel Cells (SC-SOFCs) were developed. Their performance is related to the selectivity of the electrodes. Tests are carried out on lab-scale devices with YSZ pellets as solid electrolytes in electrolyte supported cells. Selecting methane as a fuel, a gas mixture in the ratio CH₄/O₂ = 2 was chosen. The Ni-YSZ (NiO:YSZ=60:40) anode was optimized through CeO₂ nanocatalysts infiltration to enhance the anode catalytic activity and make its reduction easier. Several infiltration amounts were compared, from null to 15% of the electrode weight. Both symmetric and complete cells (with LSCF-based cathodes) were tested in H₂ and CH₄/O₂. For increasing amounts of infiltrated CeO₂, symmetric cells tests describe an area specific resistance (ASR) reduction from 40 Ω cm² to 1.7 Ω cm² in hydrogen and from 11 Ω cm² to 3.9 Ω cm² in the methane/oxygen mixture. While complete cells tests displayed an ASR drop from 30 Ω cm² to 2.9 Ω cm² in H₂, and from 8.7 Ω cm² to 4.3 Ω cm² in the methane/oxygen mixture, while OCP and power grew from 478 mV and 3.7 mW cm⁻² to 766 mV and 13 mW cm⁻².

1 Introduction

Single Chamber Solid Oxide Fuel Cells (SC-SOFCs) represent a particular branch of SOFCs technologies that aims to overcome the main flows of the dual chamber devices, mainly due to the sealing, that makes the device design more complex and make it hard to be employed for portable applications [1]. Some of the greatest benefits of single chamber SOFCs are the easier fabrication, the great potential for miniaturization, the easier preparation of a stack assembly and the presence of exothermic reactions to sustain the cell temperature [2,3]. Despite the advantages, the main challenges bound to this technology are the intrinsic necessity for highly selective and catalytically active materials, the lower fuel utilization and efficiency, due to parasitic reactions, and the risk of explosion due to fuel and air being mixed together at high temperatures [4,5]. These critical aspects made research on single chambers to become little appealing in the latest years [6], yet its employment for specific applications would make it a competitive technology, as in portable power applications [7], cogeneration [8] or in a context where the high fuel use efficiency is not a fundamental requirement, as sensors [9] or in residual fuel in engine exhaust [10].

Of all possible fuels, methane is a largely available and safe one. In fact, methane must undergo partial oxidation on the anode surface to produce syngas, which is the actual fuel [4,5]. Because of catalytic activity toward the partial oxidation of methane, Ni is the most used catalyst [11,12],

despite it is far from being an ideal catalyst [13,14]. Ni-YSZ is one of the most employed anodic materials, even though YSZ is not an ideal material for intermediate temperature applications, below 700°C [4], however, this ionic conductor has great chemical and mechanical stability. Metal oxides can boost the activity of the anode [15–17]. They are often investigated and represent ideal catalysts whenever balance between costs and performance improvement is reached. Doping with precious metals like Pd or Ru, is not a preferential option though. A material often accounted for in catalysis is CeO₂ [18], a promising material for improving Ni-YSZ anode efficiency. Different approaches have been followed to couple these materials, i.e. preparing a solid solution [19] and by infiltration [20]. In this last case, in the work of Yang *et al.* (2014), it was emphasized the stability of the infiltrated CeO₂ nano-catalysts, their ability to catalyse the deep oxidation of methane and their ability in helping the reduction of NiO to Ni. The infiltrated amount was 3% of the weight (3wt%) of the NiO-YSZ unreduced electrode. Aim of this work, was to test the correlation between the anode performance in SC-SOFCs and the increasing infiltration amount of CeO₂ into the electrode (3wt%, 6wt%, 9wt% and 15wt%). This was mainly done by means of Electrochemical Impedance Spectroscopy (EIS) where the spectra variation can give insights on a modified ability of the electrode to retain and conduct electrical charge and influence the reaction rate of the fuel. It was chosen to employ a CH₄/O₂=2 ratio for safety reasons, to work above the upper flammability level [2], and to avoid the redox

* Corresponding author: giovanni.dandrea.1@unipd.it

Exsolution in La and Ni co-doped strontium titanate: a suitable anode for running SOFCs on ammonia as alternative fuel

Jonathan Cavazzani^{1,*}, Enrico Squizzato¹, Elena Brusamarello¹ and Antonella Glisenti^{1,2}

¹Department of Chemical Science, University of Padova, Via F. Marzolo 1, 35131, Padova, Italy

²ICMATE - Department of Chemical Science, University of Padova, Via F. Marzolo 1, 35131, Padova, Italy

Abstract. Ammonia exhibits interesting features as fuel to feed Solid Oxide Fuel Cell. Herein, Ni and La co-doped strontium titanate was synthesized using wet chemistry route. Ni nanoparticles emerged via exsolution in reducing environment to decorate the surface. X-Ray Diffraction measurements exhibit perovskite structure was also preserved after the exsolution, as expected. H₂ – Temperature Programmed Reduction highlights the great resistance of titanates in anode operation condition. Ammonia conversion in nitrogen and hydrogen were investigated by catalytic tests. It begins to decompose at 560°C and the full yield was achieved at 720°C. Electrochemical measurements were recorded at 800°C using 10% of ammonia in Ar. They were analysed through the model of equivalent circuit and two processes were attributed. Results certify Ni exsolution strongly enhances the hydrogen oxidation and the total polarisation resistance in ammonia approaches to the one in hydrogen.

1 Introduction

During the current transition towards renewable energy sources, the demand for versatile devices able to store and re-use the excess of energy production is increasing [1–4]. In this scenario, Solid Oxide Fuel Cells (SOFCs) exhibit tempting features, such as high efficiency and low environmental impact [5–8].

Although hydrogen is the most conventional and studied fuel for this application, ammonia is constantly gaining more attention as alternative [9–14]. Ammonia is mainly synthesized through Haber-Bosch method, however more environmentally friendly routes are under investigation [15,16]. Ammonia is largely used in household cleaning products, fertilizers and nitric acid production [17]. It does not present severe safety concerns: it is toxic but human nose is sensible below a concentration of 1 ppm so the detection of leakage is easy [9]. In addition, ammonia has a narrower combustion range than hydrogen [14]. All these features promote the ammonia as an interesting hydrogen carrier and then it deserves a deeper study in SOFC technology.

In 1980, Farr and Vayenas [18] investigated the odds to synthesize NO and obtaining an electrical current during the same process. In the early 2000s, Wojcik and co-workers [19] explored the use of ammonia as fuel to feed a SOFC and they collected promising results.

It has been proposed a two-step mechanism when anode is fed by ammonia in oxygen anion conducting SOFC: first ammonia cracks in nitrogen and hydrogen via thermal decomposition mediated by a catalyst. Then the hydrogen diffuses across the interface reacting with the

oxygen to form water [12]. Ni cermet, such as Ni-Yttria Stabilized Zirconia (YSZ) and Ni-Gadolinium Doped Ceria (GDC), have been largely studied for running SOFC on ammonia as fuel [20–23].

Hereby, we propose Ni and La co-doped strontium titanate as anode material. We already investigated SrTiO₃ – based materials showing interesting properties for this application [24]. In the current work, we try to impart new functionalities using the method of the exsolution [25–29]. It has been recently employed for anode application in SOFC technology and it allows to realize high dispersive nanoparticles on the surface of the catalyst for preventing drawbacks connected to sintering in long-term operation [30,31].

Ni exsolution in titanates – based materials have been studied as alternative to state-of-art Ni-YSZ for working as anode in high temperature SOFC [27,32,33]. Lanthanum aims to promote the formation of the redox couple of the titanium Ti (IV)/ Ti (III) [34].

In this contribution, we focus our attention on the response of La and Ni co-doped titanates towards ammonia decomposition. The material demonstrates suitable features in reducing environment under operation condition preserving the perovskite structure, as H₂ – Temperature Programmed Reduction (TPR) establish. Catalytic tests prove a totally conversion of ammonia at working temperature (800°C), although the whole decomposition, in nitrogen and hydrogen, occurs at 720°C. From the measurements Ni exsolved nanoparticles do not affect the catalytic activity towards the ammonia cracking. Instead, Ni nanoparticles strongly boost the electrochemical performances, as detected in

Acknowledgements:

La prima persona che voglio ringraziare per questa tesi è sicuramente la Prof.ssa Antonella Glisenti. Se non fosse stato per te non avrei mai intrapreso l'entusiasmante strada del dottorato. La tua umanità e la tua dedizione al lavoro dovrebbero essere d'esempio per ogni docente. Al di là del tuo aiuto dal punto di vista professionale, sempre fondamentale e illuminante, quello per cui ti voglio ringraziare è per tutte quelle volte che sono entrato nel tuo ufficio abbattuto e triste, ma, dopo averti parlato, ne uscivo sollevato e sorridente. Grazie davvero!

Poi sicuramente questo lavoro non sarebbe lo stesso se non ci fosse stata la Dott.ssa Caterina Sanna. Infatti, difficilmente avrei ottenuto gli stessi risultati dal mio lavoro senza averti conosciuto alla conferenza di Napoli. Costruire insieme una collaborazione e portare a casa i risultati che abbiamo ottenuto non è stato semplice, ma ne sono davvero orgoglioso. Non per ultimo ho guadagnato un'ottima amica con cui andare per le calli veneziane o per i carugi genovesi a bere spritz al Select o al Camatti.

Ovviamente ringrazio anche la Prof.ssa Paola Costamagna che ha sempre creduto nella collaborazione tra i nostri gruppi di ricerca. L'unico rimpianto è non esserci mai potuti incontrare di persona, ma grazie per il suo sorriso che ha sempre accompagnato le nostre riunioni su Teams.

I would like to say thanks to Prof. Peter Holtappels and Prof. Marie Lund Traulsen for the big opportunity that they gave me to come to Denmark. It was not so easy, considering all the difficulties that we faced, but I am so happy to have spent those 3 months at DTU. Thanks also to all the new friends that I've made there, especially: Ana, Anil, Caio, Fernanda, Georges, Niki and Oscar! Even Ballerup was beautiful with you!

Finalmente posso nominare il fantastico gruppo di ricerca in cui ho lavorato per questi anni: il gruppo Impact! Vi ringrazio tutti: da quelli che ormai non fanno più parte, ai nuovi tesisti! Più che con dei colleghi ho lavorato con degli amici e mi ritengo molto fortunato. Nominarvi tutti è difficile, ma questi ringraziamenti devono sentirsi propri di ciascuno con cui ho trascorso del tempo in ufficio. Mi sento di dovermi scusare se nell'ultimo anno non ho messo il 100% come nei primi due nella gestione del laboratorio. Per fortuna che ci sono degli ottimi

membri che si prendono cura, ciascuno con le sue caratteristiche, di tutti gli aspetti del gruppo.

Spostandomi dall'aspetto lavorativo, devo ringraziare la mia famiglia. Mamma e papà per il loro appoggio incondizionato nelle mie scelte e i loro consigli, che anche se non sempre seguiti, sono stati sempre molto d'aiuto. Ringrazio Ilario che è sempre stato per me un esempio. Ringrazio Michela, Vittoria, Veronica e Maria Grazia, che siete entrate in questa famiglia portando tanta gioia e felicità.

Ringrazio anche la nuova famiglia in cui sono entrato a far parte! Grazie Daniela, Elio, Martina, Alberto e Francesca per il vostro sostegno e allegria.

Ringrazio tutti i miei amici che mi hanno dedicato il loro tempo. Sono davvero fortunato ad avervi! Anche qui nominarvi tutti è difficile, ma più sono le birre che ho bevuto e più sentitevi ringraziati. (Nicola, mi sa che meriti menzione d'onore, contando anche le abbuffate! Buon viaggio in Svezia!)

Infine, ringrazio la persona più speciale: Arianna! È difficile spiegare quanto tu mi sia stata d'aiuto in questi anni! Grazie per tutte le volte che mi hai spronato a dare il meglio di me e a fare cose che altrimenti non avrei mai fatto. Grazie per avermi mostrato cos'è la felicità, la gioia di vivere. Grazie per tutto l'aiuto che mi hai dato quando ero in difficoltà, davvero! Riassumendo: grazie per tutto l'amore incondizionato che mi dimostri ogni giorno!

*“Linea alla regia, torneremo
per la grande festa del podio”
(G. Mazzoni)*